Conception pour la fabrication de micro-treillis polymères pour des structures de micro-aérostats

par

Louis CATAR

THÈSE PAR ARTICLES PRÉSENTÉE À L'ÉCOLE DE TECHNOLOGIE SUPÉRIEURE
COMME EXIGENCE PARTIELLE À L'OBTENTION
DU DOCTORAT EN GÉNIE
Ph.D.

MONTRÉAL, LE 7 NOVEMBRE 2024

ÉCOLE DE TECHNOLOGIE SUPÉRIEURE
UNIVERSITÉ DU QUÉBEC

PRÉSENTATION DU JURY

CETTE THÈSE A ÉTÉ ÉVALUÉE

PAR UN JURY COMPOSÉ DE:

M. David St-Onge, directeur de thèse
Département de Génie Mécanique de l'École de Technologie Supérieure de Montréal

M. Ilyass Tabiai, codirecteur
Département de Génie Mécanique de l'École de Technologie Supérieure de Montréal

M. Georges Ghazi, président du jury
Département de Génie des Systèmes de l'École de Technologie Supérieure de Montréal

M. Vladimir Brailovski, membre du jury
Département de Génie Mécanique de l'École de Technologie Supérieure de Montréal

M. David Mélançon, examinateur externe
Département de Génie Mécanique de l'École Polythechnique de Montréal

ELLE A FAIT L'OBJET D'UNE SOUTENANCE DEVANT JURY ET PUBLIC

LE 9 SEPTEMBRE 2024

À L'ÉCOLE DE TECHNOLOGIE SUPÉRIEURE

REMERCIEMENTS

Je souhaite tout d'abord remercier mes superviseurs : mon directeur de thèse, le professeur David St-Onge et mon codirecteur, le professeur Ilyass Tabiai, qui m'ont tous deux conseillé et guidé pendant toutes ces années de recherche. J'ai pu compter sur leur disponibilité et leurs observations éclairées pour réaliser ce travail.

Je souligne également l'aide du personnel technique de l'ÉTS qui fut précieusement utile pour accéder aux ressources des laboratoires d'essais. En particulier l'aide de monsieur Serge Plamondon qui s'est montré particulièrement pédagogue et disponible pour supporter les travaux du laboratoire.

Merci pour le support amical de mes collègues du laboratoire INIT Robots [1] et du LIPEC [2] tout au long de ces quatre années passées à Montréal. Merci aux stagiaires et étudiants que j'ai eus plaisir à encadrer et qui ont contribué lors de ce projet : Eddie O., Ilyes H., Vanshaj M., Pierre W., Sebastián Z.R. et Pierre G. Je tiens également à souligner les nombreuses collaborations avec les laboratoires AML [3] (Pr. Nahon) à McGill et NXI Gestatio [4] (Pr. Reeves) à l'UQAM.

Pour terminer, cette thèse n'aurait pas pu voir le jour sans l'aide de mes proches aux compétences scientifiques inversement proportionnelles à la qualité de leur soutien moral, aux encouragements et à la confiance donnée. Tout d'abord, mon épouse Camille qui m'a accompagné et soutenu dans cette aventure transatlantique. Merci pour ton indéfectible confiance et aux sacrifices consentis. Je n'oublie évidemment pas mes parents, frères et sœur et mon grand-père, soutiens dès mes premiers pas dans les études supérieures qui s'achèvent enfin.

---

[1] https://initrobots.ca/equipe

[2] https://www.etsmtl.ca/en/labs/lipec

[3] https://aerospacemechatronics.lab.mcgill.ca/

[4] https://www.nxigestatio.org/

Conception pour la fabrication de micro-treillis polymères pour des structures de micro-aérostats

Louis CATAR

RÉSUMÉ

L'allègement de structure est un enjeu récurrent en ingénierie. La volonté de réduire la consommation énergétique, accroître les capacités d'emport ou améliorer les performances sont autant de raisons de désirer des conceptions toujours plus optimisées. Les micro-treillis, par leur extrême finesse, amènent cette quête aux plus petites échelles de la fabrication additive. Avec ce sujet, l'idée est de connecter la conception avec les performances des structures en micro-treillis polymères en prenant comme support de travail les petits aérostats. Outre les nouvelles opportunités offertes par le développement de ce type d'aéronef, les dirigeables ont cette particularité d'être extrêmement sensibles à la masse de ses composants. Aucun compromis n'est autorisé et chaque nouveau gramme est un litre supplémentaire d'hélium à ajouter. Cette exigence fait des aérostats le terrain d'expérimentation idéal pour chercher de nouvelles solutions.

En un premier lieu, plusieurs techniques de fabrication additive à base de résines photosensibles ont été étudiés mécaniquement à l'aide de tests de micro-traction quasi-statique sur des structures en micro-treillis. Les essais ont été associés à une mesure des déformations plein champ. Les procédés ont également fait l'objet d'une étude de l'anisotropie de la fabrication pour mieux comprendre leur impact sur les propriétés mécaniques des micro-treillis.

Dans un deuxième temps, une méthodologie de priorisation multicritères est présentée. Cet outil permet de comprendre et de visualiser l'impact de chaque exigence d'un cahier des charges complexe sur le choix de la combinaison finale. Elle permet de rationaliser la prise de décision quelles que soient les métriques et les domaines : critères mécaniques, manufacturiers, de forme, etc. Un dirigeable est un objet physique complexe et cette méthode permet d'accélérer le processus de développement.

Dans un troisième temps, des structures en micro-treillis ont été caractérisés pour leurs propriétés d'absorption d'énergie d'impact. Pour ce faire, un banc de test a été spécialement conçu et fabriqué pour s'adapter aux conditions de vol d'un petit aéronef léger. Les résultats ont été utilisés pour sélectionner les motifs, matériaux et compacités requises pour respecter les exigences d'emploi de l'aérostat.

Enfin, ce travail se termine par la création d'un dirigeable robotique rigide mais pliant adapté à l'exploration d'espaces étroits. Il intègre un exosquelette inspiré de l'origami pour procurer des propriétés uniques aux aérostats. Le processus de conception du robot a été automatisé pour optimiser sa forme en fonction de toutes les contraintes imbriquées de volume, fabrication ou encore de la mécatronique.

Mots-clés: fabrication additive, micro-treillis, aérostat, polymère

Design for Manufacturing of Polymer Micro-Lattices for Micro-Aerostat Structures

Louis CATAR

ABSTRACT

Structural lightening is a recurring challenge in engineering. The will to reduce energy consumption, increase carrying capacity, or improve performance are all reasons to aim for ever more optimized designs. Micro-lattices, with their extreme thinness, bring this quest to the smallest scales of additive manufacturing. With this subject, the idea is to connect design with the mechanical performance of polymer micro-lattice structures using small aerostats as the working platform. Besides the new opportunities offered by the development of this type of aircraft, airships have the particularity of being extremely sensitive to the mass of their components. No compromise is allowed, and every new gram is an additional liter of helium to be added. This requirement makes aerostats the ideal testing base for seeking new solutions to optimize mass.

First, several additive manufacturing techniques based on photosensitive resins were mechanically studied using quasi-static micro-tension tests on micro-lattices structures. The tests were associated with full-field deformation measurements. The processes were also the subject of a study on the anisotropy of manufacturing to better understand their impact on the mechanical properties of micro-lattices.

Secondly, a multi-criteria prioritization methodology is presented. This tool allows understanding and visualizing the impact of each requirement of a complex specification on the choice of the final combination. It helps to rationalize decision-making regardless of metrics and domains : mechanical criteria, manufacturing, shape, etc. An airship is a complex physical object, and this method accelerates the development process.

Thirdly, micro-lattice structures were characterized for their impact energy absorption properties. For this purpose, a test bench was specially designed and manufactured to adapt to the flight conditions of a lightweight indoor aircraft. The results were used to select the patterns, materials, and compacity required to meet the operational requirements of the aerostat.

Finally, this work concludes with the design, manufacturing and assembly of a rigid but foldable robotic airship adapted for exploring narrow spaces. It incorporates an exoskeleton inspired by origami to provide unique properties to the aerostats. The robot design process was automated to optimize its shape according to all intertwined constraints of volume, manufacturing or mechatronics

Keywords: additive manufacturing, micro-lattices, aerostat, polymer

TABLE DES MATIÈRES

Page

INTRODUCTION 1

CHAPITRE 1 REVUE DE LITTÉRATURE 3
1.1 Micro-treillis 3
1.1.1 Définition 3
1.1.2 Critère de Maxwell 4
1.1.3 Propriétés mécaniques des structures cellulaires 5
1.2 Fabrication additive de polymères 7
1.2.1 Définition 7
1.2.2 Procédés 7
1.2.3 Techniques de fabrication non-conventionnelles 11
1.2.4 Limites des procédés 12
1.2.5 Conception pour la fabrication additive 12
1.3 Dirigeables : typologies et structures standards 14
1.3.1 Différentes stratégies de classement 14
1.3.2 Structure 14
1.3.3 Flottabilité 15
1.3.4 Configuration 16

CHAPITRE 2 OBJECTIFS DE RECHERCHE 17
2.1 Opportunités de recherche 17
2.2 Objectifs 19
2.2.1 Objectif 1 : Caractérisation mécanique de micro-treillis polymères en résine photosensible 19
2.2.2 Objectif 2 : Blocs fonctionnels ultralégers à base de micro-treillis pour aérostat modulaire en milieu restreint 20
2.2.3 Objectif 3 : Procédure de rigidification ultralégère d'une enveloppe d'un aérostat pour espaces étroits 20

CHAPITRE 3 TENSILE TESTS OF DIFFERENT FAMILIES OF ULTRA-LIGHTWEIGHT PHOTOSENSITIVE POLYMER MICRO-LATTICES 23
3.1 Avant-propos 23
3.2 Résumé 28
3.3 Abstract 29
3.4 Introduction 29
3.5 Materials and Methods 35
3.5.1 Micro-lattice patterns selection 35
3.5.2 Specimen design for micro-traction tests 36
3.5.3 AM technology selection for micro-lattice manufacturing 38

3.5.4 Network relative density measurements 40
3.5.5 DIC methodology 40
3.5.6 Total number of samples and distribution 41
3.6 Results and discussion 41
3.6.1 Bulk material characterization 41
3.6.2 Pattern relative density 44
3.6.3 Strength and elasticity of the patterns 45
3.6.4 DIC analysis 48
3.6.5 Impact of the printing direction 51
3.7 Conclusion 53

CHAPITRE 4 ADDITIVE MANUFACTURING STRATEGY FOR ULTRA-LIGHTWEIGHT HIGH VALUE-ADDED COMPONENTS 55
4.1 Avant-propos 55
4.2 Résumé 55
4.3 Abstract 56
4.4 Combining design and manufacturing methodologies 58
4.4.1 What : Design thinking 58
4.4.2 How : Double diamond method 60
4.4.3 Unified evaluation metric 62
4.4.4 Evaluation of the manufacturing processes 63
4.5 The indoor airship use case 64
4.5.1 Discover : Empathy exploration 66
4.5.2 Define : Airship design requirements 67
4.5.2.1 Requirements interdependence 68
4.5.3 Define : select additive manufacturing technology 69
4.5.4 Develop : Requirements evaluation 70
4.5.5 Develop : Manufacturing technology prototypes 71
4.5.6 Deliver : Rank and sort 73

CHAPITRE 5 POLYMER MICRO-LATTICE BUFFER STRUCTURE FREE IMPACT ABSORPTION 79
5.1 Avant-propos 79
5.2 Résumé 80
5.3 Abstract 81
5.4 Introduction 82
5.5 Micro-lattices energy absorption behavior 86
5.6 Methods and materials 88
5.6.1 Patch design 88
5.6.2 Patch manufacturing 91
5.6.3 Patch compression tests 93
5.6.4 Custom impact bench 94
5.7 Results and discussion 96
5.7.1 Compression tests 96

5.7.2 Impact tests 99
5.7.3 Specific energy absorption and efficiency 102
5.7.4 Association of multiple micro-lattices 104
5.8 Conclusion 106

CHAPITRE 6 EXPLORING THE DEPTHS : DESIGN OF THE FOLDABLE CAVERNAUTE AIRSHIP FOR LONG-LASTING SUBTERRANEAN MISSIONS 109
6.1 Avant-propos 109
6.2 Résumé 110
6.3 Abstract 111
6.4 Introduction 111
6.5 Related work 114
6.5.1 Rigid airship designs 114
6.5.2 Airship design pipeline 115
6.5.3 Folding airships 116
6.5.4 Impact absorption for blimp 118
6.6 CAVERNAUTE design 120
6.6.1 Kresling-inspired structure 120
6.6.2 Exoskeleton design for manufacturing 123
6.6.3 Parametric design 126
6.7 Flight control 128
6.8 Use case : cave exploration as an artistic manifestation 131
6.8.1 The cave 131
6.8.2 Mapping the cave 133
6.8.3 Applied parametric design 135
6.8.4 Benefits of origami properties for an indoor airship 139
6.8.5 Controller Optimization 141
6.8.6 Simulation 144
6.8.7 Deployement 147
6.9 Conclusion 149

CONCLUSION ET RECOMMANDATIONS 153

ANNEXE I MODÉLISATION D'UN DIRIGEABLE 161

ANNEXE II SCRIPT D'ANALYSE DES RÉSULTATS DU LOGICIEL DICE 175

ANNEXE III SCRIPT DE CLASSEMENT DE CONFIGURATIONS MULTICRITÈRES 181

ANNEXE IV FABRICATION DE DIRIGEABLE PYRAMIDAL EN MYLAR ET CONCEPTION DE GONDOLES ULTRALÉGÈRES 185

ANNEXE V PROTOCOLE DE FABRICATION DES MICRO-TREILLIS EN RÉSINE PHOTOSENSIBLE DU CHAPITRE 5 189

ANNEXE VI PROTOCOLE D'INITIALISATION ET D'UTILISATION DU BANC D'ESSAI D'IMPACT LIBÉRÉ 193

BIBLIOGRAPHIE 197

LISTE DES TABLEAUX

Page

Tableau 3.1 Machines and associated materials selected. 39

Tableau 4.1 Evaluation of design criteria for simplified geometries - in parenthesis the value resulting from the simulation or the calculations and transformed into a score out of 100 points according to the unified scoring formula 70

Tableau 5.1 Diameter of the struts or thickness of the shell of micro-lattices in millimeters to keep all patches at 2 g weight 90

Tableau 5.2 Energy and velocity required to break rigid micro-lattices. 105

Tableau 6.1 Input parameters editable in Grasshopper, with values used in the current specifications. Some are fixed by the mission, others can be chosen by the user (number of motors, multi-body airship, etc.) and finally, three parameters can be optimized according to the configuration (n, m, λ). 128

Tableau 6.2 Extra-payload, height and bending angle relative to $\lambda = 0.9$ for the selected configurations. 138

Tableau 6.3 Power consumption for each of the devices used for CAVERNAUTE . 141

LISTE DES FIGURES

Page

Figure 1.1 les structures dominées par la flexion se trouvent le long d'une trajectoire de pente 1.5. Les structures dominées par l'étirement se trouvent le long d'une trajectoire de pente 1 (Ashby, 2006) 5

Figure 1.2 Comportement typique d'un micro-treillis soumis à la compression (Maconachie, Leary, Lozanovski, Zhang, Qian, Faruque & Brandt, 2019) 6

Figure 1.3 Schéma de fonctionnement des machines d'agrégation de résine photosensible. Pour une même technique, on remarque une grande variété de façons de solidifier la même forme de matière (résine photosensible). 9

Figure 1.4 Différence intrinsèque entre un dirigeable souple (en haut) dont la forme est définie par la pression du gaz interne et le dirigeable rigide avec une forme qui peut être choisie (en bas). Illustration tirée Stockbridge, Ceruti & Marzocca (2012). 15

Figure 3.1 Machine de micro-traction pour les essais de caractérisation mécanique des micro-treillis. Équipé avec un dispositif pour la corrélation d'image et la mesure fine de l'élongation. 24

Figure 3.2 Déplacement d'une section de micro-treillis BCC (4×4 cellules). La FEA a été réalisée sur *Autodesk Fusion 360*® montrant les déplacements théoriques des entretoises du motif. On peut visualiser les effets de bord sur les quatre coins. La rupture est donc susceptible de commencer aux bords. La manière dont la charge est appliquée est montrée dans le zoom. 26

Figure 3.3 Analyse par éléments finis réalisée avec Abaqus : représentation de la distribution des contraintes de Von Mises sur une cellule de chacun des motifs étudiés. Pour le même matériau, la conception de la cellule a un fort impact sur le comportement structurel. Le matériau est un matériau élastique « custom » créé à partir des propriétés mécaniques obtenues à partir des résultats expérimentaux de la résine SLA standard grise de Formlabs® présentés dans la Section 3.6.1. Le motif *(A)* est BCC, *(B)* est Gyroïde, *(C)* est Réentrant, *(D)* est Kelvin et *(E)* est HPD . 27

Figure 3.4 Different families of micro-lattices : strut-based unit cells (A), triply periodic minimal surface (TPMS) unit cells (B) and shell lattice unit

cells (C). Lattices A and C have discrete junctions, while lattice B is made of continuous surfaces. 31

Figure 3.5 Lattices selection for our micro-traction tests campaign. Reentrant and Voronoi micro-lattices are not self-supporting. They will be manufactured on a single printing machine that has the capacity to build unsupported geometries. The color of the patterns corresponds to the color of the plots in the results of this paper. 36

Figure 3.6 Specimen design : On the left, a batch of specimens made on the Stratasys ® PolyJet Objet30 printer. From left to right : BCC, Kelvin cells, HPD, Voronoï, reentrant and gyroid specimens. On the right, is a detailed view of the micro-lattice specimen geometry. The thickness (t) of the struts is functionally graded to ensure the breaking zone appears in the middle of the lattice with a quadratic function 37

Figure 3.7 Left : Tensile test results with standard specimens (3 repetitions — 1-dev standard). The tensile specimen geometry is shown in the top-left corner, with a circular section of 2 mm in diameter and 100% infill. The sample is loaded along the printing Y axis. Right : DMA test results with the three materials-printer combinations used. Curve colors show the mechanical property and curve bullets, the printing process. We observe significant variability between each UV resin in the mechanical property. SLA is stiffer than PolyJet resin, which is itself stiffer than MSLA resin 43

Figure 3.8 Relative density measurement for the six selected micro-lattices. Values are given for a single cell of each pattern. In the top left, density measurement of the raw resins. 44

Figure 3.9 Tensile test results. Left : BCC, gyroid, HPD and Kelvin micro-lattices made on MSLA, SLA and PolyJet printers. Right : re-entrant pattern and Voronoi that could only be achieved with the PolyJet. Measurements' uncertainties of the sample repetitions are represented by lighter-colored envelopes around each curve. The re-entrant pattern shows the highest load, and the Voronoi one. 46

Figure 3.10 Work for each micro-lattice pattern during their tensile tests until 95% of the first failure. It corresponds directly to the mechanical properties targeted for a micro-lattice shell : the ability to resist stresses without damage thanks to structural deformation. 47

Figure 3.11 DIC time-lapse : visualization of ε_1 strain field. The first column represents the unloaded state. The second presents the moment right

before the initiation of rupture, and the last one is the sample right after failure. After rupture, the tracking is lost due to the sudden displacement of struts at the breaking point. The white squares represent areas that are detailed in Fig.3.12 where the deformations in the principal directions are represented by the computation of θ_p. The white circles indicate the initial failure zone. 49

Figure 3.12 Representation of the main strain directions for four of the six lattices : BCC (A), HPD (B), Kelvin (C) and gyroid (D). We see the transition zones, *i.e.,* change of direction of strain, which helps predict the location likely to fail first. 50

Figure 3.13 Multi-directional X, Y and Z tensile tests. Left : MSLA printer — This material shows a near-isotropic behavior. Right : SLA printer — we observe strong anisotropy. 51

Figure 3.14 Multi-directional X, Y and Z tensile tests for the PolyJet printer — These tests show significant anisotropies. 52

Figure 4.1 Double diamond tool diagram adapted to an engineering approach using AM inspired from Santos, González Lema, Miño Puga, Párraga & Calderon (2017), Preez, Futerman & Barnes (2014) and Segonds (2019) 60

Figure 4.2 Few concepts were extracted from the brainstorming. Fish-box concept (1), multi-body airship (2), deformable (3), jellyfish inspired (4) and improved traditional airship (5) 66

Figure 4.3 3D printers used. From left to right we find the MSLA, the SLA and the PolyJet (photos of the machines relatively not to scale) 69

Figure 4.4 Work for each pattern selected. The Gyroid stands out from the previous graphical representations with its ability to support large constraints and a consequent displacement. 72

Figure 4.5 Criteria tree for an indoor airship project. Each floor has its own criteria. Some of them are dependent on those below and are therefore calculated by combining the corresponding performance indexes. 73

Figure 4.6 Manufacturing complexity based on machines characteristics and operations 74

Figure 4.7 Performance index. Each combination is analyzed and sorted. 75

Figure 5.1 Coquille uniformément converte de micro-treillis utilisant des cellules Voronoi très larges pour une sphère de 70 cm de diamètre 80

Figure 5.2 Micro-lattices pattern selection : Face Centered Cubic—FCC (**A**), Gyroid—GY (**B**), Kelvin—K (**C**), and Diamond—D (**D**) and example of the three levels of compactness to fill the 15 × 15 × 15 mm^3 volume with the FCC pattern. The number of micro-lattice stages changes, but the diameters of the struts are adapted to have the same relative mass. The patch samples have a total volume of 45 × 45 × 15 mm^3. 89

Figure 5.3 Figure nomenclature : There are so many possible combinations that we've created this nomenclature, which serves as a standard for all the figures in this paper. 91

Figure 5.4 Patch design : (**A**) Optimized sole plate design, (**B**) Furrows section with minimized surface in contact with the print bed, (**C**) a cross-section of the furrows grooves, and (**D**) the detail of the successive part layers. 93

Figure 5.5 Compression test device with diamond (D) sample and view of a patch (FCC_50 sample) 94

Figure 5.6 Overview of the custom impact test bench. The first main rail (green) is used to propel the second rail (red). The sample trolley (yellow) holds the sample (blue). Just before impact, it is released to translate freely along the red rail. 95

Figure 5.7 Load-Displacement of softer (**A**) and most rigid (**B**) configurations (not same scale for readability). Both sides present similar behaviors : peaks of strength associated with loading plateaus. These peaks are particularly noticeable with the FCC pattern, directly correlated to the number of layers. Measurements' uncertainties of the three samples' repetition are represented by the colored shaded area around each curve. We deliberately did not represent the final consolidation part of the compression test to better highlight the initial variations. Therefore, the deformation stops at 10 mm and load above 100 N. 97

Figure 5.8 Stiffness score for all tested combinations, showing a wide range of performances. On the right side of the graph : micro-lattices made of flexible materials obtain the highest score. 98

Figure 5.9 Force with respect to displacement for the FCC micro-lattice with a compactness of 75. The curves show results for the soft material (left : A & B) and the rigid material (right : C & D) both for the impacts (top : A & C) and the compression (bottom : B & D). Under the curve,

in red, the absorbed energy before the rupture of the micro-lattice is represented. Measurements' uncertainties of the three samples' repetition are represented by the colored shaded area around each curve. Different Focus Areas (FA) are highlighted in orange to support the analysis of (C). 100

Figure 5.10 Time-lapse of the impact of a rigid (R) and flexible (S) sample. The outcome of the impact is significantly different, with the rigid micro-lattice exploding and the flexible micro-lattice deforming without breaking. The first force peak corresponds to FA n°1 and the second force peak to FA n°3 in Fig. 5.9. 101

Figure 5.11 SEA of micro-lattices specimens in quasi-static (blue shaded area) and impact (brown shaded area) tests. Rigid and soft material show an inverted tendency between the two test protocols due to the change in loading speed. 103

Figure 5.12 Energy absorption efficiency of our micro-lattices in comparison with existing works. We address the lowest density with a significant distribution of efficiency. 104

Figure 5.13 Result of possible associations between rigid and soft micro-lattices. Most combinations with rigid material and compactness 50 or soft material and compactness 150 are eliminated by the two association criteria. 106

Figure 6.1 Origami folding pattern. Valley creases are shown in dotted green and mountain creases in solid blue. 117

Figure 6.2 Score obtained for each micro-lattice combination based on the tests presented done by Catar, Tabiai & St-Onge (2024a). The FCC_75 combination achieves the highest score, followed by the D_75 and K_75 patterns, which are mechanically interesting but less suitable for mass production due to lower print success rates. 119

Figure 6.3 Elegoo® print bed with twenty patches printed at once 120

Figure 6.4 Folding motion of a Kresling pattern ($n = 7,\ m = 2,\ \lambda = 0.9$). Folding follows a shearing movement. Due to segment symmetry, there is only pure translation for each bi-segment. 121

Figure 6.5 Kresling geometrical parameters of one segment ($n = 6,\ m = 1$). α is the angle of rotation to unfold the geometry between the folded *(0)* and unfolded *(1)* state. The valleys are in green and the mountains in blue. $\alpha_{(0)} = 2\lambda\gamma$ and $\alpha_{(1)} = 2(1-\lambda)\gamma\ \forall\lambda > 0.5$ 122

Figure 6.6 Evolution of the length of h and b as a function of the bending angle α. With the geometric description, the diagonal d_g and the sides of polygons s do not vary as a function of α. However, this variation in b creates a constraint that can be represented in Fig. 6.8 123

Figure 6.7 Normalized energy E_S as a function of the relative height of a Kresling segment. This shows the bistability between the folded and unfolded configurations. 123

Figure 6.8 Exoskeleton tube junction : (a) simple and (c) to host lattices. Manufacturing features are highlighted in blue. Sub-figure *(c)* shows the micro-lattices junction with the micro-lattices soil *(d)* return spring and ball joint connection. Sub-figure *(e)* shows the micro-lattice buffer structure. 124

Figure 6.9 Diagram of the CAVERNAUTE design and manufacturing pipeline. The geometric capabilities of the Grasshopper software combined with Rhino are mixed with mathematical capabilities to create a pipeline that considers the many multidisciplinary constraints of a foldable airship design. 127

Figure 6.10 Control scheme, the SMA of the applied force is reintroduced in the controller before being applied to the system to reduce steady-state errors. 130

Figure 6.11 Saint-Léonard “Aquatic part”. The three places where U-turns are possible are indicated by circular arrows. Ceiling heights are indicated at various checkpoints. The water level varies according to season and weather. 132

Figure 6.12 Geometric dimensions constrained by the cave. The folded height H_0 and diameter D of the CAVERNAUTE are dictated by the narrow passage to the exploration zone. The photo shows the tool used to measure and validate the ability to pass with the CAVERNAUTE. 133

Figure 6.13 On top, a photo of the device with two LiDARs. Bottom left, is an in-cavern photo of the device with three LiDARs, and the bottom right is in use with remote SSH access with a rugged tablet. 134

Figure 6.14 CAVERNAUTE footprint in the exploration area mapped by the team .. 135

Figure 6.15 Design window map and projection. Configurations that float (Payload > 0) and respect the geometric constraints of the cavern are highlighted in green. 137

Figure 6.16 Display of the weight distribution for the 30 realistic configurations. The red stars represent the best choice of the pair n, m. Here, respectively, n = 7 and m = 4. 137

Figure 6.17 Schematic of all CAVERNAUTE's design and motor position. The photo at bottom left shows the actual assembly of the side-mounted motor with carbon tube structure and micro-lattice patch. 139

Figure 6.18 Schematic of all CAVERNAUTE's mechatronic : components with gray backgrounds are on the ground. The external camera is only for retransmitting the artistic installation. 142

Figure 6.19 Relation between flight velocity and estimated total energy consumption (in blue). The total available energy provided by the battery is presented in the dashed red line. 143

Figure 6.20 Motion in the Z-axis. The top graphs present the position, for the different SMA durations. The bottom graph presents the velocity achieved (v_z). 145

Figure 6.21 Motion in the X-axis. The two graphs present the position to achieve the desired position of 2 m, and the effect of the SMA terms. 146

Figure 6.22 Motion in the X-axis. The two graphs present the velocity (vx) while moving towards the position of 2 m, presenting the effect of the SMA terms. 146

Figure 6.23 Steps of the CAVERNAUTE deployment in the St-Léonard cave. After passing through the first narrow section (A), the folded CAVERNAUTE is connected to the hose (B) and filled with helium. The four Kresling cells unfold progressively during inflation (C-D-E-F). 147

Figure 6.24 Loss-rate measurements 148

Figure 6.25 CAVERNAUTE flight above water at St-Léonard aquatic section. The two side motor pods equipped with their micro-lattices patches can be seen. 149

Figure 7.1 Illustration d'impression non-planaire par Nayyeri, Zareinia & Bougherara (2022). Cette coupe montre une des stratégies d'impression non-planaire avec une adaptation dynamique de l'épaisseur de chaque couche. 158

Figure 7.2 Illustration — Solution de multi-MSLA utilisant un racleur. La paroi sépare la deux résines (bleu et orange) au sein du même bassin

et de la même zone d'impression. Cette configuration procure un encombrement limité et un impact limité sur la fabricabilité grâce à la stabilité de la zone d'impression (schématisation illustrée par Sebastián Zagal Rojas, stagiaire supervisé sur le projet). ……159

LISTE DES ABRÉVIATIONS, SIGLES ET ACRONYMES

AM	Additive Manufacturing
AML	Aerospace Mechatronics Lab (McGill)
ASTM	American Society for Testing and Materials
BCC	Body Centered Cubic
CAD	Computer-Aided Design
CA0	Conception Assistée par Ordinateur
CAVERNAUTE	Compact Airship Vehicle for Expeditions into Remote Natural Abysses and Underground TunnEls (en) ou Concept Aérostatique Volant Et Rigide pour Naviguer et Accéder aux Univers TroglodytEs (fr)
CdG	Centre de Gravité
CFD	Computational Fluid Dynamics
CPA	Centre de Pression Aérodynamique
DfAM	Design for Additive Manufacturing
DfM	Design for Manufacturing
DIC	Digital Image Correlation
DMA	Dynamic Mechanical Analysis
DoE	Design of Experiments
ÉTS	École de Technologie Supérieure
EOS	Electro-Optical Systems
FA	Fabrication Additive
FDM	Fused Deposition Modeling
FEA	Finite Elements Analysis
FEP	Fluorinated Ethylene Propylene
HPD	Hexa Prism Diamond
INIT Robots	Interaction Naturelle et Intuitive pour la Téléopération de Robots (ÉTS)
IPA	IsoPropyl Alcohol (Alcool isopropylique)

LIPEC	Laboratoire d'Ingénierie des Polymères et Composites (ÉTS)
MSLA	Masked Stereo-Lithography Apparatus
NF	Norme Française
PA	PolyAmide
PLA	PolyLactic Acid
SCADA	Supervisory Control And Data Acquisition
SEA	Specific Energy Absorption
SLA	StereoLithography Apparatus
SLS	Selective Laser Sintering
TPMS	Triply Periodic Minimal Surface
TPU	Thermoplastic Polyurethane
UAS	Unmanned Aircraft Systems
UQAM	Université du Québec À Montréal
UV	Ultra-Violets

LISTE DES SYMBOLES ET UNITÉS DE MESURE

Symbole	**Définition**	**[unité]**
A	surface transversale	mm^2
B	poussée d'Archimède	N
C_x	coefficient de trainée	S.U.
D	diamètre	mm
E et E"	module de conservation et module de perte	MPa
η	efficacité énergétique	%
ε	déformation	S.U.
ε_1	déformation normale maximale	S.U.
F	force	N
H	hauteur	mm
λ	ratio d'angle d'un Kresling	S.U.
n	nombre de côtés du polygone	$\mathbb{N}$
m	nombre de segments du CAVERNAUTE	$\mathbb{N}$
M_i	échelle de mesure	%
S_t	rigidité	N/mm
σ	contrainte	MPa
σ_p	contrainte maximale avant densification	MPa
$tan(\delta)$	facteur d'amortissement	S.U.
T_g	température de transition vitreuse	°C
θ_p	orientation principale de la contrainte	deg
ρ_{gaz}	densité du gaz	kg/m^3
SEA	Absorption d'énergie spécifique	J/kg
W	travail	J

INTRODUCTION

La quête de légèreté est au cœur de la plupart des enjeux d'ingénierie aérospatiale : alléger un avion et c'est la consommation qui diminue ou son autonomie qui est préservée. Être capable de proposer des pièces avec une résistance spécifique intéressante répond aux besoins de domaines cherchant des pièces à haute valeur ajoutée dotées de caractéristiques aptes à être employées dans des conditions exigeantes où résistance mécanique et légèreté ne sont pas dissociables. Ces aspects concernent aussi bien l'aéronautique, le spatial ou encore les prothèses biomédicales.

Les aérostats ou dirigeables ont connu leurs heures de gloire lors des premières décennies du XXe siècle. Leur paroxysme au cours des années trente a vu émerger des engins aériens dont le gigantisme n'a pas été égalé. Véritables paquebots du ciel, les traversées transatlantiques de luxe offert par ce type d'appareils n'ont pas leur pareil. Néanmoins, l'emploi d'hydrogène comme gaz porteur va définitivement discréditer auprès du grand public l'usage des dirigeables à la suite d'une série d'accidents dont le plus emblématique est le Zeppelin Hindenburg (Stockbridge *et al.*, 2012). Tel le crash du Concorde en 2000, l'accident n'aura été que le catalyseur d'un échec commercial : l'essor de l'aviation civile finira d'achever la fin de ces modes de transport. Aujourd'hui encore, les dirigeables sont associés à cette idée d'appareils aériens patauds en forme de cigare, peu fiables et démodés.

Ces dernières années, nous observons une remontée de la popularité des dirigeables en raison d'une meilleure connaissance des technologies de membrane et l'utilisation de matériaux ou de composants de haute performance issus de l'industrie aéronautique et spatiale. Des entreprises se sont lancées dans la fabrication de dirigeables de grandes envergures comme le projet de dirigeable grue-cargo de Flying Whales[5] en France et au Québec. Le marché des drones commence à suivre une tendance similaire avec l'émergence de projets de drone dirigeables. Les drones aérostats présentent l'avantage d'une très grande autonomie qui ne peut pas être

[5] https://www.flying-whales.com/en/home/

satisfaite par les classiques multicoptères très énergivores. Le gaz porteur permet de ne plus à se préoccuper de la sustentation de l'engin, les différents actionneurs servants exclusivement aux mouvements « utiles » de l'aéronef.

Malgré cela, la fragilité des enveloppes contenant le gaz porteur limite leur utilisation dans des espaces confinés où l'environnement peut être agressif pour leurs membranes fines et fragiles. Pour cette raison, l'idée de protéger l'enceinte souple grâce à une coquille ultralégère rendrait l'engin plus résilient et apte à opérer dans davantage de configurations (inspection de site industriel, exploration souterraine, etc.). Si cette configuration rigide est depuis longtemps celle privilégiée pour les grands dirigeables extérieurs (Liao & Pasternak, 2009), la force de portance limitée des engins de petites tailles utilisés à l'intérieur pose un défi considérable. Le volume évolue au cube tandis que la surface évolue au carré. Cet aspect n'est pas à l'avantage des tailles réduites. Néanmoins, les récents développements en fabrication additive laissent entrevoir une possibilité de produire des coquilles ultralégères pour envisager la conception d'un petit aérostat rigide d'intérieur. De plus, un aérostat rigidifié par cette coquille susciterait de nouvelles possibilités : docking, amélioration des performances en vol par un placement optimisé des actuateurs et liberté de morphologie.

Les dirigeables sont des machines aux caractéristiques uniques soumises aux lois de l'aérostatique strictes pour demeurer dans le domaine de vol des plus légers que l'air. Un litre d'hélium ne permet de porter qu'un seul gramme environ. Ainsi, à travers ce travail, nous présenterons la façon de rigidifier un petit dirigeable pour explorer des espaces hostiles et complexes. Comment utiliser la fabrication additive de micro-treillis polymères afin de répondre aux défis d'un cahier des charges restrictif pour la masse et aux spécifications intriquées ?

CHAPITRE 1

REVUE DE LITTÉRATURE

Ce chapitre présente tout d'abord une présentation générale des micro-treillis puis toutes les technologies de fabrication additive ainsi que leurs limitations. Ensuite, nous ferons un survol des typologies de dirigeables. La revue de littérature intégrée au chapitre-article 3 présentera les micro-treillis et leur caractérisation mécanique, notamment via la corrélation d'images numériques. Celle intégrée au chapitre-article 5 détaillera les travaux de caractérisation par impacts sur les structures en micro-treillis. Enfin, le chapitre-article 6 présentera l'usage d'aérostats sans pilote et les cadres de conceptions. Nous présenterons également les travaux mêlant origami et mécanismes robotiques ou structures à grands volumes d'expansion.

1.1 Micro-treillis

1.1.1 Définition

Plusieurs définitions du terme micro-treillis co-existent dans la littérature, sans pouvoir en dégager une définition consensuelle. Certains réfèrent à l'échelle de la structure et parlent de nano-treillis, micro-treillis en fonction de sa dimension caractéristique (Deshpande, Fleck & Ashby, 2001b; Xiong, Mines, Ghosh, Vaziri, Ma, Ohrndorf, Christ & Wu, 2015; Garcia-Taormina, Alwen, Schwaiger & Hodge, 2021). Néanmoins, en majorité, les micro-treillis sont définis comme appartenant à la famille plus large des matériaux cellulaires (Ashby, 2005). C'est une géométrie constituée d'entretoises, de surfaces ou de pores.

Un des principaux avantages des matériaux cellulaires et de pouvoir atteindre des densités bien inférieures au matériau originel tout en augmentant la résistance spécifique, c'est-à-dire la résistance mécanique par rapport à la masse (Schaedler & Carter, 2016).

Parmi les matériaux cellulaires, on retrouve également les mousses possédant une structure stochastique. À l'inverse, les micro-treillis sont architecturés autour de cellules périodiques.

À densité égale, les performances mécaniques sont meilleures (Evans, Hutchinson, Fleck, Ashby & Wadley, 2001).

La conception des matériaux cellulaires dépend de trois facteurs clés (Ashby, 2006) :

- Les propriétés du matériau qui compose les parois cellulaires.
- La topologie de la cellule (la forme et la connectivité des entretoises ou des faces des cellules).
- La densité relative de la structure cellulaire.

1.1.2 Critère de Maxwell

Deshpande et al. ont décrit la structure d'un motif cellulaire comme des jambes de forces articulées et en détaillent deux principes différenciant : les structures dominées par la flexion et celles dominées par l'étirement (Deshpande, Ashby & Fleck, 2001a). Le critère de Maxwell est pour cela un outil algébrique permettant de déterminer si une structure poutre est stable (Maxwell, 1864). Une généralisation du critère de Maxwell est donnée par Calladine (1978) :

$$M = b - 3j + 6 \tag{1.1}$$

Avec j le nombre d'articulations (nœuds) et s le nombre d'entretoises.

- Si M < 0, c'est un mécanisme : la structure est dominée par la flexion
- Si M > 0, c'est une structure rigide : la structure est dominée par l'étirement
- Si M = 0 indéterminé de façon statique

À partir de cette classification, Ashby (2006) a représenté l'évolution du module de Young pour ces deux sous-familles de structure, montrant que pour une même densité relative, les structures dominées par l'étirement montrent une rigidité plus élevée (Fig. 1.1). Les structures en étirement

sont mieux adaptées pour les applications où la rigidité et la résistance sont critiques, tandis que les structures en flexion sont préférées pour l'absorption des chocs et l'isolation.

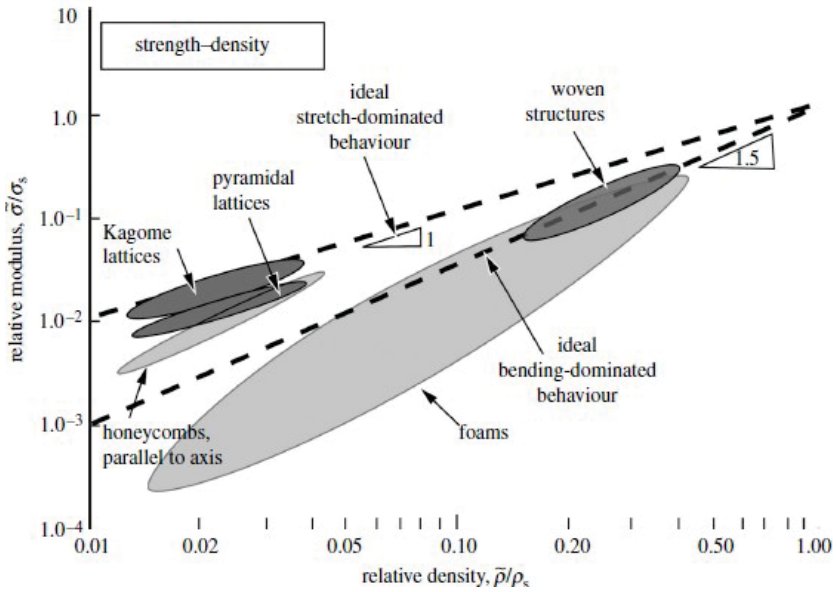

Figure 1.1 les structures dominées par la flexion se trouvent le long d'une trajectoire de pente 1.5. Les structures dominées par l'étirement se trouvent le long d'une trajectoire de pente 1 (Ashby, 2006)

1.1.3 Propriétés mécaniques des structures cellulaires

Gibson & Ashby (1997) ont énoncé un modèle reliant les propriétés mécaniques macroscopiques d'un matériau cellulaire avec la densité relative (ρ_R) par rapport à la densité du matériau brut :

$$\rho_R = \frac{\rho^*}{\rho_S}, \tag{1.2}$$

avec ρ^* la densité du matériau cellulaire et ρ_S la densité du matériau solide. Le module d'élasticité apparent peut alors être calculé comme étant :

$$E^* = E_S\, C_1 (1-\phi)^{n_1}, \tag{1.3}$$

avec E_S le module d'élasticité du matériau solide, $\phi = (1 - \rho_R)$ est la porosité, C_1 et n_1 des coefficients qui dépendent de la géométrie de la cellule élémentaire et d'aspects liés à la microstructure (fabrication).

Du point de vue du comportement mécanique, le micro-treillis se comporte en trois phases distinctes décrites Fig. 1.2. La première phase est élastique linéaire, la deuxième phase est un plateau à contrainte constante caractérisé par le flambement et l'écrasement de la structure. La dernière phase correspond à une densification pendant laquelle les cellules écrasées réagissent comme le matériau solide d'origine.

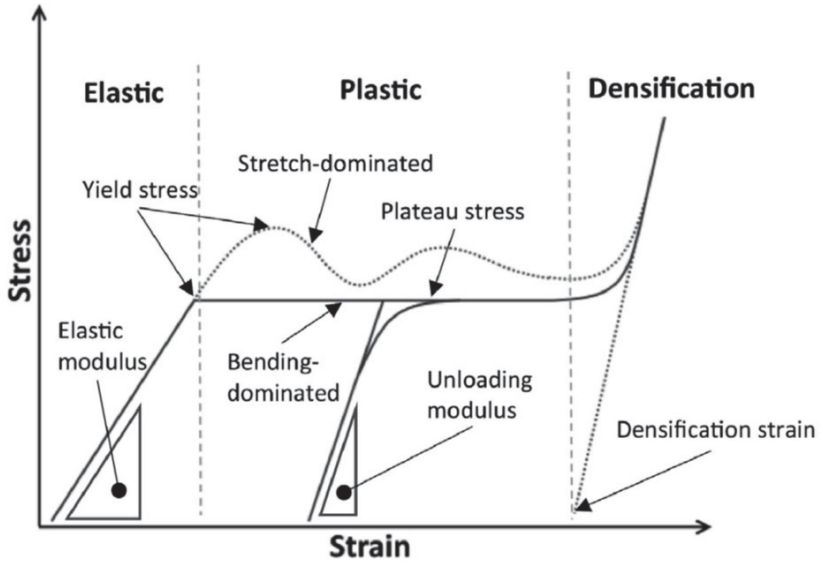

Figure 1.2 Comportement typique d'un micro-treillis soumis à la compression (Maconachie *et al.*, 2019)

La revue de littérature intégrée aux chapitres-articles 3 et 5 couvre avec davantage de détails les procédés de caractérisation mécaniques et des cas d'application.

1.2 Fabrication additive de polymères

1.2.1 Définition

La norme ISO/ASTM 52900 définit la fabrication additive (FA) comme « l'ensemble des procédés permettant de fabriquer, couche par couche, par ajout de matière, un objet physique à partir d'un objet numérique » (ISO-ASTM 52900 (2015)).

1.2.2 Procédés

Différentes classifications de procédés existent en fonction d'un regroupement par architecture de machine et de mécanisme physique de transformation des matériaux (liquide vers solide, solide/filament vers solide, etc.). Il existe sept catégories de FA (Beaman, Bourell, Seepersad & Kovar, 2020) : Photo-polymérisation en cuve, fusion sur lit de poudre, projection de liant, extrusion de matériaux, projection de matériaux, laminage de feuilles et dépôt d'énergie dirigée. En fonction de la performance (poids, contrainte, esthétique, etc.) visée, une technique est sélectionnée en tenant compte également de la faisabilité de la géométrie et de sa structure interne, ainsi que de la résolution du processus (Guerra Silva, Torres, Zahr Viñuela & Zamora, 2021).

Avant même de se plonger dans les différentes techniques, une différenciation notoire peut être apportée selon les matériaux. Il est aujourd'hui possible d'imprimer les quatre familles de matériaux : métaux, polymères, céramiques et composites (Bourell, Kruth, Leu, Levy, Rosen, Beese & Clare, 2017). Les polymères sont les plus rependus avec la présence des thermoplastiques et des résines thermodurcissables. Les thermoplastiques sont sous forme solide (poudre, filament) et les thermodurcissables sous forme liquide.

On s'intéresse ici principalement aux matériaux polymères en raison de leur densité comparée aux matériaux métalliques vis-à-vis de l'exigence de masse pour les aérostats.

Voici un détail des sept techniques de FA expliquant leur principe de fonctionnement et des exemples de machines.

- Photo-polymérisation en cuve : une résine photosensible liquide présente dans une cuve est durcie par polymérisation grâce à un laser. On retrouve dans cette catégorie les SLA (Stéréolithographie) avec la Form3 de Formlabs®, DLP (Digital Light Processing), MSLA (Masked Stereolithography) avec la Mars ou Saturn S fabriquées par Elegoo®. La Figure 1.3 montre le principe de fonctionnement des technologies SLA et MSLA ;
- Projection de matière : semblable aux imprimantes à jet d'encre, des têtes d'impression viennent projeter des gouttelettes de matière sur la zone de fabrication. On retrouve la technologie PolyJet™ avec la Objet 30 de Stratasys®. La Figure 1.3 montre le fonctionnement de l'impression PolyJet™ ;
- Projection de liant : à l'image de la projection de matière, un liant est projeté sur une poudre. Ce procédé nécessite la plupart du temps un post-traitement important pour fritter la poudre et ne convient pas aux applications mécaniques ;
- Fusion sur lit de poudre : grâce à une source d'énergie, on vient fusionner une fine couche de poudre ajoutée à chaque nouvelle strate comme la Formiga P110 de EOS® ou la Formlabs Fuse 1 de Formlabs® ;
- Extrusion de matière : Procédé le plus courant qui consiste à chauffer un matériau proche de sa température de fusion (température de transition vitreuse) puis à l'extruder à travers une buse qui se déplace. La solidification est quasi immédiate sur la couche précédente. On retrouve les machines FDM (Fused Deposition Modeling) très répandues dans l'impression 3D grand public et la production de pièces polymères avec notamment les machines Creality Ender-3 [1], Prusa I3 [2] et plus récemment BambuLab X1C [3] ;
- Dépôt de matière sous énergie concentrée : on fusionne une surface à l'aide d'un apport d'énergie tout en apportant simultanément un jet de poudre ou un filament dans la zone de fusion protégée par un gaz inerte. Cela permet de réaliser des pièces avec des gradients de propriétés des matériaux et sans utilisation de supports (robots 6-axes) ;

---

[1] https://www.creality.com/products/ender-3-3d-printer

[2] https://www.prusa3d.com/fr/produit/original-prusa-mk4-2/

[3] https://ca.store.bambulab.com/products/x1-carbon

- Stratification de couches : des feuilles sont découpées puis assemblées pour chaque nouvelle couche par soudage, collage, etc.

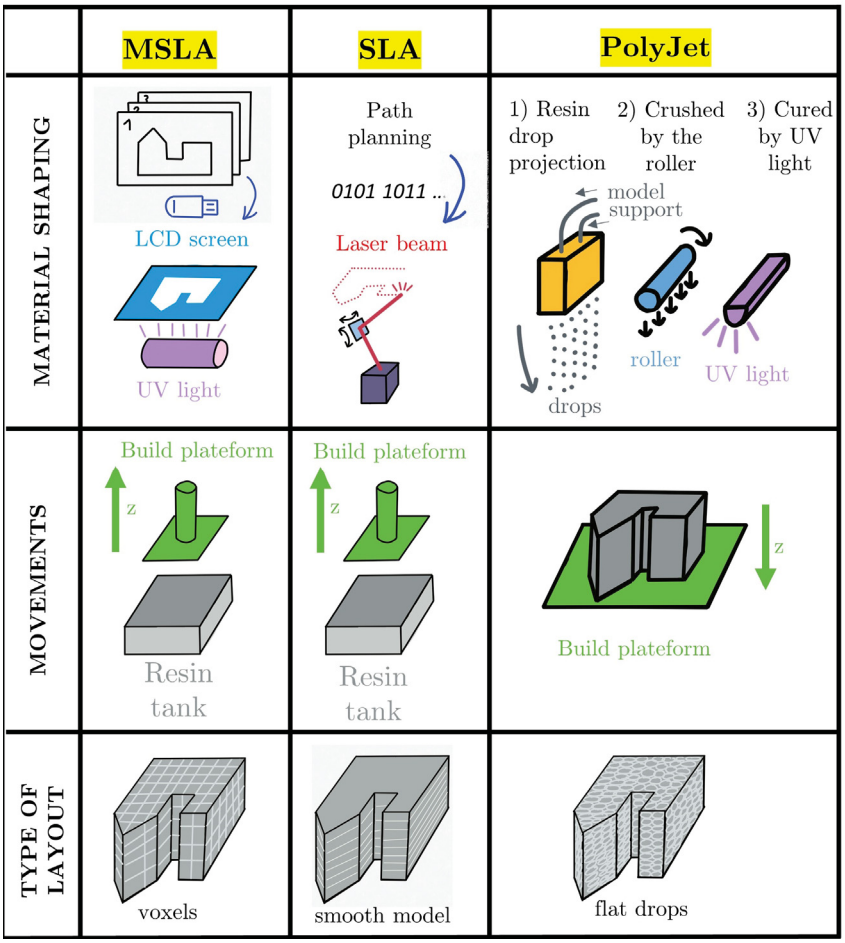

Figure 1.3 Schéma de fonctionnement des machines d'agrégation de résine photosensible. Pour une même technique, on remarque une grande variété de façons de solidifier la même forme de matière (résine photosensible).

La FA est une nouvelle révolution de la fabrication, car elle propose une nouvelle flexibilité des processus et des stratégies d'optimisation. La consommation de matières premières est fortement réduite en améliorant le rendement, elle élargit l'espace de conception et peut être géométriquement moins contraignante (Faludi, Bayley, Bhogal & Iribarne, 2015).

Dans l'industrie, la fabrication additive s'est considérablement développée avec les technologies d'impression métalliques : elle offre de nouveaux espaces de conception, comme la possibilité de fabriquer un assemblage complexe en une seule pièce. Les améliorations majeures sont plus rares pour les technologies des matériaux polymères, qui restent confinées à un rôle de prototypage rapide (Thomas, Davoine & Drawin, 2019). Lorsque l'objectif est de construire un modèle réduit esthétique d'un futur produit, les propriétés mécaniques sont peu importantes. Néanmoins, les matériaux polymères procurent des propriétés de résistance spécifique et un coût inférieur aux solutions métalliques. Cela a permis de démocratiser l'impression 3D auprès d'un plus large public à l'aide de machines qui coûtent seulement quelques centaines de dollars (machines FDM - Dépôt de Fil Fondu ou MSLA - Stéréolithographie masquée).

Les technologies de fabrication additive apportent plusieurs avantages clés au processus de conception (Laverne, Segonds & Dubois, 2016) :

1. Complexité géométrique : il y a peu de limitations en termes de conception ;
2. Complexité matériaux : avec certains procédés, la conception multi-matériaux est possible ainsi que des pièces avec des paramètres variables, comme la densité ;
3. Complexité hiérarchique : les produits présentant des structures internes complexes en treillis, en mousse ou organiques peuvent être créés à différentes échelles (micro ou macroscopique) ;
4. Complexité fonctionnelle : des dispositifs fonctionnels (pas seulement des pièces individuelles) peuvent être produits en une seule fois. Les structures et les géométries peuvent être conçues en fonction des propriétés fonctionnelles à obtenir tout en procurant la possibilité d'une intégration dans une seule pièce.

Il est possible de tirer parti des imprimantes de bureau en polymère pour des applications techniques difficiles et plus industrielles que le simple maquettage, mais les méthodes de production doivent d'abord être caractérisées, rendues fiables et mieux comprises. Cela créera de nouvelles opportunités pour la fabrication industrielle à faible coût (Steenhuis & Pretorius, 2016).

1.2.3 Techniques de fabrication non-conventionnelles

Pour des applications très spécifiques, des machines peuvent spécialement être réalisées afin d'apporter de nouvelles possibilités de fabrication. Par exemple, dans l'article de Coulter, Coulter, Marks & Ianakiev (2018a) et Coulter, Coulter, Papastavrou & Ianakiev (2018b) un procédé a été développé pour adapter l'impression FDM à des surfaces gonflées. Il s'agit d'une imprimante 3D à 4-axes : une imprimante cartésienne avec un mandrin tournant qui crée ce quatrième axe. Les étapes de fabrication sont les suivantes :

1. Création d'une surface gonflée : un jet de silicone est projeté sur un mandrin en gypse. Ce dernier a été spécifiquement créé pour avoir une perméabilité la plus homogène possible sur toute sa longueur (Coulter *et al.*, 2018b) — partie 1. Cela permet d'avoir le gonflage d'une forme axisymétrique.
2. Cartographie de la surface : afin de détecter les irrégularités de gonflage, la surface est pointée à l'aide d'un laser afin de déterminer sa topographie.
3. Création de la structure numérique : à partir de la forme idéale, la trajectoire de la tête d'impression est corrigée pour correspondre aux mesures de la surface faite précédemment.
4. Impression : plusieurs couches successives permettent d'obtenir des motifs variés. La tête se déplace constamment pour conserver la même distance avec l'enveloppe de silicone.

Il est intéressant de voir que des fonctions de fabrication peuvent être combinées. Cette machine peut créer une surface de travail aléatoire, déterminer sa topologie et s'adapter en fonction.

Ces travaux sont très intéressants dans le cadre de la fabrication d'un dirigeable rigide. Cela permet de créer des motifs auxétiques (module de Poisson négatif : le motif s'étend dans la direction transversale à la traction au lieu de subir la striction) qui renforcent l'enveloppe souple tout en se déformant de façon cohérente avec elle grâce à ces formes particulières.

1.2.4 Limites des procédés

Les résines photosensibles peuvent être problématiques dans la durée. Le vieillissement rend le matériau cassant, ce qui peut poser des problèmes de conservation des propriétés mécaniques pour un prototype par exemple. Ce vieillissement dépend de nombreux facteurs, mais est souvent lié à l'exposition aux UV (Marin, Boschetto, Zanocco, Doan, Sunthar, Kinashi, Iba, Zhu & Pezzotti, 2021).

La technologie FDM a une plus forte sensibilité à la délamination par rapport à d'autres procédés. Cela a essentiellement un impact lorsqu'on a affaire à une structure chargée mécaniquement. On observe de grandes différences par rapport à d'autres procédés de fabrication additive où la tenue des couches est plus homogène (Ligon, Liska, Stampfl, Gurr & Mülhaupt, 2017). À la moindre concentration de contraintes, la propagation de fissure suit ces zones inter-couches (Zhang & Yanagimoto, 2021). En revanche, cette façon de faire de la fabrication additive permet un grand contrôle sur les paramètres et se prête à la fabrication multidirectionnelle lorsque l'on fixe la buse d'extrusion au bout d'un système six axes. Cela permet de ne plus dépendre d'une verticalité des couches et donc d'ajuster les performances mécaniques d'une pièce.

1.2.5 Conception pour la fabrication additive

Avec cette méthode de fabrication, il n'y a qu'une seule étape entre le modèle numérique et le composant fabriqué. Cette séquence rapide crée les défis du *« Design for Additive Manufacturing »* – DfAM – Conception pour la fabrication additive avec ses distinctions par rapport aux notions plus classiques de *« Design for Manufacturing »* – DfM (Gibson, Rosen, Stucker & Khorasani, 2021) – Conception pour la fabrication. Le DfAM correspond aux méthodes et outils de conception permettant d'optimiser les performances fonctionnelles ou certains aspects du cycle de vie des produits (fabricabilité, coût, etc.) en fonction des capacités de la fabrication additive (Tang & Zhao, 2016). La fabrication additive regroupe, en effet, de nombreuses techniques avec leurs spécificités (Medellin-Castillo & Pedraza Torres, 2010) qui doivent être explorées et

détaillées grâce aux plans d'expérience. Ces outils d'étude standardisés (Davis & John, 2018) ont été largement utilisés pour différents systèmes industriels. Aujourd'hui, avec les progrès réalisés dans la numérisation de l'espace de fabrication, de nouvelles stratégies sont mises en œuvre pour passer de la conception pour la fabrication à la fabrication pour la conception. L'objectif est de réduire la distance entre les concepteurs et les fabricants avec ce nouveau paradigme de fabrication qui permet plus de flexibilité pour répondre aux nouveaux besoins de rapidité et de personnalisation. L'avènement de l'usine intelligente favorise l'émergence de ces nouveaux concepts (Chu, Kim, Jang, Song, Rodrigue, Chun, Cho, Ko, Cho, Cha, Min, Jeong, Jeong, Lee, Chu & Ahn, 2016). Dans le cadre de la fabrication additive, c'est principalement la production de pièces métalliques qui a bénéficié des travaux de recherche en caractérisation en raison de leurs nombreuses applications industrielles (Moradi, Hasani, Pourmand & Lawrence, 2021; Maconachie *et al.*, 2019; Gu, Meiners, Wissenbach & Poprawe, 2012; Klocke, Arntz, Teli, Winands, Wegener & Oliari, 2017). La technologie FDM a également été assez bien caractérisée et optimisée en raison de son accessibilité dans le monde universitaire (Durão, Barkoczy, Zancul, Lee Ho & Bonnard, 2019). Parmi les considérations les plus discutées figurent les aspects d'orientation de la construction des pièces, les limitations géométriques ou la planification des trajectoires (Medellin-Castillo & Zaragoza-Siqueiros, 2019). En revanche, les moyens de production basés sur des résines photosensibles ont été beaucoup moins abordés dans la littérature.

Si elle est suivie, la DfAM permet, entre autres, de minimiser le nombre de pièces, de créer des assemblages modulaires et intégrés ou de réduire la masse. Ce sont des aspects en constante évolution qui mettent en évidence l'exploration du potentiel d'exploitation de la fabrication additive dans l'industrie (Thompson, Moroni, Vaneker, Fadel, Campbell, Gibson, Bernard, Schulz, Graf, Ahuja & Martina, 2016).

1.3 Dirigeables : typologies et structures standards

1.3.1 Différentes stratégies de classement

Selon les approches, il est possible de décomposer différentes familles de dirigeables :

1. par type de structure ;
2. par forme de portance ;
3. par familles de configurations ;

Ces classements sont un moyen de faire des rapprochements entre configurations semblables ou encore d'emprunter des techniques de conception propre à d'autres aéronefs.

1.3.2 Structure

Tout d'abord, une caractéristique principale de différenciation des types de dirigeables peut être établi par la nature de sa structure (Liao & Pasternak, 2009) :

- Souple : la forme du dirigeable est déterminée par l'enveloppe contenant le gaz de levage. La forme sera donc de type ovoïde — Figure 1.4.
- Rigide : une structure définit la forme du dirigeable. Cela donne à l'aérostat une meilleure tenue aérodynamique — Figure 1.4.

  De plus, dans le cadre de l'étude d'une solution de dirigeable rigide d'intérieur, une structure rigide est intéressante pour la protection de l'enveloppe (environnement abrasif), un contrôle de la forme (esthétisme, efficacité, etc.) ou encore d'autres avantages comme la possibilité de docking (entre modules, bloc de charge, etc.).
- Semi-rigide : C'est la combinaison d'une enveloppe souple et d'une armature rigide pour limiter les effets aéroélastiques non linéaires des structures souples. L'armature permet, par exemple, de joindre les divers éléments de propulsion, surfaces de contrôle et gondole.

La Figure 1.4 suivante avec la coupe montre la façon dont la gondole (pilote, passagers et propulsion) est maintenue grâce à la présence de câbles en traction pour un dirigeable souple. Le dirigeable rigide est lui composé d'une forme définie par les treillis. Le gaz porteur est contenu

dans différents ballonnets cloisonnés. Le cockpit, les organes de propulsion peuvent directement être intégrés à la structure.

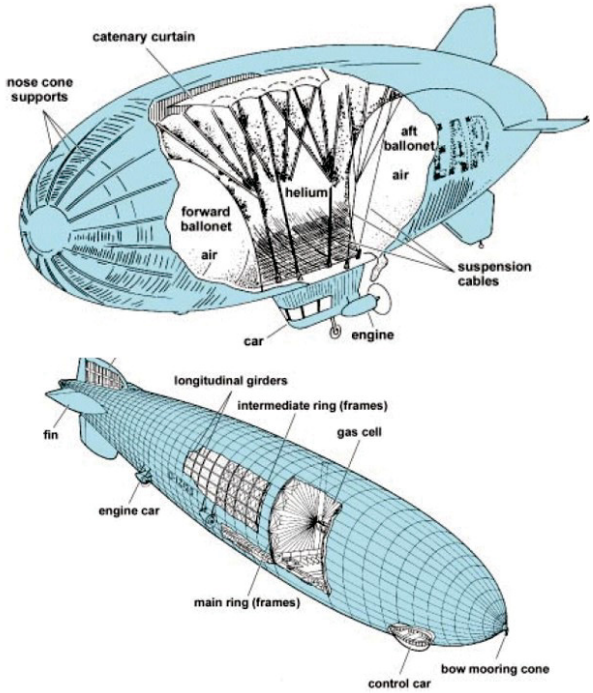

Figure 1.4 Différence intrinsèque entre un dirigeable souple (en haut) dont la forme est définie par la pression du gaz interne et le dirigeable rigide avec une forme qui peut être choisie (en bas). Illustration tirée Stockbridge *et al.* (2012).

1.3.3 Flottabilité

La masse volumique d'un dirigeable est une donnée critique définissant sa capacité d'emport, son altitude de croisière et son endurance. Contrairement à ce que l'on pourrait croire, tous les types de dirigeables n'ont pas une portance statique positive. On différencie donc ces aérostats en fonction de leur flottabilité :

- plus légers que l'air (LTA : Lighter Than Air) : la sustentation est assurée par la poussée d'Archimède

- plus lourds que l'air (HTA : Heavy Than Air) ou hybride : dirigeable ayant certaines caractéristiques des aérodynes en ayant sa portance assurée en partie par des éléments aérodynamiques comme des voilures fixes ou une géométrie de corps portant.

1.3.4 Configuration

Un dirigeable peut être décrit comme étant conventionnel lorsqu'on retrouve la forme traditionnelle ellipsoïde à poussée aérostatique avec une coque contenant du gaz. Tous les autres cas de figure peuvent être regroupés sous l'appellation non-conventionnelle. Cette différenciation peut aussi bien être due à un mode de propulsion d'un nouveau genre (électrique, pile à combustible, etc.) ou bien dans la plupart des cas à la forme de sa coque. On retrouve une classification par formes géométriques (Ceruti & Marzocca, 2014) :

- Traditionnelle (C-T) — ellipsoïde ;
- Multi-coque (C-MH) ;
- Tortue (C-TS) ;
- Baleine (C-WS) ;
- Aile (C-WI) ;
- Arrondi (C-RS) ;
- Brique (C-BS) ;

Ces géométries non-conventionnelles sont essentiellement explorées dans le cadre de la recherche de performances aérodynamiques (Liao & Pasternak, 2009).

Une section en Annexe détaille la modélisation dynamique de ces aérostats.

CHAPITRE 2

OBJECTIFS DE RECHERCHE

2.1 Opportunités de recherche

Certaines conclusions ou limites des travaux précédents ont pu être pointées spécifiquement par rapport à leur champ d'étude. D'autres remarques peuvent être mises en valeur lorsque l'on commence à entrecroiser les aspects au regard de l'application finale désirée.

Avec ce sujet de micro-treillis appliqués à la conception de dirigeables, nous avançons dans un domaine où à ce jour la fabrication additive et les micro-treillis n'ont pas été entremêlés à des problématiques de développement d'aérostats. Sur les aspects de caractérisation de micro-treillis, ces derniers ont pour la plupart été testés en compression. Selon Maconachie *et al.* (2019), le comportement en traction des structures en treillis reste un domaine sous-exploré qui nécessite des recherches supplémentaires. En effet, lorsqu'une pièce géométriquement complexe est sollicitée mécaniquement, les forces se décomposent en tension, compression et cisaillement. Dans le cadre d'une utilisation des micro-treillis comme coquille de protection d'une enveloppe, le gonflage aura tendance à mettre en tension les micro-treillis. Il est donc important de caractériser également la résistance à la traction des micro-treillis.

On peut ajouter à cela que les micro-treillis présentent des caractéristiques géométriques très particulières avec des surplombs et des entretoises très fines. Ces propriétés morphologiques sont particulièrement difficiles à fabriquer par fabrication additive. Le moindre défaut affecte immédiatement l'intégrité de la structure (SakshiKokil-Shah, Sur, Darvekar & Shah, 2021). Il est donc intéressant d'utiliser les micro-treillis comme modèle de référence pour comparer différentes méthodes de fabrication en termes de précision et de répétabilité du processus et de résistance des pièces ultra-minces obtenues.

Quant à la configuration du dirigeable (souple ou rigide), il est certain que les gains sont à l'avantage d'une rigidification du dirigeable grâce à la stabilité de forme, la protection de l'enveloppe et les performances de déplacement. Néanmoins, les travaux en ce sens se heurtent à

la faible portance générée lorsque l'on souhaite réaliser des drones d'intérieur. De façon générale, les configurations rigides ont été étudiées en se concentrant sur l'accroissement des performances aérodynamiques en vol alors que les petits dirigeables d'intérieur de cette recherche se prêtent à l'exploration de formes moins conventionnelles avec moins d'emphase sur les performances aérodynamiques. La perception sociale d'un objet a un impact de plus en plus intégré aux projets d'ingénierie. Un petit drone dirigeable d'intérieur y échappe encore moins, car il est appelé à interagir à proximité des usagers. La forme a donc une importance capitale tant pour la mission à effectuer que l'idée/émotion qu'elle véhicule. Il est également capital de protéger l'enveloppe dans les espaces restreints car à ces échelles les membranes sont très légères et sensibles aux déchirures.

Sur les aspects de caractérisation, la mécanique des fluides et l'étude aérodynamique passe en second plan lorsqu'on traite d'un dirigeable d'intérieur qui se déplace à faible vitesse et sans perturbations extérieures majeures.

À ceci, on peut ajouter que les méthodes de conception de structures de dirigeables rigides ont été développées à un temps où les choix de matériaux et de fabrication étaient plus limités et adaptés à des dirigeables d'extérieur de grande taille. La mise à l'échelle est un processus complexe qui est au désavantage des petites tailles dans le cas des dirigeables. La portance diminue en suivant une loi cubique, au carré pour la surface. Le ratio surface (masse de l'enveloppe) et volume (portance) est une limite. De plus, certains éléments ne sont pas maîtrisables et restes invariants, quelle que soit l'échelle :

- La masse volumique de l'air environnant ou de l'hélium porteur
- Les effets de la gravité

Ainsi, pour compenser les effets constants qui s'appliquent au dirigeable de petite taille, il faut revoir les gammes de matériaux utilisés pour réaliser la structure ainsi que les formes de l'exosquelette. D'après (Konstantinov, 2003), la masse de l'enveloppe a pu être divisée par deux par rapport aux dirigeables d'il y a cent ans et la masse de la structure pourrait être optimisée de 25 %. Cependant, la réduction d'échelle nous donne une marge insuffisante pour conserver les

mêmes techniques d'architecture. Néanmoins, la petite taille nous permettrait de nous affranchir des problèmes logistiques auxquels on est confronté pour un dirigeable de plusieurs centaines de mètres de long. À l'ordre du mètre, on peut avoir des éléments structurels de la même dimension et donc se passer d'assemblages complexes : tiges en fibre de carbone, en balsa, etc.

Les derniers développements en termes de cadre de conception sont intéressants à suivre dans le cadre de ce projet dont les résultats doivent mener à la réalisation d'un prototype. Néanmoins, il n'existe pas de méthodologie systématique et robuste. En particulier, aucun lien n'est à ce jour fait avec les méthodes de fabrication additive. Ces moyens de production peuvent être utilisés dans le processus de fabrication d'éléments mais ces aspects sont toujours secondaires et ne font pas l'œuvre d'une véritable inclusion dans le cadre méthodologique. D'autres inspirations pourront être néanmoins trouvées dans les domaines de l'aérospatial avec l'accroissement constant de l'utilisation de la fabrication additive pour réaliser des pièces aéronautiques (Bikas, Lianos & Stavropoulos, 2019; Garcia-Colomo, Wood, Martina & Williams, 2020).

2.2 Objectifs

L'objectif principal est d'arriver à fabriquer des ensembles structuraux ultralégers capables d'absorber efficacement les chocs dans un espace étroit, de protéger l'enveloppe du dirigeable, de servir d'interfaces pour la mécatronique grâce à l'usage de micro-treillis et de techniques d'assemblage de composants à haute résistance mécanique spécifique. Les travaux sont appliqués au développement d'un drone aérostat d'intérieur rigide pour l'exploration de cavernes.

2.2.1 Objectif 1 : Caractérisation mécanique de micro-treillis polymères en résine photosensible

Il existe un grand nombre de motifs de micro-treillis. Chacun change le comportement de la structure. Nous avons également plusieurs moyens de fabrication additive à notre disposition. Ces moyens de production polymérisent et cicatrisent différemment la matière. Ces variations de la microstructure ont un impact important sur la performance mécanique du réseau final. Le

premier objectif sera de caractériser de façon croisée les moyens de production et une sélection de motifs de micro-treillis aptes à répondre aux critères de réalisation d'une coquille de protection.

2.2.2 Objectif 2 : Blocs fonctionnels ultralégers à base de micro-treillis pour aérostat modulaire en milieu restreint

La généralisation des résultats permet de travailler à la conception de blocs ultralégers à base de micro-treillis. La fabrication est adaptée à la quantité de blocs à produire ainsi qu'au volume des pièces individuelles. Une standardisation des blocs sera visée afin de permettre une architecture de dirigeable reconfigurable selon les besoins des missions. Une caractérisation des gains en termes de capacité d'absorption permettra d'observer le niveau de protection offert par le dispositif en micro-treillis et son aptitude à préserver l'enveloppe et encaisser les impacts.

2.2.3 Objectif 3 : Procédure de rigidification ultralégère d'une enveloppe d'un aérostat pour espaces étroits

Les premières expériences fournissent un grand nombre de données et de possibilités. Les résultats de la caractérisation mécanique des micro-treillis doivent être remis dans leur contexte d'utilisation : la réalisation d'un dirigeable d'intérieur. Ce troisième objectif va consister à analyser la répartition fonctionnelle des éléments constituant le drone. Une fois déterminé les sections à renforcer et le positionnement des différents composants, il faudra proposer une façon d'assembler les modules. Pour cela, des techniques d'assemblage non-permanentes seront développées. Avec l'achèvement de ce troisième objectif, un prototype de dirigeable sera construit en synthétisant les avancées techniques du projet. Les contraintes du déploiement dans des espaces étroits seront tout particulièrement prises en considérations et illustrées à travers un scénario d'utilisation dans une caverne.

Le contenu des chapitres suivants est relié aux objectifs identifiés ci-dessus. Le chapitre 3 traitera de la caractérisation en micro-traction quasi-statique à travers un article de journal (Objectif 1). Le chapitre 4 s'intercale ensuite pour présenter avec un article de conférence une méthodologie de sélection multicritères utile à l'analyse des résultats de l'objectif 1 avec une remise en contexte

dans le monde des aérostats. Il sera également utile pour le classement des performances des structures avant leur intégration sur le drone aérostat de l'objectif 3. Le chapitre 5 abordera le développement et les tests des blocs d'absorption avec un deuxième article de journal (Objectif 2). Le chapitre 6 clôturera ce travail avec la conception pour la fabrication du drone aérostat (Objectif 3) avec le cas d'application du déploiement robotique au sein d'une caverne présenté dans un dernier article de journal.

CHAPITRE 3

TENSILE TESTS OF DIFFERENT FAMILIES OF ULTRA-LIGHTWEIGHT PHOTOSENSITIVE POLYMER MICRO-LATTICES

Louis Catar[1] , Ilyass Tabiai[1] , David St-Onge[1]

[1] Département de Génie Mécanique, École de Technologie Supérieure,
1100 Notre-Dame Ouest, Montréal, Québec, Canada H3C 1K3

Article soumis à la revue « Journal of Engineering Materials and Technology » en juin 2024.

3.1 Avant-propos

Ce premier volet du travail concerne l'exploration du comportement de différents motifs de micro-treillis et leurs interactions avec les matériaux et procédés de fabrication additive utilisés. La première piste envisagée est la création d'une coquille homogène de micro-treillis pour constituer un bouclier pour l'enveloppe. D'autres éléments comme les nacelles pour les moteurs ou les capteurs pourront également être constitués de micro-treillis. Pour cela, nous devons caractériser le comportement plus complexe à étudier avec des essais de traction.

Après avoir sélectionné une gamme de machines apte à fabriquer des micro-treillis polymères, la sélection de motifs permettra de mettre en place un protocole expérimental de caractérisation mécanique des différentes structures. La sélection initiale des machines est faite de façon croisée entre le niveau de détails requis pour les micro-treillis et les équipements disponibles dans les laboratoires à l'ÉTS. Il s'agit de l'imprimante PolyJet Objet30 de Stratasys®, de la SLA Form 3 de Formlabs® ainsi que de la MSLA Mars de Elegoo®. En plus d'avoir différentes technologies d'agrégation de la matière, ces machines offrent également un panel de complexité technique. Pour le choix des motifs de micro-treillis, l'objectif sera de relier les travaux de caractérisation existants tout en proposant une manière de comparer les différentes familles de micro-treillis grâce à l'adoption d'un protocole expérimental commun, et donc des éprouvettes en mesure de tester l'ensemble des motifs. Le logiciel nTopology® sera utilisé afin de bénéficier d'un outil de création des modèles suffisamment souple pour s'adapter à la pluralité des designs de micro-treillis. Des essais de micro-traction seront conduits. La machine utilisée est décrite

Figure 3.1. Les résultats de ces essais permettront l'étude de l'interaction des différents niveaux structurels constituants les micro-treillis. La corrélation d'image numérique seront des moyens de comprendre ces phénomènes. L'ensemble des résultats seront remis dans le contexte de la FA par l'étude de l'impact de l'anisotropie des moyens de fabrication sur les performances finales des échantillons.

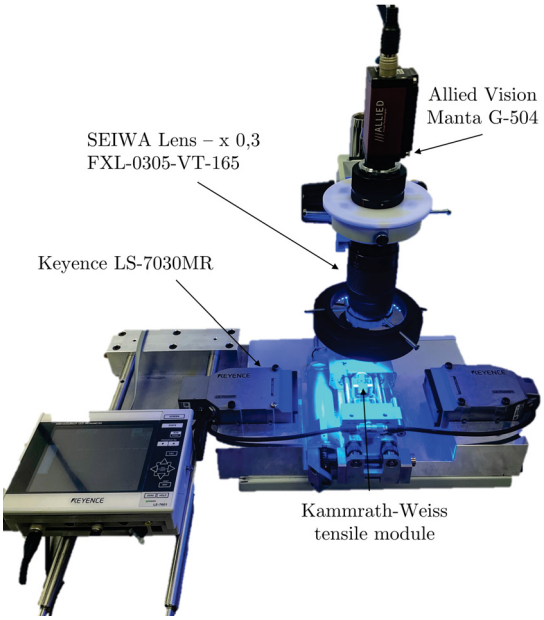

Figure 3.1 Machine de micro-traction pour les essais de caractérisation mécanique des micro-treillis. Équipé avec un dispositif pour la corrélation d'image et la mesure fine de l'élongation.

Études par éléments finis

Aujourd'hui, l'approche la plus courante pour calculer et valider la résistance mécanique des structures non triviales est l'analyse par éléments finis (FEA). Cependant, les différences macroscopiques, mésoscopiques et microscopiques entre le modèle numérique et la pièce fabriquée sont très importantes. Il est parfois possible de reconstruire géométriquement le modèle final grâce à un scanner CT (Xiao, Song & Xu, 2020a). Cependant, l'adhésion inter-couches (niveau microscopique) affecte les performances mécaniques des pièces. Plusieurs

travaux de recherche commencent à proposer des modèles comme la simulation établie à partir des voxels (Park & Rosen, 2016) pour l'adhésion inter-couches. Plus spécifiquement, il n'y a pas de travaux pour modéliser les défauts dans les pièces imprimées en résine. Les auteurs se concentrent sur les effets des procédés FDM et à base de poudre, bien que ce travail résume une méthodologie très intéressante pour étudier les micro-treillis grâce à la FEA (Dong, Tang & Zhao, 2017). Il reste encore beaucoup à faire pour adapter ces techniques à d'autres procédés, car la microstructure change avec chaque méthode et machine.

Malgré ces limitations, la FEA peut être appliquée à l'échelle de la cellule du micro-treillis. Elle fournit des informations uniques : l'étude de sections à cette échelle est impossible avec des spécimens physiques car la cellule est trop petite pour être mécaniquement chargée avec l'équipement disponible. Néanmoins, les résultats sont tout au plus indicatifs, car la microstructure n'est pas modélisée numériquement.

Nous avons d'abord réalisé une analyse de traction sur un groupe de cellules micro-treillis BCC de 4×4 cellules de taille 2,5 mm dans le module « simulation » de *Autodesk Fusion 360®*. La Figure 3.2 illustre la distribution du déplacement entre les cellules. Une section de préhension a été fixée à une extrémité et une charge de 100N a été appliquée à l'autre. La construction architecturale d'un réseau divise la charge à chaque nœud le long de la géométrie. La Figure 3.2 montre une grande discontinuité en fonction de la localisation de la cellule dans le micro-treillis. Par exemple, les effets de bord résultent de l'absence de cellules voisines comme illustré par les zones rouges à la frontière du micro-treillis. Ces différences de déplacements auront un impact sur l'emplacement de la première rupture qui se propagera sous les contraintes, comme démontré par Yoder, Thompson & Summers (2019). Les auteurs ont quantifié la perte de rigidité sur les bords libres du maillage par calcul : la taille du réseau de cellules et son agencement auront également un grand impact sur la distribution des contraintes et des déformations. Ce sont des outils utiles pour mettre rapidement en évidence les zones de défaillance critique.

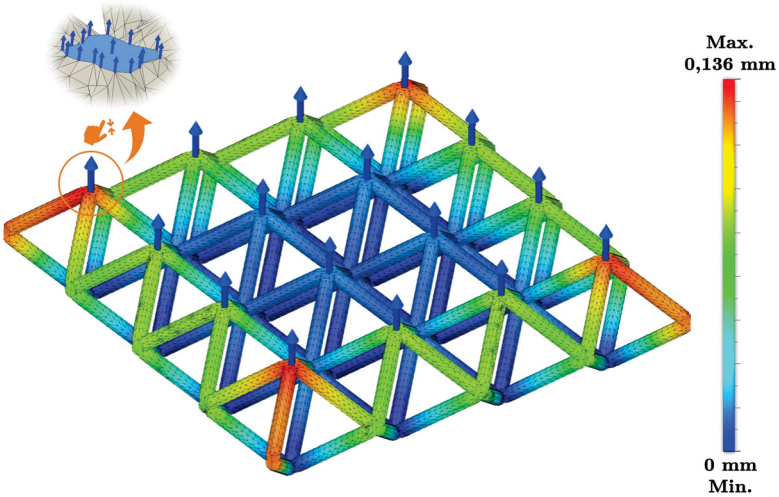

Figure 3.2 Déplacement d'une section de micro-treillis BCC (4×4 cellules). La FEA a été réalisée sur *Autodesk Fusion 360*® montrant les déplacements théoriques des entretoises du motif. On peut visualiser les effets de bord sur les quatre coins. La rupture est donc susceptible de commencer aux bords. La manière dont la charge est appliquée est montrée dans le zoom.

La deuxième série de tests s'est concentrée sur des cellules 2 × 2 × 2 de chaque motif illustré à la figure 3.3. De grandes différences de distribution des contraintes sont observées entre les maillages TPMS (Gyroïde) où les zones de contraintes sont largement distribuées par rapport aux autres motifs à entretoise où les nœuds des micro-treillis montrent de fortes zones de concentration de contraintes dans la figure 3.3. Le modèle de matériau est élastoplastique avec un matériau isotrope dont les caractéristiques sont tirées des tests préliminaires de la Section 3.6.1. Le solveur est Abaqus® avec un maillage libre tétraédrique. Cette étude FEA permet de mieux comprendre le chargement du micro-treillis à l'échelle mésoscopique : les cellules.

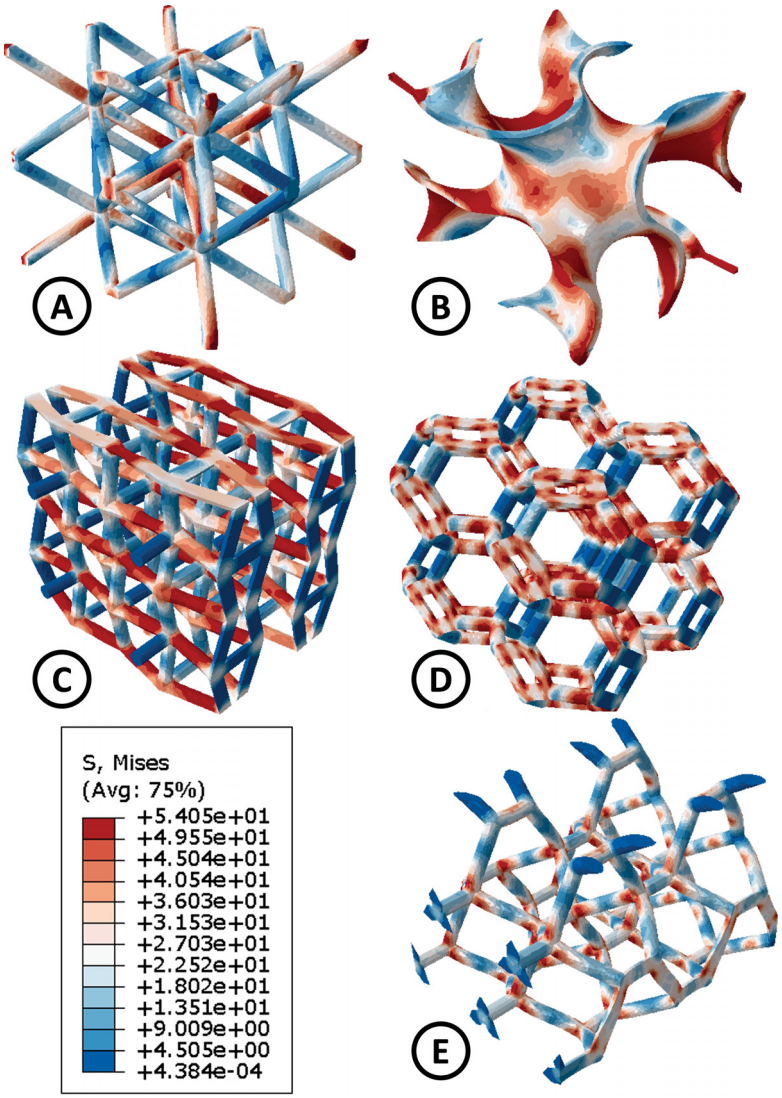

Figure 3.3 Analyse par éléments finis réalisée avec Abaqus : représentation de la distribution des contraintes de Von Mises sur une cellule de chacun des motifs étudiés. Pour le même matériau, la conception de la cellule a un fort impact sur le comportement structurel. Le matériau est un matériau élastique « custom » créé à partir des propriétés mécaniques obtenues à partir des résultats expérimentaux de la résine SLA standard grise de Formlabs® présentés dans la Section 3.6.1. Le motif *(A)* est BCC, *(B)* est Gyroïde, *(C)* est Réentrant, *(D)* est Kelvin et *(E)* est HPD

3.2 Résumé

Dans les applications aérospatiales, la réalisation de conceptions légères est cruciale pour des performances optimales, nécessitant souvent l'utilisation de matériaux avec les meilleurs rapports rigidité-masse lorsque le budget le permet. Au niveau de la conception, les structures en micro-treillis polymériques peuvent encore optimiser les pièces, mais leur fabrication reste difficile. Leur utilisation dans l'industrie aérospatiale est encore limitée en raison de la connaissance insuffisante des propriétés mécaniques associées aux machines, aux matériaux et aux paramètres de géométrie.

Ce chapitre examine et compare différentes technologies d'impression photosensibles et familles de micro-treillis. Nous explorons comment des motifs spécifiques de micro-treillis peuvent être utilisés pour atteindre des comportements structurels souhaités au-delà des propriétés inhérentes des matières premières. Compte tenu des effets structurels hautement imbriqués aux niveaux micro, méso et macroscopique dus au processus d'ajout de matière en fabrication additive, notre étude se concentre sur les technologies de fabrication additive basées sur les UV en raison de leur accessibilité et leur haute résolution.

Une connaissance précise des propriétés mécaniques est essentielle pour le processus de conception, mais les fiches techniques des matériaux manquent souvent d'informations normalisées. Par conséquent, nous étendons la caractérisation des micro-treillis en résine UV grâce à des tests expérimentaux approfondis. Nous analysons les résultats d'une campagne complète de tests de traction sur divers motifs de micro-treillis, en utilisant des techniques de corrélation d'images numériques pour révéler la distribution des déformations au sein des spécimens pendant l'évolution de la rupture. Nos résultats procurent une compréhension plus approfondie de la propagation des propriétés mécaniques multi-échelles aux niveaux micro, méso et macroscopique en fabrication additive de micro-treillis, grâce à une évaluation des propriétés mécaniques de chaque résine utilisée et à la caractérisation de l'anisotropie de chaque imprimante 3D.

3.3 Abstract

In aerospace applications, achieving lightweight designs is crucial for optimal performance, often necessitating using materials with the best stiffness-to-mass ratios when budget permits. At the design level, polymeric micro-lattice structures can further optimize parts, but their manufacturing remains challenging. Their use in the aerospace industry is still limited due to insufficient knowledge of the mechanical properties associated with machine, materials, geometries parameters.

This paper investigates and cross-compares different photosensitive printing technologies and families of micro-lattices. We explore how specific micro-lattice patterns can be utilized to achieve desired structural behaviors beyond the inherent properties of the raw materials. Given the highly intertwined structural effects at micro, meso, and macroscopic levels due to the material addition process in AM, our study focuses on UV-based AM technologies for their accessibility and high resolution.

Accurate knowledge of mechanical properties is essential for the design process, yet material datasheets often lack standardized information. Therefore, we extend the characterization of UV resin micro-lattices through extensive experimental testing. We analyze the results of a comprehensive tensile test campaign on various micro-lattice patterns, utilizing techniques of digital image correlation to reveal strain distribution within specimens during damage evolution. Our findings provide a more in-depth understanding of multiscale mechanical property propagation across micro, meso, and macroscopic levels in AM of micro-lattices, thanks to an assessment of the mechanical properties of each resin used and the characterization of the anisotropy of each 3D printer.

3.4 Introduction

The aerospace industry continually seeks to design and manufacture lighter structures without compromising mechanical performance. Lightweight aircraft reduce fuel consumption and launch costs while maximizing payload capacity. Traditional manufacturing methods enable

designers to optimize the geometry and topology of components to minimize material usage, for instance by utilizing isogrid surfaces Tripathi, Kukreja & Gupta (2022). However, these methods are costly and generate substantial raw material waste.

Achieving an optimal balance among resistance, stiffness, and weight requires a careful combination of material selection, microstructural design, and manufacturing process. Additive manufacturing (AM), or 3D printing, represents a transformative shift from traditional subtractive manufacturing methods Shahrubudin, Lee & Ramlan (2019). AM not only reduces raw material consumption by improving casting yield but also expands the design space, introducing fewer geometrical constraints.

These advantages have become accessible to multiple industries, especially as metallic AM technologies have advanced significantly over the past decade, offering new design possibilities, such as manufacturing complex assemblies as single parts. While progress in polymeric printing has been slower, largely limited to rapid prototyping applications Thomas *et al.* (2019), recent developments in both desktop and large-scale polymer printers have enabled users to take advantage of AM's geometric flexibility. These printers can now produce complex, ultra-light structures—such as the micro-lattices explored in this work—at reduced costs.

A micro-lattice is an architectured cellular structure with a repeating pattern. Although filled with interstices and porosities, the sparse material is periodically organized, offering excellent mechanical properties at very low densities Zheng, Lee, Weisgraber, Shusteff, DeOtte, Duoss, Kuntz, Biener, Ge, Jackson, Kucheyev, Fang & Spadaccini (2014). Within additive manufacturing, the structural properties of a micro-lattice involve multiple scales, as defined by Carneiro et al. Carneiro, Rawson, Puga & Withers (2021) : (1) the microscale, encompassing material arrangement and printing artifacts ; (2) the mesoscale, referring to the lattice's inter-cell pattern ; and (3) the macroscale, representing the complete assembly of cells. Manufacturing micro-lattices requires attention across all three scales, as factors like exposure time influence material properties at the microscopic level, while LCD pixel size and layer height in Masked-Stereo-

Lithography Apparatus (MSLA) resin manufacturing affect layer cohesion and feature resolution. Ultimately, micro-lattice parts are macroscopic structures composed of mesoscopic cell patterns.

The primary distinction among micro-lattice families lies in their underlying cell structure, which can consist of struts in various geometries or curved and flat surfaces. Maconachie et al.Maconachie *et al.* (2019) identified three main families of micro-lattices -strut-based, triply periodic minimal surface (TPMS), and shell-based lattices- as illustrated in Fig.3.4.

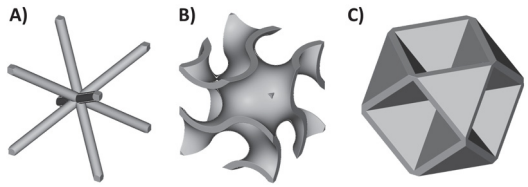

Figure 3.4 Different families of micro-lattices : strut-based unit cells (A), triply periodic minimal surface (TPMS) unit cells (B) and shell lattice unit cells (C). Lattices A and C have discrete junctions, while lattice B is made of continuous surfaces.

Among micro-lattice patterns, the body-centered cubic (BCC) has been widely studied Ushijima, Cantwell, Mines, Tsopanos & Smith (2011); Mines, Tsopanos, Shen, Hasan & McKown (2013); Gümrük, Mines & Karadeniz (2013); Boniotti, Beretta, Foletti & Patriarca (2017); Xiao, Xu, Song & Hu (2020b) due to its ease of modeling, with long, straight struts oriented at 45° that provide nearly isotropic mechanical behavior. This structure distributes manufacturing defects evenly, resulting in a more uniform behavior.

Less studied patterns include the octahedron-based Kelvin cell, identified as bending-dominated structures by Maxwell's criterion. They exhibit strong energy storage capacity thanks to a large area under the stress-strain curve Saremian, Badrossamay, Foroozmehr, Kadkhodaei & Forooghi (2021). Also part of the strut-based structures, the diamond pattern reflects the structure of 2D honeycombs but introduces open, three-dimensional characteristics, with the Hexa Prism Diamond (HPD) version achieving extremely low density Guerra Silva *et al.* (2021).

Some strut-based designs, such as reentrant networks, demonstrate unique mechanical metaproperties. Effective at impact absorption, reentrant networks regain shape quickly after deformation, a

critical feature for aerospace applications Mir, Ali, Sami & Ansari (2014). Known for their auxetic properties (Poisson's ratio ≤ 0), they self-retract under load, decoupling the out-of-plane compression and traction loads and the shear modulus, thus minimizing displacements to its neighbors Alderson & Alderson (2007).

While strut-based lattices remain the most prominent micro-lattices family studied Doyoyo & Hu (2006); du Plessis, Yadroitsava, Yadroitsev, le Roux & Blaine (2018); Syam, Jianwei, Zhao, Maskery, Elmadih & Leach (2018); Echeta, Dutton, Leach & Piano (2021); Jeong, Lyu & Park (2021); Nayfeh & Hefzy (1978), their nodal geometry concentrates stress, which can lead to structural collapse Boniotti, Foletti, Beretta & Patriarca (2019). This limitation has driven the development of alternative lattice families, including triply periodic minimal surfaces (TPMS) and shell-based lattices Yan, Hao, Hussein & Young (2015). TPMS lattices reduce stress concentrations compared to those with junction nodes and are well-suited to multidirectional loads Dharmalingam, Aute & Ling (2022). Examples include gyroid, primitive, and diamond structures, which offer configurable cell densities Maskery, Sturm, Aremu, Panesar, Williams, Tuck, Wildman, Ashcroft & Hague (2018). As for shell-based lattices, they are formed from plate structures that create enclosed volumes, which makes them challenging to manufacture using powder and resin technologies like Stereolithography (SLA) or Selective Laser Sintering (SLS).

In contrast to these structured micro-lattices, foams exhibit stochastic properties, with randomly distributed cells rather than periodic arrangements. Voronoi networks, for example, conform flexibly to complex geometries as their pattern is defined by 3D points, making them ideal for covering surfaces and filling volumes Aurenhammer (1991); Nowak (2015). Their unmatched flexibility in variable node density can also serve to optimize mechanical properties Tonelli, Pietroni, Puppo, Froli, Cignoni, Amendola & Scopigno (2016), though as it is the case with reentrant, Voronoi patterns lack self-support and require additional support structures, limiting their manufacturability.

Compared to traditionally manufactured parts, micro-lattices require a more intricate design phase due to unique features like overhanging angles and thin struts Rashed, Ashraf, Mines & Hazell (2016); Després, Cyr, Setoodeh & Moham-madi (2020). These microscale characteristics make manufacturing nearly impossible with conventional methods and still challenging with AM. Even minor defects can compromise the integrity of the entire lattice network, positioning micro-lattices as effective benchmarks for evaluating manufacturing precision, repeatability, and strength over the resulting ultra-thin structures.

Given the delicate nature of micro-lattices, manufacturing methods must be chosen carefully. For instance, while Fused Deposition Modeling (FDM) remains the most accessible AM technology, it struggles to produce resilient, thin structures, often resulting in inaccuracies or complete failure Kisgergely (2020); Guerra Silva *et al.* (2021). Selective Laser Sintering (SLS) is commonly used in industry Bhushan & Caspers (2017), where low-density polyamide powder is fused by a laser to create ultralight lattices. The unfused powder acts as a support structure that can be easily removed. Despite its benefits, SLS resolution is typically limited to around ten microns, and thermal distortion restricts vertical strut diameters to about 0.8 mm Cao, Qiu, Wei & Zhang (2015); Kisgergely (2020).

For finer precision, photosensitive printing techniques, including Vat Photopolymerization and Material Jetting, are preferred Liu, Zhang, Chen, He, Cheng, Huo, Yin, Hao, Chen, Wang, Yi, Wan, Mao, Chen, Wang, Cao & Lu (2021). Vat Photopolymerization comprises processes like Stereolithography (SLA), Masked SLA (MSLA), and Digital Light Processing (DLP), each employing different curing mechanisms. MSLA, for example, cures resin into pixel-sized cubes, while SLA uses a laser for a smoother progressive cure. Material Jetting technologies, such as PolyJet, project and smooth resin droplets layer by layer, achieving accuracies within tens of microns Patpatiya, Chaudhary, Shastri & Sharma (2022). Most of these methods require solvent-based post-processing Dizon, Gache, Cascolan, Cancino & Advincula (2021), which can soften the polymer, affecting properties like viscosity, density, and tensile strength Cingesar, Marković & Vrsaljko (2022). This step is critical for precision but introduces the risk of damaging fragile lattice structures before they fully harden, especially during handling.

Given the critical need for precision in micro-lattices, most mechanical studies focus on stress concentrations at the lattice/grip interface Alsalla, Hao & Smith (2016); Drücker, Inman & Fiedler (2018). While numerous studies characterize compression behavior, only a few, such as Gümrük *et al.* (2013) and Drücker *et al.* (2018), present tensile tests for micro-lattices. Compression tests are generally simpler to control and align with many micro-lattice applications, particularly in the biomedical field, where components primarily support weight. Consequently, compression characterization is well-documented Ushijima *et al.* (2011); Vanderesse, Richter, Nuno & Bocher (2018); Vilardell, Takezawa, du Plessis, Takata, Krakhmalev, Kobashi, Yadroitsava & Yadroitsev (2019); Intrigila, Nodargi & Bisegna (2022). In aerospace, micro-lattices are commonly used in sandwich panels subjected to flexion loads Mines *et al.* (2013) and these complex mechanical loads often combine tension, compression, and shear. For instance, small-scale micro-lattices, as studied here, have direct applications in nano-satellites, where weight-optimized structures must withstand tensile loading Balaji, Talasila, Oblisamy, Ajith & Basithrahman (2022). Similarly, micro-lattices hold promise for ultralight spars in UAVs, complementing composite materials Rumayshah, Prayoga & Moelyadi (2018) or as structural support for small airship mechatronics. Applications like these underscore the need for tensile characterization to fully leverage micro-lattice potential - a topic that remains under-explored Maconachie *et al.* (2019). As a reference, for compression strength, prior tests indicated that relative strength generally decreases in the order : gyroid > Kelvin > BCC > HPD.

In addition to tensile testing, understanding micro-lattice strain distribution is crucial, with Digital Image Correlation (DIC) proving highly effective. DIC, a non-destructive optical method, calculates 2D displacement fields by cross-correlating images taken throughout the deformation. This method was used in Vanderesse *et al.* (2018) to analyze strain gradients in three metallic lattices (TA6V-ELI) under tensile load, demonstrating that localized plastic deformations cannot always predict final failure locations. DIC has shown that, while macroscopic stress at failure may be consistent, localized deformation varies, influencing lattice durability Tabiai, Delorme, Therriault & Levesque (2018); McCormick & Lord (2010).

Contributions

This work aims to characterize a selection of micro-lattice structures made with less common photosensitive resin techniques to provide a clearer understanding of relative mechanical behavior across different patterns, materials, and manufacturing methods. It contributes to additive manufacturing and materials engineering in three core areas : *(1)* tensile cross-testing of six distinct micro-lattice patterns produced with three photosensitive manufacturing techniques, using a micro-tensile machine and Digital Image Correlation (DIC) ; *(2)* evaluation of the effects of printing direction on interlayer mechanical strength ; and *(3)* mechanical characterization of commercial photosensitive resins and their manufacturing processes, incorporating tensile tests and three-point bending Dynamic Mechanical Analysis (DMA).

3.5 Materials and Methods

3.5.1 Micro-lattice patterns selection

We targeted various topologies to examine the geometric attributes that influence mechanical performance. To keep our results independent of the manufacturing process, we selected patterns that are compatible with photosensitive resin printing. The micro-lattice selection in this study is based on three criteria : *(1)* providing a reference base comparable to previous studies, *(2)* ensuring a wide diversity in topologies, and *(3)* selecting self-supporting cell geometries suitable for all three manufacturing processes. For design comparisons, this last criterion can be adapted based on manufacturing constraints. Our literature review informed the final selection of micro-lattice patterns. We chose the BCC structure as a well-established benchmark in lattice studies, and the HPD pattern for its low density and honeycomb-like geometry. The Kelvin pattern, known for its rigidity, offers high energy absorption under mechanical stress, while the gyroid represents the TPMS family. The Voronoi pattern links to foam-like microstructures, and the reentrant pattern was included to explore potential auxetic behavior under the study's manufacturing conditions. The final selection includes BCC, gyroid, Kelvin, HPD, reentrant,

and Voronoi patterns, as shown in Fig. 3.5. The nomenclature for these micro-lattices follows the *nTopology*® naming system.

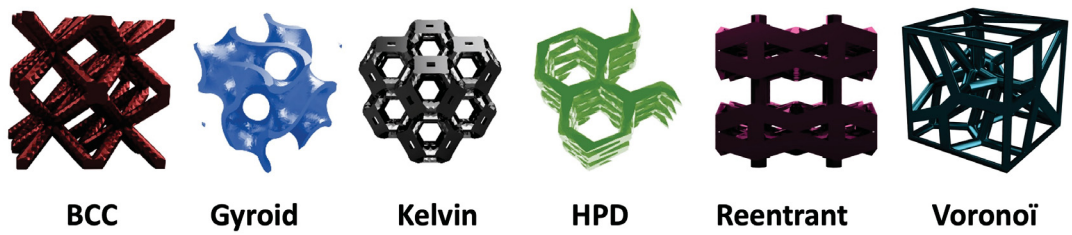

Figure 3.5 Lattices selection for our micro-traction tests campaign. Reentrant and Voronoi micro-lattices are not self-supporting. They will be manufactured on a single printing machine that has the capacity to build unsupported geometries. The color of the patterns corresponds to the color of the plots in the results of this paper.

Taking into account machine resolution, support-free printing requirements, and geometric constraints highlighted in prior studies on micro-lattices, we selected a minimum strut diameter of 0.3 mm for all patterns. This dimension aligns with the recommended minimum wall thickness or column diameter for the UV printers used in this study.

3.5.2 Specimen design for micro-traction tests

Micro-tensile tests were conducted using a Kammrath and Weiss Systems tensile testing device, equipped with Allied Vision Manta G-504 cameras for Digital Image Correlation (DIC) analysis. The detail of the devices and our test setup is available online [1]. For all tests, the displacement speed was set to 25 µm/s. We maintained consistent loading settings for all micro-lattice specimens, with loading applied along the X-axis of the printing direction (Fig. 3.6). The grip section includes studs compatible with a laser extensometer, achieving a displacement measurement accuracy of $\pm 2\mu m$.

[1] Micro-tensile setup and datasheet: https://initrobots.ca/meshproc/

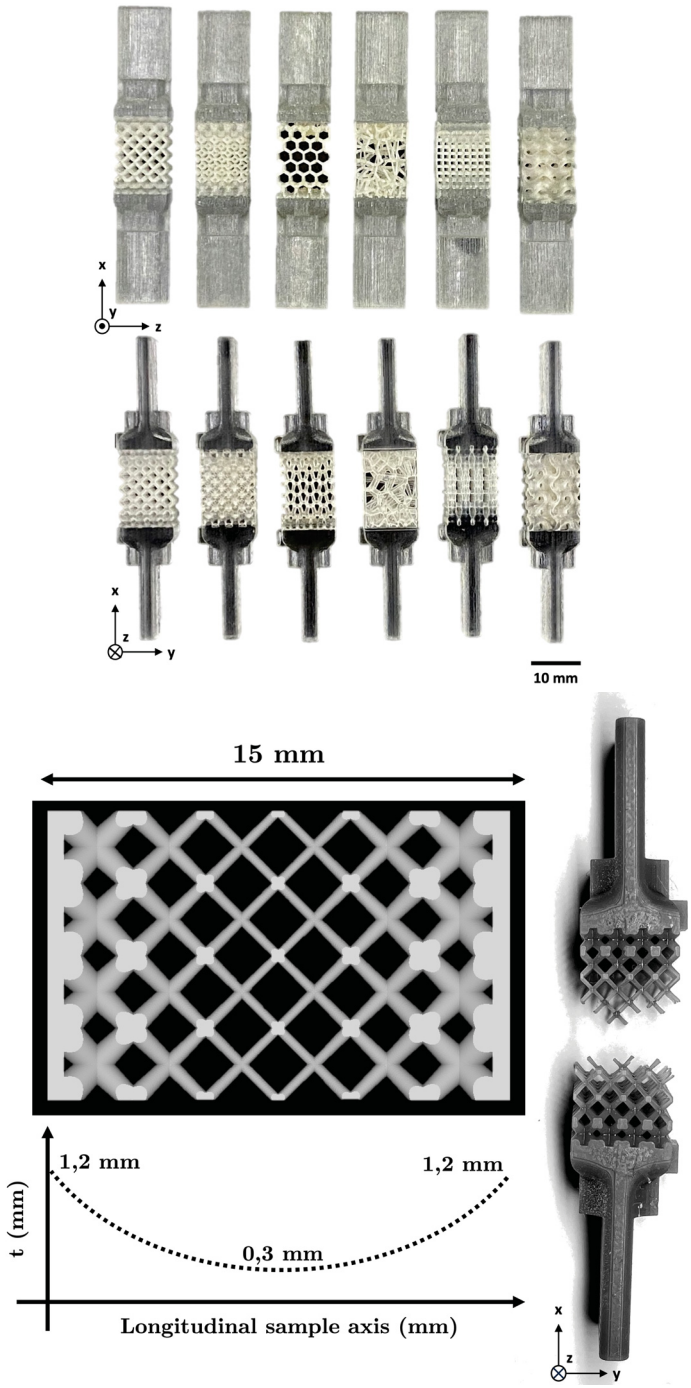

Figure 3.6 Specimen design : On the left, a batch of specimens made on the Stratasys ® PolyJet Objet30 printer. From left to right : BCC, Kelvin cells, HPD, Voronoï, reentrant and gyroid specimens. On the right, is a detailed view of the micro-lattice specimen geometry. The thickness (t) of the struts is functionally graded to ensure the breaking zone appears in the middle of the lattice with a quadratic function

. Otherwise, fracture tends to occur at the interface between the lattice and the grip section due to the stress concentrations involved in this steep transition. X, Y and Z coordinates are the printing bed coordinates. The Z direction corresponds to the printing direction.

Specimens were designed in *Autodesk Fusion 360*®and exported as *.step* files for micro-lattice generation in *nTopology*®. The grip sections of each specimen are 3 mm thick to ensure centered load application and a secure fit in the clamping jaws. All micro-lattice specimens share a consistent volume of 10×10×15 mm. Figure 3.6 shows a set of printed specimen samples.

Despite identical lattice volumes, achieving a consistent and comparable cross-sectional geometry across patterns is challenging. Cross-sections vary within a micro-lattice depending on whether the slice location passes over nodes or struts, making identical cross-sections infeasible for comparing different patterns. To standardize the samples, we used a common parameter across all : a transverse cell count of 4×4 cells.

Aiming to characterize lattice geometry, we designed for failure to occur as close to the center of the lattice as possible, requiring careful control over stress concentrations. Figure 3.6 shows our sample design, inspired by Drucker's geometric optimization of metallic tensile specimens Drücker *et al.* (2018). To minimize boundary condition effects, lattice thickness was gradually increased toward the grip sections.

3.5.3 AM technology selection for micro-lattice manufacturing

Manufacturing micro-lattices presents challenges, even for AM processes. Our selection of printing technology is based on two key criteria : *(1)* the steepest overhangs achievable and *(2)* the ability to print fine details such as columns for strut-based micro-lattices or walls for TPMS or shell-based structures. To test various materials and evaluate these manufacturing processes, three technologies were selected and named as such in the rest of this paper : SLA, MSLA and PolyJet. The models, brands, and specifications are presented in Table 3.1.

Tableau 3.1 Machines and associated materials selected.

CATEGORY	MSLA	SLA	PolyJet
MACHINE	Elegoo ® Mars	Formlabs ® Form3	Stratasys ® Objet30 Pro
MATERIAL	Black Nova3D	Grey standard	VeroClear model and SUP706B support
LAYER-HEIGHT	50 µm	25 µm	16 µm
SLICER USED	Chitubox Basic	Formlabs ® Preform	*Objet Studio™*

Because of the criticality of post-processing, which is often lacking as highlighted in the literature review, the detailed protocol of post-processing is available online [2]. All micro-lattices are printed with their loading direction aligned with the X-direction of the printing bed (Fig. 3.6 — Z is the printing direction), which is recommended as the most resistant by the manufacturer for PolyJet. To avoid differentiation, we have applied the same orientation for printing the other samples. This assumption was verified experimentally in Section 3.6.5). Additionally, we carefully selected the resin and post-processing steps for each technology to ensure consistency and reliability in our comparisons :

- **SLA** : All samples were made with Standard Grey Resin (Product code : RS-F2-GPGR-04). After printing, the parts were cleaned in an isopropyl alcohol (IPA) bath and then post-cured with UV light in the Form Wash and Form Cure stations.
- **MSLA** : The parts were made with black Nova resin and a layer height of 50 µm. The resin was cleaned with water, and the curing process was the same as for the samples made with SLA.
- **PolyJet** : The printer has two resin tanks : one for printing the model itself (VeroClear resin) and one for the support material (SUP706B resin). VeroClear resin allows for the smallest layer height of 16 µm in high-definition mode. The supports are usually removed using a cleaning station equipped with a pressure jet. However, because of the fragility of our

[2] Detailed protocol: https://initrobots.ca/meshproc/

lattice struts, this method was not feasible. Stratasys ® provides a soluble support material (SUP706B resin) that reduces the need for pressure jet cleaning. This material is soluble in a water-based solution. Despite this, the density of the micro-lattice prevented the solution from reaching the core of the network. To clean the smallest areas, we developed a two-step post-processing method repeated over four cycles : *(1)* dipping the sample in the IPA solution for ten minutes and *(2)* rinsing it with water to remove pieces of support [3].

3.5.4 Network relative density measurements

As noted earlier, achieving a fair comparison between the micro-lattice tensile tests requires a consistent scaling method based on relative density. Relative density accounts for the combined density of the resin material and the truss geometry, reflecting the empty spaces within the lattice structure. We used a Sartorius Secura 224 1S hydrostatic balance, which employs Archimedes' principle to determine the density of each material by measuring the mass and volume per cell. This device provides a repeatability of 1 mg. The results of these density measurements are discussed in Section 3.6.2.

3.5.5 DIC methodology

As previously mentioned, the deformations we aim to observe are small so we rely on DIC to capture the specimen behavior. DIC tracking requires a good visual texture. To address this, the surface of each sample was covered with a speckle pattern, as shown in Fig. 3.6. This speckle pattern must be random to increase the algorithm's robustness in tracking displacements. For our small samples, we manually achieved a random speckle pattern using a mist of spray obtained from a white paint from a distance of about 20 cm.

The 2000 × 1000 pixel images were captured at one frame per second (1 Hz). We ran DIC analysis using the open-source software DICe Turner, Crozier & Reu (2015) and the ParaView visualization tool Ayachit (2015). A *Python* package to better control the graphical representation

[3] Video of the post-treatment protocol: https://youtu.be/nenjaGyFybw?feature=shared

of the results was developed and used to present the results of this work [4] and extend the variables extracted from DIC. This tool can be used to analyze the displacement obtained with DIC and to generate contour plots with adjustable parameters. With this script, we gained access to two physical values particularly relevant to this work : the principal strain and principal angle (ε_1, θ_p). We can also illustrate the evolution of these quantities over time and plot the relative displacements of the lattice during the different phases of the experiment, as well as overlay the strain field on the deforming part visualization [5].

The micro-tensile device has limited space with a good viewing angle of the sample. Thus, we are using a single camera in our setup [6]. Image analysis during experimental tests can therefore only be based on a 2D view of one side of the micro-lattice.

3.5.6 Total number of samples and distribution

A total of 108 specimens were produced : 42 micro-lattices for tensile testing, 12 bulk material specimens for tensile testing, 36 specimens for studying differences between manufacturing directions, 12 rectangular parallelepipeds for viscoelasticity analysis via DMA testing, and 9 for density measurements. For each pattern type, three specimens were printed to assess experimental reproducibility and gauge the reliability of the manufacturing process.

3.6 Results and discussion

3.6.1 Bulk material characterization

For the three selected AM processes, the respective manufacturers provide varying levels of detail on technical specifications and the mechanical properties of their resins and the resulting manufactured parts. The amount of information given depends on the target market and company

[4] https://github.com/lcatar91/DICe_plotlib

[5] Time-lapse of the DIC experiments: https://initrobots.ca/meshproc/

[6] Micro-tensile and DIC setup: https://initrobots.ca/meshproc/

policy. For example, more detailed information is provided by Stratasys[7] and Formlabs[8] compared to Elegoo[9]. To address the lack of information provided by some manufacturers, we conducted tensile tests on specimens and Dynamic Mechanical Analysis (DMA) tests to better characterize the tensile strength, glass transition temperature, storage, and loss modulus of the resins. Figure 3.7 presents the results of the tensile tests on ASTM D5023 standard specimens, specifically 2 mm rods with 100% infill.

The MSLA resin has no data provided by the manufacturer; our tests found that it has the lowest tensile strength. The SLA resin (Formlabs) is well documented, but its performance is highly dependent on the handling of the material, parts, and post-cure conditions. Our results show a maximum stress resistance of 55 MPa, slightly below the 65 MPa claimed by Formlabs®. Furthermore, since there is no data about the impact of PolyJet's post-treatment on the mechanical properties of the parts, we conducted additional tensile tests. PolyJet's post-treatment involves an aqueous solution with 2% mass caustic soda and 1% mass sodium metasilicate, impacting not only the support material but also the printed structure. From Fig. 3.7, we observe that the PolyJet resin undergoes substantial elongation before breaking in the longitudinal direction; the chemical solution deteriorates this behavior by almost 30%.

---

[7] PolyJet Materials: https://www.stratasys.com/en/materials/materials-catalog/polyjet-materials/

[8] Formlabs Materials: https://formlabs.com/materials/standard/

[9] Elegoo Materials: https://www.elegoo.com/collections/resin/Resin

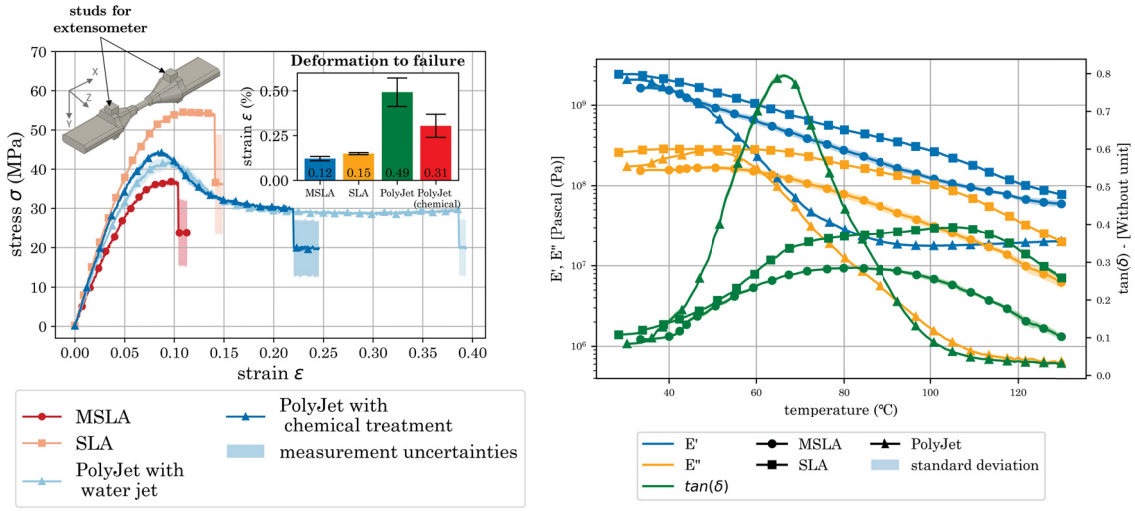

Figure 3.7 Left : Tensile test results with standard specimens (3 repetitions — 1-dev standard). The tensile specimen geometry is shown in the top-left corner, with a circular section of 2 mm in diameter and 100% infill. The sample is loaded along the printing Y axis. Right : DMA test results with the three materials-printer combinations used. Curve colors show the mechanical property and curve bullets, the printing process. We observe significant variability between each UV resin in the mechanical property. SLA is stiffer than PolyJet resin, which is itself stiffer than MSLA resin

While the tensile test provides maximum stress and elongation, the viscoelastic properties must be assessed with DMA tests. Figure 3.7 shows three properties extracted from this test : the storage modulus—elastic component (E'), the loss modulus—viscous damping component (E"), and the phase angle $tan(\delta) = \frac{E'}{E''}$. We conducted a three-point bending test with parallelepiped samples (5 × 3 × 25 mm). We found that the SLA material has the highest storage modulus, while the MSLA material has a similar curve but slightly lower values. However, there is a clear increase in performance with the PolyJet resin in the temperature range of 50-130 °C. Additionally, the storage modulus shows a clear inflection for the PolyJet resin only, allowing us to measure a glass transition temperature of about 70 °C, confirmed by the tan(δ) curve. For E", the opposite trend is observed with the loss modulus. The resin used with SLA is the stiffest and most viscous. This information will be useful for interpreting the results of Section 3.6, as the behavior of the micro-lattice depends strongly on the behavior of the bulk material.

3.6.2 Pattern relative density

Before analyzing the tensile properties of the micro-lattices, we must establish a normalization method to allow fair comparisons between patterns. The relative density measurements of each pattern enable us to contextualize the mechanical resistance variations of each micro-lattice. While the common denominators of the samples are the number of cells (4) and the diameter/thickness of the struts or surfaces (0.3 mm), some patterns are more sparse than others and must be compared regarding their mass. The results of the relative density measurements for each pattern are shown in Fig.3.8. The figure also includes the measured density of the resins.

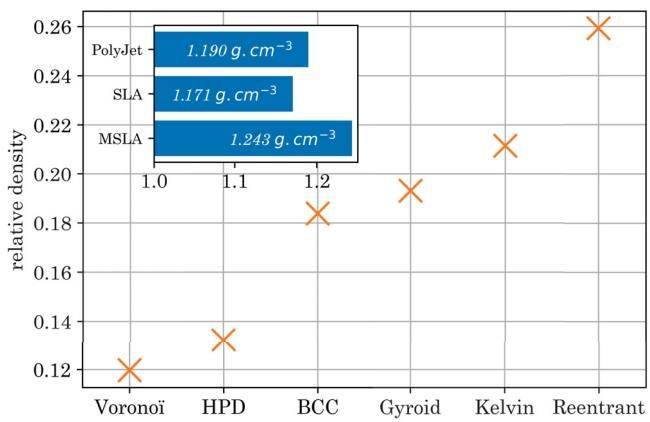

Figure 3.8 Relative density measurement for the six selected micro-lattices. Values are given for a single cell of each pattern. In the top left, density measurement of the raw resins.

The respective resin densities are almost equivalent, with the SLA resin being slightly lower. These results refine the manufacturers' data, which only provided a vague range for these properties. The sparse information can be partially explained by the high influence of post-treatment and its duration (Moosburger-Will, Greisel, Sause, Horny & Horn, 2014).

Surprisingly, the gyroid lattice, despite being made of surfaces instead of struts, does not weigh significantly more. Its mass is similar to that of the BCC and Kelvin lattices, all of which are close to the general average mass of the lattices. This similarity is due to the maximization of the internal cavity volume achieved with the gyroid pattern. Conversely, the re-entrant structures

require additional material to support their auxetic behavior, resulting in a higher relative density. With these values in hand, we can now more accurately compare the mechanical properties of the micro-lattices.

3.6.3 Strength and elasticity of the patterns

Four of the six lattices (BCC, Gyroid, HPD, Kelvin) can be manufactured using all the printing technologies selected for this study (see Section 3.5.3). Their respective load-elongation curves are presented together in Fig.3.9. The other two shapes (Voronoi and re-entrant) can only be manufactured using the PolyJet technology and are shown separately.

The results for each manufacturing method and micro-lattice, shown in Fig.3.9, differ significantly, likely due to disparities in the stresses transmitted within the micro-lattices.

Our results demonstrate good reproducibility of failure in terms of maximum load and elongation values. The uncertainties in measurements across sample repetitions are represented by lighter-colored envelopes around each curve. The behavior becomes less predictable after failure, as most rupture profiles exhibit jumps corresponding to the sequential failure of cells. In some cases, if the cells hold until enough internal struts rupture, the resulting failure smoothens and delays the final rupture. This phenomenon is particularly observable in the Kelvin lattice curves, where the slope variation of the load-elongation curves is very smooth.

Regarding strain behavior, the BCC lattice sample performs better, with the largest elongation at breakage. The gyroid and re-entrant lattices yield at higher loads but break at lower elongation values. However, the gyroid pattern stands out in terms of mechanical ultimate load, which, combined with a relative density (Fig 3.8) in the center of the specimens' distribution, results in a superior stiffness-to-mass ratio. Differences are also evident between materials of varying stiffness. The combination of interlayer adhesion and resin printed with SLA is much stiffer than PolyJet resin, which is itself stiffer than MSLA resin, as expected from the DMA test (Fig. 3.7). This is consistent for every micro-lattice pattern in Fig.3.9. These differences align with the

material tensile tests presented in Section 3.6.1, confirming the order of sample failure for each pattern : SLA, MSLA, PolyJet.

The manufacturing process significantly influences the resulting lattice properties. Specimens printed with the Objet30 Pro contrast sharply with the others, as expected from the material tensile and DMA tests in Section 3.6.1. Lattices made with the PolyJet underperform in terms of strength and deformation, likely due to the chemical post-treatment. The contact surface area increases with the number of cells in the micro-lattice, impacting mechanical resistance and resulting in decreased work performance for all lattices manufactured with PolyJet. Each manufacturing process also varies in interlayer cohesion, a crucial aspect discussed in more detail in Section 3.6.5.

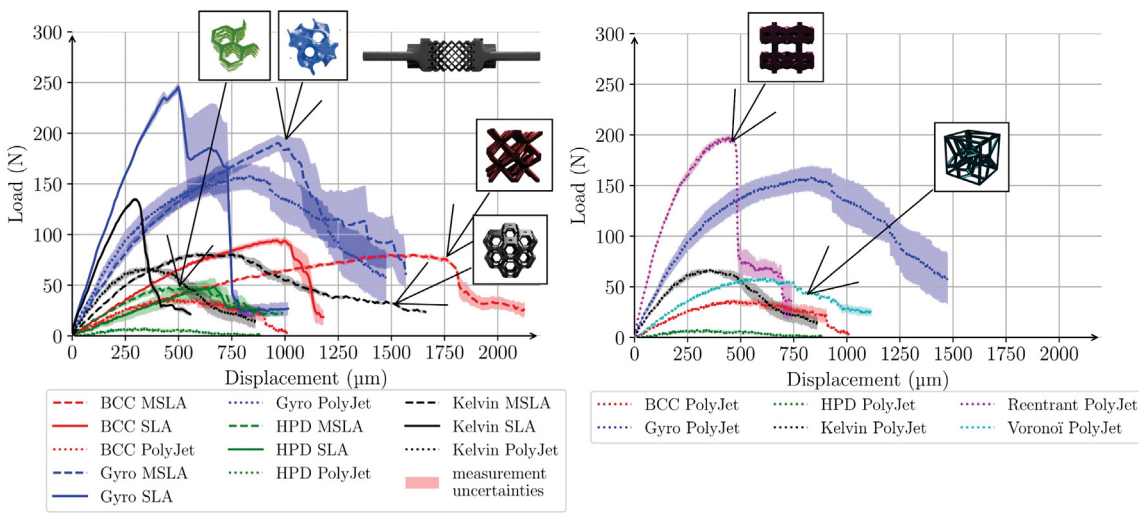

Figure 3.9 Tensile test results. Left : BCC, gyroid, HPD and Kelvin micro-lattices made on MSLA, SLA and PolyJet printers. Right : re-entrant pattern and Voronoi that could only be achieved with the PolyJet. Measurements' uncertainties of the sample repetitions are represented by lighter-colored envelopes around each curve. The re-entrant pattern shows the highest load, and the Voronoi one.

The load-elongation curves do not clearly distinguish between respective load and elongation performance. A sample might excel in load but be poor in elongation, or vice versa, or exhibit balanced properties. To address this limitation, we calculated the work required to reach failure for each lattice. The work is defined as the area under the load-elongation curve, considering everything from the beginning of the test up to the point where the load falls below 95% of

its maximum value. Figure 3.10 presents the work values for each design and manufacturing method used. The gyroid lattice stands out significantly, regardless of the printing method employed. In terms of materials, the resin printed with the MSLA printer demonstrates more flexibility and absorbs elongation with a maximum value of 63 mJ. Other resins exhibit stiffer behaviors. Notably, the HPD pattern turned out to be weak in both load and displacement during these experiments. This is particularly evident from the work values shown in Fig. 3.10. This micro-lattice does not allow loading-misalignment. Despite several precautions taken during handling the parts in the manufacturing process, the micro-lattice was very sensitive to mechanical stress. The micro-lattice breaks quickly at low loads and low displacements. Since the work is composed of both, the HPD pattern is the weakest overall.

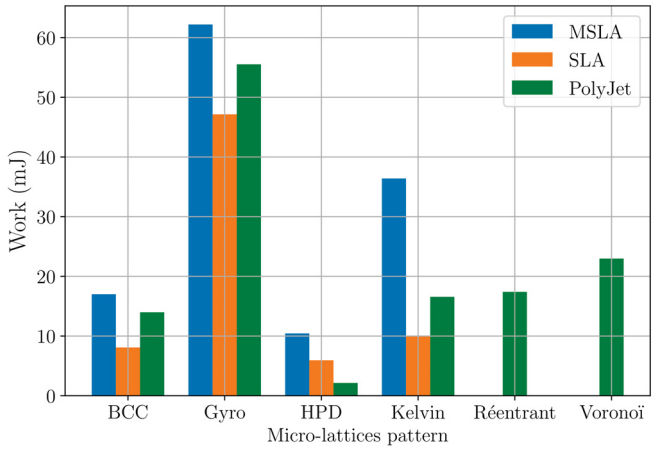

Figure 3.10 Work for each micro-lattice pattern during their tensile tests until 95% of the first failure. It corresponds directly to the mechanical properties targeted for a micro-lattice shell : the ability to resist stresses without damage thanks to structural deformation.

Interestingly, the order of failure observed in our tensile tests matches the results of Maconachie's compressive tests (Maconachie *et al.*, 2019), from best to worst : gyroid—Kelvin—BCC—HPD patterns. This behavior is partially related to the density of the lattices, as illustrated by the authors with an Ashby plot, which shows significant contrasts for gyroid and Kelvin micro-lattices that tend to be more massive. These results encompass several factors, and comparing these heterogeneous factors requires an analysis of their respective impacts on the final design (Catar, Tabiai & St-Onge, 2022).

3.6.4 DIC analysis

Up to now, the results curves illustrate the overall behavior resulting from contributions at all scales (micro, meso, and macro). To refine our analysis, we need *in-situ* full field measurements of the deforming structure. The graphical representation of DIC results provides macroscopic information about the deformation of the micro-lattice over the entire sample, and the digitization of the experimental images allows for more detailed calculations in specific areas of interest within the structure. We applied this method to BCC, HPD, Kelvin, and gyroid micro-lattices printed with the SLA printer. For the other two mesh types, re-entrant and Voronoi, printed using the PolyJet machine only, the visibility of the speckle pattern on struts was limited due to the internal displacement of the mesh and its auxetic behavior.

Figure 3.11 presents three image excerpts from a time-lapse of the DIC results, providing a more in-depth understanding of how each lattice distributes loads and illustrating the weak points of each lattice [10]. Notably, we observed that the BCC and gyroid lattices distribute the load uniformly along the loading direction, while the other two experienced local concentrations of stress that caused earlier failure. This can be seen in Fig. 3.11 with a more pronounced change in the color gradient in HPD and Kelvin cells.

Furthermore, the rupture line shown in Fig. 3.11 matches the center line expected by design (see Section 3.5.2, Fig. 3.6). In Section 3.5.1, we mentioned that the BCC lattice has all its struts oriented at 45°. The probability of lattice weakness is equal in all cells (with the same strut diameter throughout). Thus, the BCC lattice rupture profile broadly follows the theoretical center line : in addition to the lowest cross-section due to the progressive changes in diameter, the defects are also uniformly distributed across its cells. This results in a regular break of the micro-lattice. Lattices with greater variation in their strut orientation may exhibit longer resistance. The Kelvin lattice has beams in the loading direction that will not present a manufacturing staircase effect due to the layer-by-layer printing process, which usually weakens the lattice. Therefore, failure will follow beams that are likely to have more defects or stress concentration imposed by

[10] The full video of the time-lapse is available online : https://initrobots.ca/meshdic

the staircase effect. Consequently, Kelvin's profile of the rupture will not perfectly follow the theoretical line of rupture. Figure 3.11 shows a clean and straight profile of rupture for the BCC micro-lattice, while the path is tortuous for the Kelvin micro-lattice.

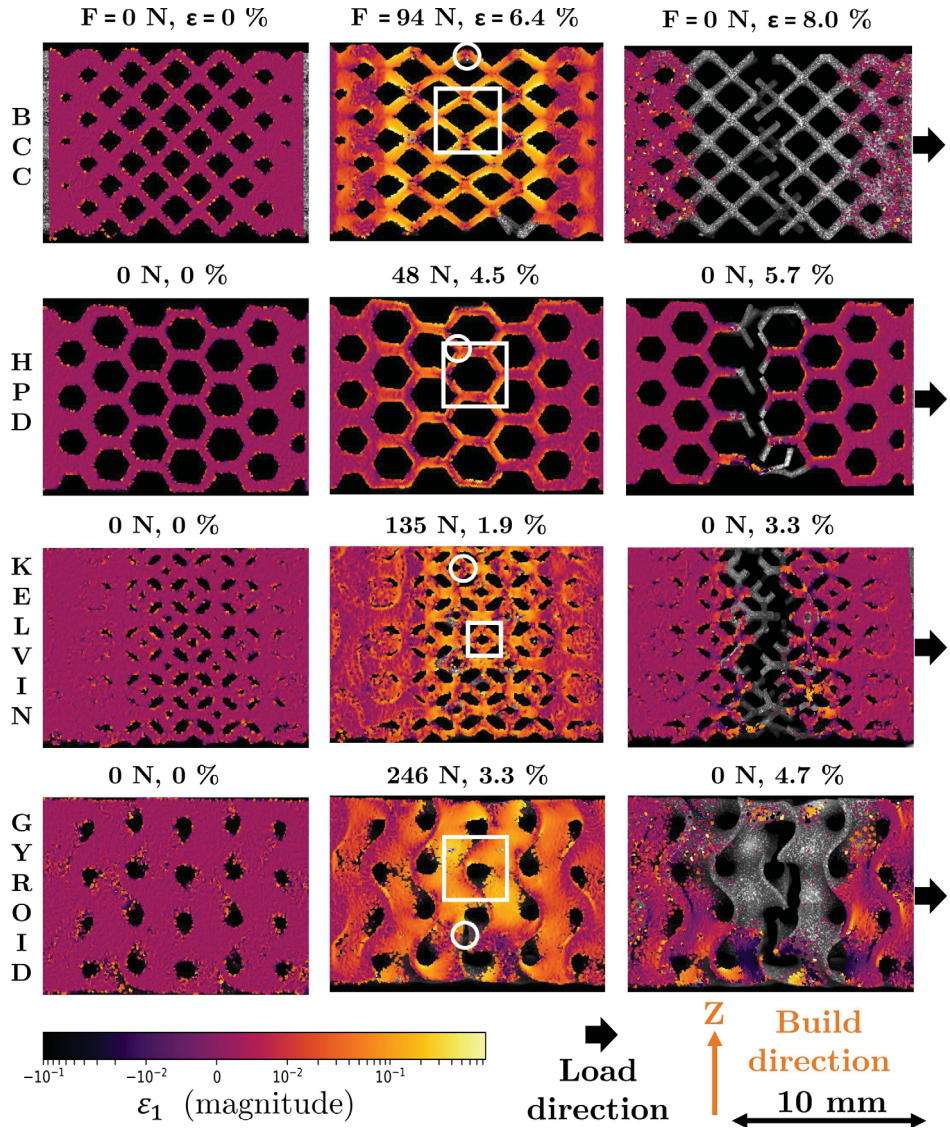

Figure 3.11 DIC time-lapse : visualization of ε_1 strain field. The first column represents the unloaded state. The second presents the moment right before the initiation of rupture, and the last one is the sample right after failure. After rupture, the tracking is lost due to the sudden displacement of struts at the breaking point. The white squares represent areas that are detailed in Fig.3.12 where the deformations in the principal directions are represented by the computation of θ_p. The white circles indicate the initial failure zone.

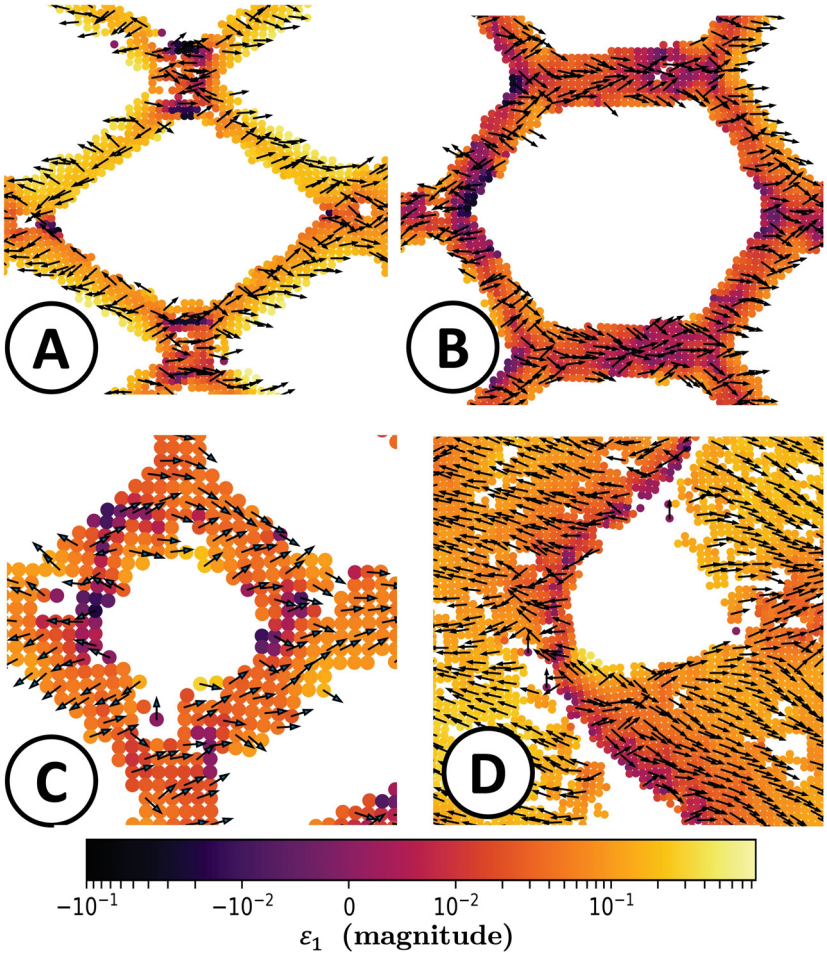

Figure 3.12 Representation of the main strain directions for four of the six lattices : BCC (A), HPD (B), Kelvin (C) and gyroid (D). We see the transition zones, *i.e.,* change of direction of strain, which helps predict the location likely to fail first.

The directions of the principal strain ε_1 were then plotted for these four patterns in Fig. 3.12. This highlights the failure initiation zone and the motion of each material area inside the lattice. From one micro-lattice to another, the geometry of the cell changes the way the motions are organized. We see varying degrees of discontinuities in the cell, with discrete transition zones for BCC and Kelvin lattices. For HPD and gyroid micro-lattices, we observe similar deformation in each cell. Although the rupture initiation zones are known for the BCC and Kelvin patterns, the location of rupture is uncertain for the HPD and gyroid patterns.

3.6.5 Impact of the printing direction

When studying the mechanical properties of parts made from AM processes, it is crucial to consider the effect of the printing direction. AM is highly anisotropic due to the layer-by-layer construction process. The phenomena are indeed complex to model : they depend on many aspects such as the characteristics of the machine, the chemical interface of the resin, the slicer's parameters, and the geometry of the part. Differences in mechanical performance according to printing direction are significant in this study, since micro-lattices are 3D structures that leverage mechanical performance in the X, Y, and Z directions.

To better assess the impact of the printing direction on our resin-lattice combinations, we conducted an additional series of tests. We used the same tensile sample as in Section 3.6.1, but changed its orientation on the printing bed along the X, Y, and Z directions. The results are shown in Figs.3.13 and 3.14. For the MSLA machine, the voxel construction provides fairly good homogeneity among directions, as observed in Fig.3.13. Interlayer cohesion is therefore not always complete. The height of the layer is also greater than the pixel width of the LCD screen, which further reduces the uniformity of cohesion between the resin close to the LCD screen and that which must adhere to the previous layer.

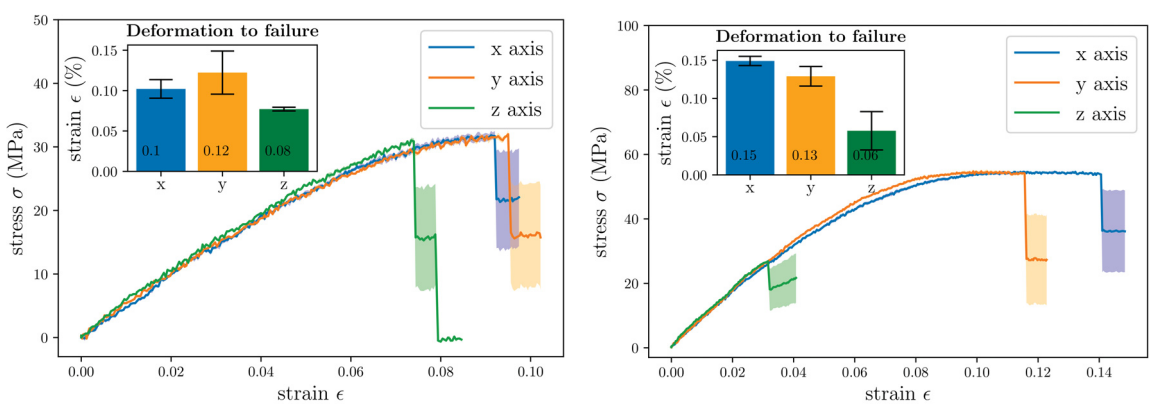

Figure 3.13 Multi-directional X, Y and Z tensile tests. Left : MSLA printer — This material shows a near-isotropic behavior. Right : SLA printer — we observe strong anisotropy.

For the SLA printer, Fig.3.13 shows a significant loss of mechanical strength when loaded along the printer Z-axis. The spot-on laser curing is involved in this behavior, whereas the LCD of the MSLA machines manages to maintain a greater homogeneity, showing only a small decrease in performance in the Z-axis.

For the PolyJet printer, the maximum stress values along the X and Y-axis are significantly higher compared to the other two processes, indicating better mechanical resistance and a highly ductile behavior. A key feature of the PolyJet machine is its ability to allow the user to select a "matte" or "glossy" finish for the part. We tested the impact of this feature on the maximum elongation value and found that the "glossy" finish reduced elongation performance. On the other hand, the strength along the printer's Z-axis is quite low, as shown in Fig. 3.14. This is critical for our usage of micro-lattice structures, which are generally built along all three axes with no preferential direction.

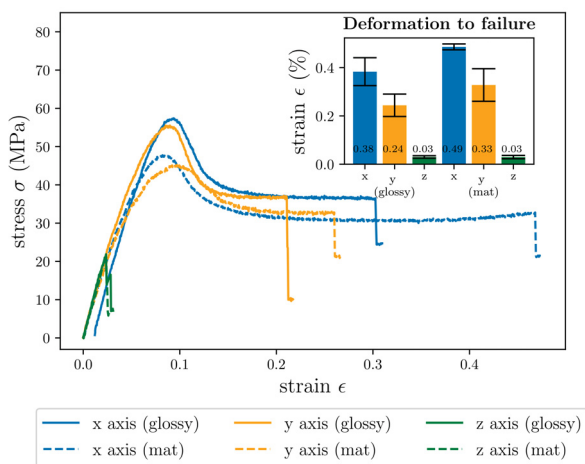

Figure 3.14 Multi-directional X, Y and Z tensile tests for the PolyJet printer — These tests show significant anisotropies.

These results, demonstrating different performances for different print directions, highlight the significant influence of anisotropy in the manufacturing process. Homogeneity is critical for micro-lattices built in 3D. For instance, the HPD lattice made with PolyJet fails faster than those made with SLA or MSLA. The orientation of the lattice relative to the printing direction plays a

crucial role. The micro-lattice will react more uniformly to the load if the geometry helps to smooth the distribution of defects (see Fig. 3.11).

3.7 Conclusion

In this study, we characterized micro-lattices and photosensitive materials through micro-tensile tests, presenting a sample design that controls the fracture zone during tensile testing and integrates features to enhance measurement accuracy. These experiments not only provide valuable data on the micro-lattices but also deepen our understanding of how manufacturing processes impact structural performance. Our findings underscore that the aggregation techniques of light-sensitive resins significantly influence the mechanical properties of the parts, with micro-lattice design amplifying the effects of manufacturing defects.

Tensile tests revealed the impact of cell geometrical configuration on rupture propagation. The results, showing considerable deviations between micro-lattices with identical patterns, highlight the combined influence of material properties and manufacturing steps. Anisotropy, resulting from differences in interlayer and transverse adhesion, further elucidates how manufacturing processes interfere with mechanical test outcomes. This reinforces the notion that selecting a material, process, and pattern involves finding the optimal combination of properties and manufacturing parameters rather than merely choosing the strongest option.

However, the lack of standardization in lattice studies complicates comparisons across different papers, as testing procedures vary significantly. To our knowledge, this is the first work to experimentally investigate tensile testing of polymeric photosensitive resin lattices. Despite the challenges, we corroborated some results with previous works on compression tests for similar patterns. The high mechanical performance of the Gyroid pattern suggests that further exploration of other TPMS patterns, such as Schwartz or Schowen types, would be beneficial.

Our experimental campaign highlighted numerous parameters and factors influencing performance, including bulk material, process, and relative density. While we gained significant insights into micro-lattice behavior, attributing the effects to specific factors with certainty remains

challenging. Future studies could focus on better understanding the relative importance of these factors on mechanical performance. Adapting the micro-tensile setup for a two-camera system to employ stereo-DIC could enhance data collection.

Given the various experimental elements, rationally ranking the available choices is essential. From a defined set of requirements, we should consider all aspects of the project, including manufacturing, mechanical resistance, lightness, and other relevant criteria. This ongoing work has been tentatively framed in previous research (Catar *et al.*, 2022).

Finally, scaling up the fabrication of ultra-light panels with larger cell sizes while maintaining low density presents significant challenges. However, the potential applications, particularly in aerospace structures, justify the continued efforts. By advancing our understanding and refining our techniques, we move closer to realizing the full potential of these innovative materials and structures in practical, large-scale applications.

CHAPITRE 4

ADDITIVE MANUFACTURING STRATEGY FOR ULTRA-LIGHTWEIGHT HIGH VALUE-ADDED COMPONENTS

Louis Catar[1] , Ilyass Tabiai[1] , David St-Onge[1]

[1] Département de Génie Mécanique, École de Technologie Supérieure,
1100 Notre-Dame Ouest, Montréal, Québec, Canada H3C 1K3

Article de conférence ASME-IDETC CIE 2022 publié en novembre 2022

4.1 Avant-propos

En se basant sur les résultats du chapitre 3, cette deuxième publication pointe la difficulté d'établir une priorisation rationnelle d'une combinaison de choix lorsque nous avons affaire à de nombreuses combinaisons de procédés, matériaux, structures, etc. De façon plus élargie, nous cherchons à visualiser l'impact de chaque décision sur la performance du système final, au regard de critères multidisciplinaires et scientifiquement pas comparables. Par exemple, la forme d'un dirigeable et le motif d'un micro-treillis. Afin d'y remédier, nous avons proposé une démarche qui apporte des réponses tant sur le plan de la fabrication que de la conception. Nous avons en particulier mis en lumière la complexité des méthodes de fabrication additive qui requiert de nombreuses étapes de préparation, de mise en œuvre et de post-traitement.

4.2 Résumé

La fabrication additive et sa croissance dans les domaines industriels avancés changent de nombreux paradigmes de processus pour le développement de composants hautement personnalisables. Elle condense les approches traditionnelles pour produire des assemblages de plus en plus intégrés à différents niveaux : fonctionnalité (résistance, légèreté), productivité (flexibilité, personnalisation) et développement (passage de la pièce numérique à la pièce finale).

Ce travail présente une méthodologie pour aider à sélectionner une combinaison de possibilités (matériaux, processus, etc.). Dérivée de la méthode du double diamant, cette méthodologie vise

à proposer une rationalisation des choix disponibles aux concepteurs de produits à forte valeur ajoutée avec des exigences strictes et mutuellement imbriquées. L'ensemble de la méthodologie est ensuite illustré par la conception d'un drone aérostat d'intérieur qui illustre la mise en œuvre de certains des éléments clés du processus proposé.

4.3 Abstract

Additive manufacturing and its growth in advanced industrial fields are changing many process paradigms for the development of highly customizable components. It condenses the traditional approaches to produce assemblies that are more and more integrated at different levels : functionality (strength, lightness), productivity (flexibility, customization) and development (passage from the digital part to the final part).

This work presents a methodology to help select a combination of possibilities (materials, process, etc.). Derived from the double diamond method, this methodology aims to propose a rationalization of the choices available to designers of high value-added products with strict and mutually intertwined requirements. The whole methodology is then illustrated with the design of an indoor aerostat drone which illustrates the implementation of some of the key elements of the proposed process.

Introduction

In a highly competitive context, creativity is the key to stand out with product innovation. Several companies already embed creativity-enhancing techniques within their product development process. However, it is not enough to «think outside the box» to create an effective creative environment. It requires methods and skills acquired from rigorous processes to support the generation of ideas without constraining the imagination. This is why *Design Thinking*, a user-centered iterative design method, showed to be an excellent tool for supporting innovation. In parallel, additive manufacturing is becoming more prevalent in industries, providing the designers with more freedom on geometry and prototype accessibility. Thus, it is necessary

to work on combining these new manufacturing means with the creative development process. The designers can start with the integration of the production characteristics into their design process : an approach known as *Design for Manufacturing (DfM)*.

More than a procedure to bring a concept to its prototype, DfM is a way of thinking involved from the design stage, where we must consider early how the part will be manufactured. Indeed, each manufacturing technology has advantages and disadvantages, so the entire production system must be integrated into the design (thinking) process (Poli, 2001). If we take the example of casting, the designers must consider the position of the parting lines of the mould : apparent fillets and the need for clearance angles to remove the part from the mould are mandatory and must be included in the part design. They must also choose the appropriate casting process according to the number of parts to be produced (taking into account tooling costs, etc.) (Wakil, 2019).

The recent progress made in digitizing manufacturing spaces is nowadays steering towards switching the paradigm from Design for Manufacturing to Manufacturing for Design. The advent of the smart factory is pushing the emergence of these new concepts (Chu *et al.*, 2016). Digital production means allowing the creation of an efficient feedback loop so that production generates more activity than design. In particular, additive manufacturing is characteristic of these new digitized means of production. Additive Manufacturing (AM) is defined as a process of adding material layer-by-layer to produce a physical object from its digital model (F2792-12a, 2012). With this manufacturing method, there is only one step between the digital model and the manufactured component. This rapid sequence creates the challenges of Design for Additive Manufacturing (DfAM) with its distinctions compared to DfM (Gibson *et al.*, 2021). AM indeed gathers numerous techniques with their specificities (Medellin-Castillo & Pedraza Torres, 2010) which must be explored and detailed thanks to the Design of Experiments. These standardized study tools (Davis & John, 2018) have been widely used for different industrial systems. In the context of AM, it is mainly the production of metallic parts that have benefited from the characterization research work because of their numerous industrial applications (Moradi *et al.*, 2021; Maconachie *et al.*, 2019; Gu *et al.*, 2012; Klocke *et al.*, 2017). Fused Deposition Modeling

(FDM) technology has also been the subject of numerous characterization and optimization studies because it is so accessible in the academic world (Durão *et al.*, 2019). Among the most discussed considerations are the aspects of part construction orientation, geometrical limitations or path planning (Medellin-Castillo & Zaragoza-Siqueiros, 2019). In contrast, the means of production based on photosensitive resins have been much less discussed in the literature.

If followed, DfAM allows, among other things, to minimize the number of parts, create modular and integrated assemblies or reduce the mass. These are ever-evolving aspects that highlight the exploration of the potential for exploitation of AM in the industry (Thompson *et al.*, 2016).

This work starts with an explanation of Design Thinking theory to allow the introduction of intermingling product design and design for additive manufacturing. To support this integration, we present a quantitative method with universal factors and we then focus on the specific but illustrative use case of an airship drone design.

4.4 Combining design and manufacturing methodologies

In this section, we reuse the main steps of the Design Thinking methodology and adapt them to the potential of AM in order to maximize creativity without restricting the design environment (Fig.4.1). Our unified evaluation tool provides quantitative data to guide the design and manufacturing choices among the wide range of possibilities. This requires the selection of relevant criteria based on DfAM guidelines. Combining creative innovation with manufacturing process understanding, the potential of AM is maximized to limit its impact on creativity.

4.4.1 What : Design thinking

Design Thinking is a creativity enhancement technique inspired by an industrial designer’s approach. First seen in the sixties, the development of the “product design" methodology included brainstorming techniques to encourage creativity, and is still a common popular approach (Cross, 2011). In 1986, Peter Rowe publishes « Design Thinking » laying down the key principles of

this novel approach (Rowe, 1986). It is based on collaborative intelligence and co-creation over three basic principles :

1. User-centered : adopt the users' point of view and include them in the process ;
2. Experimentation : transform the selected ideas into prototypes and confront them with the opinions of users ;
3. A five-point methodology :
    a. Use empathy : define the audience, its problems and needs (empathy map, immersion, survey).
    b. Diagnosis : objectives, challenges, points of friction and other constraints. Definition of the "problems statements".
    c. Build the concept : through co-creation and collective intelligence, several ideas must emerge. Quantity is favoured over quality. Break the ice (introduce yourself quickly) so that the participants more easily open up to each other. Encourage decompartmentalized brainstorming and then select ideas according to the criteria established from empathy.
    d. Prototype : bring the ideas to reality. A demonstrator allows having tangible objects to better *feel* the ideas.
    e. Testing : collecting users' opinions

The overall objective of Design Thinking is to generate ideas that meet the user's needs and that can be executed quickly with a minimum of risk thanks to the contribution of a multidisciplinary team.

As a practical implementation of the Design Thinking process, AM can meet its need for quick turnover and versatile parts production. Used with the right tools, this creativity-enhancing technique can be adjusted to industrial contexts where creativity is already perceived as the key to better meeting the users' requirements. The notion of rapid prototyping directly echoes the wide range of possibilities opened by these manufacturing approaches.

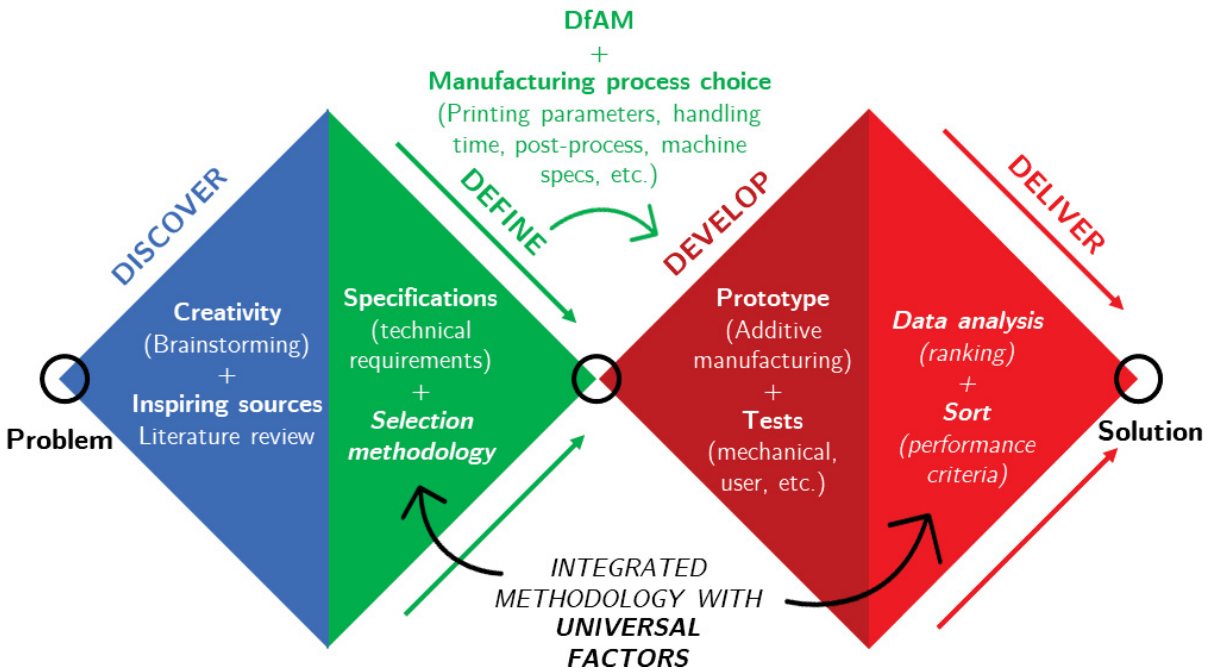

Figure 4.1 Double diamond tool diagram adapted to an engineering approach using AM inspired from Santos *et al.* (2017), Preez *et al.* (2014) and Segonds (2019)

4.4.2 How : Double diamond method

The double diamond method is one of the implementation tools of Design Thinking. It is a design model following several successive divergent and convergent phases, which allows designers to organize and improve the creative design process. Fig. 4.1 shows a schematic view of the different key elements of this method adapted to the technical requirements of AM.

The first diamond corresponds to the design strategy : the objective is to identify the problem and define the key issues. The first sequence corresponds to discovery (Research and Empathy). These are stages of benchmarking, immersion and knowledge of the existing situation. In the second phase, it is the definition and the analysis that take precedence. Targeted workshops allow surveying the users (Define). The technical specifications sort out the generated proposals to keep only the feasible ones according to the preliminary constraints of the project.

The second phase is focused on execution : designing new solutions until a satisfactory one is reached. After we agree on which problem to solve (first diamond), research can explore different ways to solve this problem and help refine the best method. That is first done through prototyping and ideation. This involves building scale models, testing configurations, etc. The final step is validation : refining the finished solution. Depending on the complexity of the project, this may very well require several iterations and evaluations.

This double diamond method is well adapted to AM workflow (Segonds, 2019). In the first stage of discovery, it is possible to collect existing AM structures (topology and geometry) and combine them with sources of inspiration for the project. More and more today the solutions come from art and nature (bio-inspired) to give solutions with organic but resistant geometry, such as for topological optimization using generative design (Da & Qian, 2020)). The definition stage corresponds to the selection of an AM process. The potential wide range of possibilities depends on many factors. The design team must reduce the list of ideas previously generated by confronting them with the different processes and their constraints (economic, geometric, materials, etc.). The following step, within the second diamond, produce concepts that have emerged and can be manufactured very quickly (rapid prototyping) to perform tests. These tangible evaluations allow proposing a final concept according to the project that integrates all dimensions, such as weight optimization, reduction of the number of parts or the use of complex geometry.

In this context, the AM processes provide the designers with several specific advantages Laverne *et al.* (2016) :

1. Geometrical complexity : there are few limitations in terms of design. The 3D volume is broken down into a series of 2D problems, which are easier to solve ;
2. Material complexity : with some processes, multi-material design is possible as well as parts with variable parameters, such as density ;
3. Hierarchical complexity : products with complex internal lattice, foam or organic structures can be created at different scales (micro or macroscopic) ;

4. Functional complexity : functional devices (not just individual parts) can be produced in one build.

Based on the advantages that DfAM brings to design creativity, we propose a tool to integrate it into the two double diamond convergence situations. Our universal factors allow us to process many inputs to get to a unique solution.

4.4.3 Unified evaluation metric

When we compare values of different dimensions, in some cases for rather distant physical concepts, their scale and relative importance must be aligned. The method we proposed is to use an interval scale with ratios. Given a list L of values, the position of measurement i in its respective measurement scale is given by the following formula :

$$M_i = \left(1 \pm \frac{L[i] - min(L)}{max(L) - min(L)}\right) \times \tag{4.1}$$

The above ratio can be used as a percentage and the selection of + or − depends on whether one wishes to minimize or maximize the criterion (ranking in ascending or descending order). This straightforward method allows for keeping the order but also the relative positioning between the elements of the same measurement.

For example, with a list [1, 3, −6, 9, 7], it becomes [46.7, 60, 0, 100, 86.7] if a maximum value is ideal and [53.3, 40, 100, 0, 13.3] if a minimum one is preferred. The different measurements (evaluation metrics) can then be added to one another without concern of their units while still consistent.

All metrics are on the same scale but most of the time they do not share the same importance for the end user and designers. Thus, we need to associate corresponding weights (importance) to each parameter. Using the previous list example (weight = 25%), with a second list [3, 8, 5, 3, 9] (weight = 75%), the combination weighted becomes [96, 28, 100, 64, 0] (minimum) or

[29.4, 70.6, 0, 76.5, 100] (maximum). Weighting the metrics allow to add a hierarchy to their contribution in the design selection.

For this, we recommend using the procedure elaborated for the NASA-Task Load Index (NASA-TLX). This method was developed to handle multifactorial weighting problems for evaluating the operator's workload (mental, physical, etc.) (Hart & Staveland, 1988). It has been used for years in many fields of physical and numerical experiments (aircraft cockpit certification, nuclear power plant control room, etc.) (Hart, 2006), and so it is considered a proven weighting technique applicable to the different requirements of a product design. Whereas workload has been divided by Hart into six dimensions (mental, physical and temporal demands, frustration, effort and performance), here we define each requirement of our design as a dimension. The method consists in comparing two-by-two each combination of requirements to extract the relative importance of each in an objective and quantifiable way. It is recommended to base that evaluation step on a panel of experts and a sample of end users, if available. The experts must come from a wide range of disciplines Sauro (2014).

If no such evaluation committee is available, we recommend an alternative method to minimize bias on the weight attributions : the functional tree. Split the concept into the smallest number of functions and then divide these functions until you get direct measurements. Attribute the weights by dividing from the treetop.

4.4.4 Evaluation of the manufacturing processes

As seen previously, AM techniques are disrupting the traditional design and engineering processes in many industrial fields. On the one hand, it unlocks the delay between idea/design and part production by the speed of implementation and its inherent geometric flexibility. On the other hand, it forces designers to have a more integrated approach to the manufacturing process. Thus, the "Design for Additive Manufacturing" has become a must (Thompson *et al.*, 2016). This approach is closely intertwined with the characteristics of each AM process. Integrating them properly into the design method implies a good knowledge of the capabilities of the

technology : expertise most often acquired by working directly on process engineering and through specialized training courses.

To evaluate these technologies, we highlight five categories of criteria :

1. The slicing parameters : the manufacturing choices are crucial for the final result of the printing. These parameters are crucial to the evaluation process since they directly impact the mechanical properties of the part as well as its feasibility ;
2. The printer specifications : Each machine has its strengths and limitations based on the manufacturer's design choices ;
3. Out of printer processes : several machines cannot produce a finished part by themselves. It is necessary to use other machines such as a UV light curing booth ;
4. The handling times : each technology requires different preparation steps in the software, sometimes with the material, and even manoeuvres between two stages of the manufacturing process ;
5. Post-processing time : even if the operator is inactive in some post-process steps (i.e. chemical baths for the parts), the time spent decreases the production rate and increases the technical support requirements.

We clearly understand from the previous list that the respective data of these criteria are not directly mathematically comparable : durations, volumes, dimensions, etc. However, by using the previous formula (equations 4.1), each of the criteria can easily be ranked. As it goes with these kinds of tools and methods, it is most often in the implementation that complexity and confusion arise. The rest of the paper details a representative use case to showcase the methodology.

4.5 The indoor airship use case

Our use case aims at the design of a small indoor airship. Aerostats or airships had their heyday in the first decades of the 20th century. Their peak in the 1930s saw the emergence of aerial machines of unrivalled gigantic size. Real liners of the sky, the luxury transatlantic crossings

offered by this type of aircraft had no equal. Nevertheless, these machines had their weaknesses at the heart of their particularity : the use of hydrogen as a lifting gas will definitively discredit the use of airships following a series of accidents, the most emblematic of which was the Zeppelin Hindenburg (Stockbridge *et al.*, 2012). Today, airships are still suffering from their association with the history of unreliable and old-fashioned cigar-shaped aircraft (von Braun, 1975).

However, recent years have changed the face of air transport. Where the aeroplane and helicopter once dominated, the progressive use of drones has turned this ecosystem upside down. Aircraft of all shapes and sizes are invading the airspace, and the withdrawal of the human pilot has made it possible to create flying platforms designed for very specific missions. Aerostat drones have great potential in applications requiring a very large autonomy that cannot be satisfied by the energy-consuming multicopters. The lifting gas (Helium is nowadays often preferred to Hydrogen), makes it so that we no longer have to worry about the aircraft's lift since the various actuators are used almost exclusively for the aircraft's mission-related movements.

Despite this, the fragility of the envelopes containing the lifting gas limits their use in confined spaces where the environment can be aggressive to their fine and fragile membranes. For this reason, the idea of protecting the flexible enclosure with an ultralight shell would make the indoor blimp more resilient and able to operate in more configurations (industrial site inspection, underground exploration, etc.). While this configuration has long been the preferred one for large outdoor airships (Liao & Pasternak, 2009), the limited lifting power of small airships used indoors poses a considerable challenge. Indeed, the surface-to-volume ratio does not favour small sizes : where the volume evolves in cubes, the surface evolves in squares. Nevertheless, recent developments in AM suggest it could be now possible to produce ultra-light shells. Moreover, an aerostat stiffened by this shell would grant new possibilities : docking, more freedom on the actuators' position and more freedom on the airship's morphology.

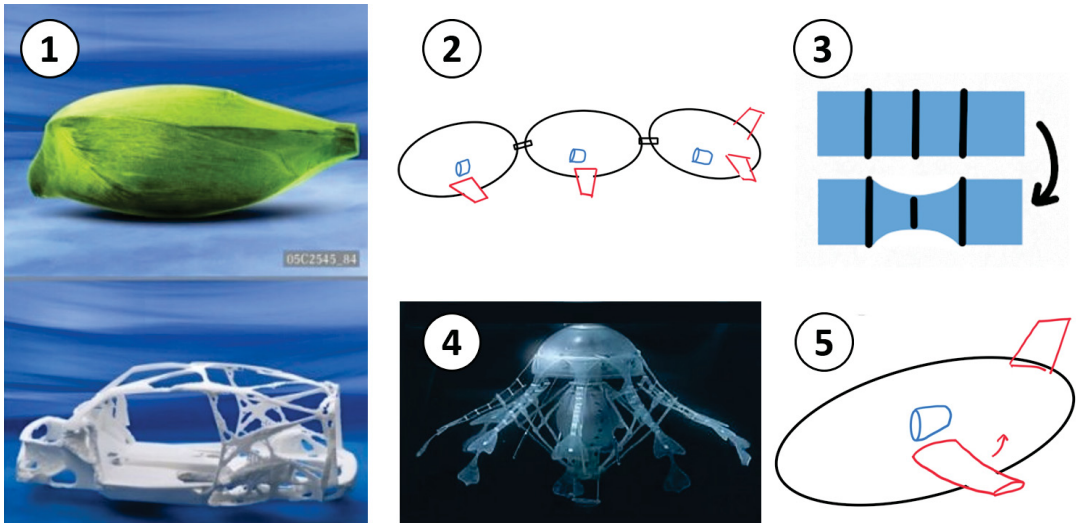

Figure 4.2 Few concepts were extracted from the brainstorming. Fish-box concept (1), multi-body airship (2), deformable (3), jellyfish inspired (4) and improved traditional airship (5)

4.5.1 Discover : Empathy exploration

Empathy is the first step of the design methodology and we implemented it with a multidisciplinary brainstorming activity. One of the key aspects of this implementation is the participant's selection : the airship's shape calls for aesthetic considerations that are difficult to evaluate on a purely technical ground.

The mobile robotics lab (INIT Robots [1]) partnered with the design lab (NXI Gestatio [2]) in an online thinking activity. The participants were distributed as follows : technical/engineering (7 people), industrial/object design (4), biology (2), architecture (1), art (2), and physics (1). Small teams were then created to encourage exchanges across different expertise. Only four participants were already familiar with aerostat drone engineering.

The objective of this activity was to generate different concepts for indoor airship drones. Thus, after a short introduction on the main requirements of the project such as the maximum size

[1] https://initrobots.ca

[2] https://www.nxigestatio.org

(doorways) or example usage scenario (telepresence, surveillance, etc.), participants in small teams were asked to defend a concept with minimal graphical support.

The proposals we extracted from this activity are illustrated in Fig. 4.2. Several concepts are bio-inspired, a common inspiration at this stage of design. The first concept is a takeover of the Mercedes Bionic concept car (Yang, Ju-Ying, Yuan-Li & Yu-Hsuan, 2019) which combines a large volume (fish box) and a light rigid structure : compactness and manoeuvrability. The second one suggests the use of several distinct airship bodies (Fig. 4.2-2) regrouped in a modular snake-like flying structure. Similarly, a last bio-inspired concept takes the shape of a jellyfish to generate holonomous movements (Fig. 4.2-4). Then comes one design focused on the functional aspect with the ability to pass through narrow passages thanks to a deformable structure (Fig. 4.2-3). Finally, a concept with a more classical ellipsoidal shape has been proposed associated with the use of fins for manoeuvrability (Fig. 4.2-5).

Once the original ideas have been generated, we sort them to keep the few most valuable concepts.

4.5.2 Define : Airship design requirements

By definition, an airship drone must be able to float. Immediately, this aspect imposes a relationship between the total mass of the aircraft and the volume of gas that the envelope can contain. The relationship given by the aerostatic is directed by the Archimedes formula : $B = V.\rho_a$ where B is the buoyancy force applied the opposite to the weight (gravity) of the body, V is the volume of the body, and ρ_a is the average density of the local atmosphere.

Secondly, attention must be paid to the shape. The shape will determine whether the concept aims to enhance the volume and the payload mass or the aerodynamics (velocity). Many other considerations are also related to the airship's shape : inertia (including added-mass), and manoeuvrability (position of the actuators). An airship can be described as conventional when it has the traditional ellipsoidal shape with an aerostatic lift from a hull containing a gas lighter than air. All other cases can be grouped under the category non-conventional : a new type of

propulsion (electric, fuel cell, etc...), a different shape of its hull, etc. Airship concepts can be categorized by their geometry (Ceruti & Marzocca, 2014) :

1. Traditional (C-T) - ellipsoid ;
2. Multi-hull (C-MH) ;
3. Turtle-shaped (C-TS) ;
4. Whale-shaped (C-WS) ;
5. Wing-shaped (C-WI) ;
6. Rounded-shaped (C-RS) ;
7. Brick-shaped (C-BS) ;

These unconventional geometries are mainly explored in the context of aerodynamic performance research (Liao & Pasternak, 2009). Nevertheless, it is interesting to observe that several concepts proposed by the participants in our brainstorming activity are of natural inspiration. So these aerodynamic shapes are *a priori* aesthetically accepted by the users.

4.5.2.1 Requirements interdependence

The parameters discussed previously are rather complex to evaluate because they are heavily intertwined : the performance of the aerostat depends simultaneously on the aerostatics, aerodynamics, etc. Requirements such as payload mass determine the volume of gas needed to provide lift (or the other way around). Once this volume is allocated, the way to organize this mass of gas impacts the aerodynamics by choosing more or less streamlined shapes. This shape gives the structural constraints to adjust the position of the engines, and sensors and ensure the rigidity of the whole. The inertia of the aerostat is thus adjusted according to the chosen materials and the distribution of the various structural components. This distribution impacts the general aesthetics of the machine and thus its perception by the users and the public. This last aspect, as mentioned previously, is what defines the airship's fit in an ecosystem and the social acceptance of the technology.

Figure 4.3 3D printers used. From left to right we find the MSLA, the SLA and the PolyJet (photos of the machines relatively not to scale)

This interdependence arises from several other aspects. In particular, how the different elements are manufactured will depend on mechanical data and will have an impact on the final visual aspect. Thus, the ability to fulfil a mission or to unlock different innovative capabilities will result from a sum of multi-disciplinary criteria with non-comparable characteristics. For example, the manufacturing volume of a machine and the mechanical performance of a structure may look unrelated, but this volume will define the number of parts of the final assembly which will greatly impact the resistance of the resulting shell.

4.5.3 Define : select additive manufacturing technology

Initial weight estimates of the concept structures steer towards extremely fine structures. This calls for technologies that grant great geometric flexibility : the ability to make bridges, and very high manufacturing angles. Considering this as the main constraint for manufacturing process selection, we have chosen to restrict ourselves in this use case to machines using photosensitive resins : a consumer MSLA *Mars* [3] from Eleego, an SLA *Form3* [4] from Formlabs and a PolyJet *Objet30 pro* [5] from Stratasys (Fig. 4.3). The Elegoo printer will create cubic micro-structures

[3] https://www.elegoo.com/collections/mars-series/products/

[4] https://formlabs.com/3d-printers/form-3/

[5] https://www.stratasys.com/3d-printers/objet30

Tableau 4.1 Evaluation of design criteria for simplified geometries - in parenthesis the value resulting from the simulation or the calculations and transformed into a score out of 100 points according to the unified scoring formula

Project requirements	Sphere	Cube	Ellipsoid
Aesthetic review from an expert	**40**	**80**	**100**
Drag coefficient	**56,9** (0,59)	**0** (1,32)	**100** (0,04)
Max. Stress (MPa)	**0** (4,28)	**13,3** (4,04)	**100** (2,48)
Added-mass coefficient	**100** (0,142)	**0** (0,456)	**82,8** (0,196)
Typical size at equal payload (m)	**100** (0,26)	**58,3** (0,61)	**0** (1,1)
Average	**59,37**	**30,34**	**76,56**
Ranking			

that are much more capable of deforming in all directions than the Formlabs. On the other hand, the SLA will homogenize the curing of the part which will make it more resistant. As for the PolyJet, it offers the best resolution in layer thickness despite a strong anisotropy according to the build direction and a relatively complicated use (important post-processes) compared to the two other printers.

Following the list of criteria mentioned in Section 4.4.4, the layer height is chosen as the slicing parameter and the build volume as the most relevant specification for the machines. The layer height (z-direction) has a major impact on the quality of ultra-light parts : the struts are oriented in such a way that at a small scale there is a staircase effect with the stacking of the layers. If the layer height is low, this effect can be blurred. Finally, the manufacturing volume of the machine is a parameter that affects the structural strength of large parts : limiting the number of assemblies.

4.5.4 Develop : Requirements evaluation

The different geometries resulting from the brainstorming can be linked to simple geometrical shapes : sphere (jellyfish), cube boxfish), and ellipsoid (traditional, multi-body, deformable

concept). This simplification allows for fast numerical results as a first iteration of the design process.

Different characteristics are associated with these geometries including the general aesthetic appearance, the drag, the mechanical strength of a tubular structure maintaining the shape, the envelope surface (even more relevant for a rigid shell) or the useful mass depending on the characteristic dimension of the airship. Table 4.1 shows numerical values for the measurements selected for each design criteria. The aesthetic criterion comes from the opinion of a designer who classified the shapes according to his expertise regarding the social acceptance of a flying machine, the drag from a Computational Fluid Dynamics (CFD) software and the structural mechanical resistance from a Finite Elements Analysis (FEA) software. The envelope surface is given by geometrical calculations and the mass by application of Archimedes' formula. The added-mass is a non-stationary aerodynamic phenomenon that accounts for the displacement of a volume of fluid (Pham, 1977). The added mass must be taken into account in the case of lighter-than-air vehicles and its value depends on a coefficient proportional to the density of the fluid. The coefficients are taken from the literature (Newman, 2018).

4.5.5 Develop : Manufacturing technology prototypes

The weight constraint forces us to consider methods to lighten the density of the aerostat. Micro-lattices are the only viable choice to realize such an ultra-lightweight structure for a protective shell. In a micro-lattice, materials are organized architecturally to provide good mechanical properties, as well as a low density. A lot of different patterns of micro-lattices can be tested ; so many it would be unproductive to test them all in a design process (Maconachie *et al.*, 2019). We selected one representative pattern from each of the six micro-lattice families with different characteristics in order to cover a large part of the design space in terms of lightness or impact resistance. (Fig. 4.4). These lattices can be organized homogeneously in polyhedrons or conformal in curved panels.

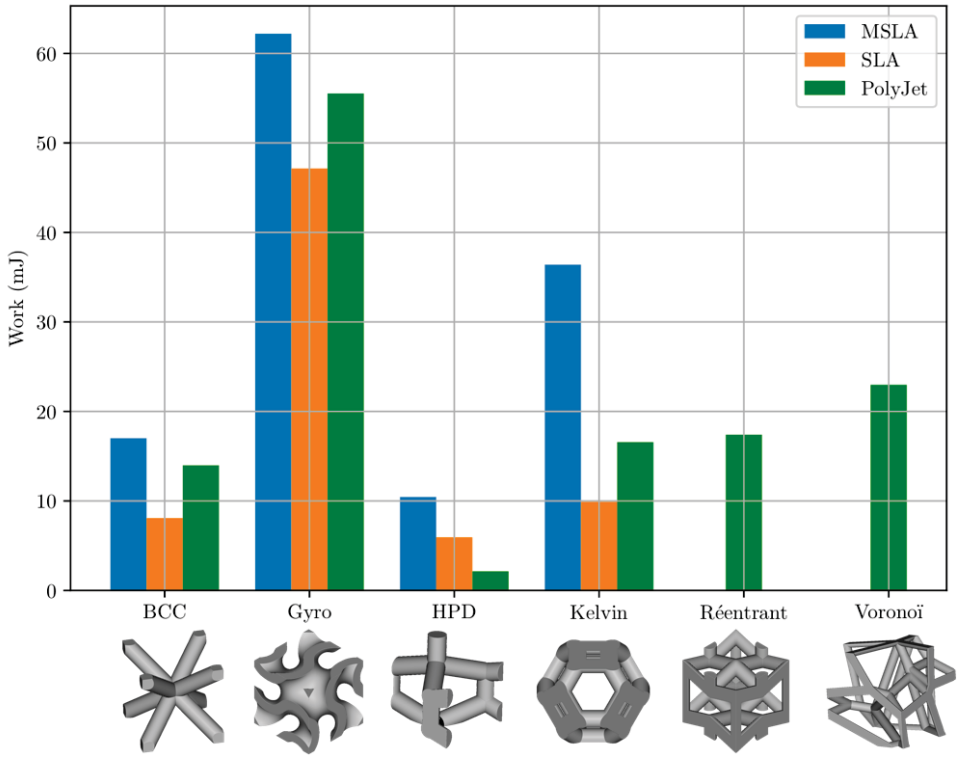

Figure 4.4 Work for each pattern selected. The Gyroid stands out from the previous graphical representations with its ability to support large constraints and a consequent displacement.

As part of a process of cross-evaluation of micro-lattices, materials, and fabrication methods, mechanical tests were performed on samples. When looking at different patterns, the material section cannot be identical. Thus, it was decided that the common parameter of the samples is a square of four by four cells with a thickness/diameter of 0.3 mm. Fig. 4.4 shows the summary of the test results. The selected metric, work, is the combination of tensile force and displacement data ; calculated with their integral. Mechanical performance alone cannot dictate the manufacturing and topology method, this aerostat project calls for more criteria such as the relative lightness of each of the lattices, the ease of manufacture, etc.

Regarding the evaluation of the manufacturing complexity, Fig. 4.6 summarizes the whole methodological classification. Thus the PolyJet has the largest manufacturing volume : it obtains a score of 100% on the volume and is ahead of the SLA machine at 45% and MSLA which is last

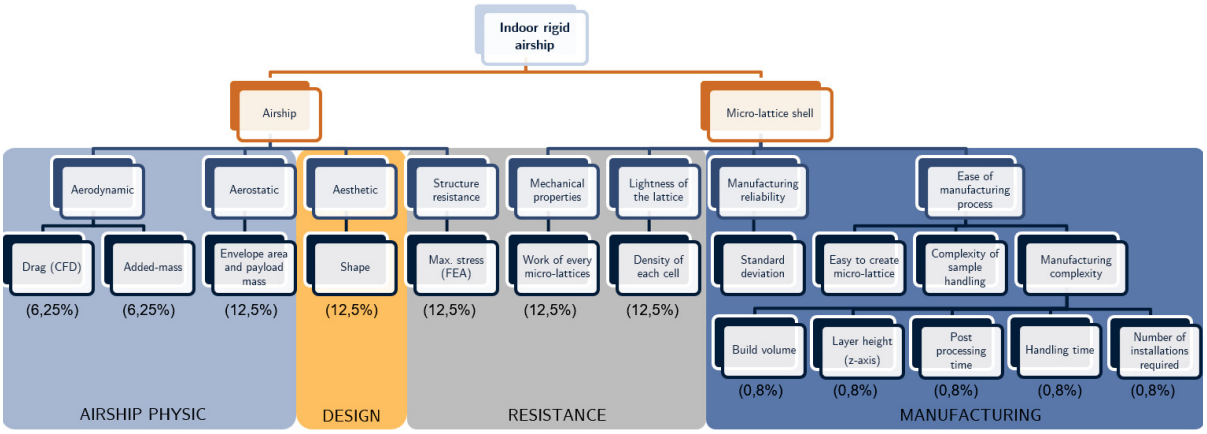

Figure 4.5 Criteria tree for an indoor airship project. Each floor has its own criteria. Some of them are dependent on those below and are therefore calculated by combining the corresponding performance indexes.

and thus obtains a score of 0% on this aspect. When we proceed in this way with all the criteria, we can then compare everything and establish a global score per machine by representing the relative contributions of each of the criteria. As an example, the MSLA comes second by being first on the number of pieces of equipment (in red, minimized), second and close to the SLA for handling operations (in green, minimized) and first for post-processing time (in orange, minimized). It loses ground due to its lower manufacturing volume (in blue, maximized). In the end, the SLA stands out by not necessarily being first on any of the individual criteria, but overall it offers the best compromise.

4.5.6 Deliver : Rank and sort

To select the best fit micro-lattice and the AM process, a criteria tree was derived, as shown in Fig. 4.5. Some constraints are independent (separate columns), while others depend on the same aspect (connected lines). For example, the weight of the lattice has no relation to the mechanical properties, but it depends on the density of each cell, which was experimentally obtained. We also find the criterion of manufacturing complexity which depends on the five aspects represented graphically in Fig. 4.6. Manufacturing complexity combines two criteria

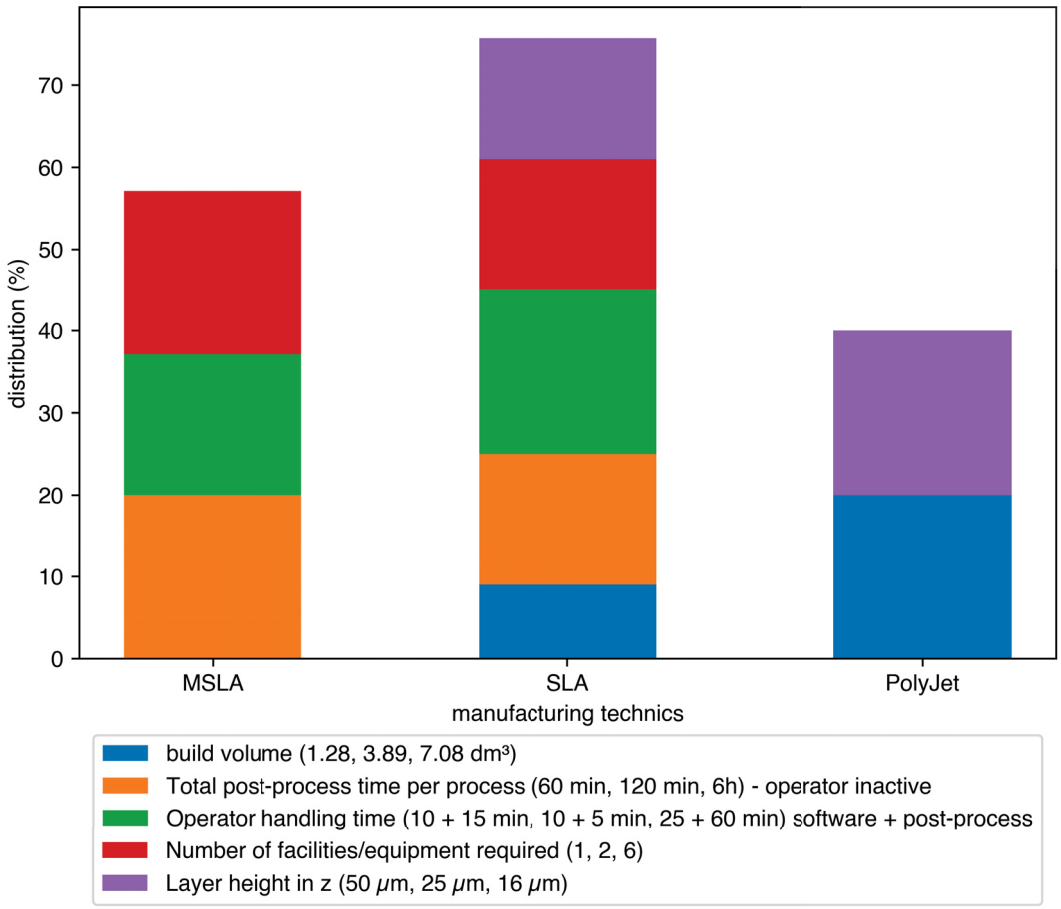

Figure 4.6 Manufacturing complexity based on machines characteristics and operations

related to the opinion of the operator. These three parameters (ease to create, the complexity of handling and manufacturing complexity) define the facility of the manufacturing process. The weights were derived directly from the functional tree. The weights of the direct measurements are shown in percentages in Fig. 4.5.

Fig. 4.7 summarizes all design parameters for the use case project in a single graphical representation. The eight intermediate requirements of the criteria tree in Fig. 4.5 are shown.

All realistic combinations of airship shapes, micro-lattice patterns and manufacturing means were explored. Each bar shows the contribution of each requirement to the overall score obtained for a given combination. One can thus immediately see the winning combination : ellipsoid

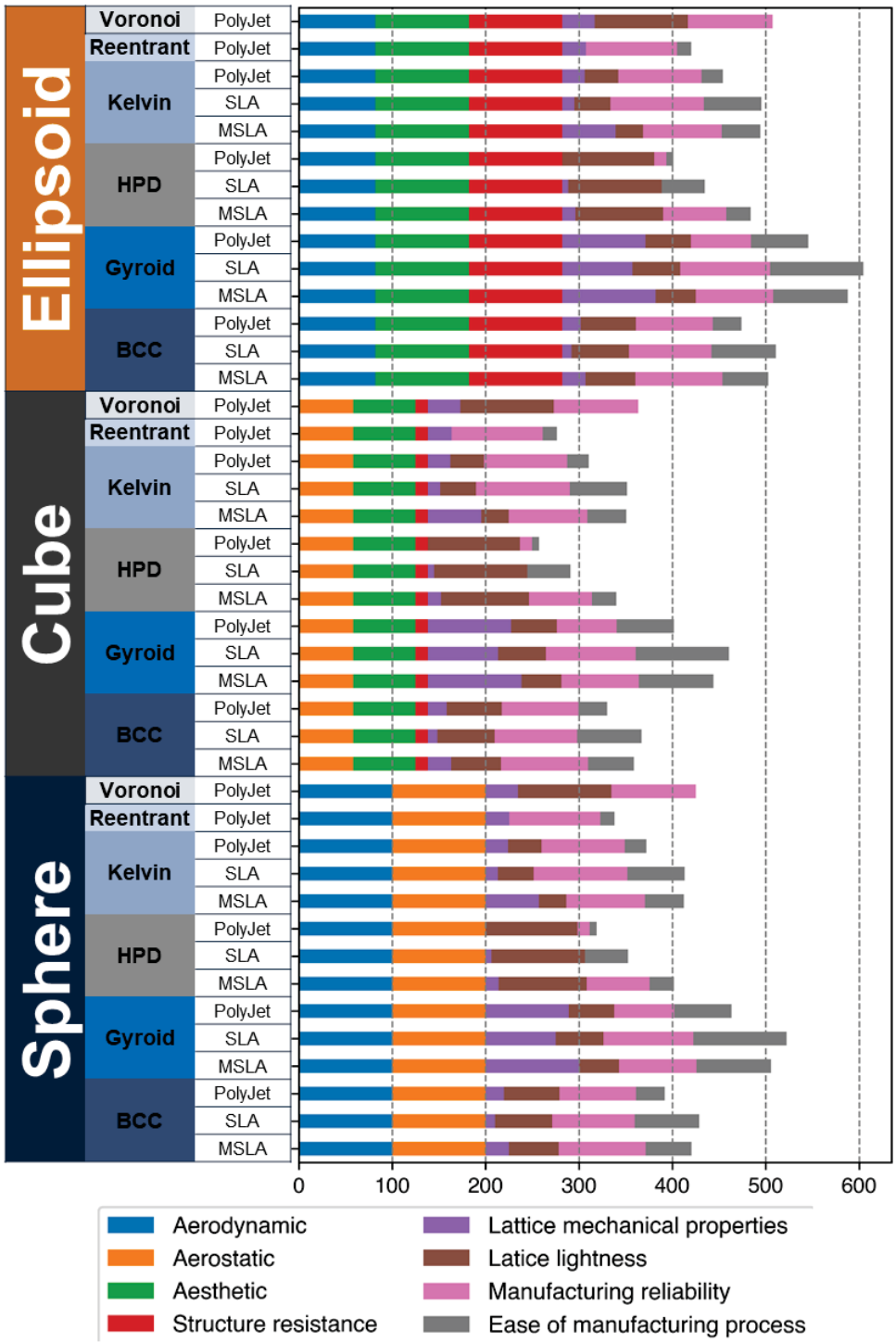

Figure 4.7 Performance index. Each combination is analyzed and sorted.

shape with gyroid micro-lattices manufactured by the SLA machine (Form3). This graphic representation has the advantage of allowing to visually represent the points of improvement for a chosen combination or realistic alternatives close to the ideal situation despite the fact of having a large number of possibilities. Set up at the beginning of the project, it allows navigating through the different milestones. This method is flexible because the score can be updated as we go along if we want to add new requirements. The implementation is fast while keeping the same standardized logic.

Conclusion

This paper presents an extension of the Design Thinking toolbox to integrate additive manufacturing technology. The method allows for a fast visual representation of a large amount of information and simplifies the process of selecting the right option. The use case showed that the method can bridge two distinct fields (airship mechanics and additive manufacturing of micro-lattices) within the same project. It paves the way for its application in several other multidisciplinary projects and other fields. This approach is easily scalable to take into account a lot more parameters.

Experts working on a design project often lack of a bird view of their project ; a holistic view of all aspects to be considered and their role in the technology selection. Our approach frees the creativity of the design team leveraging a wide spectrum of potential manufacturing technology while rationalizing the decisions based on numerical criteria. This process allows the experts to justify and qualify their intuitions, and on the other hand, it facilitates the implementation of certain decisions. Our next steps will address both the use case results and the methodology in parallel. We are now to refine the designs and create a functional aerostat prototype. A more refined consideration of printing parameters and manufacturing limitations is also needed. The meso-scale characterization of micro-lattices (cell scale) needs to be extended to the macro-scale (part scale) with ultralight panel assemblies and to the micro-scale modeling of printing artefacts. In addition, a dictionary of additive manufacturing processes could be introduced to help determine the important parameters of the most common technologies. These parameters can

be extracted from a review of the literature and supported with design of experiments for multi-parameters processes.

CHAPITRE 5

POLYMER MICRO-LATTICE BUFFER STRUCTURE FREE IMPACT ABSORPTION

Louis Catar[1] , Ilyass Tabiai[1] , David St-Onge[1]

[1] Département de Génie Mécanique, École de Technologie Supérieure,
1100 Notre-Dame Ouest, Montréal, Québec, Canada H3C 1K3

Article soumis à la revue « International Journal of Solids and Structures » en juillet 2024.

5.1 Avant-propos

À l'issue du premier objectif, nous avons bénéficié de l'espace d'une arène de vol pour expérimenter l'allègement de structure et la construction de dirigeables. Plusieurs axes ont été explorés. Tout d'abord, toujours dans l'objectif de réaliser une coquille en micro-treillis pour un dirigeable, des essais d'impression ont été effectués pour produire des panneaux de micro-treillis conçus pour une sphère (Fig. 5.1). Sans chercher à intégrer de la mécatronique à ce stade, la densité des micro-treillis de la sphère a été ajustée pour assurer minimalement, et uniquement, la flottabilité de la structure. Plusieurs limitations ont été relevées lors de ces tests de fabrication :

- la densité requise impose des cellules de grandes tailles (> 15 mm) et avec des diamètres d'entretoises au limites de la capacité du processus de fabrication (< 0,5 mm).
- ces grands élancements dans le micro-treillis apportent de nouveau défis : dans le bain de résine, les entretoises non durcies peuvent fléchir en contact avec le liquide lors des allers-retours effectués par le plateau d'impression entre deux couches, résultat du manque de rigidité de l'ensemble de la structure.
- la multiplication des supports avec des formes de micro-treillis convexes rend les étapes de post-traitement extrêmement complexes avec la rétractation de la résine au post-traitement et les manipulations requises pour enlever ces supports.

De nombreux prototypes (portions de sphère) ont permis d'explorer les paramètres de fabrication sans résultat fonctionnel. En raison des dimensions réduites de l'aérostat, une coquille

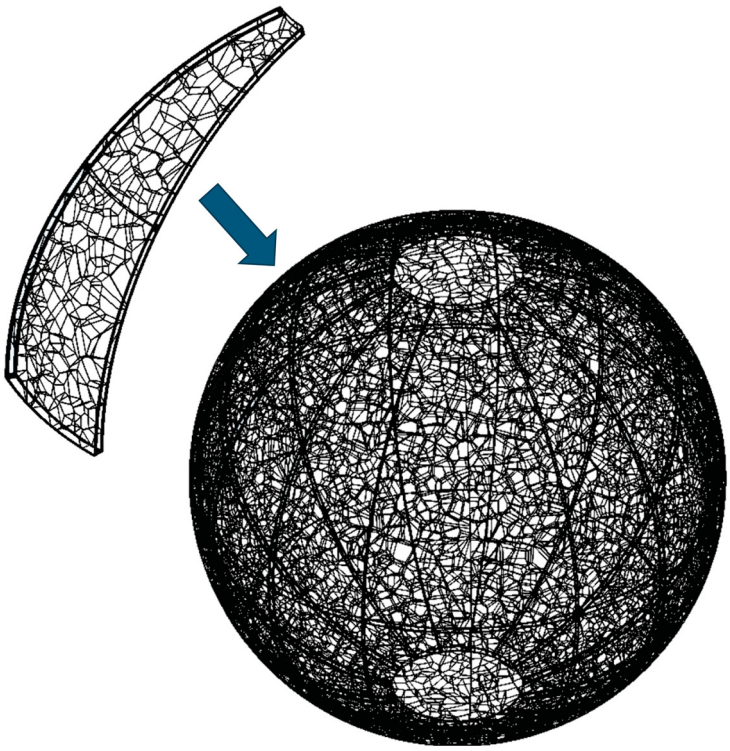

Figure 5.1 Coquille uniformément converte de micro-treillis utilisant des cellules Voronoi très larges pour une sphère de 70 cm de diamètre

uniformément couverte de micro-treillis n'est pas compatible avec la rigidification de l'enveloppe soumise à la pression du gaz porteur. Pour cela, une approche hybride consiste à conserver certaines portions plus lourdes pour la résistance aux impacts avec à l'utilisation de micro-treillis et à alléger le reste de l'enveloppe au strict minimum pour assurer de respecter les requis de géométrie, flottabilité et protection. Les micro-treillis sont exploités tout particulièrement pour absorber les collisions entre le dirigeable et les parois de l'espace de vol.

5.2 Résumé

L'industrie des systèmes aériens sans équipage (Uncrewed Aerial Systems - UAS) se développe rapidement grâce aux avancées dans les petits composants électroniques, les capteurs intelligents,

les contrôleurs de vol avancés et les modules de perception embarqués utilisant l'intelligence artificielle. Ces progrès technologiques ont ouvert de nouvelles applications en intérieur pour les UAS, y compris la gestion des stocks d'entrepôt, les inspections de sécurité des espaces publics et des installations, et l'exploration souterraine. Malgré les conceptions innovantes des fabricants d'UAS, il n'existe pas de normes pour garantir la sécurité des UAS et des humains dans ces environnements. Cette étude explore le développement et l'évaluation de structures micro-treillis pour la résistance aux impacts dans les UAS légers. Nous examinons des conceptions de patch utilisant les motifs Cubique à Faces Centrées (FCC), Diamant (D), Kelvin (K) et Gyroïde (GY) et détaillons les processus de création d'échantillons pour les tests d'impact et de compression, y compris les protocoles de fabrication et de test.

Notre évaluation comprend des tests de compression et d'impact pour évaluer le comportement structurel, révélant l'influence de la géométrie, de la compacité et des propriétés des matériaux. Les motifs Diamant et Kelvin se sont avérés particulièrement efficaces dans la distribution de la charge et l'absorption d'énergie lors des tests de compression. Les tests d'impact ont montré des différences significatives de réponse entre les matériaux flexibles et rigides, les patchs flexibles présentant une dissipation d'énergie et une intégrité structurelle supérieures sous des charges dynamiques.

L'étude fournit une analyse détaillée de l'absorption spécifique d'énergie (SEA) et de l'efficacité, offrant des perspectives sur les conceptions optimales de structures micro-treillis pour la résistance aux impacts d'UAS ultralégers.

5.3 Abstract

The uncrewed aerial systems industry is rapidly expanding due to advancements in smaller electronics, smarter sensors, advanced flight controllers, and embedded perception modules leveraging artificial intelligence. These technological progress have opened new indoor applications for UAS, including warehouse inventory management, security inspections of public spaces and facilities, and underground exploration. Despite the innovative designs from

UAS manufacturers, there are no existing standards to ensure UAS and human safety in these environments. This study explores developing and evaluating micro-lattice structures for impact resistance in lightweight UAS. We examine patch designs using Face-Centered Cubic (FCC), Diamond (D), Kelvin (K), and Gyroid (GY) patterns and detail the processes for creating samples for impact and compression tests, including manufacturing and testing protocols. Micro-lattices have a relative density of 65 kg/m^3.

Our evaluation includes compression and impact tests to assess structural behavior, revealing the influence of geometry, compactness, and material properties. Diamond and Kelvin patterns were particularly effective in load distribution and energy absorption over the compression tests (> 1000 J/kg). Impact tests demonstrated significant differences in response between flexible and rigid materials, with flexible patches exhibiting superior energy dissipation and structural integrity under dynamic loading.

The study provides a detailed analysis of specific energy absorption (SEA) and efficiency, offering insights into optimal micro-lattice structure designs for impact resistance in lightweight UAS applications.

5.4 Introduction

The uncrewed aerial systems (UAS) industry is rapidly expanding due to advancements in smaller electronics, smarter sensors, advanced flight controllers, and embedded perception modules leveraging artificial intelligence. These technological progresses have opened new indoor applications for UAS, including warehouse inventory management, security inspections of public spaces and facilities, and underground exploration. Despite the innovative designs from UAS manufacturers, there are no existing standards specific to these systems to ensure human and UAS safety in shared environments. As these aerial vehicles are integrated into more tasks, they operate closer to operators and users, calling for new safety measures for safe human-UAS

interaction. Additionally, several recent applications target indoor cluttered spaces, requiring protection of their valuable payloads from impacts [1].

Polymer materials are widely used across various industrial sectors due to their diverse manufacturing processes and the extensive range of properties they can achieve. However, their low mechanical strength often limits their use in aerospace applications. Polymer micro-lattice structures can address this issue by providing enhanced specific mechanical properties through their intricate cell patterns. Micro-lattices are structures composed of periodic cells, granting variable mechanical properties compared to bulk material (Zheng *et al.*, 2014). The mechanical properties of a micro-lattice depend on the interplay between the material properties, the geometry of the unit cell, the macroscopic structure of the part, the density of the structure (cells per volume), and the manufacturing technique (Evans, Hutchinson & Ashby, 1998). These different levels of complexity make each use case unique.

Micro-lattice structures have a wide range of potential applications in various fields such as aerospace, biomedical engineering, and energy storage (Yeo, Oh & Yoo, 2019). In aerospace, micro-lattice structures can be used to develop lightweight structures with high specific strength and stiffness, which can improve the efficiency and performance of aircraft and spacecraft. In biomedical engineering, these structures can be used to create scaffolds for tissue engineering or drug delivery systems because their high surface area and porosity enable efficient transport of nutrients and drugs (Fina, Goyanes, Madla, Awad, Trenfield, Kuek, Patel, Gaisford & Basit, 2018). In energy storage, micro-lattice structures can be used as electrodes in batteries and supercapacitors, as their high surface area and porosity enable rapid charge and discharge rates (Xiong *et al.*, 2015). Despite their potential, experimental studies are still necessary to better understand the failure mechanisms of micro-lattices (Wu, Fang, Wu, Li, Sun & Li, 2023). While our study focuses on small aerial vehicle impact protection, the findings can be extended to these other domains.

[1] https://www.flyability.com/elios-3

Despite their potential, micro-lattices are not yet common in commercial products due to the complexity of their manufacturing. The advent of polymer additive manufacturing (AM) offers the opportunity to build complex geometric structures at low costs. However, not all AM techniques meet the high-resolution and support-free requirements essential for micro-lattice production (Nazir, Abate, Kumar & Jeng, 2019). One viable option is Masked Stereolithography Apparatus (MSLA) technology, which solidifies photosensitive resin with a high level of detail on affordable machines with a printing resolution of around 20 to 50 µm.

A wide variety of polymer materials have been proposed for impact protection. In the aerospace sector, micro-lattice sandwich panels are considered an alternative to 2D-honeycomb structures for shielding sensitive equipment (Mines *et al.*, 2013). For single-impact applications, expanded polystyrene foam (EPS), and rigid polyurethane foam (PU) are commonly used in the transportation and aerospace industries for their potential to reduce weight while enhancing safety (Blazy, 2003). For example, EPS is often used in motorcycle and bicycle helmets, but these helmets must be discarded after a single impact. For multiple-impact applications, expanded polypropylene foam (EPP), PU foam, and vinyl-nitrile foam (VN) are recommended. In combat helmets and American football helmets, shock attenuation micro-lattice structures with multi-impact capability are employed to maximize protection against repeated impacts (Clough, Plaisted, Eckel, Cante, Hundley & Schaedler, 2019). Various other industries are investigating polymer structures capable of withstanding significant impacts while maintaining their functional integrity in applications such as shoe soles, airless tires, and biomorphic prostheses (Nazir *et al.*, 2019). The application's requirements also shape the way these structures are tested : impact tests are categorized into four families based on the speed of the impact, or application : low-velocity test (below 10 m/s), intermediate velocity test (10 m/s to 50 m/s), ballistic velocity (50 m/s to 1000 m/s) and high-velocity impact (1000 m/s to 5000 m/s) (Ismail, Sultan, Hamdan, Shah & Jawaid, 2019). Despite the growing interest across these domains, there remains a limited understanding of the mechanical characteristics and variability among different micro-lattice patterns.

As for the cell geometry, they can be grouped into three families : micro-lattices composed of struts, triply periodic surfaces (TPMS), and shell micro-lattices. Up to 2016 (SakshiKokil-Shah *et al.*, 2021), BCC patterns were the most studied because they are easy to manufacture using a wide range of processes. AlMahri, Santiago, Lee, Ramos, Alabdouli, Alteneiji, Guan, Cantwell & Alves (2021) compared five patterns of TPMS metallic surface micro-lattices. TPMS limits macro defects thanks to the continuity of the structure, which limits deformations during fabrication.

Xiao & Song (2018) studied the influence of step-wise density gradient versus a uniform structure in TPMS manufactured in Titanium and Aluminum alloys via SLM. Samples were subjected to high-velocity impacts using a Split Hopkinson bar device. The results showed a superior SEA by 28% for gradient micro-lattices. Evans, He, Deshpande, Hutchinson, Jacobsen & Carter (2010) worked on micro-lattices with hollow nickel tubes to provide higher energy absorption per unit mass (Xiong *et al.*, 2015). With blast tests, they compared them to stochastic foams and honeycomb structures. They observed four to five times the SEA of foams and honeycomb in experimentation, which they explained with the variety of deformation modes, such as cell buckling and accordion folding. Cui, Zhao, Wang, Zhao & Fang (2012) confirms this finding on their tetrahedral micro-lattice panels compared to honeycomb structures. They also highlighted densification regions under the impacter, followed by a transition zone.

With the availability of consumer-grade AM machines that cost a few hundred dollars, research institutions have started to push their limits (Catar *et al.*, 2022; Hassan, Enab, Fouda & Eldesouky, 2023). These new additive manufacturing processes have unlocked a wide range of possibilities for process technique variations and the versatility of micro-lattice geometries. This finding makes the characterization of mechanical performance and the use of micro-lattices increasingly relevant.

The contributions of this paper are *(1)* the study of micro-lattices for low-speed impact attenuation in realistic experimental conditions ; *(2)* a classification of loading cases relative to the flexibility of the material ; *(3)* to the best of our knowledge, the first studies on micro-lattices made by

MSLA machine and at a low density (under 100 g/m^3) and *(4)* our micro-lattices patches emphasizes a significant reduction in the relative density of micro-lattices while maintaining comparable effectiveness in absorbing impact energy.

5.5 Micro-lattices energy absorption behavior

Before analyzing impact mechanics and the performance of micro-lattice patches, it is essential to outline the energy absorption mechanisms specific to micro-lattices. Guillon's work Guillon (2008) provides a thorough examination of energy absorption phenomena, noting that polymers exhibit viscoelastic behavior and respond differently based on loading speed. During impacts, when polymer chains lack the time to realign, the material's stiffness and strength increase (Menard & Menard, 2020). Barring special cases like friction or multistability, energy absorption arises from the plastic deformation of the structure, occurring over two distinct phases. The initial damage phase forms a stabilized crushing front, typically marked by a peak in load curves. This may be followed by a stall in load as deformation modes contribute differently. For low-stiffness polymers, the prevalent "folding" or "local buckling mode" dissipates energy through localized buckling, shown by oscillations in the force/displacement curve as folds form. Rupture modes and propagation front evolution can be manipulated by triggers, such as notches (Guillon, 2008). Depending on material rigidity, micro-lattices may undergo destruction or enter a consolidation phase with folding. This phenomenon is observable as it generates peaks in the force distribution (Clough *et al.*, 2019). To quantify performance, Ramakrishna, Hamada, Maekawa & Sato (1995) introduced the Specific Energy Absorption (SEA), defined as the energy absorption per unit mass, and derived as follows :

$$SEA = \frac{E}{m} = \frac{F_{avg}}{A\rho} \tag{5.1}$$

With E as the absorption energy, m as the mass, F_{avg} as the average load, A as the cross-section, and ρ as the density.

Several studies have explored SEA characterization through simulation, although finite element models often diverge in representing the loading history of structures despite accurately capturing experimental stiffness values (Gümrük & Mines, 2013). This gap may result from structural instabilities (Xiong *et al.*, 2015) or manufacturing imperfections (Wu *et al.*, 2023), impacting the simulation's realism. Rathbun et al. Rathbun, Radford, Xue, He, Yang, Deshpande, Fleck, Hutchinson, Zok & Evans (2006) found that dynamic SEA values are higher than those in quasi-static conditions, complicating the simulation of real load cases. Zhang, Zhou, Zhou, Huizhong, Zhang Xiaoyu, Zhang, Yang, Lei Hongshuai, Lei & Han (2021a) achieved experimental results aligning closely with theoretical models and finite element analysis, with errors under 22%. Their study on BCC/FCC-type structures revealed that adding vertical struts greatly enhances specific strength and SEA, whereas diagonal struts offer a lesser effect. Realistic finite element modeling of micro-lattice structures becomes exceedingly complex as larger structures demand more mesh elements (Smith, Guan & Cantwell, 2013). Nonetheless, fundamental properties can be estimated by examining a single micro-lattice cell. While finite element models approximate maximum stress values under compression or impact effectively, they often fall short in accurately representing local deformations or damage within the micro-lattice (Feng, Wang, Li, Xiao & Song, 2022).

Schaedler, Ro, Sorensen, Eckel, Yang, Carter & Jacobsen (2014) introduced the energy efficiency metric η to quantify energy absorption efficiency in cellular architectures, foams, or micro-lattices, providing a comparative perspective on SEA relative to the theoretical maximum absorption potential of a structure.

It is defined as :

$$\eta = \frac{1}{\sigma_p} \int_0^{\epsilon_d} \sigma(\varepsilon)\, d\varepsilon \tag{5.2}$$

σ_p is the maximum stress before densification. In this equation, the ratio η is calculated between the area under the stress-strain curve of the structure and that of an ideal material, keeping a maximum stress σ_p and a maximum strain of 1. Based on the data from the literature, the information from Schaedler *et al.* (2014) is particularly interesting because they also conducted

quasi-static compression tests (1 mm/min) and impact tests (5 m/s). We are leveraging these results to compare with our values in Section 5.7.3.

5.6 Methods and materials

To contextualize the results of our extensive test campaign, we provide a detailed account of the design of the test patches (specimens), their manufacturing processes, and the protocols used for compression and impact testing.

5.6.1 Patch design

The patch specimen was designed as a square with 45 mm sides and a thickness of 15 mm, which limits each patch's weight to 10 g, including 2 g of micro-lattice. The 15 mm thickness can consist of a single layer of lattice cells, 2 layers or at most 3 layers (5mm each).

We selected four micro-lattice patterns : Face Centered Cubic, Diamond, Kelvin, and Gyroid. We focused on those providing mechanical properties relevant to ultra-light aerospace structures plus three criteria : *(1)* providing a reference base comparable with previous studies, *(2)* aiming for a wide diversity in typologies, and *(3)* ensuring a self-supporting cell geometry for all manufacturing processes (Catar, Tabiai & St-Onge, 2024b). The FCC pattern (Fig. 5.2-A) ensures stability during the manufacturing process and has been extensively studied. Secondly, the diamond pattern (Fig. 5.2-B) offers geometric homogeneity and lightweightness. Its geometry is similar to that of a honeycomb strut-based 3D structure. Then, we add the Kelvin pattern (Fig. 5.2-C), which has large internal cavities. The planar and inclined strut orientations of the Kelvin pattern provide interesting structural rigidity for dissipating energy during an impact (Saremian *et al.*, 2021). This lattice features longitudinal struts in the loading direction, potentially leading to behavioral differences and visible instabilities during testing, as shown by Xiong *et al.* (2015). The gyroid pattern (Fig. 5.2-D), known for its high-energy absorption under compression (Abueidda, Elhebeary, Shiang, Pang, Abu Al-Rub & Jasiuk, 2019), represents the family of triply periodic surfaces (TPMS). Fig. 5.2 shows the geometry and related information.

In addition to comparing different micro-lattice patterns, we look into the influence of micro-lattice compactness, or density. We defined three levels of compactness : cells of 15 mm, 7.5 mm, and 5 mm, allowing for 1 to 3 layers of micro-lattice in the 15 mm patch as shown in Fig. 5.2. We designed the volumes and mounting plates for all patches using Autodesk Fusion 360 software. The space allocated for micro-lattices was filled using nTopology software, which provides extensive options for creating micro-lattices with its implicit design engine. Among the different variants, the thickness of the struts or walls was adjusted to ensure that all samples had the same mass. Table 5.1 presents the diameters or wall thickness values for each of the patterns and their respective compactness levels.

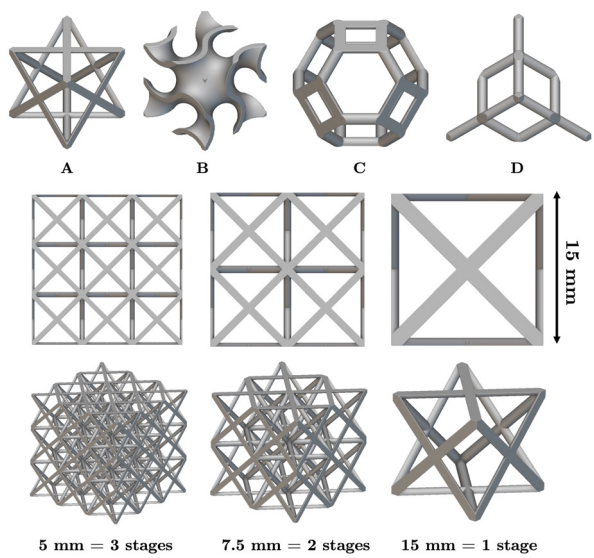

Figure 5.2 Micro-lattices pattern selection : Face Centered Cubic—FCC (**A**), Gyroid—GY (**B**), Kelvin—K (**C**), and Diamond—D (**D**) and example of the three levels of compactness to fill the 15 × 15 × 15 mm^3 volume with the FCC pattern. The number of micro-lattice stages changes, but the diameters of the struts are adapted to have the same relative mass. The patch samples have a total volume of 45 × 45 × 15 mm^3.

We also studied two different materials : a flexible resin (Tenacious [2]) and a rigid resin (Build [3]). Both materials are chemically similar, derived from the same urethane acrylate base, and

[2] Datasheet Tenacious (Soft)

[3] Datasheet Build (Rigid)

Tableau 5.1 Diameter of the struts or thickness of the shell of micro-lattices in millimeters to keep all patches at 2 g weight

	Compacity		
Pattern	**50**	**75**	**150**
■ **FCC**	0.48	0.73	1.5
♦ **D**	0.52	0.78	1.56
★ **K**	0.48	0.72	1.46
• **GY**	0.275	0.57	0.82

manufactured by the same company, SirayaTech®. It is even possible to mix them to create new material variations. The densities of the materials were measured using a hydrostatic balance with a cubic specimen at 100% infill. The rigid material showed a density of 1.237 ± 0.001 g/cm^3 while the flexible one had a density of 1.214 ± 0.08 g/cm^3. The manufacturer provides values of 33 MPa for ultimate tensile stress with 8% elongation at break for the rigid resin using ASTM D638. For the flexible resin, the values are 5 MPa for tensile stress at break and 70% elongation at break. We conducted mechanical tensile tests following the ASTM D638 standard to validate these values. For the rigid resin, we obtained 22.7 MPa with 3% elongation (underperformance), and for the flexible resin, we obtained 7.9 MPa with 78% elongation (overperformance). These discrepancies from the manufacturer's data are likely due to the duration of UV exposure during printing and curing. Results can also vary depending on room humidity and the duration of alcohol exposure when cleaning the parts.

Throughout the paper, we will use the following abbreviations : FCC, GY, K, and D, for the micro-lattices patterns, with the compacity 150, 75, and 50 and the resins will be abbreviated as R and S. Three samples are evaluated for each combination to assess repeatability. This brings the total number of samples to be manufactured to 144. Figure 5.3 shows the nomenclature standard to represent the selection of patches for all graphs in this paper.

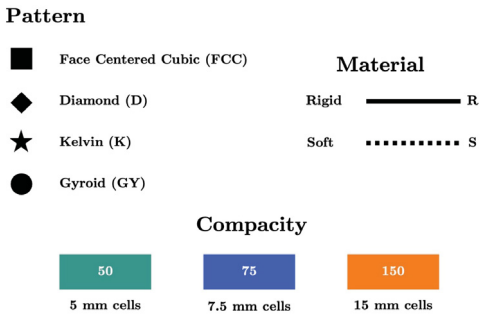

Figure 5.3 Figure nomenclature : There are so many possible combinations that we've created this nomenclature, which serves as a standard for all the figures in this paper.

5.6.2 Patch manufacturing

To manufacture the micro-lattice patches, we used the MSLA AM technique. It is the best resolution-to-price ratio 3D printer technology. The MSLA process uses an LCD screen to create a mask between the UV light and the resin tank. When cured, the polymerized resin forms small parallelepipeds (voxels) whose dimensions correspond to the pixel size in the XY plane and the layer height in the Z direction. Thus, the machine's resolution in the XY fabrication plane is directly correlated to the screen's resolution. Thanks to this voxel manufacturing, MSLA provides isotropy-like mechanical properties in the resulting parts. This isotropy is beneficial for manufacturing various micro-lattice patterns that are inherently multidirectional. The use of this technology is advantageous because MSLA machines support a wide variety of materials from different manufacturers (not a proprietary technology) and are generally composed of simple, inexpensive components. For this study, we used an © *Elegoo Saturn S*, equipped with a 4K 9.1-inch LCD screen. The size of a pixel and the resolution in the XY-plane is 48 µm. The minimum layer height is 10 µm. For slicing the parts, we used the open-source Chitubox software.

Given the selected manufacturing technology, the parts must be designed to meet specific requirements. For instance, samples must be designed to avoid the need for printing supports, minimizing the risk of pattern alteration during post-processing. This approach reduces printing

failures, manufacturing time, material consumption, and costs while ensuring a high printing success rate.

The patch geometry is 45 mm x 45 mm x 15 mm and must be mechanically attached to the impact bench (see Sec. 5.6.4). Therefore, the samples require mounting holes and a structure to protect them. With a substantial contact surface with the printing bed, adhesion can be too strong for the small struts of the micro-lattices. This could result in the piece being destroyed or damaged when manually removed with a spatula at the end of the print. Conversely, if the contact surface is too small, for instance, if supported by narrow pillars, the piece may deform during polymerization. This can lead to detachment from the printing bed, halting production to remove the part, or, worse, damaging the machine if the piece becomes stuck at the bottom of the resin tank.

To address these challenges, we propose an optimized sole plate for MSLA printing that provides several benefits. Firstly, it serves as a mounting interface between the micro-lattice area and various testing platforms, such as the compression bench and impact bench. Secondly, it ensures that the micro-lattices are not affected by sample manufacturing, acting as a support while allowing easy manual detachment. The optimized sole plate, shown in Fig. 5.4, is composed of several layers, all made from the same material, each with distinct roles.

The underneath furrows reduce the contact surface with the printer's bed, with each furrow having only a 1 mm thick plateau in contact with the printing bed. The lines then taper to create a self-supporting surface at a 45° angle to the printing direction. This area serves as a transition between the furrow zone and the platform that hosts the micro-lattice. It also provides space to manipulate the piece more easily when detaching it from the bed. Finally, the platform on which the micro-lattice is built is thick enough to be rigid, preventing any risk of flatness deformation.

The complete step-by-step manufacturing protocol can be found here [4].

[4] https://git.initrobots.ca/lcatar/micro-lattices-patches-manufacturing

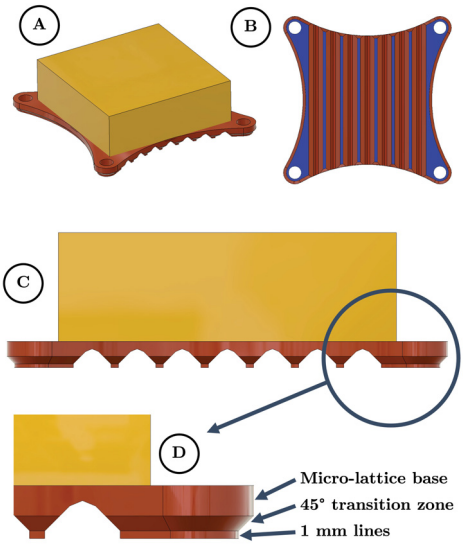

Figure 5.4 Patch design : (**A**) Optimized sole plate design, (**B**) Furrows section with minimized surface in contact with the print bed, (**C**) a cross-section of the furrows grooves, and (**D**) the detail of the successive part layers.

5.6.3 Patch compression tests

Compression tests are useful in the preamble of impact tests because they provide detailed information on how the cells of the micro-lattice deform under a constant load.

Compression tests were conducted on an Alliance RF/200 machine from the MTS System. It is equipped with a load cell with a rated load of 1000 N and a sensitivity of 2.51 mV/V. The displacement speed was set at 5 mm/min for rigid samples and 10 mm/min for flexible samples that correspond relatively at 5.60 $10^{-3}s^{-1}$ and 11.1 $10^{-3}s^{-1}$ strain rates. Each sample was placed on a support adapted to the sole size to center the compression (Fig. 5.5).

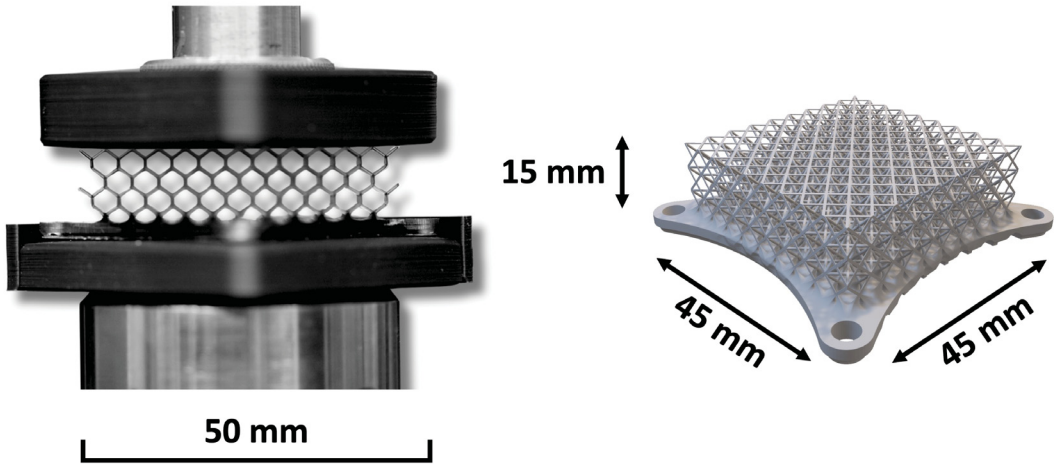

Figure 5.5 Compression test device with diamond (D) sample and view of a patch (FCC_50 sample)

5.6.4 Custom impact bench

For low-velocity impacts, the recommended impact standards from the literature are Charpy or Izod tests for material (da S. Vieira, Lopes, de Moraes, Monteiro, M. Margem, Margem & Souza, 2018; Patterson, Pereira, Allison & Messimer, 2021) and drop-weight tower for structures (Mines *et al.*, 2013; Abrate, Epasto, Kara, Crupi, Guglielmino & Aykul, 2018). However, these tests do not accurately reflect the reality of UAS impacts, as they do not account for the possibility of the structure rebounding upon impact.

We designed a custom impact test bench for this study, shown in Fig. 5.6. It consists of a linear catapult driven by an electric motor, allowing for the testing of aerial vehicle structures or complete micro-UAS under conditions close to their real-world use. The bench enables controlled-speed impacts. At launch, a propulsion trolley is accelerated on the main rail. Just before impact, a sample-holding trolley, initially fixed to the propulsion trolley, is released on its secondary rail (atop the propulsion trolley). This design allows the sample to freely rebound upon impact. In this study, all impacts are performed at 2 m/s. This is representative of an

inspection aerial system, where the goal is to control the position rather than the velocity, as one would do with movement phases. The trolley holding the samples is loaded with calibrated weights to simulate the inertia of the final flying device. For this work, the UAV's inertia is set to 1 kg.

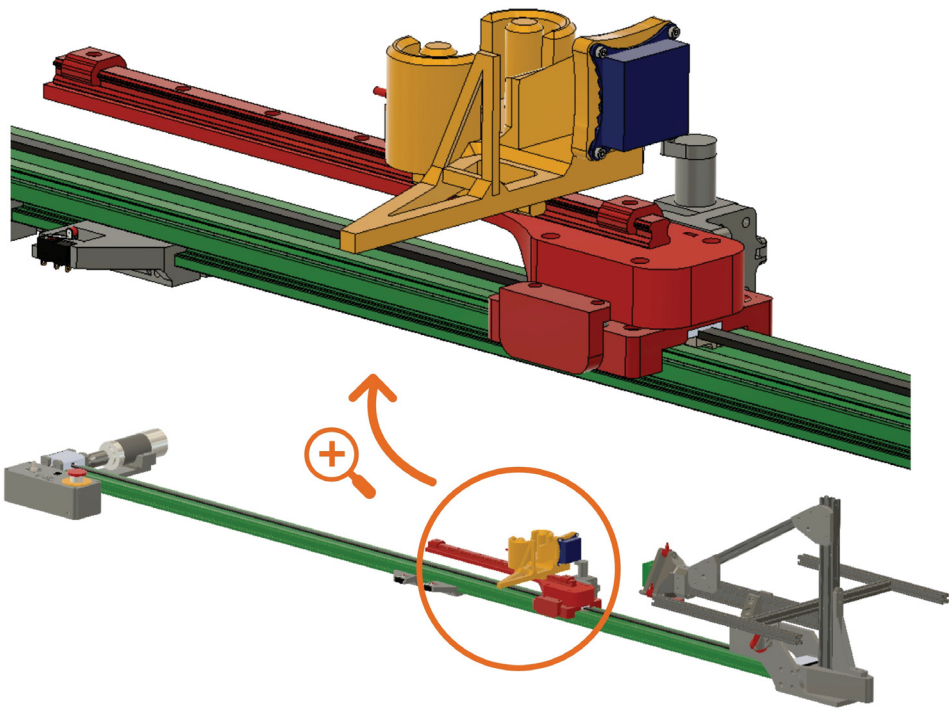

Figure 5.6 Overview of the custom impact test bench. The first main rail (green) is used to propel the second rail (red). The sample trolley (yellow) holds the sample (blue). Just before impact, it is released to translate freely along the red rail.

The bench is equipped with a set of sensors to capture the critical and fleeting moments of the crash. Specifically, we have a PCB Piezotronics© single-axis accelerometer (352C34) to measure deceleration, three PCB Piezotronics© load cells (208C03) positioned at the vertices of an equilateral triangle to measure force during impact, a LeddarOne distance sensor from which we calculate speed before impact, and a P3 America© potentiometer (LMCR13) for high-precision distance measurement during impact. Additionally, we use a high-speed Chronos 2.0 camera to better interpret and discuss the impact behavior.

The PCB Piezotronics© sensors (accelerometer and load cells) and the potentiometer were connected to a Siemens© SCADAS acquisition system, capturing data at 6250 Hz. The Leddar sensor's data were acquired at a rate of 100 Hz using a Python script on a Linux laptop. To synchronize the acquisition systems before launch, a 5V 'trigger' signal is sent from the laptop to the SCADAS system.

5.7 Results and discussion

Based on the raw data from the compression and impact test campaign, we calculated and represented various metrics that provide a more in-depth understanding of the micro-lattices' behavior.

5.7.1 Compression tests

The time-lapse of the compression tests of the samples is available here.

Several factors influence the behavior of micro-lattices under compression, which can be regrouped into geometry, compactness, and materials, as illustrated in Fig. 5.7. Some effects can be combined. For example, the buckling of the struts in each micro-lattice depends on both the geometry and the level of compactness. This is particularly evident in the FCC micro-lattice, where the force curve shows sequential yielding stages. The number of rows per sample is directly correlated to the number of peaks in the force curve, as highlighted in (A) Fig. 5.7 with FCC_75).

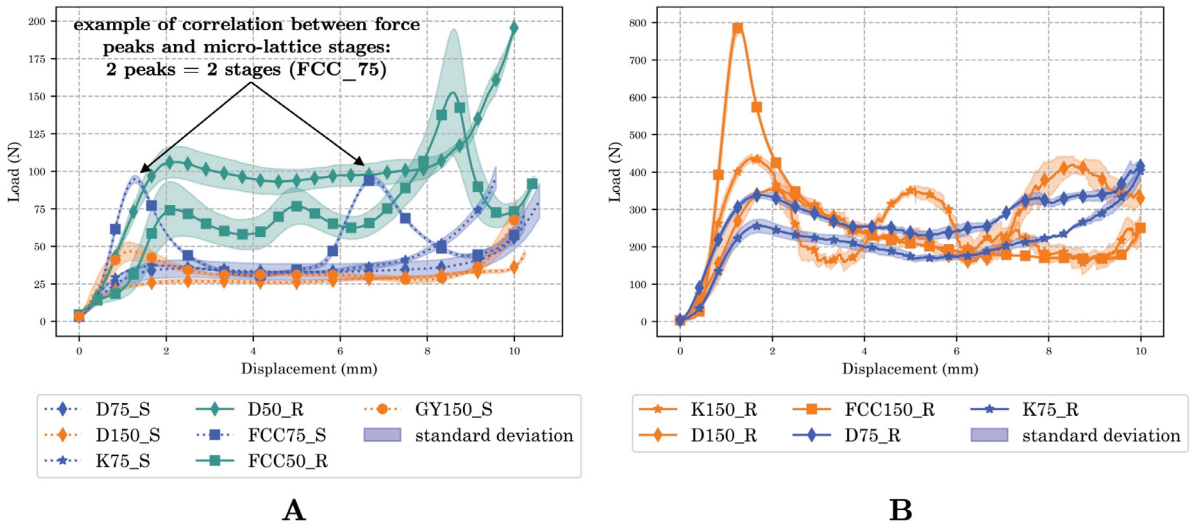

Figure 5.7 Load-Displacement of softer (**A**) and most rigid (**B**) configurations (not same scale for readability). Both sides present similar behaviors : peaks of strength associated with loading plateaus. These peaks are particularly noticeable with the FCC pattern, directly correlated to the number of layers. Measurements' uncertainties of the three samples' repetition are represented by the colored shaded area around each curve. We deliberately did not represent the final consolidation part of the compression test to better highlight the initial variations. Therefore, the deformation stops at 10 mm and load above 100 N.

With smaller cells, we observe a longer stress plateau during loading. The same effect is seen when increasing the number of struts along the loading axis. For example, the Diamond or Kelvin patterns have more struts than the FCC pattern. The gyroid pattern, with its continuous surfaces, has a very limited contact area compared to other patterns, making the loading more variable.

In terms of material, differences in viscoelastic properties and rigidity lead to a significant decrease in maximum force, with flexible resin showing five to ten times less force than rigid resin. Larger cells (compactness 150) provide greater rigidity, even though they are fewer in number.

As previously described, each combination impacts load distribution. To emphasize this and compare all patterns, we calculated the stiffness of each micro-lattice structure. We employed an analogy with springs, defining stiffness S_t as :

$$S_t = \frac{dF}{dx} \; [N/m] \tag{5.3}$$

where F is the force and x is the displacement during the compression for each time increment. The plateau phases then strike out as their derivative is close to zero. We defined a threshold of ± 10 N/mm and each increment is labeled as a plateau or not and then reduced to a percentage of the test duration to determine a "stiffness score". The higher the score, the more effectively the micro-lattice smooths the stress into a plateau form. Fig. 5.8 shows the stiffness score for all samples, with clear differences observed, ranging from 3.6% to 87.7%.

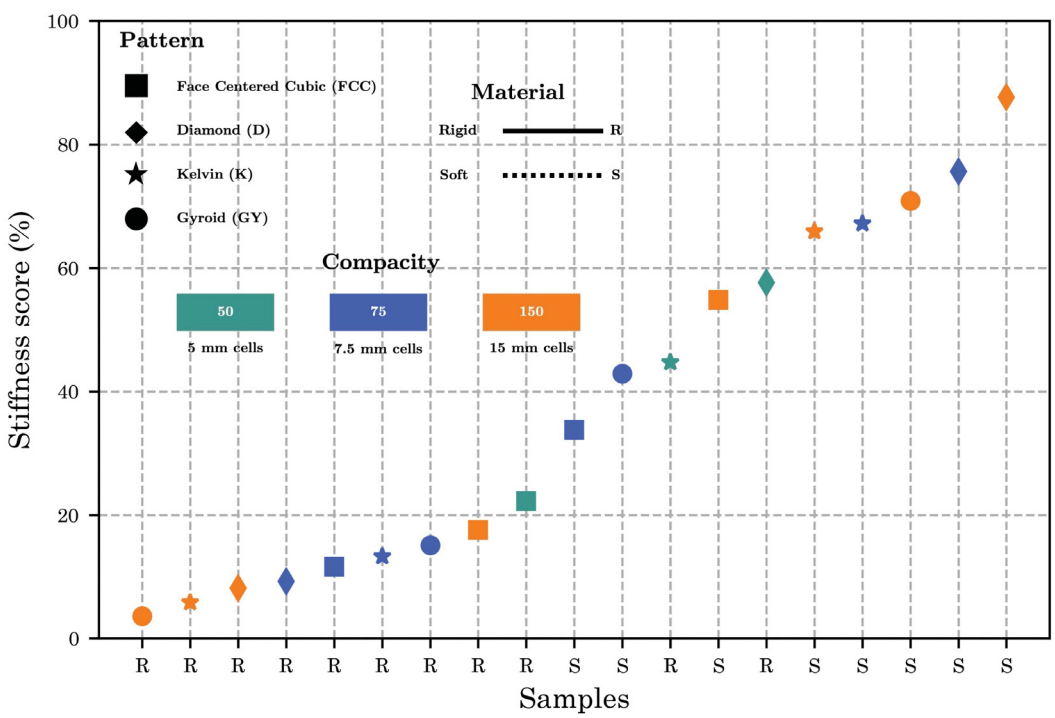

Figure 5.8 Stiffness score for all tested combinations, showing a wide range of performances. On the right side of the graph : micro-lattices made of flexible materials obtain the highest score.

This metric provides insight into how well each combination can adapt to constraints without creating hysteresis reactions under load. Flexible materials and diamond micro-lattices are the most effective. The order from highest to lowest stiffness score is diamond, Kelvin, and gyroid, consistently across different levels of compactness and material types. The FCC pattern shows more variability due to a regular plateau between two peaks, resulting in an excellent stiffness score between buckling stages, which nuances its overall performance. Conversely, the gyroid pattern is the least effective, likely due to the very limited contact surface between the compression surface and the micro-lattice.

5.7.2 Impact tests

A video of all impact tests is available here [5]. Fig. 5.9 shows the typical behavior of a flexible (A) and rigid (C) micro-lattice subjected to impact. Several key observations can be made from these comparative representative results.

First, the reaction under load is unique for each test and material. The only similarity is between the behavior of the soft and rigid micro-lattices under quasi-static compression tests (B and D). The force peaks are identical but have smaller amplitudes for the soft material. Those peaks correspond to the two layers of cells in the 75 configuration. In the soft micro-lattice under impact, these two peaks are also present, but a rebound occurs before the consolidation phase. The maximum displacement is just over 7 mm, indicating complete buckling of the first layer. However, the rebound happens before the second layer is folded.

[5] https://git.initrobots.ca/lcatar/micro-lattices-patches-manufacturing

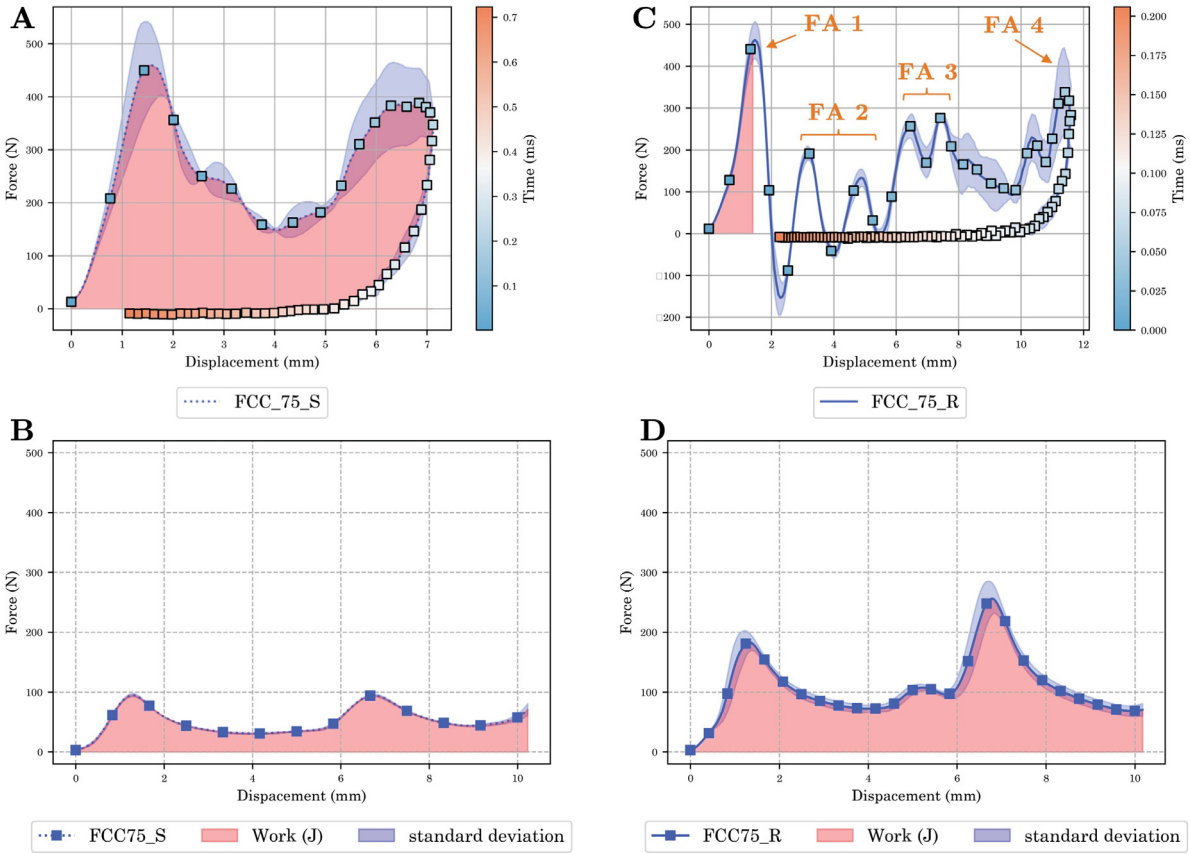

Figure 5.9 Force with respect to displacement for the FCC micro-lattice with a compactness of 75. The curves show results for the soft material (left : A & B) and the rigid material (right : C & D) both for the impacts (top : A & C) and the compression (bottom : B & D). Under the curve, in red, the absorbed energy before the rupture of the micro-lattice is represented. Measurements' uncertainties of the three samples' repetition are represented by the colored shaded area around each curve. Different Focus Areas (FA) are highlighted in orange to support the analysis of (C).

In contrast, the rigid micro-lattice shatters under impact (C), a behavior observed in all rigid samples subjected to impact. The deformation modes described by Guillon (2008) and discussed in Section 5.5 are found and verified with the high-speed camera images, of which an overview is given in Fig. 5.10. The first peak of force corresponds to the buckling of the first stage of cells (Focus Area — FA n°1 of (C) in Fig. 5.9). Following the explosion of this stage, the cells were cut in two. We then observe peaks of lower amplitudes : a first series under 200 N with the bending of the struts that remained attached to the sample (FA n°2), then a second series

where we go back up to nearly 300 N with the rupture of the second stage of cells located at about 7 mm of deformation (FA n°3). This distance is also similar to compression tests (rigid and flexible). The very last peak shows the shock with the sample holder trolley (FA n°4). At this stage, the micro-lattice is destroyed.

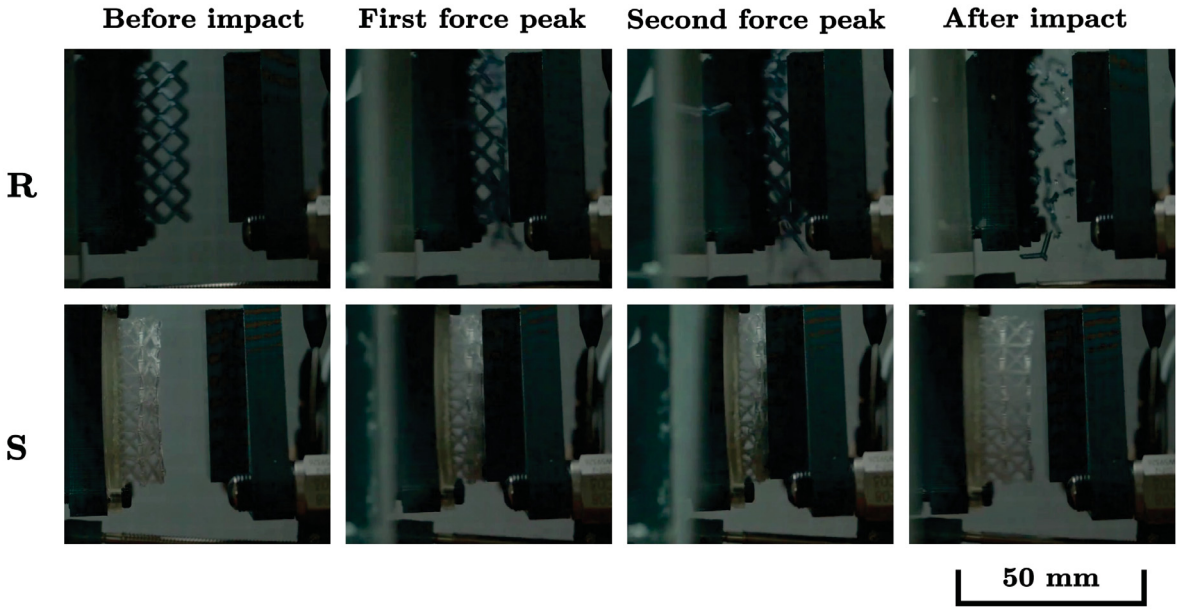

Figure 5.10 Time-lapse of the impact of a rigid (R) and flexible (S) sample. The outcome of the impact is significantly different, with the rigid micro-lattice exploding and the flexible micro-lattice deforming without breaking. The first force peak corresponds to FA n°1 and the second force peak to FA n°3 in Fig. 5.9.

Another interesting element is that the maximum force amplitude is higher in the results of impact tests than in quasi-static compression tests. This phenomenon has been observed in the literature on numerous occasions and reported in the literature review we conducted earlier. Inertia is reported to be the main cause of this difference in absorption quality Ramakrishna *et al.* (1995); Rathbun *et al.* (2006); Vaughn, Canning & Hutchinson (2005).

Finally, the elapsed time during the impact is represented by the color bar on the right side of the graph. The impact duration is longer for the flexible material, exceeding 0.7 s, while the rigid

material reaches the same state in 0.2 s. The explosion of the micro-lattice in the rigid material involves a much more abrupt deceleration.

5.7.3 Specific energy absorption and efficiency

Using Equation 5.1, we calculated the Specific Energy Absorption (SEA) of each micro-lattice combination. As noted by Ramakrishna *et al.* (1995), significant variation occurs depending on the loading rate. Across all tested patterns and materials, a complete inversion between the results of quasi-static tests and impact tests is observed. Fig. 5.11 shows a crossover between flexible and rigid micro-lattices : those with the highest SEA in compression exhibit the lowest SEA in impact, and vice versa.

At low loading rates, flexible micro-lattices flow due to the viscoelastic properties of the polymer, resulting in a low force below 100 N before consolidation, as seen in Fig. 5.7 A. Rigid micro-lattices, however, undergo buckling, with the cells closing on themselves and bending while maintaining a very high reaction force throughout low-speed loading. The force experienced by the rigid micro-lattices is more than twice that of flexible ones, around 200 to 300 N, with some peaks exceeding 500 N.

In contrast, during an impact, the rigid material shatters under shock, preventing the energy from dissipating within the structure. Flexible materials, on the other hand, can withstand bending without breaking, leading to excellent performance for certain patterns at the left end of the graph.

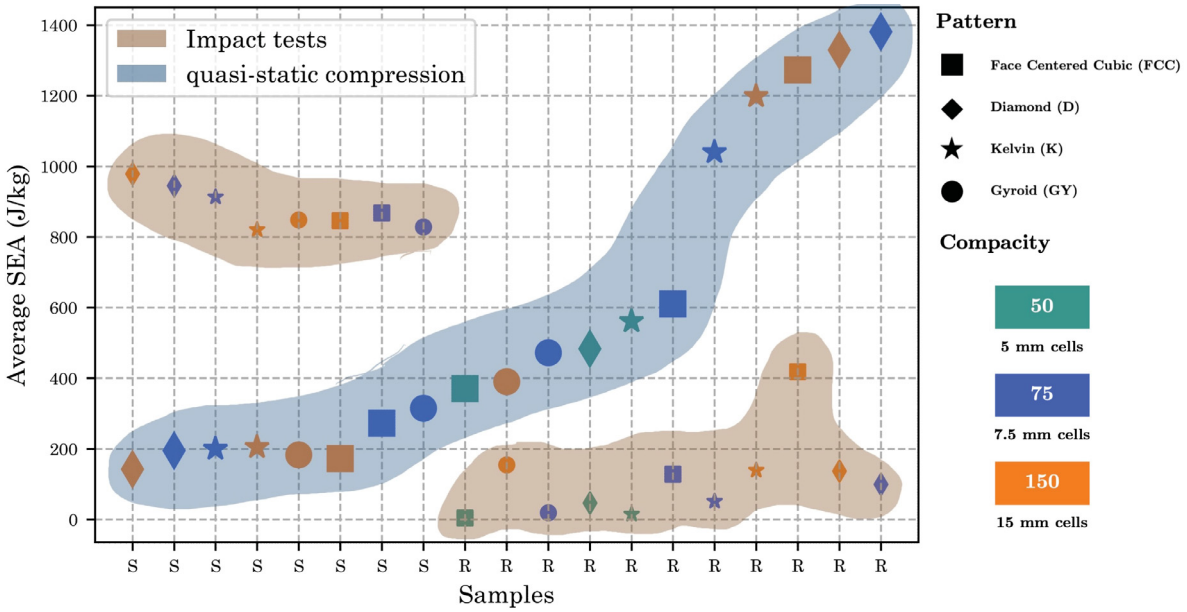

Figure 5.11 SEA of micro-lattices specimens in quasi-static (blue shaded area) and impact (brown shaded area) tests. Rigid and soft material show an inverted tendency between the two test protocols due to the change in loading speed.

To compare our work with others, we plot η with respect to the density of the micro-lattice using Equation 5.2. All our samples were created with an equal mass of 2 g, resulting in a density of 65 kg/m^3 for all specimens. In Fig. 5.12 shows the micro-lattice patches with the highest and lowest η performance from the compression and traction tests of our study. We have also included references from the literature, consisting of polymer micro-lattices made with photosensitive resins, thermoplastics manufactured using Selective Laser Sintering, and hollow metal micro-lattices.

Our work explores the limits of ultralightness, with densities set below the 100 kg/m^3 threshold. This ensures increased lightness with absorption-efficiency performances compared to the state-of-the-art (10%-70%). The micro-lattices with the closest performance in comparison are plated with nickel, which complicates implementation, especially for large-scale production. On the contrary, the use of LCD technology in additive manufacturing ensures increased ease of production and reduced production costs.

Previous work (Schaedler *et al.*, 2014), observed less than 10% variation in performance regardless of the configuration studied : micro-lattice, foam, or honeycomb. In contrast, our tests show an efficiency range exceeding 35%.

Our findings are particularly valuable in cases where lightness is a critical requirement, such as the development of micro-UAS weighing less than 250 g, which falls within a more advantageous regulatory limit (Hassanalian & Abdelkefi, 2017).

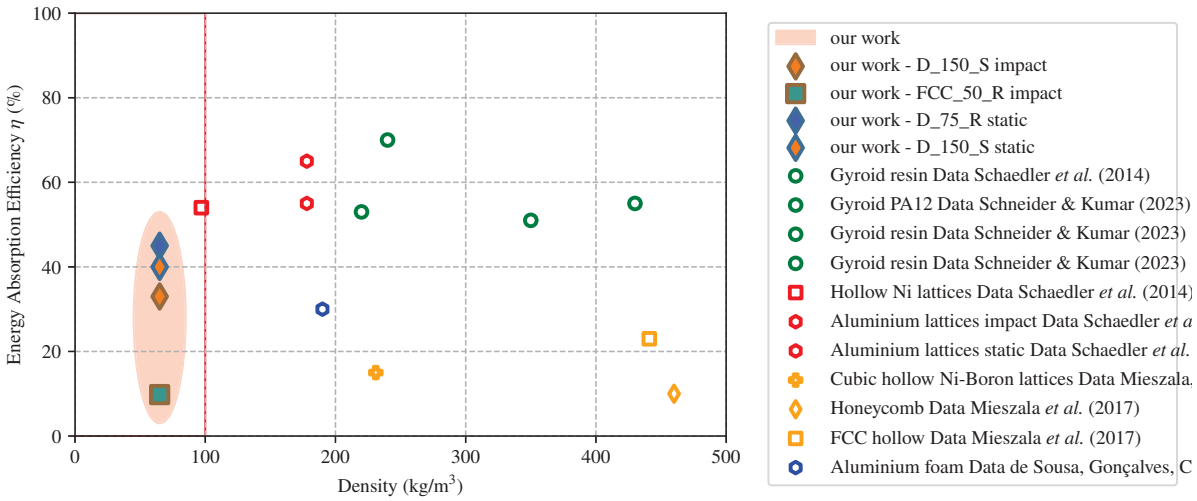

Figure 5.12 Energy absorption efficiency of our micro-lattices in comparison with existing works. We address the lowest density with a significant distribution of efficiency.

5.7.4 Association of multiple micro-lattices

For practical use in aerial vehicles, subjects to complex loading profiles, several micro-lattices will likely need to be combined. The differences in mechanical behavior between micro-lattices with soft or rigid resin offer a range of possibilities while maintaining the same lightness. Therefore, we studied the combination of a soft patch and a rigid patch. This combination is possible if two criteria are respected : first, the force absorbed by the soft micro-lattice must be lower than that of the rigid micro-lattice so that the soft micro-lattice deforms first ; second, the

energy absorbed by the soft micro-lattice must be greater than the energy required to break the rigid micro-lattice. Using the results of the impact tests, we calculated all the necessary metrics.

Tableau 5.2 Energy and velocity required to break rigid micro-lattices.

Sample	**Energy (J)**	**Max speed (m/s)**
GY_50_R	none	none
FCC_50_R	0.0084	0.1300
K_50_R	0.0298	0.2441
GY_75_R	0.0392	0.279
D_50_R	0.0941	0.4339
K_75_R	0.1041	0.4563
D_75_R	0.1980	0.6295
FCC_75_R	0.2553	0.7146
D_150_R	0.2741	0.7404
K_150_R	0.2798	0.7481
GY_150_R	0.3095	0.7868
FCC_150_R	0.8351	1.2924

From the definition of kinetic energy, we derive the speed required to break the micro-lattice. Table 5.2 shows the velocity values associated with each rigid combination. This “speed table” translates the energy level that must not be exceeded when using a rigid micro-lattice as a structural element in combination with a soft micro-lattice. By evaluating all possible soft and rigid combinations, we can create a compatibility map that identifies associations meeting the two criteria stated above in Fig. 5.13.

This compatibility map reveals that less than 30% of the associations are viable. We summarize the relationship between the calculated stiffness score and the SEA of each combination. For example, the 75 compactness achieves a balance between absorption efficiency and stiffness, smoothing the constraint without exceeding a threshold where the transmitted energy could break the rigid micro-lattice.

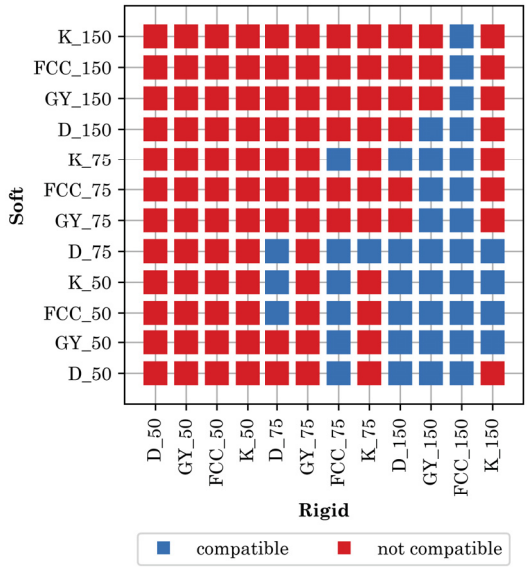

Figure 5.13 Result of possible associations between rigid and soft micro-lattices. Most combinations with rigid material and compactness 50 or soft material and compactness 150 are eliminated by the two association criteria.

5.8 Conclusion

Ultimately, we explored three variations of micro-lattices : pattern, compactness, and materials. To protect small, lightweight aerial systems, these structures demonstrated energy-absorption efficiency comparable to previous work while significantly reducing density to below the 100 g/m^3 threshold. Our study also highlighted the critical influence of loading speed by examining the same geometries of samples subjected to both compression and impact tests, revealing an inversion of the SEA between these two test protocols.

Additionally, by establishing micro-lattice association criteria, we created a table of viable combinations of rigid and flexible structures. This enables the selection of compatible patterns for use in aerial vehicles, enhancing their structural resilience.

Our test system, developed with a custom free impact test bench, allowed us to characterize our structures in a controlled environment that closely simulates real-world conditions. While

this new test bench may have potential inaccuracies compared to standardized devices, we demonstrated good repeatability. We plan to address this limitation by performing a performance characterization of our impact bench against a standard drop tower in future work.

This research not only advances the understanding of micro-lattice behavior under different loading conditions but also offers practical solutions for enhancing the durability of aerial vehicles. The significant density reduction and tailored energy absorption properties have the potential to impact the design and performance of lightweight, efficient aerial systems.

Declarations

Funding

The authors acknowledge the financial support of the NSERC CREATE UTILI program [6], and FRQNT Team grant (#283381).

Competing Interests

The authors have no relevant financial or non-financial interests to disclose.

Author Contributions

All authors contributed to the conception and design of the study. Louis Catar performed material preparation, data collection, and analysis. The first draft of the manuscript was written by Louis Catar and all authors commented on previous versions of the manuscript. All authors read and approved the final manuscript.

[6] https ://carleton.ca/utili/

CHAPITRE 6

EXPLORING THE DEPTHS : DESIGN OF THE FOLDABLE CAVERNAUTE AIRSHIP FOR LONG-LASTING SUBTERRANEAN MISSIONS

Louis Catar[1] , Jorge E. Salas Gordoniz[1] , Ilyass Tabiai[1] , David St-Onge[1]

[1] Département de Génie Mécanique, École de Technologie Supérieure,
1100 Notre-Dame Ouest, Montréal, Québec, Canada H3C 1K3

Article soumis à la revue « Autonomous Robots » en juillet 2024.

6.1 Avant-propos

Une fois la caractérisation mécanique des micro-treillis réalisée, nous pouvons nous atteler au développement d'un nouveau type de dirigeable pour l'exploration de caverne : le CAVERNAUTE (Concept Aérostatique Volant Et Rigide pour Naviguer et Accéder aux Univers TroglodytEs).

Des étapes de rationalisation sont nécessaires pour standardiser la fabrication tout en s'adaptant aux contraintes de production ainsi que les souhaits de l'équipe « Design » partenaire du projet (UQAM). Des techniques d'assemblage démontable sont utilisées. Cela permettra à l'avenir d'avoir un aérostat réparable et reconfigurable selon les besoins des missions. Cette troisième étape permet de réaliser un exosquelette qui assure la cohésion structurelle du prototype. Les requis de conception d'un dirigeable sont considérés pour assurer la compatibilité des solutions conçues. Un cadre de travail semi-automatisé est mis en place afin de pouvoir avancer sur l'élaboration de méthodes de fabrication tout en optimisant la forme. Après concertation avec les différentes parties prenantes du projet, il est décidé de s'orienter vers des formes de dirigeables polyédriques. Cette configuration apporte un visuel apte à interpeller les personnes qui interagissent avec le futur aérostat conformément aux objectifs initiaux de ce projet. Le cadre de travail est réalisé à partir de plusieurs briques : une optimisation de la forme qui intègre la géométrie, la fabrication, l'assemblage et la validation de l'aérostatique. Le logiciel Grasshopper®permet de réaliser la modélisation 3D (moteur CAO Rhino®) et d'implémenter des blocs de scripts Python pour extraire les informations pour trouver la combinaison idéale.

L'exosquelette est composé de jonctions en TPU imprimées en FDM et optimisées pour la légèreté et les règle de DfAM. Elles sont conçues sur Fusion 360®à l'aide d'un modèle paramétrique pour pouvoir changer aisément la géométrie des jonctions en fonction des résultats de l'optimisation de forme.

Arrivé à cette étape, il est possible de construire le prototype de dirigeable rigide d'intérieur. Pour réaliser les blocs de micro-treillis, une machine MSLA est utilisée. Cette machine permet d'imprimer des micro-treillis souples. Des interfaces rigides sont imprimées en PLA-aéro ("foam-PLA") afin d'assembler le tout à l'exosquelette du dirigeable. L'exosquelette est rigide, mais pliant grâce à l'utilisation de géométrie origami optimisée grâce au cadre de travail.

6.2 Résumé

Les dirigeables, principalement reconnus pour leur rapport unique charge utile/énergie, présentent un défi fascinant pour le domaine de l'ingénierie. Leur construction et leur fonctionnement nécessitent un équilibre délicat des matériaux et des règles, en faisant un objet d'étude captivant. Ils incarnent une intersection de la physique, du design et de l'innovation, proposant un large éventail de possibilités pour le transport et l'exploration futurs. Grâce à leur endurance pour les vols de longue durée, ils sont adaptés aux missions à long terme. Pour opérer dans des environnements complexes tels que les espaces encombrés en intérieur, leur membrane et leur mécatronique doivent être protégées des impacts. Cet article présente un nouveau design de dirigeable d'intérieur inspiré de l'origami et du motif Kresling. La structure du dirigeable combine un exosquelette en fibre de carbone et des micro-treillis en résine UV pour l'absorption des chocs. Notre design renforce le robot tout en lui permettant d'accéder à des espaces étroits en pliant la structure — jusqu'à un ratio d'expansion de volume de 19,8. Pour optimiser les nombreux paramètres du dirigeable, nous présentons une chaîne de conception, de fabrication et d'assemblage. Elle prend en compte les contraintes de fabrication, les dimensions de la zone de déploiement cible et l'aérostatique, permettant un test facile et rapide des nouvelles configurations. Nous présentons également des fonctionnalités uniques rendues possibles par la combinaison de l'origami avec le design du dirigeable, ce qui réduit les risques de défaillances

compromettant les missions. Nous démontrons le potentiel du design avec une simulation complète incluant une stratégie de contrôle efficace exploitant la mécatronique légère pour optimiser l'autonomie de vol dans des missions d'exploration d'environnements non structurés.

6.3 Abstract

Airships, best recognized for their unique quality of payload/energy ratio, present a fascinating challenge for the field of engineering. Their construction and operation require a delicate balance of materials and rules, making them a compelling object of study. They embody a distinct intersection of physics, design, and innovation, offering a wide array of possibilities for future transportation and exploration. Thanks to their long-flight endurance, they are suited for long-term missions. To operate in complex environments such as indoor cluttered spaces, their membrane and mechatronics need to be protected from impacts. This paper presents a new indoor airship design inspired by origami and the Kresling pattern. The airship structure combines a carbon fiber exoskeleton and UV resin micro-lattices for shock absorption. Our design strengthens the robot while granting the ability to access narrow spaces by folding the structure — up to a volume expansion ratio of 19.8. To optimize the numerous parameters of the airship, we present a pipeline for design, manufacture, and assembly. It takes into account manufacturing constraints, dimensions of the target deployment area, and aerostatics, allowing for easy and quick testing of new configurations. We also present unique features made possible by combining origami with airship design, which reduces the chances of mission compromising failures. We demonstrate the potential of the design with a complete simulation including an effective control strategy leveraging lightweight mechatronics to optimize flight autonomy in exploration missions of unstructured environments.

6.4 Introduction

The demand for underground Unmanned Aircraft Systems (UAS) is increasing. Aging infrastructures require inspection (Zhang, Hao, Zhang & Li, 2023), glacier geologic features need exploration to study their growth mechanisms (Das, Chakraborty, Rai, Dhar, Sadhu, Gautam, Verma,

Singh, Sherpa & Chakraborty, 2019), and Search & Rescue (S&R) operations aim to protect rescue teams (Bogue, 2019). Ground robots struggle to manage the complex terrains' topology, crawling and rolling robots are slow solutions that are less adapted to large or unstructured areas, making multicopters aerial vehicles a popular option. However, these vehicles face significant autonomy challenges. Commercial solutions designed for exploration and data collection in complex indoor or subterranean environments, such as the Elios 3 from Flyability (Adrien, 2024), cannot fly for more than 13 minutes. Their autonomy decreases further with inspection payloads like LiDAR. Similarly, vehicles developed in university laboratories have flight times that do not exceed 5 minutes (Briod, Kornatowski, Zufferey & Floreano, 2014; Falanga, Kleber, Mintchev, Floreano & Scaramuzza, 2019) or 15 minutes (Krátký, Petráček, Báča & Saska, 2021). These limited flight durations restrict mission outcomes. In this paper, we focus on the use of airship UAS. With these vehicles, power is almost exclusively used for movement, while the lighter-than-air gas provides lift. Airships lend themselves well to long-lasting missions. Thanks to their autonomy and a lower cruising speed than a multicopters, their deployment is perfectly fitted to gradual acquisition of data such as LiDAR scanning. Palossi et al. highlight the relevance of small indoor airships compared to flying wings and multicopters (Palossi, Gomez, Draskovic, Keller, Benini & Thiele, 2017). They specify their uniqueness in terms of maneuverability, their ability to govern, and agility, i.e., their maneuverability in a restricted space at low speed. Still, for a practical use case, the payload often requires rather large volumes, such as the one designed by Salas Gordoniz, Reeves & St-Onge (2021, 2022) : a bio-inspired multi-body architecture to move a high-lift aerostat in caves and tunnels. Many control challenges are associated with this type of architecture, as it is radically different from the common ellipsoid, but also large with respect to the cluttered environment targeted for their missions.

Indoor airships have already been proposed for underground applications (Wang, 2022). The flight longevity offered by buoyancy is a game changer for long missions in complex environments. Deployment in confined spaces (such as the DARPA Subterranean Challenge) is not an obstacle for this type of aerial system, though its size must adapt to narrow passages (Huang, Lu, Chen, Ser, Huang, Shen, Chen, Chang, Lee & Wang, 2019; Lu, Huang, Huang, Liu, Hsu, Huang,

Huang, Chang, Ewe, Huang, Li, Wang, Yim, Huang, Bai & Wang, 2022; Hudson, Talbot, Cox, Williams, Hines, Pitt, Wood, Frousheger, Lo Surdo, Molnar, Steindl, Wildie, Sa, Kottege, Stepanas, Hernandez, Catt, Docherty, Tidd, Tam, Murrell, Bessell, Hanson, Tychsen-Smith, Suzuki, Overs, Kendoul, Wagner, Palmer, Milani, O'Brien, Jiang, Chen & Arkin, 2022). With these challenges in mind, we propose a new indoor airship architecture.

Most examples of indoor airships are soft blimps supporting a gondola of actuators and mechatronics. A blimp is an airship whose shape is maintained by the pressure of the gases within its envelope (Hecks, 1972). For small airships, the ratio of the lift provided by the gas (volume) to the mass of the envelope (surface) is generally not sufficient to support heavier structures. Nevertheless, rigid airships can provide increased reliability and durability, which are critical for harsh environment missions. A rigid configuration can help to reduce drag, increase flight speed, improve balance and control by maintaining an aerodynamic shape, and provide greater design flexibility for the position of the propulsion system. (Konstantinov, 2003). While the surface/volume ratio favors the sphere, its excessive drag is incompatible with operations in outdoor spaces. Therefore, streamlined shapes offer good aerodynamic performance that only a rigid or semi-rigid structure can ensure. Indeed, soft blimps require increased gas pressure on the envelope to maintain their shape, which increases the weight. Conversely, in indoor spaces, fewer external aerodynamic disturbances affect the flight and shape of the airship, allowing for innovative rigid structures to be explored and created.

Knowing these ratio constraints, another problematic point is accessibility to remote and narrow interior areas. These large structures need to be transported and pa for field missions. This work introduces a rigid but foldable autonomous airship UAS named CAVERNAUTE (Compact Airship Vehicle for Expeditions into Remote Natural Abysses and Underground Tunnels) for deployment inside a hard-to-reach natural cave. To further push both the geometrical design of an unconventional airship and provide a complete field deployment experience, this project is part of an artistic performance. The CAVERNAUTE is expected to explore a restricted-access cave while broadcasting its journey into an immersive room open to the public. The constraints of this artistic context are thus integrated into the design presented throughout this paper.

This work contributes to the field of robotic design and exploration in complex environments in three core aspects : *(1)* the development of a rigid foldable geometry by applying origami techniques to airship structures ; *(2)* the pipeline of the design of a LTA robot with weight, volume, geometric, and manufacturing intertwined constraints for underground mission ; and *(3)* a control adapted in regard of flight-autonomy with ultralight-weight mechatronic limitations.

6.5 Related work

6.5.1 Rigid airship designs

In the vast majority of literature, small indoor airships (less than 3 m in length) are based on a combination of ellipse, circle, and/or parabola geometries like GNVR-type shape (Gawale, Raina, Pant & Jahagirdar, 2008; Joshi, Raina & Pant, 2009; Ram & Pant, 2010; Adeel, Suvarna & Pant, 2017; Mistri & Pant, 2017; Biju & Pant, 2017). Other less conventional shapes still rely on inflated volumes, as they do not have a stiff envelope : the gondola is suspended under the airship, or the structure is semi-rigid with rings placed at sections corresponding to the gondola (Gorjup & Liarokapis, 2020; Zheng, Li, Agrawal, Lei, John-Sabu & Mehta, 2021). Standing out from conventional designs are studies with more complex shapes, such as wing-like profiles, torus, or bio-inspired shapes like the ray (hybrid airship) (Edge, Collins, Brown, Coatney, Roget, Slegers & Johnson, 2010). Our work is inspired by a previous experiment involving a cubic-shaped airship with a rigid exoskeleton, named Tryphon, deployed in the La Verna cave in France (St-Onge, Reeves & Gosselin, 2011).

From the perspective of rigid structures, small airships have not, to our knowledge, gone beyond semi-rigid designs. The semi-rigid structure does not hold the shape without gas (Liao & Pasternak, 2009). Typically, rigidity is achieved by rings surrounding the flexible envelope, allowing for better control of the shape either by restricting expansion due to gas pressure (Sharf, Persson, St-Onge & Reeves, 2013; Mistri & Pant, 2017), or by tensioning the envelope (Edge *et al.*, 2010; St-Onge *et al.*, 2011). In the latter case, the forces on the structure, made up of carbon fiber beams and sometimes honeycomb sandwich panels, can be very demanding without directly

taking up the loads via tension elements (cables), which significantly lighten the structure. In the work of Anil, Kshirsagar & Pant (2016), the authors detail a wide range of ultralight materials for making a semi-rigid airship, including balsa wood and composite materials.

6.5.2 Airship design pipeline

Adopting standardization and modularization in airship design, akin to practices in aerospace, could provide significant benefits. Standardization has the potential to lower production and maintenance costs by enabling large-scale manufacturing of interchangeable parts, economies of scale, and simplified supply chains (Titenkov & Zhuravlev, 2018). Modularization divides functions into discrete modules, allowing for easier updates, repairs (Larsson, 2018), and design flexibility for modules with varied requirements (Dmitriev & Mitroshkina, 2019). However, the airship industry remains relatively nascent, limiting incentives for such design approaches.

Few studies have proposed a comprehensive framework for airship design. Recent airship projects often feature unconventional configurations (Ceruti & Marzocca, 2014), resulting in disparate design approaches. Nonetheless, airships share core technical requirements related to flight performance, such as lift and structural integrity. Introducing structured, nested requirements could improve alignment throughout the design cycle, impacting final model performance. Using genetic algorithms to explore configurations, for example, can leverage airship modeling insights and reduce reliance on conventional aircraft design expertise (Liao & Pasternak, 2009). While Zheng *et al.* (2021) proposed a modular design framework for custom airships, it is currently limited to a single geometry parameter (diameter) and a traditional GNVR envelope (Suvarna, Joshi, Dubey & Pant, 2019).

Further complicating the establishment of a standardized design framework, the autonomy of airship models remains underexplored in the literature, with most focus placed on control challenges. While current research addresses control mechanisms, there is limited emphasis on optimizing endurance or flight duration. Examples include the GT-MAB blimp, with a two-hour endurance (volume of 0.12 m^3)(Cho, Mishra, Tao, Vamell, King-Smith, Muni,

Smallwood & Zhang, 2017) ; the “Tryphon” cubic airship, capable of six-hour flights (volume of 9.85 m^3)(St-Onge, 2011) ; and the robot designed by Salas Gordoniz, Saad & St-Onge (2024), achieving 41-minute flights (volume of 2.4 m^3). Developing standardization frameworks that consider both structural and autonomy requirements will be essential for advancing airship applications in practical, large-scale use cases.

6.5.3 Folding airships

There are many advantages to creating a folding airship. On large aircraft, it helps to reduce drag (Chillara & Dapino, 2019; Zhang, Li, Wang & Yan, 2021b), and to design more efficient aerodynamic control surfaces (Cozmei, Hasseler, Kinyon, Wallace, Deleo & Salviato, 2020). It also allows being more compact to meet specific mission requirements, such as an airship project for space exploration of Titan, which has to fit into the nose cone of a rocket (Duffner, Liu, Mandy, Panish & Landis, 2007), or the foldable exoskeleton of the multi-body blimp of Salas Gordoniz et al. to better access underground areas (Salas Gordoniz *et al.*, 2022).

When it comes to creating an airship with rigid but foldable characteristics, the association evokes origami. Origami, a Japanese art that uses folding to create three-dimensional structures, has found extensive applications in engineering due to its unique properties : deployability, scalability, self-actuation, reconfigurability, tunability (capability to be optimized), and ease of manufacturing (Callens & Zadpoor, 2017; Meloni, Cai, Zhang, Sang-Hoon Lee, Li, Ma, Parashkevov & Feng, 2021). The aerospace field has been particularly prolific in adopting origami techniques, largely due to the constraint of transporting structures in cramped rocket fairings before deployment in space (Zirbel, Trease, Thomson, Lang, Magleby & Howell, 2015; Chen, Bilal, Lang, Daraio & Shea, 2019; Yang, Defillion, Scarpa & Schenk, 2023). Additionally, origami has numerous applications in the biomedical field, such as in surgical devices (Suzuki & Wood, 2020; Banerjee, Li, Ponraj, Kirthika, Lim & Ren, 2020) and implants (Kuribayashi, Tsuchiya, You, Tomus, Umemoto, Ito & Sasaki, 2006; Kim, Lee, Yu, Han, Lee, Kim, Ahn, Han, Lee, Kim, Kwon, Im & Hwang, 2015; Bobbert, Janbaz, van Manen, Li & Zadpoor, 2020).

Robotics has also benefited from various mechanisms inspired by origami, including those that enable crawling robots (Onal, Wood & Rus, 2013; Pagano, Yan, Chien, Wissa & Tawfick, 2017; Lee, Kim, Sohn, Heo & Cho, 2021) and create complex mechanisms (Kim, Lee, Jung & Cho, 2018; Novelino, Ze, Wu, Paulino & Zhao, 2020; Zhang, Chen, Wu, Kong & Wang, 2020; Zhang, Fan, Chen, Luo, Lu & Wang, 2021c). Among these mechanisms, origami structures with enclosed volumes are particularly suitable for shaping airships. These structures can be categorized into four main families : Miura-Ori, Kresling, Yoshimura, and Waterbomb patterns (Fossati, 2022). The folding patterns of the individual cells of each type are shown in Fig.6.1. Among these, the Kresling pattern is peculiar : a biomimetic design that draws inspiration from natural forms like the abdominal bellows of moths(Kresling, 2008) and phenomena of dynamic shear rupture (Kresling, 2020).

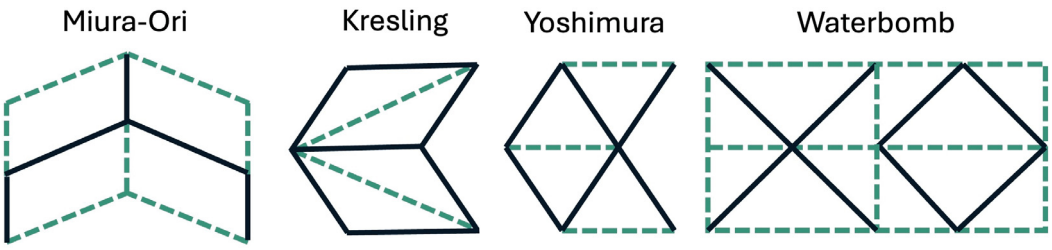

Figure 6.1 Origami folding pattern. Valley creases are shown in dotted green and mountain creases in solid blue.

Origami structures have typically been studied for their kinematics and the forces they can produce. There are some works that consider the thickness of the material for manufacturing (Hwang, 2021; Li, Zhou, Hao, Yu, Chen & Ma, 2023), but studies on the contained volume are sparse (Lynch & Raney, 2020). Notably, Yang et al. optimized the volume for a space habitat to fit inside a SpaceX Falcon 9 rocket payload fairing using a genetic algorithm, showing that the Miura-Ori pattern had a favorable radial expansion compared to the Kresling pattern (Yang *et al.*, 2023). However, their study was volume-driven, and more research is required to include additional manufacturing constraints and mission requirements.

6.5.4 Impact absorption for blimp

Due to their lightweight and maneuverability, airship drones are particularly vulnerable to impacts during collisions. It is therefore essential to develop structures capables of effectively absorbing kinetic energy to protect both the drone and its environment.

In the context of airship drones, integrating such structures can provide effective protection without compromising the aircraft's lightness and maneuverability. The work of Park, Lee, Jang & Han (2023) explored the use of origami and kirigami-inspired structures for energy absorption in drone shields. These geometries allow for controlled deformation, efficiently dissipating impact energy while maintaining a lightweight structure. However, these shields represent a significant mass when it comes to covering the entire envelope of an airship. We therefore opted for the use of micro-lattices. These ultralightweight structures have already been used to create the frame of a drone with the objective to increasing its self-sufficiency (Xiao, Li, Jia, Surjadi, Li, Lin, Gao, Chirarattananon & Lu, 2021), but here we want to use them as impact absorbers.

We employ the multi-criteria selection method from Catar *et al.* (2022) to determine the ideal absorbent structure for the CAVERNAUTE, derived from a preliminary impact testing study (Catar *et al.*, 2024a). This method identifies the most advantageous pattern and compactness based on a list of criteria (mechanical, manufacturing, etc.).

Six criteria are considered :

- Maximum deformation : The aim is for maximum deformation to use the entire patch thickness to cushion the impact, thereby minimizing deceleration (coef. 1).
- η (absorption efficiency) : calculated from Schaedler *et al.* (2014), we seek the highest efficiency (coef. 1).
- Maximum force : We aim to limit force peaks during impact to smooth the stress (coef. 1).

- SEA : We seek the highest possible energy absorption. For flexible micro-lattices, experiments showed SEA was equivalent across patterns and compactness, so its weight in the final selection is reduced (coef. 0.5).
- Print failure : Based on production experience, we aim for the lowest failure rate (coef. 1).
- Contact surface : This is the area in contact with the build plate, which limits the ability to print multiple elements in a single 3D print session (coef. 1).

Figure 6.2 presents the optimized ranking. The chosen combination for the CAVERNAUTE is therefore the FCC pattern with 75 compactness.

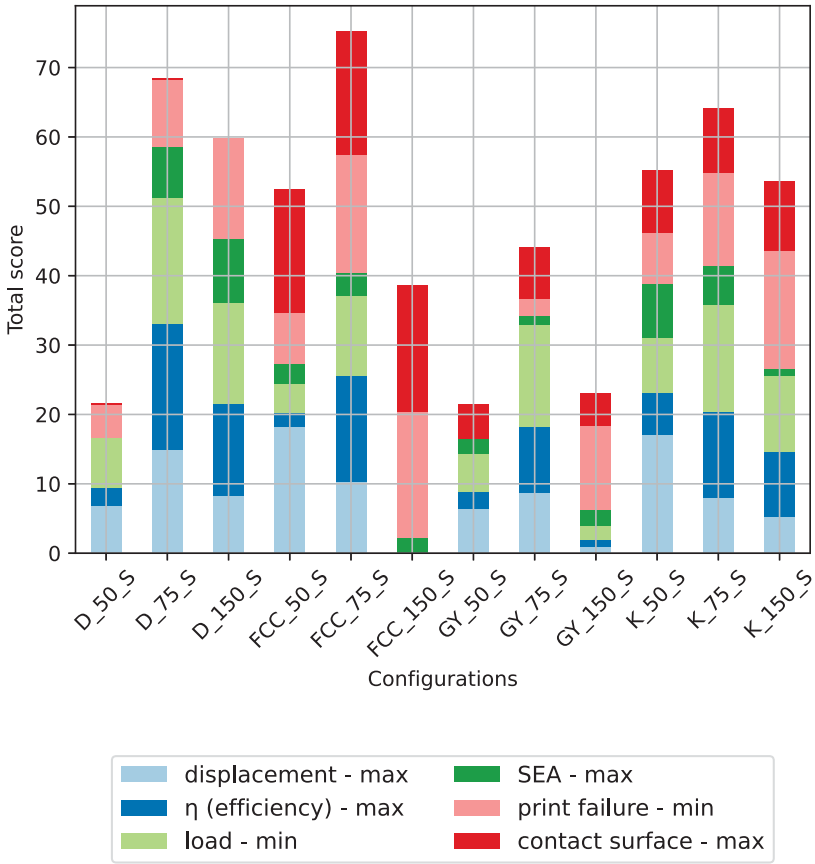

Figure 6.2 Score obtained for each micro-lattice combination based on the tests presented done by Catar *et al.* (2024a). The FCC_75 combination achieves the highest score, followed by the D_75 and K_75 patterns, which are mechanically interesting but less suitable for mass production due to lower print success rates.

Figure 6.3 shows the print bed during micro-lattice patch printing. Twenty patches are produced in a single print.

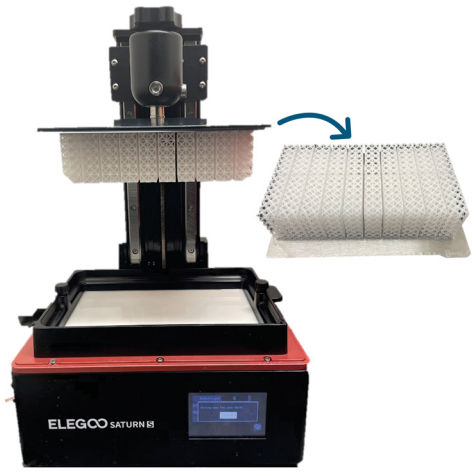

Figure 6.3 Elegoo® print bed with twenty patches printed at once

6.6 CAVERNAUTE design

Full surface coverage with rigid structure, even ultra-lightweight such as micro-lattices, are too heavy to be considered as a realist solution. In this section, we will first introduce an origami pattern fit for airship design. We will then detail the elements that compose the structure of the CAVERNAUTE before presenting the parametric design pipeline that encompasses the geometry, manufacturing, and assembly requirements of the aerial vehicle.

6.6.1 Kresling-inspired structure

Kresling pattern is selected because of the low number of edges required to create a cylinder compared with other patterns. It is composed of congruent parallelograms containing diagonal folds that form a cylinder when the mountains and valleys are folded (Fig. 6.4). Each stage constitutes a segment. A Kresling cylinder can be described using six independent parameters : H_1 (unfolded height), H_0 (folded height), D (external cylinder diameter), n (sides number of polygon), m (number of segments) and λ (one angle ratio). An example is shown in Fig. 6.4.

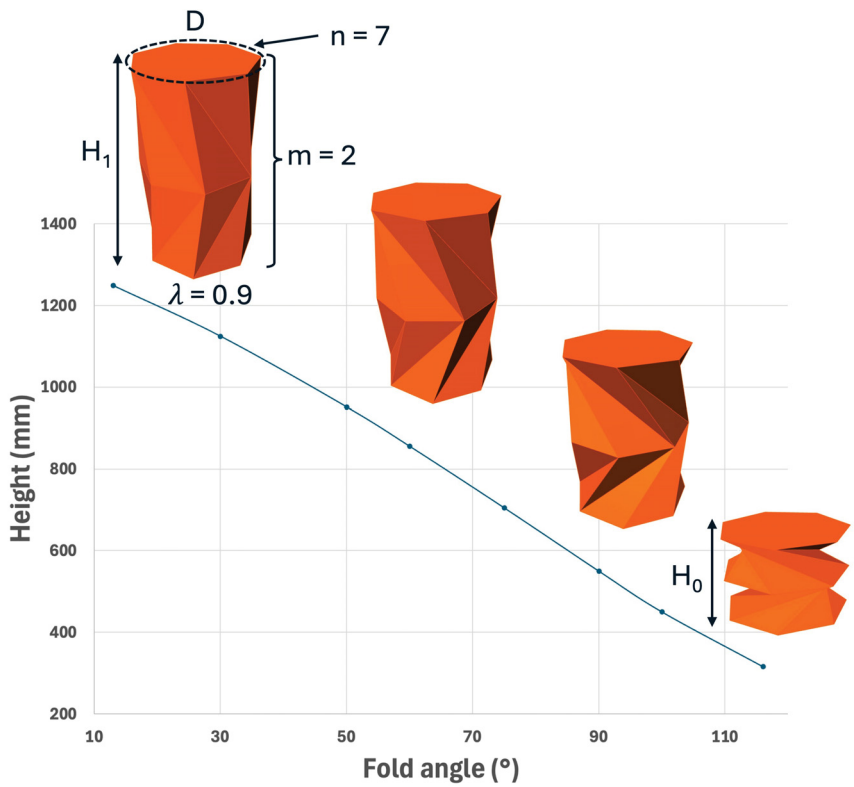

Figure 6.4 Folding motion of a Kresling pattern ($n = 7,\ m = 2,\ \lambda = 0.9$). Folding follows a shearing movement. Due to segment symmetry, there is only pure translation for each bi-segment.

The notations and equations are taken from the geometric description of a Kresling segment done by Bhovad & Li (2018); Bhovad, Kaufmann & Li (2019).

The schematic diagram of a Kresling segment is shown in Fig. 6.5. The opening angle $\varphi = \frac{\pi}{n}$ defines the opposite angle $\gamma = \frac{\pi}{2} - \varphi$ and the side length $s = 2\ R\ sin(\varphi)$. The angle ratio λ, is the ratio of the angle of the diagonal crease to half the internal angle of the base polygon γ. From the two classical parameters of side $b_c = \sqrt{s^2 + {d_c}^2 - 2\ s\ d_c\ cos(\lambda\gamma)}$ and diagonal $d_c = 2\ R\ cos(\gamma - \lambda\gamma)$, we can describe generalized parameters that consider the thickness of the material with a minimum bent height $h_0 : b_g = \sqrt{{b_c}^2 + {h_0}^2}$, $d_g = \sqrt{{d_c}^2 + {h_0}^2}$ as well as the angle $\theta_g = cos^{-1}\left(\frac{s^2 + {d_g}^2 - {b_g}^2}{2\ s\ d_g}\right)$. These three generalized parameters define the shape of the Kresling segment envelope. For the opening kinematics of the Kresling pattern, only two parameters

(height h and b) vary according to the α opening angle. These are described in correspondent equations 6.1 and 6.2 and Fig. 6.5.

$$h(\alpha) = \sqrt{{h_0}^2 + 2\ R^2\ [cos(\alpha + 2\varphi) - cos(\alpha_0 + 2\varphi)]} \tag{6.1}$$

$$b(\alpha) = \sqrt{2\ R^2\ (1 - cos(\alpha)) + h(\alpha)^2)} \tag{6.2}$$

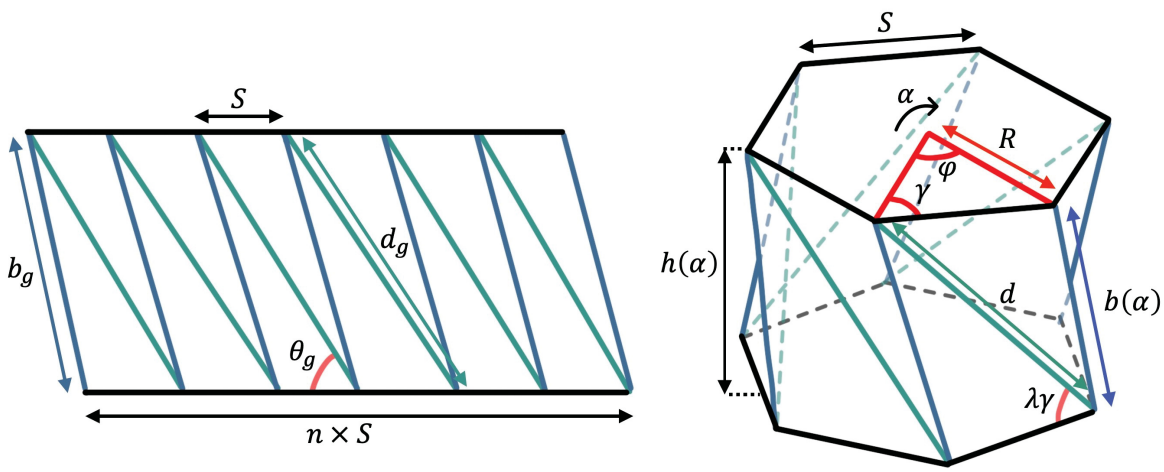

Figure 6.5 Kresling geometrical parameters of one segment ($n = 6,\ m = 1$). α is the angle of rotation to unfold the geometry between the folded *(0)* and unfolded *(1)* state. The valleys are in green and the mountains in blue. $\alpha_{(0)} = 2\lambda\gamma$ and $\alpha_{(1)} = 2(1 - \lambda)\gamma\ \forall\lambda > 0.5$

.

The Kresling pattern has been adjusted so that it is bistable ($\lambda > 0.5$). Figure 6.7 shows that the height $b(\alpha)$ of the segment changes according to the opening of the Kresling. Equivalent strain $\varepsilon = \frac{b(\alpha)}{B_g} - 1$ and strain energy $U = \frac{1}{2}\ K\ \varepsilon^2$ can be defined with K, the material stiffness. Then normalized strain energy is computed as : $E_S = \frac{1}{2}\ \varepsilon^2$. This variation of energy potential induces a bistability of CAVERNAUTE (Fig. 6.8). In the folded and unfolded position.

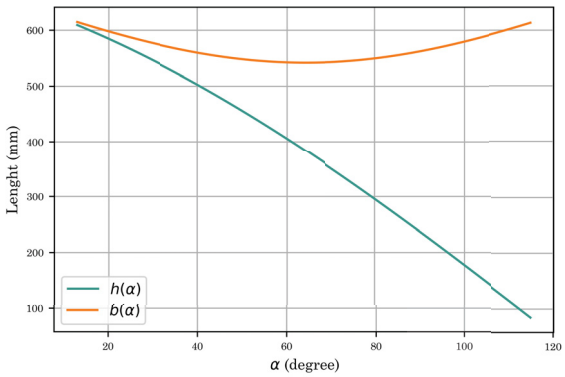

Figure 6.6 Evolution of the length of h and b as a function of the bending angle α. With the geometric description, the diagonal d_g and the sides of polygons s do not vary as a function of α. However, this variation in b creates a constraint that can be represented in Fig. 6.8

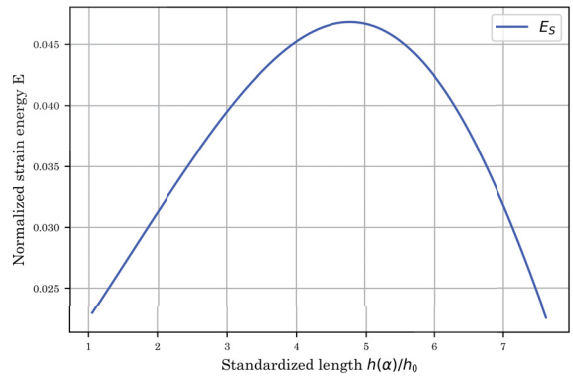

Figure 6.7 Normalized energy E_S as a function of the relative height of a Kresling segment. This shows the bistability between the folded and unfolded configurations.

6.6.2 Exoskeleton design for manufacturing

The exoskeleton is the rigid structure that maintains the shape of the airship's envelope and ensures the structural coherence of all CAVERNAUTE components, while offering foldable characteristics for compactness. It must be as light as possible. Therefore, the exoskeleton design process focuses on each part separately to leverage the best mechanical performance of each.

In order to joint the tubes and provide folding capability, 3D-printed parts in TPU95 were created. These parts were specifically designed to minimize mass, utilize the flexibility of the material to create a compliant mechanism, while still easily printable. The TPU junctions are displayed in Fig. 6.8. All Design for Additive Manufacturing (DfAM) rules were employed, and print parameters were optimized (Fig. 6.8) : to improve the print, the first layer is continuous to facilitate adhesion *(b)*. Sub-figure *(a)* shows the parts removed after printing to help stability during manufacture. Sub-figure *(b)* details the part's overhangs. TPU is a material that tends to ooze during printing, so we benefit from high travel speed features of the printer (500 mm/s)

to eliminate this effect. The final iteration of these junctions (simple configuration shown in Fig. 6.8(a)) have a weight of m = 0.75 g each.

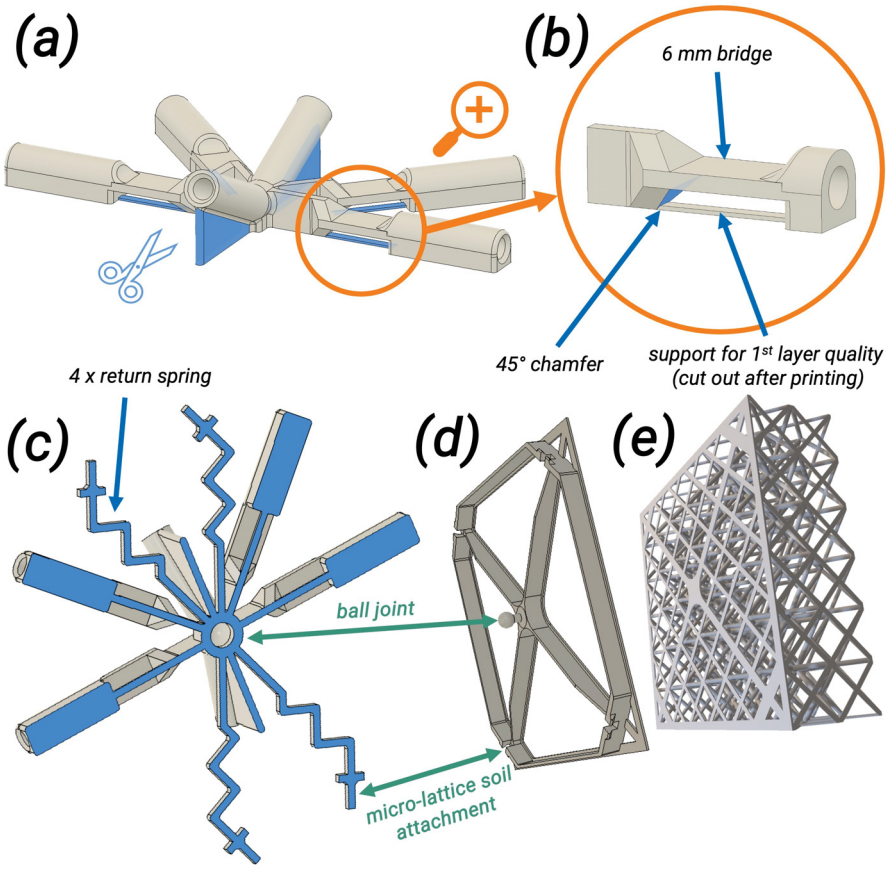

Figure 6.8 Exoskeleton tube junction : (a) simple and (c) to host lattices. Manufacturing features are highlighted in blue. Sub-figure *(c)* shows the micro-lattices junction with the micro-lattices soil *(d)* return spring and ball joint connection. Sub-figure *(e)* shows the micro-lattice buffer structure.

At the ends most exposed to the external environment, micro-lattice structures (e) were added to absorb impact energy. The pattern, material, and cell size are derived from a previous characterization work (Catar *et al.*, 2024a). A wide range of configurations have been evaluated on a test rig specially designed for crash-testing small, light aircraft. In the end, the face-centered-cubic (FCC) pattern is the most suitable configuration in terms of high-specific energy absorption and efficiency for low velocity impact, as well as considered its easiness in terms

of manufacturing. A special attachment was designed to host these structures. The variant of the TPU junction includes a ball joint and return springs system, as shown in Fig. 6.8 (c) and (d). This mechanism ensures that the micro-lattice is in the optimal frontal position on impact. To interface between the micro-lattice (e), printed in UV resin (MSLA Saturn S), and the TPU junction, a LW-PLA soil was printed (d). This component is clipped onto the ball joint and secured with the ends of the return springs. LW-PLA is a type of PLA polymer with a thermally activated expanding agent, creating porosity that lighten the part by 50%. The micro-lattice, the LW-PLA soil, and the modified TPU junction have a total weight of m = 3.4 g.

The airship manufacturing requires the complete bill of material for production. The total tube length needed for a given Kresling configuration is computed with :

$$L_{CVNT} = m \times n \times (d_g + b_g + s) + n \times s, \tag{6.3}$$

where m stands for the number of segments, n the sides number of the polygon. d_g, b_g and s are described in Fig.6.5.

Then the total envelope surface for that exoskeleton structure is calculated from the following formula (derived from Heron's formula — (Sangwin, 2024)) :

$$S_{CVNT} = \frac{2\,s^2\,n}{4\,tan(\varphi)} + 2\,n\sqrt{\frac{s+d+b}{2}\left(\frac{s+d+b}{2} - s\right)\left(\frac{s+d+b}{2} - b\right)\left(\frac{s+d+b}{2} - d\right)} + S_{sheath} \tag{6.4}$$

Since the exoskeleton maintains the envelope of the airship passing through sheath sew to the envelope, these added membrane surface are computed with

$$S_{sheath} = L_{sheath} \times t_{sheath}, \tag{6.5}$$

with t_{sheath} the patches' width and L_{sheath} given by :

$$L_{sheath} = (L_{CVNT} - d_g \times n \times m) \times \frac{r_{\%}}{100}, \tag{6.6}$$

with $r_{\%}$ the ratio between the length of the sheaths and the length of the CAVERNAUTE edges in percentage, L_{CVNT} the total tube length needed for one CAVERNAUTE, and d_g, n and m defined in Fig. 6.5.

6.6.3 Parametric design

To generate viable designs, we created a pipeline to explore various concepts, integrating manufacturing requirements as well as aerostatic and other key considerations into a Grasshopper®visual script (available online). Grasshopper®is a visual programming software application designed to be used with the Rhino®CAD application. We have adapted its traditional use to leverage both the CAD capabilities and its mathematical blocks to evaluate the physics of the airship, automatically test different concepts, and assist in the manufacturing of the CAVERNAUTE.

Figure 6.9 shows the flow diagram of our interface. There is a "geometric" group fed by parameter constraints of the target environment (measured) and the three geometric parameters n, m, and λ to optimize. Using the equations presented in Section 6.6.2, the pipeline evaluates different characteristic quantities based on the geometry and parameters imported by the user (Table 6.1). The yellow groups allow us to calculate the weight of the onboard components, such as the weight of the exoskeleton or the envelope. From the equations of aerostatics, we can verify buoyancy. A Python script [1] explores all possible variations of the three parameters and records the data for analysis. From the geometry, we represent the volume of the CAVERNAUTE and generate the 2D pattern file for the envelope making. Finally, a last manufacturing module helps with assembly. It provides instructions for the order and lengths of tube cuts.

[1] https://git.initrobots.ca/lcatar/cavernaute.git

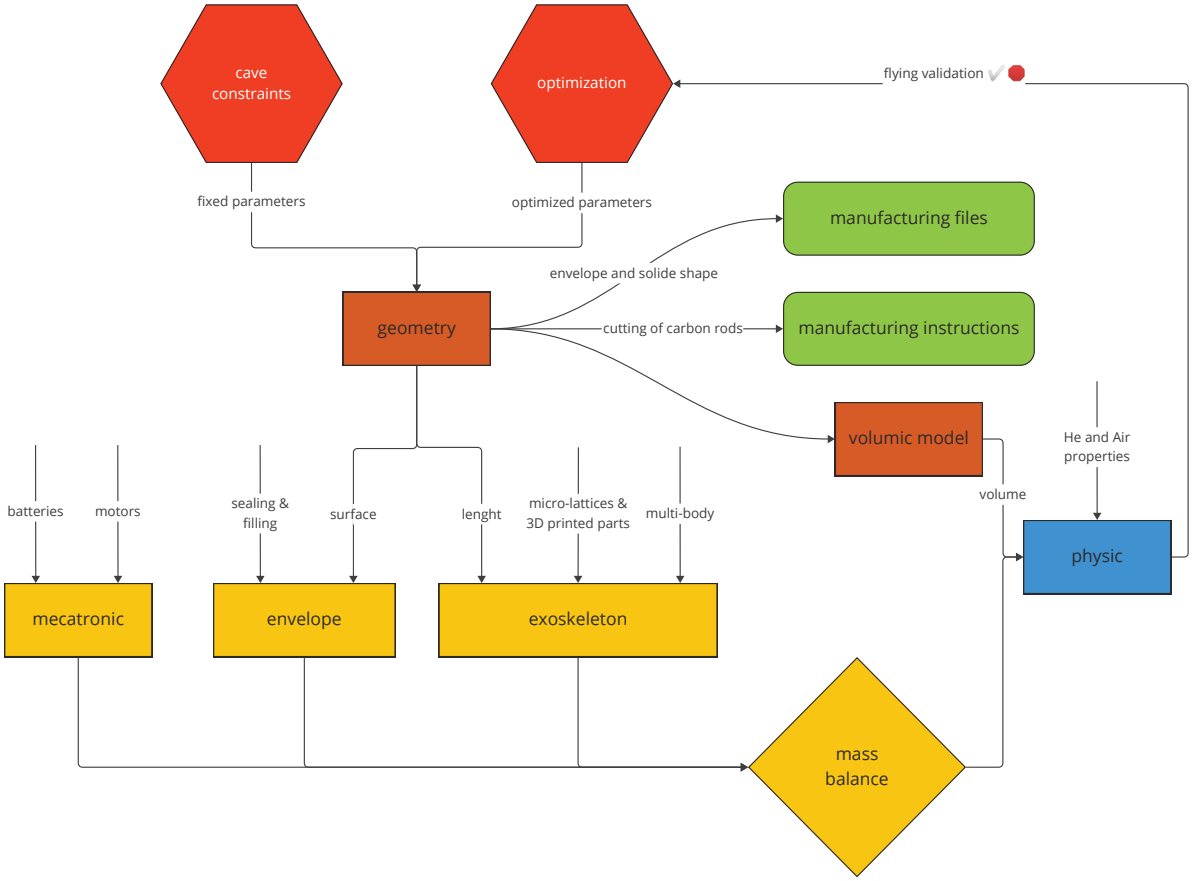

Figure 6.9 Diagram of the CAVERNAUTE design and manufacturing pipeline. The geometric capabilities of the Grasshopper software combined with Rhino are mixed with mathematical capabilities to create a pipeline that considers the many multidisciplinary constraints of a foldable airship design.

To feed this pipeline, thirty-two input parameters are editable. Three of them have to be optimized among several thousand possible combinations, others are constant data such as the density of materials, measurements from the target environment and physics as well as some preferences from the user's choices. More advanced customizations are possible, such as the ability to create multiple segments (multi-body airship). Table 6.1 groups all these parameters.

Tableau 6.1 Input parameters editable in Grasshopper, with values used in the current specifications. Some are fixed by the mission, others can be chosen by the user (number of motors, multi-body airship, etc.) and finally, three parameters can be optimized according to the configuration (n, m, λ).

N°	Parameters	Description	Value	Units	Type
1	n	number of polygon sides	$[\![3; 10]\!]$	$\mathbb{N}$	geometrical (to optimize)
2	m	number of CAVERNAUTE segment	$[\![2; 10]\!]$	$\mathbb{N}$	
3	λ	angle ratio	[0.50; 1.00]	n.a.	
4	D	CAVERNAUTE diameter	720	mm	geometrical (cavern dimensions)
5	H_0	CAVERNAUTE folded height	320	mm	
6	H_1	CAVERNAUTE unfolded height	2440	mm	
7	ρ_{air}	air density at 12 °C and 99‰ RH	1.231	kg/m^3	physic
8	ρ_{He}	helium density	0.1692	kg/m^3	
9	m_{CT}	carbon tubes linear density	3.76	g/m	manufacturing
10	$m_{mecatrn}$	mechatronics weight (board, wires)	30	g	
11	m_{motors}	motor weight	9.1	g	
12	$m_{propellers}$	propellers weight	0.46	g	
13	N_{motors}	number of motors	4	$\mathbb{N}$	
14	$m_{battery}$	battery weight	80	g	
15	$N_{battery}$	number of batteries	1	$\mathbb{N}$	
16	$m_{simpleTPUjct}$	TPU junction weight	0.75	g	
17	$m_{latticeeTPUjct}$	TPU + micro-lattice patch weight	3.4	g	
18	N_{patchs}	number of micro-lattice patches	17	$\mathbb{N}$	
19	d_{env}	envelope density	70	g/m^2	
20	d_{glue}	sealing adhesive density or thermic	0	g/m^2	
21	t_{ovlp}	weld overlap	10	mm	
22	N_{seal}	number of radial sealing lines	2	$\mathbb{N}$	
23	t_{sheath}	sheath width	35	mm	
24	$r_{\%}$	sheath ratio	10	%	
25	m_{valve}	valve weight	7	g	
26	N_{valve}	number of valves	1	$\mathbb{N}$	
27	N_{exo}	number of multi-body exoskeletons	0	$\mathbb{N}$	
28	N_{CVNT}	number of bodies	1	$\mathbb{N}$	
29	m_{kevlar}	linear density of Kevlar wire	0.28	g/m	
30	$Dist_{CVNT}$	distance between multi-bodies	0	mm	
31	L_{tubes}	raw carbon tube length	1000	mm	

6.7 Flight control

Several conditions are considered when defining the control and flight of CAVERNAUTE. It is intended to fly for several days over multiple weeks, so helium leakage is expected; due to its expansion, it is difficult to maintain a consistent quantity of helium for each flight after

re-inflation. These conditions mean that the weight and buoyancy, as well as volume and shape, will not remain exactly constant between flights. Additionally, since CAVERNAUTE is intended to fly in unstructured environments, using a precise model-based controller for a predefined trajectory is impractical.

Attempting to obtain common parameters to identify the model of the robot, such as mass and center of mass, buoyancy and volumetric center, drag estimation, and added/virtual mass/inertia, to then define a flight trajectory, set gains, and conduct several simulated and real-life tests is a tedious task that can jeopardize the deployment of the robot.

To mitigate these problems and ensure safe flight under a generalizable set of conditions, we are using the controller presented in Salas Gordoniz *et al.* (2024). This controller is based on two main known characteristics : motor actuation and the velocity optimization required to travel the necessary distances.

The version of the controller we leverage for this work does not require mass/inertia estimation. Instead, the actuation forces and moments ($\overrightarrow{\tau}$) for the inertial axes X_N, Y_N, Z_N and yaw (ψ) are defined as follows :

$$\tau_i = F_i \cdot sat\left(\frac{s_i}{\xi_i \cdot tol_i}\right) - \xi\dot{i} \tag{6.7}$$

where $i = \{x, y, z, \psi\}$, F_i is the maximum force considered for coordinate i, s_i corresponds to the sliding surface with slope $-\xi$, same as in Sliding Mode Control (SMC) (Slotine & Li, 1991; Márquez, 2003), defined as $s_i = \xi_i\tilde{i} + \dot{\tilde{i}}$ In this case, we aim to reach each point of the path at zero velocity, where $\tilde{i} = i - i_d$, and tol_i is the separation from the sliding surface $s_i = 0$, measured in distance units, marking a transition between SMC and PD control. The gain ξ is selected as $F_i/v_{i,max}$ to achieve a cruising speed of magnitude $v_{i,max}$. The saturation function sat is defined as :

$$sat\left(\frac{s_i}{\xi_i \cdot tol_i}\right) = \begin{cases} 1, & \text{if } \left(\frac{s_i}{\xi_i \cdot tol_i}\right) > 1 \\ \left(\frac{s_i}{\xi_i \cdot tol_i}\right), & \text{if } -1 \leq \left(\frac{s_i}{\xi_i \cdot tol_i}\right) \leq 1 \\ -1, & \text{if } \left(\frac{s_i}{\xi_i \cdot tol_i}\right) < -1 \end{cases} \tag{6.8}$$

Since both cruising speed and altitude control are critical for autonomy and safety, steady-state errors need to be addressed. Indeed, damping effects, as well as changes in weight and buoyancy, will induce slower velocities than v_{max}. This can be solved using a recursive Sliding Moving Average (SMA) of the applied forces (τ^*_{SMA}) to correct them in real time. This approach requires minimal tuning (compared to PID control), and the sliding time window can be selected to achieve a more reactive controller with shorter time selections. The applied force τ^* is then defined as :

$$\tau^*_i = \tau_i + \tau^*_{i,SMA} \tag{6.9}$$

and its application can be represented in the following scheme :

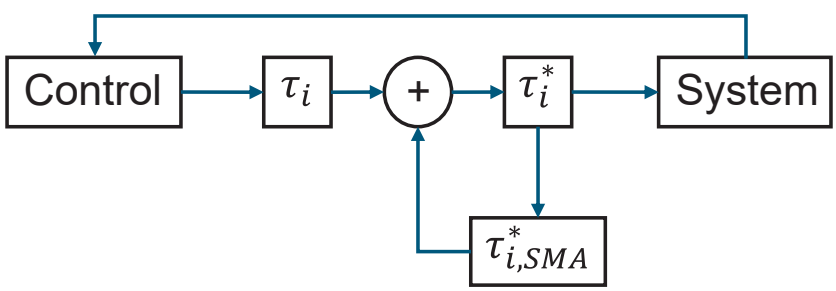

Figure 6.10 Control scheme, the SMA of the applied force is reintroduced in the controller before being applied to the system to reduce steady-state errors.

In the end, the value of F_i is determined by the capacity of the actuators and tol_i is a manually defined parameter that can be understood as the transition region between SMC and PD control. As for the value of v_{max}, it is derived from an optimization process that aims at an optimal flight of the robot, considering net weight (weight minus buoyancy), damping effects, and power consumption for its exploration mission.

6.8 Use case : cave exploration as an artistic manifestation

6.8.1 The cave

As a use case to demonstrate the adaptability of the parametric design pipeline, we aim to fly inside a newly discovered urban cave located in Montreal. This cave is unique for its glaciotectonic geological features (Pierre-Etienne, 2018). The rock and fossils date back to an early ocean over 450 million years old. Fifteen thousand years ago, gigantic glaciers caused the widening of cracks in the limestone rock, creating the cave. Initially 35 meters long (the “Public Part”), a much deeper section of 275 meters was discovered in 2017 (Cloutier & Ménard, 2017; Forget & Faure, 2019). This new section consists of a cavity (“Radiesthesia Part”) and access to a water level (“Aquatic Part”). The temperature remains constant at 12 °C, while the water temperature ranges between 6 °C and 9 °C, necessitating the use of wetsuits and safety harnesses through several technical passages, where wedges and ladders are installed at different levels of the cave.

The exploration zone for the CAVERNAUTE is the “Aquatic Part ”, which constitutes the majority of the cave in terms of area. It is a long, flooded corridor about 0.8 to 2.5 meters wide, as shown in Fig. 6.11. The ceiling starts at less than 5 meters high and gradually slopes down to the water level. Movement within that part of the cave requires small kayaks, as there are no areas to progress on foot. Getting onboard the kayak is quite technical from a narrow balcony, where one descends along a ladder directly to the kayak. Along the way in the cave, turning around with the kayak is only possible in three places, necessitating backward movement and leaning on the walls when the passage is too narrow for the paddles.

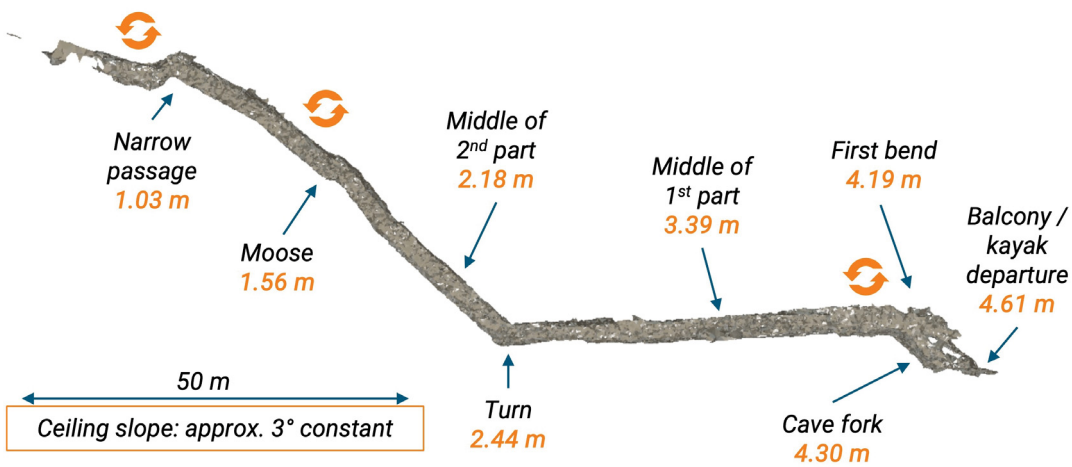

Figure 6.11 Saint-Léonard "Aquatic part". The three places where U-turns are possible are indicated by circular arrows. Ceiling heights are indicated at various checkpoints. The water level varies according to season and weather.

Among all the input parameters presented in Table 6.1, three are related to geometry and determined by the constraints of the cave dimensions. Figure 6.12 details these three critical geometric data points. The first is the height of the unfolded CAVERNAUTE, which is bounded by the minimum vertical clearance for the airship to fly. This height was measured with a laser rangefinder. The other two parameters are the height and diameter of the folded CAVERNAUTE, both bounded by the narrowest point of passage to reach the exploration area. This critical point here is a thin corridor between the "Public Part" and the large cavity of the "Radiesthesia Part". The narrowing was measured using a specially designed tool shown in Fig. 6.12. It is a cylinder whose diameter and height are adjustable to be able to test the footprint of the folded CAVERNAUTE.

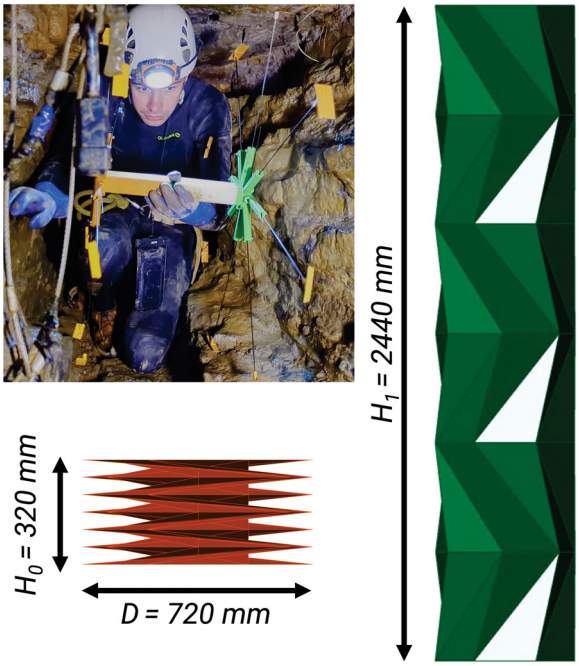

Figure 6.12 Geometric dimensions constrained by the cave. The folded height H_0 and diameter D of the CAVERNAUTE are dictated by the narrow passage to the exploration zone. The photo shows the tool used to measure and validate the ability to pass with the CAVERNAUTE.

6.8.2 Mapping the cave

The mapping of the cave was made by our team in three sessions of about 5 hours each on different dates, using a custom handheld device with two or three LiDAR devices, an inertial measurement unit and a microcomputer running Linux with ROS.

In the mapping process, a team of two traverses through the different sections of the cave. One holding the device and suitcase, and the other as a support to help when climbing or descending through certain sections of the cave. In the “Aquatic Part”, the person holding the device goes inside the kayak and the support member goes swimming and pulling/pushing the kayak. This is done to secure the smooth motion of the kayak and to avoid the occlusion of the LiDARs.

Three different LiDARs were used : an Ouster OS0 [2], a Velodyne VLP-32MR LiDAR, and a RoboSense Helios LiDAR-16 [3], working together with a VectorNav's VN-100 [4]. The devices were connected to an NVIDIA Orin Nano computer with Ubuntu 20, leveraging ROS and NorLab's ICP mapper [5].

After obtaining the point clouds, the different sections are stitched together to achieve a single combined point cloud of the cave, which we use as a reference to plan the flight of CAVERNAUTE.

Figure 6.13 On top, a photo of the device with two LiDARs. Bottom left, is an in-cavern photo of the device with three LiDARs, and the bottom right is in use with remote SSH access with a rugged tablet.

[2] https://ouster.com/products/hardware/os0-lidar-sensor

[3] https://www.robosense.ai/en/rslidar/RS-Helios

[4] https://www.vectornav.com/products/detail/vn-100

[5] https://github.com/norlab-ulaval/norlab_icp_mapper

Thanks to our preliminary mapping work, we can determine the flight zone for the CAVERNAUTE and thus the maximum height of the module to design as well as the narrowest section to transport the robotic system and its equipment. Figure 6.14 shows the 2D model of the envelope in the “aquatic” zone.

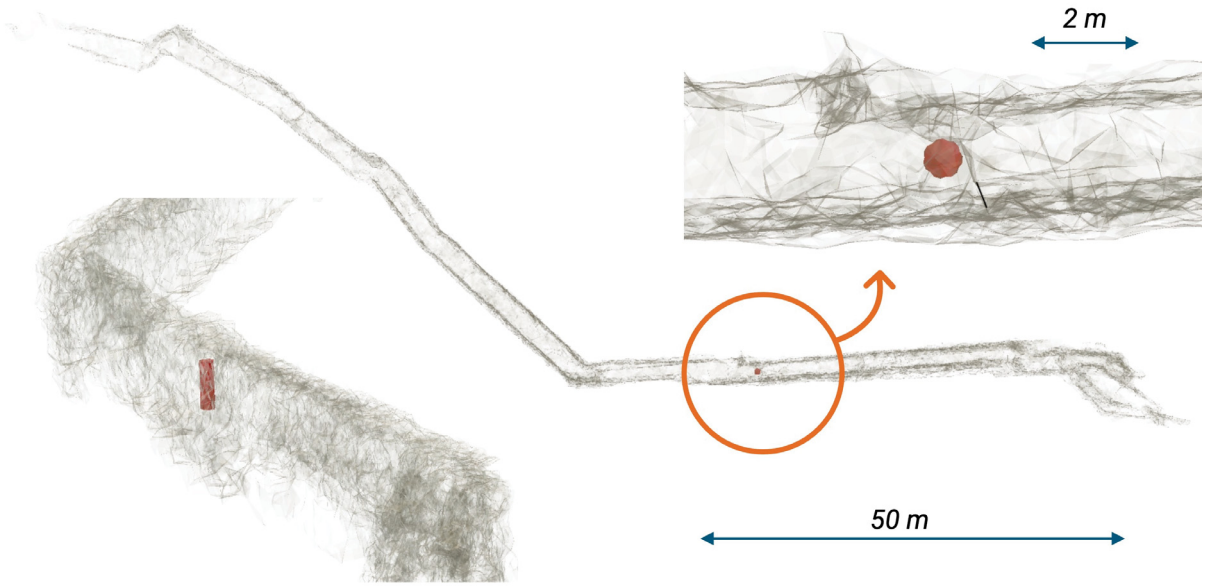

Figure 6.14 CAVERNAUTE footprint in the exploration area mapped by the team

6.8.3 Applied parametric design

The deployment of the CAVERNAUTE has an artistic scope that has imposed several choices that can sometimes go against technical performance, but which has its importance for public visibility. A visual specification therefore brings several criteria subject to aesthetics. The first major criterion is the shape of the airship. A flexible airship has a shape defined by the pressure of the internal gas. This gives it an ovoid shape. Here, the adoption of a rigid structure gives the choice to create a non-conventional shape for the airship. Always in an artistic approach, it was decided to adopt a polyhedral shape : sharp edges that break the usual curves for a blimp to catch the interest of the public, who do not expect to see such a pure geometric shape able to float.

The second criterion is that the airship must fly vertically, again with the aim of surprising. The impact on performance is the increase in drag on the axes of movement in the horizontal plane.

Next, the challenging flight environment imposes several constraints. The airship must be able to withstand impacts with the narrow walls of the cave. These same walls must not be damaged in the interest of conservation : the propellers will be protected by guards, and the sharp edges equipped with shock-absorbing structures. The speed of characterization of the structures was set at 2 m/s according to the maximum speeds observed in the literature for an indoor aerial system (Nitta, Inai, Matsumura, Ishida, Onai & Nishitani, 2017; Tao, 2020). As the exploration area is located above water, the airship must be able to land on water in case of a problem without the electronics being submerged in water.

Finally, due to the difficulty of the mission, all structural elements must be replaceable in case of breakage during the planned 2-week deployment or to evolve the shape configuration. For the airship's edges, 2 mm carbon fiber tubes with a thickness of 0.5 mm were selected. These tubes have a tensile strength of 1200 MPa and a flexural strength of 615 MPa, with a linear density of m = 3.76 g/m.

The design window for the three parameters to optimize are n = $[\![3; 10]\!]$, m = $[\![2; 10]\!]$ and λ = $[0.50; 0.90]$. The requirement to have λ less than 0.9 imposes the twisting of the structure so that it appears aesthetically more complex than a simple extruded polygon ($\lambda = 1$).This generates a total of 2880 configurations for investigation.

Figure 6.15 shows the map of these 2882 configurations based on the three parameters. The white area shows the floatability boundary. Naturally, the maximum payload is obtained for the largest n, m and λ because we are geometrically getting closer to a cylinder, which maximizes the volume and therefore the payload. On the other hand, the geometric criteria drawn from the cavern eliminate numerous configurations. The valid configurations are therefore very close to the payload limits (white area). We also notice that m < 5 because the unfolded height affects the number of possible Kresling segments. We see that the number of sides maximizes the volume but has an impact on the weight of the exoskeleton, which eliminates configurations.

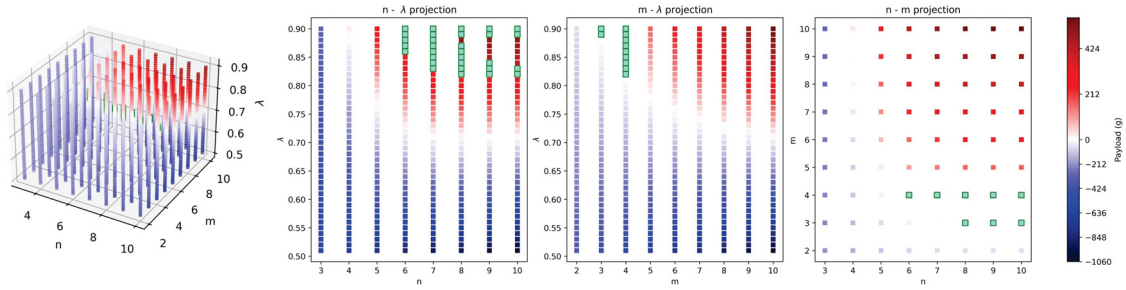

Figure 6.15 Design window map and projection. Configurations that float (Payload > 0) and respect the geometric constraints of the cavern are highlighted in green.

Figure 6.16 shows the selection of the 30 configurations that validate the criterion payload > 0 (the green squares highlighted in Fig. 6.15). The weight distribution is displayed. On average, the weight of the envelope represents more than 50% of the total weight. Therefore, the choice of the envelope material is crucial. The exoskeleton with carbon tubes and joints represents a total of 33%. Finally, mechatronics occupies less than 13%. This is the major drawback of a rigid airship : choosing to increase the resilience of the aerial system at the costs of the carrying capacity for sensors, the battery, etc.

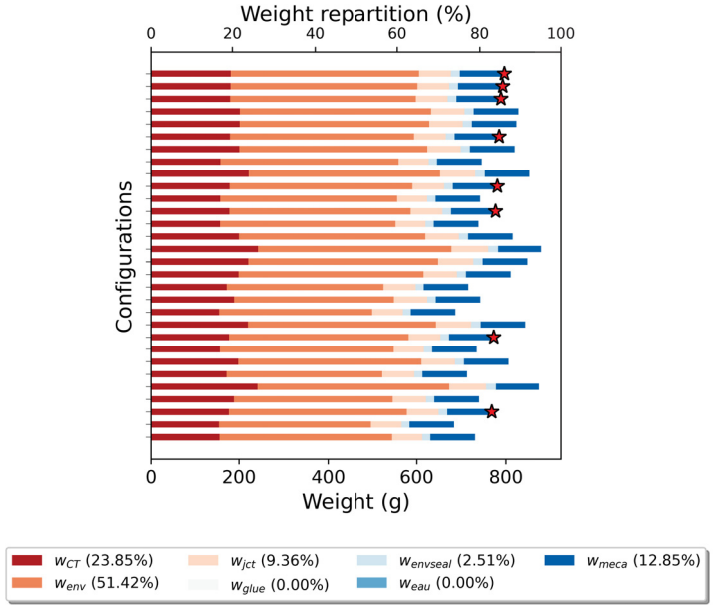

Figure 6.16 Display of the weight distribution for the 30 realistic configurations. The red stars represent the best choice of the pair n, m. Here, respectively, n = 7 and m = 4.

To select the optimal configuration for CAVERNAUTE, it should be noted that the λ parameter influences the twisting of the airship. This means that we can find a folding angle alpha for any lower λ. Thus, we are looking for the pair (n, m) with the highest number of occurrences among the valid configurations. Here, n = 7 and m = 4 is the optimal combination with λ = [0.83 ; 0.9]. The extra-payload is between 1.1 g and 68 g. Concretely, we can adjust the extra-payload by twisting the λ = 0.9 version of CAVERNAUTE. Table 6.2 summarizes the data for the selected configuration. This ability to adjust the extra-payload can be very useful for precisely balancing the airship at the time of deployment. There is a risk of having water projections, sensor changes or exoskeleton configuration changes. Thus, this flexibility is a feature of CAVERNAUTE that facilitates the use of the aircraft. Figure 6.17 shows the geometry and the mechatronic component position on the optimized shape n = 7, m = 4 and λ = 0.9

Tableau 6.2 Extra-payload, height and bending angle relative to λ = 0.9 for the selected configurations.

λ	**Extra-payload (g)**	**Height (mm)**	α_0 **(deg)**
0.83	1.1	2265	22
0.84	8.6	2288	21
0.85	25.1	2325	19
0.86	32.3	2346	18
0.87	39.3	2366	17
0.88	55	2400	15
0.89	61.5	2418	14
0.9	68	2436	13

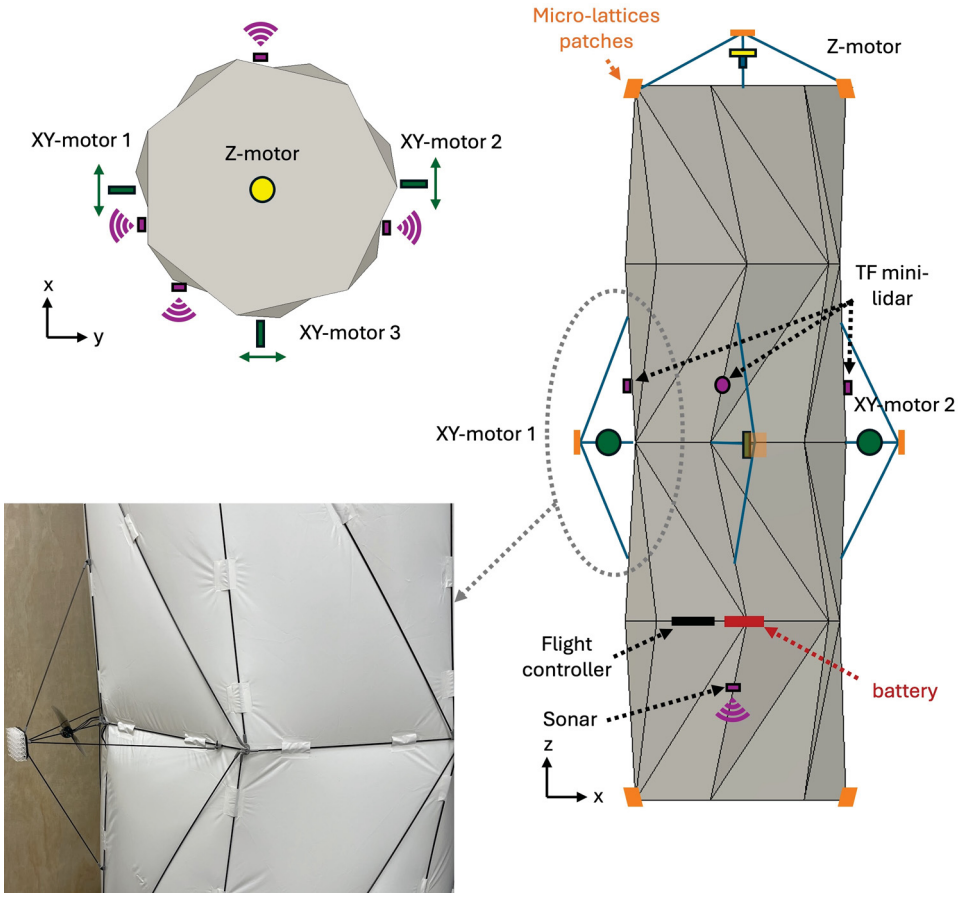

Figure 6.17 Schematic of all CAVERNAUTE's design and motor position. The photo at bottom left shows the actual assembly of the side-mounted motor with carbon tube structure and micro-lattice patch.

6.8.4 Benefits of origami properties for an indoor airship

The use of an exoskeleton as a structure stiffening the envelope of an airship is new at this scale of airship and brings a succession of unprecedented advantages compared to large rigid airships and small blimps (soft envelope).

The exoskeleton provides resistance to abrasion because it is external. The thin envelope is protected from the majority of contacts due to its concave shape.

This bistability presented in Section 6.6.1 has multiple interests. First, during transport, there are no constraints applied to the exoskeleton to keep it folded. Then, during inflation, each of the 4 segments that constitute the CAVERNAUTE can be filled and unfolded one after the other. This process limits air contamination in the helium-filled envelope. Once operational, in case of puncture of the envelope, the aerial system will be little affected by the damage. Indeed, unlike a soft blimp, the shape of the airship does not need to be maintained by the internal pressure of the carrier gas. So *(1)* the airship can be inflated to a pressure close to atmospheric pressure and *(2)* if the airship is inflated to a higher pressure, in case of a puncture, the pressure will balance to atmospheric pressure and the leak will be almost stopped.

Derived from bistability and with λ close to 1 to maximize energy potential (Fig. 6.8), another property of the Kresling pattern is its excellent shock resilience (Yasuuda, Gopalarethinam, Kunimine, Tachi & Yang, 2019; O'Neil, Salviato & Yang, 2023). Here, in addition to the high-performance absorption capabilities of micro-lattices, the exoskeleton of the CAVERNAUTE provides a second level of absorption. Thanks to the rigid exoskeleton, the inertia of the heaviest objects that make up the airship such as the battery, sensors, does not affect the envelope. A soft airship risks tears because the masses are suspended with a gondola. With the CAVERNAUTE, the loads are transmitted inside the exoskeleton and are isolated from the fragile envelope.

Finally, the volume expansion ratio is :

$$\frac{V_{deployed}}{V_{folded}} = \frac{0.825}{0.0417}[m^3] = 19.78 \tag{6.10}$$

This very high ratio allows the CAVERNAUTE to fit in a bag to get through complex passages in caving to access exploration areas. Benefiting from rigidity is therefore not a problem for remote scientific missions with this compactness.

6.8.5 Controller Optimization

In order to roughly estimate the energy required for the CAVERNAUTE's mission, we multiply the total power required by the time to travel the distance of the cave's "Aquatic Part". We can then optimize the controller's parameters with fewer degrees of freedom, namely : the global path error, the maximum velocity and the time to complete its journey. Beforehand, the consumption of the Cavernaute is estimated component by component from measurements or using the manufacturers datasheets.

We are using a Hosim RC Cars Battery of 7.4 V with 2Ah, thus delivering a capacity of 14.8 Wh used to power 4 Benewake Micro TFmini I2C LiDARs, one FPV Caddx Baby Ratel 2 camera, the ESP32 controller development kit and a small SRF02 I2c sonar. The power consumption of each device is presented in Table 6.3. Figure 6.18 shows the schematic of all mechatronic components.

Tableau 6.3 Power consumption for each of the devices used for CAVERNAUTE

Part	**Power Consumption [W]**	**Quantity**	**Total Power [W]**
TFmini LiDARs	0.7 [6]	4	2.8
Sonar	0.015	1	0.015
Video Transmitter	0.5	1	0.5
Camera	<1.2	1	<1.2
		Total	<4.515

The motors selected for our design are EMAX RS1606 3300 KV that we characterized using a TytoRobotics Series 1520 Thrust Stand [7]. We ended up with a quadratic regression between the force (in Newtons) and the power (in Watts) for the motors as :

$$P = 3.347F^2 - 25.857F + 1.69 \tag{6.11}$$

[6] We measured 0.25W when pulling data from the LiDARs at 10Hz, but we kept the datasheet's value to be conservative.

[7] https://www.tytorobotics.com/pages/series-1520

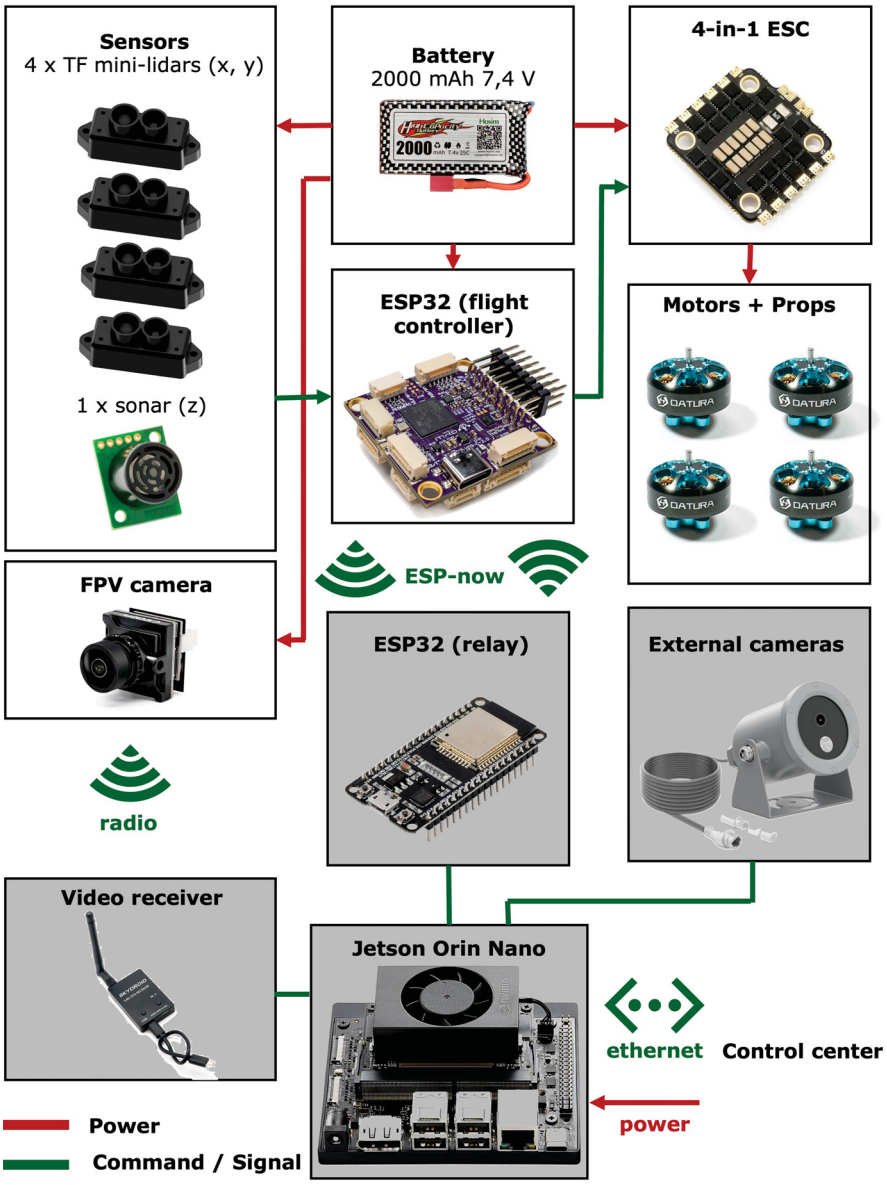

Figure 6.18 Schematic of all CAVERNAUTE's mechatronic : components with gray backgrounds are on the ground. The external camera is only for retransmitting the artistic installation.

By design, we decide on having a slight heavier-than-air prototype. This is a common design strategy to avoid fly-aways, however, in our case, the rational is rather to protect the envelop from the ceiling's stalactites, plus our design can float in the cave's water without harm (see Fig.6.17).

We consider the net-weight (weight minus buoyancy) is approximately 0.02 kgf, which means a consumption of 6.9 Watts with a single (Z-oriented) motor.

For translation motion, we need to consider damping effects, which for an airship, even at low velocity, consists in the aerodynamic drag. We approximate the cross-section of the CAVERNAUTE as a circle of area equal to 0.41 m^2, leading to a drag coefficient of about 1.2 (Bruschi, Tsang, Nishioka & Wang, 2003) at slow velocity (and low Reynolds numbers). The air inside the cavern is of the same composition and density as atmospheric air at 12 °C : 1.231 kg/m^3. The dampening force is calculated as :

$$F_D = \frac{1}{2} C_D \rho v^2 A \tag{6.12}$$

We integrate the dampening force to maintain the cruising speed, and estimate the power as :

$$P = 3.347 \left(\frac{1}{2} C_D \rho v^2 A \right)^2 - 25.857 \left(\frac{1}{2} C_D \rho v^2 A \right) + 1.69 \tag{6.13}$$

With a total electronic consumption equal to 11.4 W in hovering mode (sensors plus Z-motor), and by setting the two motors for the forward direction at cruising speed, the relation between velocity and power budget to travel 300 meters inside the cave (conservative distance) is illustrated in Fig. 6.19 for various cruising velocities.

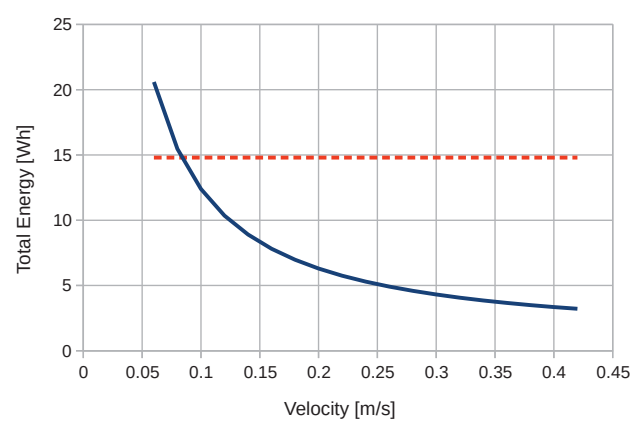

Figure 6.19 Relation between flight velocity and estimated total energy consumption (in blue). The total available energy provided by the battery is presented in the dashed red line.

From Fig. 6.19 we extract a minimum flying speed of 0.08 m/s, which corresponds to 62 minutes of flight. More efficient flights require higher speeds. Nevertheless, this first approximation does not consider the energy required to maintain the airship far from the cave's walls (Y-axis collision avoidance).

6.8.6 Simulation

To demonstrate our controller, we present a simple motion : starting from the ground up to maintain an altitude of 1 meter, then moving forward a distance of 2 meters at 0.15 m/s. This test is repeated under three conditions : one without the SMA term, and then with two with different duration (1 and 2 seconds) for the SMA term.

Our custom simulation stack solves the dynamics equations in Python at 500 Hz, and integrate the different control modules using ROS, with each node running at a realistic frequency of 40 Hz. We also used Gazebo to visualize the motion, but Gazebo's solver was not used.

We consider the added mass terms and drag for the forward direction X and the altitude Z. For Z, the approximated drag coefficient of the flat circular face is approximately 0.9, and the added mass was calculated as the contribution of the added mass of rectangular sections in rotation, following Korotkin (2009), equal to 0.29 kg. For X, the added mass obtained was equal to 1.165 kg, and the drag parameters are already presented in Section 6.8.5.

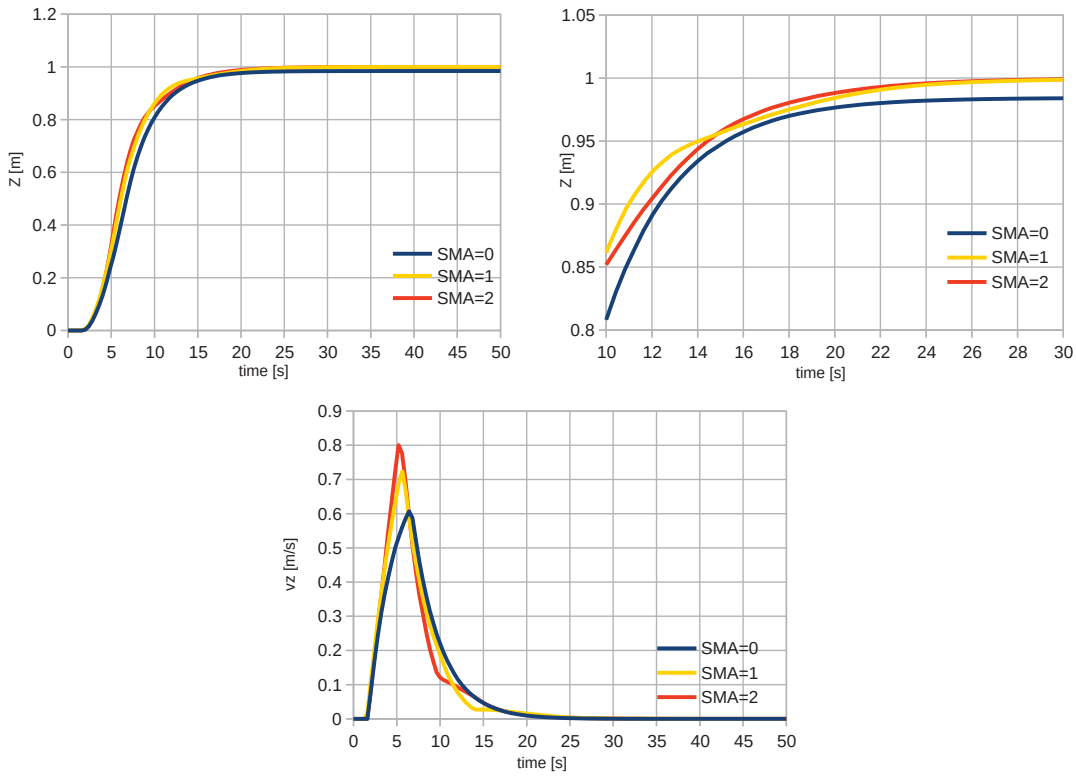

Figure 6.20 Motion in the Z-axis. The top graphs present the position, for the different SMA durations. The bottom graph presents the velocity achieved (v_z).

We set $F_x = F_z = 1.25$ N to consider the maximum actuation of the motors, $v_{x,max} = 0.15$ m/s as the selected cruising velocity, $v_{z,max} = 1$ m/s to allow for faster motion in the Z axis since we need to achieve and maintain the desired height quickly, and using $tol_x = tol_z = 0.1$ as the threshold between SMC and PD control.

Figure 6.20 presents the first 50 seconds of the complete motion in the Z axis, as the Cavernaute achieves its 1 meter target altitude. The SMA terms are correcting the small steady state error.

In Fig. 6.21 and 6.22, we observe that all the controllers were capable to achieve the desired position of 2 m. Nevertheless, there is a slight difference in the velocity, where both SMA durations were able to achieve a cruising motion of 1.5 m/s. We can attribute this difference to the small drag force produced when moving at the slow speed of 0.15 m/s.

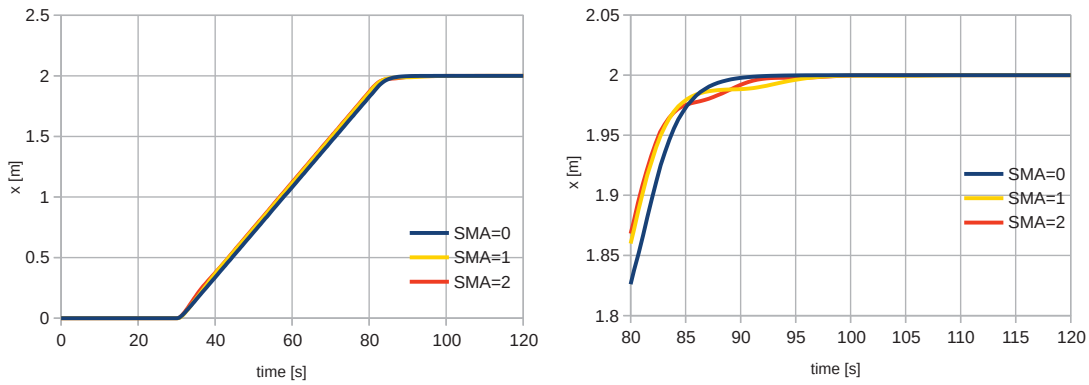

Figure 6.21 Motion in the X-axis. The two graphs present the position to achieve the desired position of 2 m, and the effect of the SMA terms.

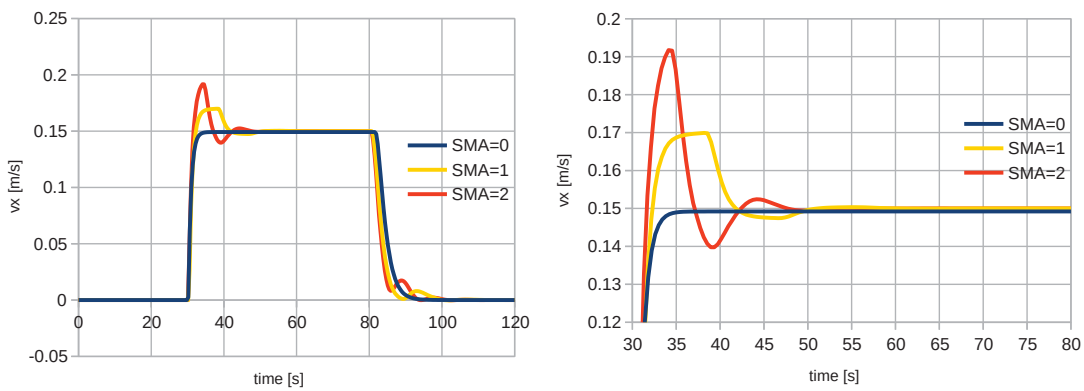

Figure 6.22 Motion in the X-axis. The two graphs present the velocity (vx) while moving towards the position of 2 m, presenting the effect of the SMA terms.

In all the cases, the simplicity of the methodology to tune the motions based on the speed requirements, maximum desired force and desired tolerance was deemed satisfactory to be applied in our robot. And, while it might not be mandatory to include the SMA term for our conditions, we could observe that its inclusion in the controller made it possible to precisely correct the robot position and velocity to the desired requirements in the presence of a force (net-weight) and damping effects.

6.8.7 Deployement

The final CAVERNAUTE design was tested over a two-week deployment in the St-Léonard cave, Montréal, Canada. The folded structure was first maneuvered through a narrow access passage to reach the exploration area (Fig.6.23 - A). An initial survey, conducted during reconnaissance visits (Fig. 6.12), confirmed the feasibility of this critical deployment step.

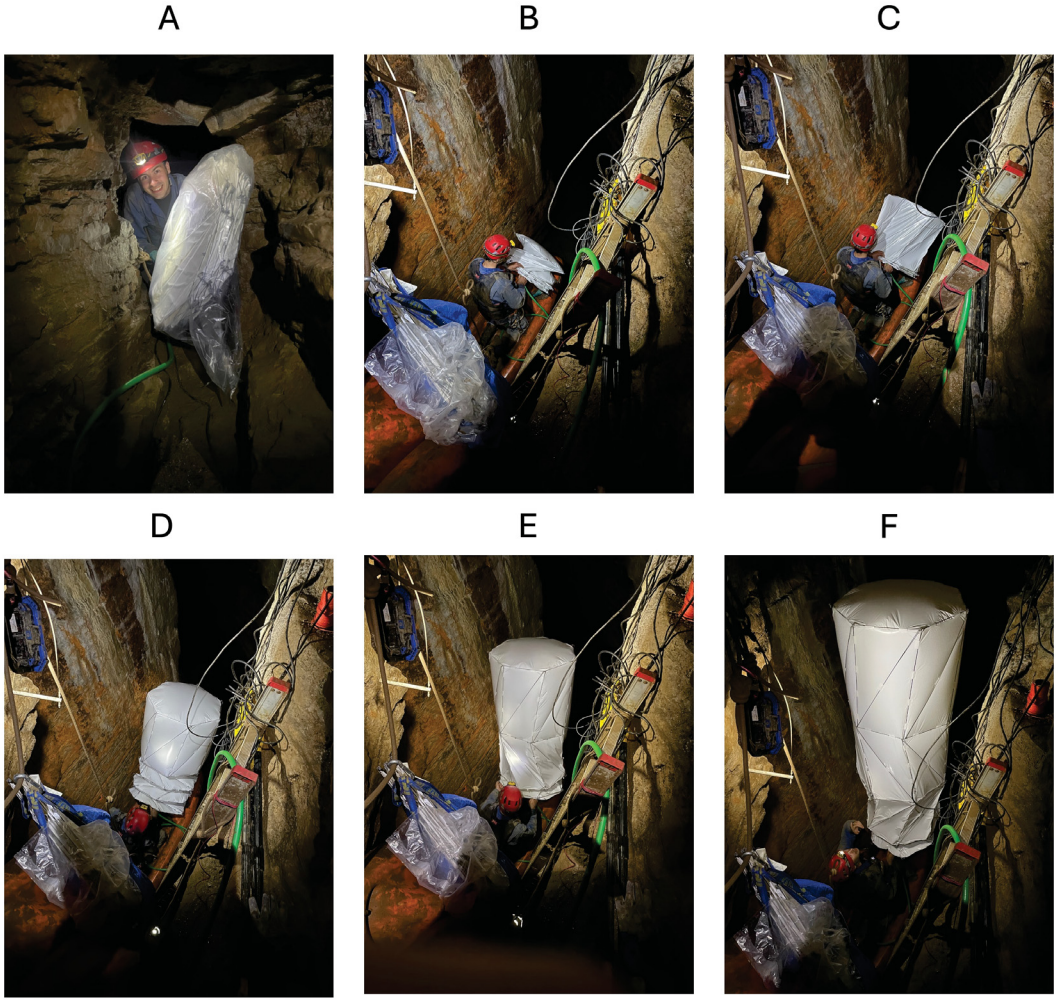

Figure 6.23 Steps of the CAVERNAUTE deployment in the St-Léonard cave. After passing through the first narrow section (A), the folded CAVERNAUTE is connected to the hose (B) and filled with helium. The four Kresling cells unfold progressively during inflation (C-D-E-F).

The inflation area was located at the beginning of the aquatic section, with helium transported via a 90-meter hose. Two operators were required : one managed the filling process, while the other controlled the helium valve from outside. Inflation was performed from a kayak to fully utilize the available height beneath the cave ceiling. Leveraging the bistability of the Kresling pattern, inflation was conducted section by section, allowing precise control and alignment to prevent the envelope from contacting the cave walls. Figure 6.23 illustrates each inflation stage, showing the sequential unfolding of the four CAVERNAUTE cells. Helium loss, measured before the mission at 4.24 g/h using a load cell (Fig. 6.24), was dynamically compensated by the controller's weight management system (Section 6.8.5), ensuring the CAVERNAUTE remained above the water throughout the deployment.

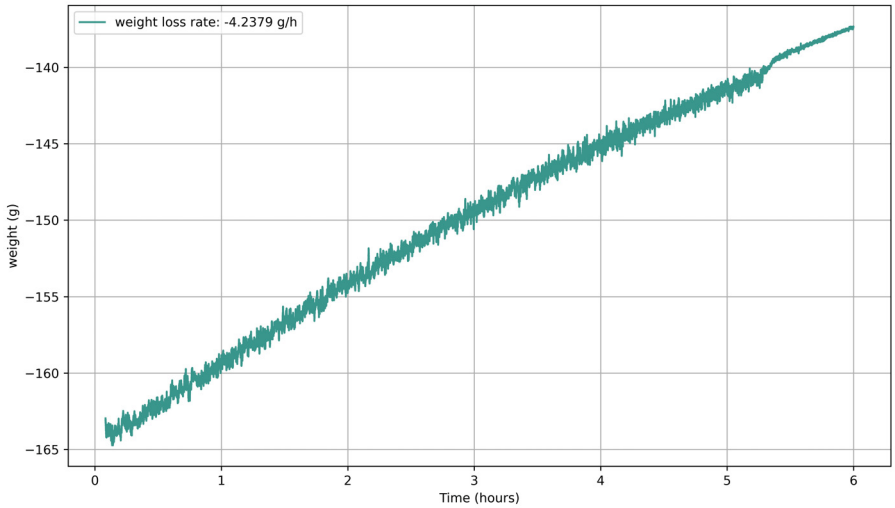

Figure 6.24 Loss-rate measurements

Once inflated, the mechatronics (motors, sensors, battery) were attached to the exoskeleton using press-fit junctions on pre-assembled, 3D-printed mounts, allowing easy setup and reconfiguration according to mission requirements.

The CAVERNAUTE was powered by a 2000 mAh battery, achieving two flight hours on two consecutive days. For context, this battery typically powers small 250 g quadcopters for about ten minutes of flight. Figure 6.25 shows the CAVERNAUTE navigating above the water between the cave walls.

Figure 6.25 CAVERNAUTE flight above water at St-Léonard aquatic section. The two side motor pods equipped with their micro-lattices patches can be seen.

6.9 Conclusion

In conclusion, we have developed a small rigid airship with unique properties, leveraging origami and the Kresling pattern to stiffen the envelope while enabling access to narrow areas through folding capability. To optimize the intricate considerations of the airship, we have implemented a design, manufacturing, and assembly pipeline that integrates the constraints of the specifications, allowing for flexible and easy testing of new configurations. This approach has identified areas for improvement, particularly the need to lighten the envelope, which currently represents more than half of the weight—a key focus for future research.

Our work highlights several features enabled by combining origami with airship design, offering significant resilience from multiple perspectives. For robotic deployment in challenging

environments, these features collectively reduce the risk of catastrophic failure that could compromise the mission.

The impact of this research extends to various applications such as structure inspection, security, and search and rescue operations. The ability to navigate confined spaces, coupled with extended flight duration and robust design, positions this airship as a valuable tool in these fields.

Future developments could further exploit these features, such as actuating the Kresling pattern to allow digital control of the extra-payload, thereby providing more precise control over buoyancy and enhancing the airship's adaptability and functionality in diverse scenarios.

Supplementary information

The data that support the findings of this study are available from the corresponding author [LC], upon reasonable request.

Acknowledgements

The authors would like to thank Raphael Desbiens, Guillaume Ricard, and Brendan Patience for their significant support in the prototyping, development and implementation of the CAVERNAUTE mechatronics.

The authors acknowledge the financial support of the NSERC CREATE UTILI program [8], and the FRQNT Team grant (#283381).

Conflict of interest

The authors declare that they have no conflict of interest.

[8] https ://carleton.ca/utili/

Authors contributions

L.C. was the project integrator for the airship aspects. He designed, manufactured and assembled the structure and mechanical components. He built the design pipeline described in this article. He wrote all the corresponding sections, the literature review and the conclusion. J.E.S.G. designed and wrote all the sections concerning airship navigation, control, and cave mapping. Both L.C. and J.E.S.G did the manual mapping and measurements of the cave as described in section 6.8.1. D.SO. provided the original concept for this work and participate to both the mechatronic and geometric designs. D.SO. and I.T. revised the manuscript and supervised the work.

CONCLUSION ET RECOMMANDATIONS

En définitive, la fabrication additive ouvre de nouvelles voies pour alléger des structures d'aérostats. Les moyens de production utilisant des résines photosensibles procurent une excellente résolution pour la réalisation de micro-treillis polymères. Elles permettent la production de pièces d'ingénierie à haute-valeur ajoutée à des faibles coûts comparés aux autres moyens de production conventionnels ou additifs usuellement utilisés en industrie.

En un premier lieu, une étude croisée a été menée pour caractériser les machines de fabrication additives photosensibles disponibles à l'ÉTS. Pour ce faire, une caractérisation expérimentale de champ plein (DIC) du comportement des micro-treillis sous chargement de traction quasi-statique a été mise en place. À l'issue de ces tests, nous avons pu continuer avec la technologie de fabrication additive la plus pertinente pour les besoins de fabrication du projet : la MSLA grâce à la souplesse d'utilisation de matériaux variés, son excellente isotropie ainsi que sa rapidité d'impression. Nous bénéficions par la même occasion d'un excellent rapport performance-prix en raison de sa disponibilité grand public.

Dans un second temps, nous avons ajusté les requis de la conception de dirigeable avec les conclusions des premières expériences exploratoires pour proposer une architecture hybride mêlant un exosquelette et des absorbeurs d'impacts exigés par le vol en espace intérieur. Ces patchs absorbants ont fait l'objet d'une étude approfondie pour choisir la meilleure configuration de motifs, compacité et matériau pour son intégration sur un dirigeable. Pour mener à bien cette caractérisation, nous avons créé notre propre moyen d'essai pour petits aéronefs d'intérieur : un banc de test de collision permettant des impacts libérés reproduisant l'utilisation finale de l'aéronef. Grâce à cet équipement, nous avons pu classer les configurations et proposer une cartographie de compatibilité des micro-treillis rigides et flexibles pour l'allègement avancé de structures.

Pour finir, nous avons conçu un dirigeable rigide mais pliant grâce à l'élaboration d'un exosquelette ultraléger pour dirigeable. L'objectif est en effet d'être en mesure d'explorer une caverne naturelle mais très étroite, imposant un design compact et résistant. La géométrie issue de l'étude des origamis a été adaptée pour être en mesure d'être fabriquée et de voler. L'emploi de cet exosquelette procure de nouvelles possibilités d'utilisation des dirigeables avec une meilleure robustesse aux impacts ainsi qu'une fiabilité améliorée. Les micro-treillis ont été intégrés à cette nouvelle architecture pour bénéficier de leurs propriétés d'absorption spécifique unique. Le processus de conception a été automatisé pour apporter toute la flexibilité de créer un dirigeable pour tout type d'espaces étroits.

Ces contributions originales ont le potentiel de créer des opportunités industrielles variées, tant pour l'emploi de dirigeable que des structures en micro-treillis.

Les dirigeables de petite taille peuvent s'insérer dans les mêmes cas d'utilisation que les drones multicoptères en proposant une autonomie accrue et un emploi plus sécuritaire pour les personnes évoluant autour l'aérostat. Les travaux visant à améliorer le contrôle de ces engins apportent une démocratisation de l'usage de ce type de drone. En ajoutant une coquille rigide et un renforcement de ses parois, les drones aérostats d'intérieur sont aptes à créer une gamme d'aéronefs pour la téléopération robotique en conditions difficiles. Les applications sont nombreuses comme le spatial (projets de sondes dirigeables pour Venus ou Mars), l'exploration (spéléologie, archéologie) et la surveillance (sites industriels, réserves naturelles) (Kantor, Wettergreen, Ostrowski & Singh, 2001; Nitta *et al.*, 2017).

En raison de leur dynamique bien particulière et de leur comportement, les dirigeables sont également des systèmes analogues aux comportements d'engin en faible gravité ou en apesanteur. Ils permettent ainsi de tester différents scénarios : expériences de rendez-vous orbitaux ou capture de satellite par un bras robotique (Sharf, Laumonier, Persson & Robert, 2008; Sharf

et al., 2013). Un exosquelette externe permet d'installer un grand nombre d'équipements sur toute la surface de l'enveloppe.

De façon plus générale, la fabrication de micro-treillis ultralégers s'applique aux domaines ayant besoin de pièces à haute valeur ajoutées dotées de caractéristiques aptes à être employées dans des conditions exigeantes où résistance mécanique et légèreté ne sont pas dissociables (aéronautique et spatial, biomédical). Dans un contexte de volonté de réduction des émissions liées au transport, ces travaux peuvent proposer de nouveaux cas d'utilisation de structures polymères allégées.

Déploiement du CAVERNAUTE au-dessus de la nappe phréatique de la Caverne St-Léonard (Montréal) - août 2024

RECOMMANDATIONS

En prenant du recul, plusieurs pistes d'exploration sont identifiées n'ayant pas été adressées ou explorées plus superficiellement dans le cadre de ces travaux.

Impression 3D non-planaire

En phase d'exploration sur les solutions de fabrication de structures ultralégères, l'idée d'utiliser l'impression non-planaire a été un temps explorée (Fig. 7.1). L'objectif était de créer une coquille rigide faite à partir de foam PLA (filament retenu pour les pièces ultralégères du CAVERNAUTE). Pour cela, nous avons étudié à travers un projet supervisé les bénéfices potentiels de la fabrication FDM non-planaire. Un des défis était de créer des trajectoires non-planaires pour une imprimante 3D conventionnelle 2.5 axes. Différentes approches sont possibles : spécialisées, et donc peu adaptables à des géométries variées, avec une génération de la trajectoire par un script spécialement conçu pour l'objet désiré. L'autre solution, plus ouverte, consiste à avoir une interface utilisateur flexible pour préparer une impression non-planaire dans un logiciel de tranchage conventionnel. Enfin, il existe également des approches hybrides en détournant l'usage de logiciels grand public comme Excel ou Rhino3D afin de générer le .GCODE non-planaire nécessaire à la machine. Pour notre étude, nous avons fait le choix de se concentrer sur une solution flexible grâce au logiciel Slic3r, solution de tranchage conventionnel auquel est ajouté un plugin communautaire de génération de couches non-planaires. Les résultats d'expériences préliminaires ont néanmoins montré une résistance mécanique (compression et flexion trois points) nettement inférieur aux pièces planaires. À notre sens, cette différence provient du manque d'adaptabilité des paramètres d'impression (extrusion, débit, etc.) en fonction de la génération de la trajectoire de l'extrudeur. Autre point notable, pour des raisons de dégagement de la zone de fabrication, les impressions étaient réalisées avec une buse plus longue qui change considérablement la qualité de la chauffe puis de l'extrusion du matériau.

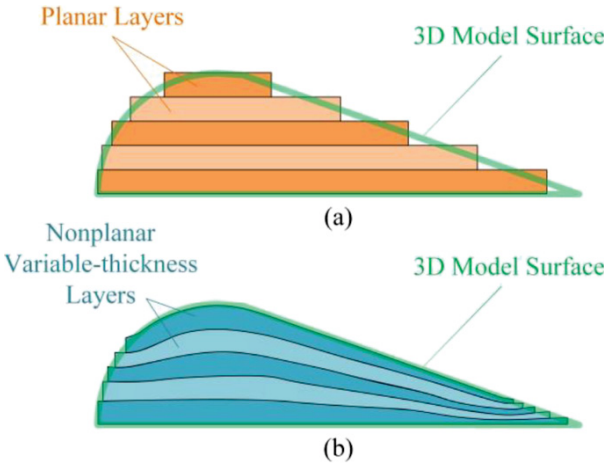

Figure 7.1 Illustration d'impression non-planaire par Nayyeri *et al.* (2022). Cette coupe montre une des stratégies d'impression non-planaire avec une adaptation dynamique de l'épaisseur de chaque couche.

Fabrication additive multi-matériaux M-MSLA

Avec les travaux de caractérisation des micro-treillis des Chapitres 3 et 5 ainsi que l'usage de notre méthodologie de classement, nous avons pu remarquer une amélioration potentielle envisageable des propriétés mécaniques des micro-treillis en exploitant davantage les propriétés de chaque matériau à notre disposition : certains ont d'excellentes propriétés de déformation, d'autres de rigidité, etc. Les cellules des micro-treillis sont sollicitées d'une telle façon qu'il serait intéressant de profiter des propriétés uniques de chaque polymère à notre disposition. Pour cela, nous devons offrir la possibilité de fabriquer des pièces multi-matériaux par fabrication additive. Il existe déjà des machines existantes mais très onéreuses. D'autres solutions impliquant des résines photosensibles présentent des lacunes techniques pour un emploi compatible avec la fabrication de micro-treillis. Nous avons eu l'idée d'un dispositif adaptable à la technologie MSLA qui utiliserait un bassin unique dans lequel deux matériaux (et théoriquement davantage) sont séparés par une paroi mobile équipée d'un racleur. Le concept est illustré Fig 7.2. Cette possibilité proposerait une flexibilité accrue aux concepteurs de micro-treillis pour améliorer ces

structures ultralégères. Ce concept a fait l'œuvre de deux stages supervisés pendant le doctorat pour travailler au prototypage d'un kit adapté à la MSLA Saturn S de Elegoo®.

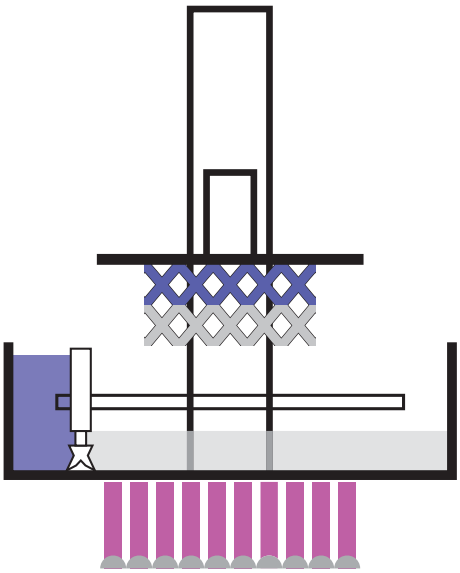

Figure 7.2 Illustration — Solution de multi-MSLA utilisant un racleur. La paroi sépare la deux résines (bleu et orange) au sein du même bassin et de la même zone d'impression. Cette configuration procure un encombrement limité et un impact limité sur la fabricabilité grâce à la stabilité de la zone d'impression (schématisation illustrée par Sebastián Zagal Rojas, stagiaire supervisé sur le projet).

Analyse des propriétés en fatigue des structures architecturées

Dans ce travail, les micro-treillis ont été évalués lors d'un impact unique ou d'une compression unique. Les échantillons rigides ont subi des déformations ou des bris irrémédiables. En revanche, la résine Tenacious a bien rempli son rôle d'absorption. Il serait pertinent, dans le cadre d'une utilisation sur un aéronef qui peut subir des chocs répétés, d'évaluer plus en détail les propriétés en fatigue. Les résines souples photosensibles sont souvent présentées comme des simili-TPU. En revanche, à l'inverse des thermoplastiques, les chaines polymériques sont beaucoup plus

courtes. La mobilité présente dans le matériau TPU n'y est qu'artificiellement copiée. Il en résulte un bien moins bonne capacité théorique à résister à la fatigue.

Caractérisation du banc d'impact pour petits aérostats

Le banc d'impact libéré conçu au Chapitre 5 doit être mieux caractériser pour évaluer ses performances, sa précision et son exactitude par rapport à des moyens conventionnels d'essai d'impact. Une tour de chute serait le dispositif le plus adapté pour réaliser cette comparaison. Elle procure les mêmes ordres de grandeur de vitesse.

ANNEXE I

MODÉLISATION D'UN DIRIGEABLE

1. Formulations

La modélisation des dirigeables ne peut pas s'appuyer sur les modélisations de configurations classiques en aéronautique. On ne peut pas l'assimiler à une voilure fixe. En effet, en ayant une masse volumique totale proche ou égale à l'air, certains phénomènes ne peuvent plus être négligés. Par exemple, les effets Coriolis sont à considérer.

1.1 Cinématique

La modélisation du dirigeable est établie à partir de celle d'un corps rigide à six degrés de liberté. Son orientation est définie par les angles d'Euler de lacet (ψ), tangage (γ) et roulis (ϕ). Une des représentations les plus répandues en aéronautique de la matrice de rotation (ψ, γ, ϕ) est fonction de ces angles :

$$R(\psi, \gamma, \phi) = R_x(\phi) R_y(\gamma) R_z(\psi) \tag{A I-1}$$

Avec :

$$R_x(\phi) = \begin{pmatrix} 1 & 0 & 0 \\ 0 & cos\phi & -sin\phi \\ 0 & sin\phi & cos\phi \end{pmatrix} \tag{A I-2}$$

$$R_y(\gamma) = \begin{pmatrix} cos\gamma & 0 & sin\gamma \\ 0 & 1 & 0 \\ -sin\gamma & 0 & cos\gamma \end{pmatrix} \tag{A I-3}$$

$$R_z(\psi) = \begin{pmatrix} cos\psi & -sin\psi & 0 \\ sin\psi & cos\psi & 0 \\ 0 & 0 & 1 \end{pmatrix} \tag{A I-4}$$

On définit la vitesse linéaire V et angulaire Ω dans le repère fixe inertiel :

$$V = \begin{pmatrix} u \\ v \\ w \end{pmatrix} \qquad \Omega = \begin{pmatrix} p \\ q \\ r \end{pmatrix} \tag{A I-5}$$

1.2 Dynamique

On peut lui prêter des ressemblances aux navires. T. Fossen a ainsi exprimé l'équation du mouvement (Newton-Euler) qui peut être adapté aux spécificités aérodynamiques du dirigeable (Thor I., 1994) :

$$\boxed{M\dot{V} = M_{RB}\dot{V_\omega} + C(V)V + \tau_s + D(\Omega)V_A + \tau_{sta} + \tau_p + M_d V} \tag{A I-6}$$

Avec (Meddahi, 2015) :

- $M = M_A + M_{RB}$ matrice de masse totale composée de la masse ajoutée M_A et de la masse du dirigeable M_{RB}

- T_C : le tenseur de Coriolis et centrifuge

$$T_C = C(V)V = \ldots$$

$$\ldots = \begin{pmatrix} 0_{3\times3} & -mSk(V + \Omega \times \overline{NG}) \\ -mSk(V + \Omega \times \overline{NG} & -Sk(I_N\Omega) - mSk(\overline{NG})V \end{pmatrix} V \tag{A I-7}$$

- τ_s : tenseur statique Le poids et la portance peuvent être exprimés tels que :

$$F_{gravity} = R^T \begin{pmatrix} 0 \\ 0 \\ mg \end{pmatrix} \tag{A I-8}$$

$$F_{lift} = -R^T \begin{pmatrix} 0 \\ 0 \\ \rho.Vol.g \end{pmatrix} \tag{A I-9}$$

avec ρ la masse volumique du gaz intérieur, Vol le volume du dirigeable et g l'accélération de la pesanteur. R^T est la transposée de la matrice de rotation issue de la description cinématique. Ainsi, le tenseur statique peut s'exprimer sous la forme :

$$\tau_s = \begin{pmatrix} F_{gravity} + F_{lift} \\ \overline{NG} \times F_{gravity} + \overline{NC} \times F_{lift} \end{pmatrix} \tag{A I-10}$$

- $\tau_a = M_{RB}\dot{V}_A + D(\Omega)V_A + \tau_{sta}$: tenseur aérodynamique lié à :
  - des termes stationnaires (distribution de la pression autour du corps, forces de frottement dues à la viscosité de l'air)
  - des termes non stationnaires (notion de masse ajoutée)

  Ces phénomènes étant préoccupants dans le cadre d'un dirigeable, une partie leur est dédiée, voir « EFFETS AÉRODYNAMIQUES »

1.3 Modélisation de la viscosité

Deux modèles proposent une description de la viscosité (Li, Nahon & Sharf, 2011) :

Modèle d'Allen : c'est un modèle continu, utile pour les applications de calcul numérique.

$$\frac{dF_N}{d\varepsilon} = (k_2 - k_1)\, q_0\, \frac{dS}{d\varepsilon}\, sin(2\alpha)\, cos\frac{\alpha}{2} + 2\, q_0\, R\, \eta\, C_{DC}\, sin^2\alpha \tag{A I-11}$$

Modèle d'Hopkins : c'est un modèle discontinu qui considère la crise de traînée à l'arrière du dirigeable due au décollement de la couche limite en ε_ν :

$$\frac{dF_N}{d\varepsilon} = \begin{cases} 2(k_2 - k_1)q_0\alpha\frac{dS}{d\varepsilon} \text{ si } 0 \leq \varepsilon \leq \varepsilon_\nu \\ 2q_0R\eta C_{DC}\alpha^2 \text{ si } 0 \leq \varepsilon_\nu \leq L_a \end{cases} \tag{A I-12}$$

avec : $\varepsilon_\nu = 0.378\ L_a + 0.527\ \varepsilon_1$

2. Effets aérodynamiques

Comme vu précédemment, le comportement du dirigeable dépend de l'aérostatique (dû au gaz) et de l'aérodynamique. Cependant, l'aérostatique est assez prévisible et facile à calculer donc les enjeux se concentrent sur les effets aérodynamiques.

2.1 Notions de masse ajoutée

Préambule : La masse ajoutée est un phénomène aérodynamique non stationnaire qui rend compte du déplacement d'un volume de fluide. (Pham, 1977)

D'après la 2ème loi de Newton, une force F appliquée à un corps de masse M communique une accélération a telle que :

$$\vec{F} = M\vec{\Gamma} \tag{A I-13}$$

Cette loi suppose que le corps est dans le vide et elle s'applique approximativement s'il se trouve dans un fluide dont la masse volumique est faible par comparaison avec sa propre masse volumique. Ce n'est pas le cas pour un dirigeable dans l'air. La force est partiellement utilisée pour communiquer une accélération aux particules fluides :

$$\vec{F} = M\vec{\Gamma} + \Delta\vec{F} \tag{A I-14}$$

En écoulement irrotationnel, les équations deviennent linéaires. Si, de plus, on néglige la viscosité (fluide parfait), la correction est proportionnelle à l'accélération du corps, le coefficient de proportionnalité M_A étant défini comme la masse ajoutée du corps :

$$\vec{F} = (M + M_A)\vec{\Gamma} \tag{A I-15}$$

Cette masse ajoutée est proportionnelle à la masse volumique ρ du fluide, le coefficient de proportionnalité étant un volume. On exprime celui-ci comme le produit d'un volume de référence V, qui est souvent le volume occupé par le corps, multiplié par un coefficient de masse ajoutée k :

$$M_A = k\ \rho\ V \tag{A I-16}$$

Pour un corps de forme irrégulière, la matrice de masse ajoutée peut être obtenue à l'aide d'approches numériques (Li *et al.*, 2011). En particulier, les résultats pour les ellipsoïdes ont été couramment utilisés pour évaluer les matrices de masse ajoutée des coques des dirigeables. Les facteurs de masse ajoutée k_1, k_2 et k' sont tracés à la Figure I-1 comme fonctions de la finesse du dirigeable définie par D_m/L_a.

Dans le cas d'un sillage tourbillonnant et en cherchant à considérer la viscosité de l'air, les coefficients peuvent être déterminés par l'expérience.

Modélisation par élément de frontière (BEM) : Au cas où l'on ne se trouverait pas en présence d'une forme conventionnelle, une approche numérique de la question permet également de déterminer les phénomènes de masse ajoutée (Brèches, 2015).

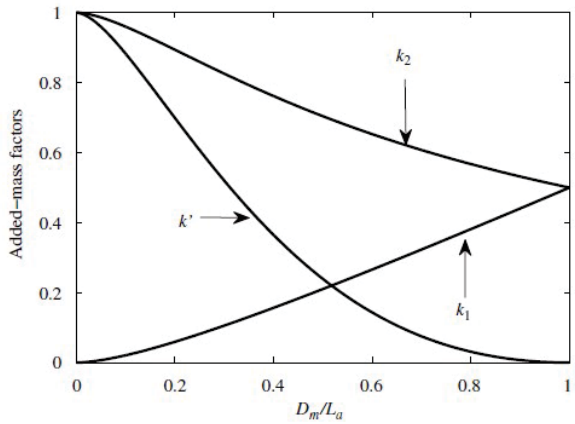

Figure-A I-1 coefficients k en fonction de la finesse du dirigeable. Ils sont utiles pour déterminer la masse ajoutée de l'aérostat

En partant de la théorie des flux potentiels, la masse ajoutée peut être extraite de la formulation de l'énergie cinétique du fluide déplacé :

$$T = -\frac{1}{2}\rho \iint_S \phi \frac{\partial \phi}{\partial n} dS \tag{A I-17}$$

or $\phi = u\phi_1 + v\phi_2 + w\phi_3 + p\phi_4 + q\phi_5 + r\phi_6$

où $\phi_1, ..., \phi_6$ sont les flux potentiels induits par u, v, w, p, q, r (issus de la cinématique).

ainsi :

$$T = \frac{1}{2}\sum_{i=1}^{6}\sum_{j=1}^{6} \lambda_{ij} u_i u_j \tag{A I-18}$$

avec $u = u_1, v = u_2, w = u_3, p = u_4, q = u_5, r = u_6$ et

$$\lambda_{ij} = -\rho \iint_S \phi_i \frac{\partial \phi_i}{\partial n} dS, (i, j) \in [1, ..., 6]^2 \tag{A I-19}$$

Les λ_{ij} sont les masses ajoutées. Les coefficients de masse ajoutée k_{ij} sont eux obtenus de la matrice de masse ajoutée $\lambda = [\lambda_{ij}]$ et la matrice de masse $M' = [m'_{ij}]$ d'un corps fictif rempli

d'air et de même forme que le dirigeable avec :

$$k_{ij} = \begin{cases} 0 \text{ pour } m'_{ij} = 0 \frac{\lambda_{ij}}{m'_{ij}} \text{ sinon} \end{cases} \tag{A I-20}$$

D'après la théorie du flux potentiel, muni des hypothèses suivantes :

- état d'équilibre (vitesse et vitesse angulaire constantes)
- fluide homogène, incompressible, idéal et non turbulent
- condition de non-glissement
- à l'infini : $\nabla\phi \rightarrow 0$ et $\phi \rightarrow 0$

Les équations de Navier-Stokes deviennent (2 premières hypothèses) :

$$\triangle\phi = 0 \tag{A I-21}$$

et la troisième hypothèse amène à :

$$\frac{\partial\phi(P)}{\partial n} = v_p.n \tag{A I-22}$$

avec n vecteur unité normal à la surface au point P et v_p la vitesse du point P.

Cette formulation des équations (A I-21) et (A I-22) de Navier-Stokes peut être discrétisée après maillage du corps sous la forme :

$$2\pi\phi_i^k = -\sum_{l=1}^{n_p} H_{kl}\frac{\partial {\phi_i}^l}{\partial n_l} + \sum_{l=1}^{n_p} G_{kl}{\phi_i}^l \tag{A I-23}$$

avec $(k, i) \in [1, ..., n_p] \times [1, ..., 6]$ ou sous la forme matricielle :

$$2\pi\mathbf{I}_{n_p}[\phi_i] = -\mathbf{H}\left[\frac{\partial\phi_i}{\partial n}\right] + \mathbf{G}[\phi_i] \tag{A I-24}$$

avec $i \in [1, ..., 6]$

La démarche globale s'effectue selon la méthodologie détaillée Figure I-2.

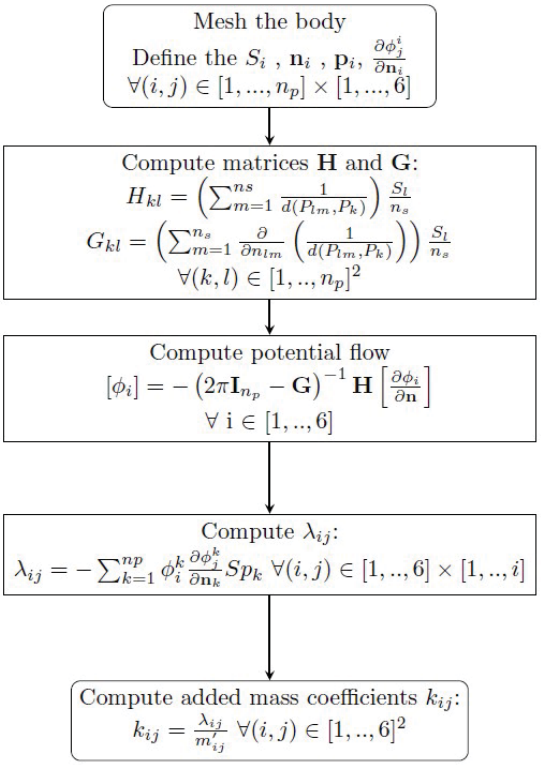

Figure-A I-2 Mise en œuvre de la modélisation par éléments de frontière — tiré de Brèches (2015)

Un protocole expérimental est également détaillé par Le Mestre, Doaré & Schotté (2019) l'utilisation d'une maquette plongée dans un bassin. Les résultats empiriques sont comparés à la méthode par élément de frontière et montrent les limitations de ce modèle lorsque la viscosité du fluide entre en ligne de compte.

2.2 Traînée

Naturellement, la traînée a un impact direct sur la propulsion et l'autonomie du dirigeable. Celle-ci peut-être due à plusieurs facteurs (W, 2017) :

- Traînée induite : la traînée qui résulte de la génération d'un système de vortex traînant en aval d'une surface de levage.
- Traînée parasite : la traînée totale d'un avion moins la traînée induite. Ainsi, c'est la traînée non directement associée à la production de la portance. La traînée parasitaire est composée de nombreux éléments tels que :
  - Traînée de forme (parfois appelée traînée de pression) : La traînée sur un corps résultant de l'effet intégré de la pression statique agissant normalement à sa surface
  - Traînée d'interférence : l'augmentation de la traînée résultant du rapprochement de deux corps. Par exemple, la traînée totale d'une combinaison aileron-coque sera généralement supérieure à la somme de la traînée des ailerons et de la coque, indépendamment l'une de l'autre.
  - Traînée de compensation : l'augmentation de la traînée résultant des forces aérodynamiques nécessaires pour compenser l'aérostat autour de son centre de gravité. Habituellement, cela prend la forme d'une traînée induite supplémentaire et d'une traînée de forme sur l'empennage horizontal.
  - Traînée de base : la contribution spécifique à la traînée de pression attribuée à l'objet profilé après la fin du corps.

Dans le modèle dynamique précédents, la traînée induite peut être défini à travers le tenseur des phénomènes aérodynamiques stationnaires τ_{sta} (Meddahi, 2015) :

$$\tau_{sta} = \frac{1}{2}\,\rho\,V_a^2\,S_{ref}\begin{pmatrix} C_T \\ C_L \\ C_N \\ C_l \\ C_n \\ C_m \end{pmatrix} \tag{A I-25}$$

Où $C_T, C_L, C_N, C_l, C_n, C_m$ sont des coefficients aérodynamiques fonctions de la forme géométrique du dirigeable et de la position des surfaces de contrôle.

Selon les estimations (Li & Nahon, 2007), la coque est responsable de 50 à 75% de la traînée totale. Les ailerons pour 7 à 27%. Les efforts d'optimisation se concentrent donc majoritairement à donner à la coque le profil le plus aérodynamique possible sur des plages de vitesse données (Fig. I-3 (Stockbridge *et al.*, 2012)).

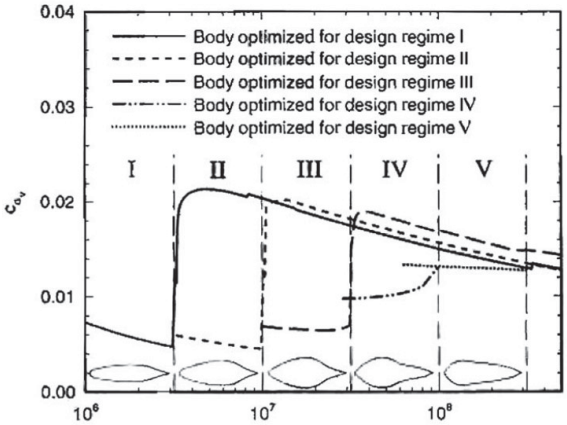

Figure-A I-3 Optimisation par algorithme génétique — la forme du dirigeable évolue selon les différents régimes de nombre de Reynolds — tiré de Stockbridge *et al.* (2012)

2.3 Réflexions sur la stabilité

La stabilité statique pour les dirigeables signifie que tout changement d'attitude crée des forces qui ramènent l'aérostat à son ancienne attitude. Nous nous intéresserons tout particulièrement au cas de la stabilité longitudinale.

D'après la théorie des corps élancés énoncée par Munk en 1921, tout corps fin en incidence dans un fluide subit un effort normal :

$$dFn = q\ dS\ sin(\alpha) \tag{A I-26}$$

La portance d'un cylindre étant négligeable (diamètre constant) mais une force normale est créée par le nez de l'appareil. Cet effort tend à déstabiliser les dirigeables. Pour contrer cet effet, des ailerons sont placés en arrière pour ramener l'aérostat dans une position d'équilibre. L'équilibre statique est atteint lorsque le centre de pression aérodynamique (CPA) se trouve en arrière du centre de gravité (CdG).
Cette théorie, développée initialement pour les besoins de l'étude des dirigeables, a été repris et amélioré pour estimer la stabilité des fusées dans les années 50 et 60. Condensée dans le rapport des Barrowman (Barrowman, 1967), la force normale aérodynamique est exprimée sous la forme :

$$N = C_{N\alpha}\ \frac{1}{2}\ \rho\ V^2\ \alpha A_r \tag{A I-27}$$

On peut déterminer $(C_{N\alpha})_n$ (nose — nez) et $(C_{N\alpha})_f$ (fins — ailerons) — Figure I-4 - pour trouver la balance entre le CPA et le CdG.

$$(C_{N\alpha})_n = 2 \text{ quelque soit la géométrie du nez}$$

$$(C_{N\alpha})_f = \frac{4\,n\left(\frac{s}{d}\right)^2}{1+\sqrt{1+\left(\frac{2\,l}{a+b}\right)^2}} \qquad \text{(A I-28)}$$

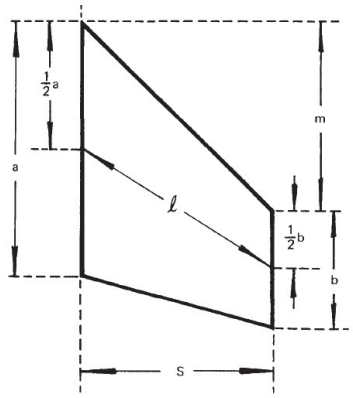

Figure-A I-4 dimensions de l'aileron

La stabilité d'un dirigeable dépend si la force de l'aileron et le moment gravitationnel de restauration sont suffisants pour contrer les moments déstabilisants de Munk. On peut tracer Fig. I-5 l'évolution de la portance des ailerons pour différentes valeurs d'envergure et la comparer à la portance due au nez du dirigeable. On respecte les critères de stabilité statique lorsque l'on est au-dessus de cette limite rouge.

Partant de ce principe, une très haute manœuvrabilité du drone dirigeable peut-elle être obtenue par un contrôle d'instabilités provoquées ?

En exploitant ces résultats, l'idée serait d'avoir un engin stable (type conventionnel fortement non holonome) équipé d'appendices rétractables ou une motorisation pouvant provoquer une instabilité dans les phases dans lesquelles on souhaite une haute manœuvrabilité. Ce type de configuration pourrait permettre de viser des rayons de braquage du même ratio que la longueur du dirigeable tout en ayant une excellente aérodynamique dans les phases d'avancées rapides en translation.

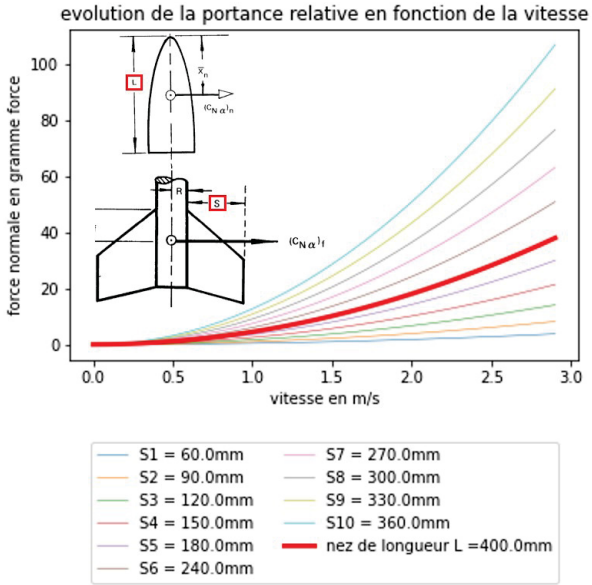

Figure-A I-5 impact de la dimension des ailerons sur la portance générée. Les appendices, une fois bien dimensionnés, permettent un retour à l'équilibre de l'engin en cas de perturbations

ANNEXE II

SCRIPT D'ANALYSE DES RÉSULTATS DU LOGICIEL DICE

Ce script Python permet d'exploiter les fichiers log de DICe [1]. Cela permet de contourner l'usage de ParaView® et donne davantage de flexibilité d'emploi : superposition des résultats de DICe avec les images capturées pendant les expériences, calcul et affichage de la déformation principale ε_1, calcul et affichage de la direction de la déformation θ_p. Ce script permet de mieux comprendre comment le polymère « s'écoule » sous la charge.

```
    # -*- coding: utf-8 -*-

import numpy as np
import matplotlib.pyplot as plt
import matplotlib.colors as colors
from PIL import Image
import PIL
import gif

def importation(nom):
    if nom<10:
        nom = '0' + str(nom)
    else:
        nom = str(nom)
    fic = open('DICe_solution_' + nom +'.txt', 'r')
    data = []
    while 1 :
        ligne = fic.readline()
        if ligne ==="":
```

[1] https://github.com/dicengine/dice

```
        break
    else:
        lg = ligne.split(',')
        data.append(lg)
fic.close()

del data[0:1] #delete title line

Subset_ID = []
x_coord, y_coord = [], []
x_displ, y_displ = [], []
sigma, gamma, beta = [], [], []
status_flag = []
uncert = []
strain_xx, strain_yy, strain_xy = [], [], []

for i in range(len(data)):
    L = data[i]
    Subset_ID.append(int(L[0]))
    x_coord.append(float(L[1]))
    y_coord.append(float(L[2]))
    x_displ.append(float(L[3]))
    y_displ.append(float(L[4]))
    sigma.append(float(L[5]))
    gamma.append(float(L[6]))
    beta.append(float(L[7]))
    status_flag.append(float(L[8]))
    uncert.append(float(L[9]))
    strain_xx.append(float(L[10]))
```

```
        strain_yy.append(float(L[11]))
        strain_xy.append(float(L[12]))
    return(x_coord, y_coord, x_displ, y_displ, sigma, gamma, beta,
    ↪  status_flag, uncert, strain_xx, strain_yy, strain_xy)

def lecture(num):
    text_num = str(num)
    x_coord, y_coord, x_displ, y_displ, sigma, gamma, beta,
    ↪  status_flag, uncert, strain_xx, strain_yy, strain_xy =
    ↪  importation(num)

    #eliminate the points where the tracking is lost (sigma = -1)
    for i in range(len(sigma)):
        if sigma[i] == -1:
            x_coord[i], y_coord[i], x_displ[i], y_displ[i],
            ↪  strain_xx[i], strain_yy[i], strain_xy[i] = 0, 0, 0, 0,
            ↪  0, 0, 0

    #apply the displacements to the points to follow the strain
    for i in range(len(x_coord)):
        x_coord[i]=x_coord[i] + x_displ[i]

    for i in range(len(y_coord)):
        y_coord[i]=y_coord[i] + y_displ[i]

    e1 = []
    e2 = []
    theta = []
    emax = []
```

```
for i in range(len(strain_xx)):
    if strain_xx[i]-strain_yy[i] != 0:
        theta_p =
        ↪  np.arctan(2*strain_xy[i]/(strain_xx[i]-strain_yy[i]))/2.
        theta.append(theta_p)
    else:
        theta.append(np.pi/2.)
    e1.append((strain_xx[i] + strain_yy[i])/2. +
    ↪  np.sqrt((((strain_xx[i] -
    ↪  strain_yy[i])/2)**2)+strain_xy[i]**2))
    e2.append((strain_xx[i] + strain_yy[i])/2. -
    ↪  np.sqrt((((strain_xx[i] -
    ↪  strain_yy[i])/2)**2)+strain_xy[i]**2))
    emax.append((e1[i]-e2[i])/2.)

cmap = 'inferno'
xmin, xmax = 850, 1150
ymin, ymax = 250, 550
w = xmax - xmin
h = ymax - ymin

plt.figure(dpi=600)
image = PIL.Image.open('0_000'+ text_num +'.bmp')
greyscale_img = image.convert(mode="LA", dither=Image.NONE)
plt.imshow(greyscale_img)
plt.scatter(x_coord, y_coord, c = e1, marker='.', s=1, alpha=1,
↪  norm=colors.SymLogNorm(linthresh=0.01, linscale=1, vmin=-0.1,
↪  vmax=0.85), cmap = cmap)
```

```
rectangle = plt.Rectangle((xmin, ymin), w, h, fc='#1C00ff00',
↪  ec='white', lw=3)
# plt.gca().add_patch(rectangle)
plt.colorbar(orientation='horizontal')
plt.axis('off')
plt.savefig('BCC.png', dpi=600, bbox_inches='tight')
plt.show()

l = 10
d = 4 #density of the arrows : 1 image on d
u, v = [], []
X, Y, E1 = x_coord, y_coord, e1
x_coord = x_coord[::d]
y_coord = y_coord[::d]
x_displ = x_displ[::d]
y_displ = y_displ[::d]
theta = theta[::d]
e1 = e1[::d]

for i in range(len(theta)):
    u.append(l * np.cos(theta[i])*x_displ[i]/abs(x_displ[i]))
    v.append(l * np.sin(theta[i])*y_displ[i]/abs(y_displ[i]))
plt.figure(dpi=600)
plt.scatter(X, Y, c = E1, marker='.', s=50, alpha=1,
↪  norm=colors.SymLogNorm(linthresh=0.01, linscale=1, vmin=-0.1,
↪  vmax=0.85), cmap = cmap)
for i in range(len(theta)):
    plt.arrow(x_coord[i], y_coord[i], u[i], v[i], head_width=2)
```

```
    plt.xlim(850,1150)
    plt.ylim(250,550)
    plt.gca().set_aspect('equal', adjustable='box')
    plt.axis('off')
    plt.show()

frames = []
for i in range(1,78):
    frames.append(lecture(i))

 # Creating a gif with gif package

gif.options.matplotlib["dpi"] = 300

gif.save(frames, 'DIC.gif', duration=4, unit="s", between="startend")
```

ANNEXE III

SCRIPT DE CLASSEMENT DE CONFIGURATIONS MULTICRITÈRES

```
import pandas as pd
import matplotlib.pyplot as plt

configurations = [
    'Configuration 1', 'Configuration 2', 'Configuration 3',
    'Configuration 4', 'Configuration 5', 'Configuration 6',
    'Configuration 7', 'Configuration 8', 'Configuration 9',
    'Configuration 10'
]

properties = [
    'Propriete 1', 'Propriete 2', 'Propriete 3',
    'Propriete 4', 'Propriete 5', 'Propriete 6'
]

data = {
    'Configuration': configurations,
    'Propriete 1': [10, 20, 15, 25, 30, 35, 40, 45, 50, 55],
    'Propriete 2': [5, 15, 10, 20, 25, 30, 35, 40, 45, 50],
    'Propriete 3': [30, 25, 35, 40, 20, 15, 10, 5, 50, 45],
    'Propriete 4': [20, 30, 25, 35, 15, 10, 5, 40, 55, 50],
    'Propriete 5': [25, 35, 30, 40, 10, 5, 15, 20, 45, 50],
    'Propriete 6': [15, 25, 20, 30, 5, 10, 35, 40, 50, 45],
}
```

```
min_max_list = ['max', 'max', 'min', 'max', 'min', 'max']
coefficients = {
    'Propriete 1': 1,
    'Propriete 2': 1,
    'Propriete 3': 2,
    'Propriete 4': 1,
    'Propriete 5': 2,
    'Propriete 6': 1,
}


somme_des_coefficients = sum(coefficients.values())

# ponderation
coefficients_normalises = {key: value / somme_des_coefficients for key,
↪  value in coefficients.items()}

df = pd.DataFrame(data)


def apply_percentage(df, min_max_list, coefficients_normalises):
    df_100 = df.copy()
    for col, min_max in zip(df.columns[1:], min_max_list):
        if min_max == 'max':
            df_100[col] = intervalle_pourcentage_max(df[col],
            ↪  coefficients_normalises[col])
        else:
            df_100[col] = intervalle_pourcentage_min(df[col],
            ↪  coefficients_normalises[col])
```

```
    return df_100

def intervalle_pourcentage_max(liste, coefficient):
    L = liste.copy()
    for i in range(len(liste)):
        L[i] = round((L[i] - min(liste)) * (100 * coefficient /
        ↪  (max(liste) - min(liste))), 2)
    return L.astype(float)  # conversion en type float

def intervalle_pourcentage_min(liste, coefficient):
    L = liste.copy()
    for i in range(len(liste)):
        L[i] = round((L[i] - min(liste)) * (-100 * coefficient /
        ↪  (max(liste) - min(liste))) + 100 * coefficient, 2)
    return L.astype(float)  # conversion en type float

df_100 = apply_percentage(df, min_max_list, coefficients_normalises)

plt.figure(dpi=600)
colors = ['#a6cee3', '#1f78b4', '#b2df8a', '#33a02c', '#fb9a99',
↪  '#e31a1c', '#fdbf6f', '#ff7f00', '#cab2d6', '#6a3d9a', '#ffff99',
↪  '#b15928']
index = df_100['Configuration']
df_100 = df_100.set_index('Configuration')
df_100.plot(kind='bar', stacked=True,
↪  color=colors[:len(df_100.columns)])
plt.grid()
plt.xlabel('Configurations')
plt.ylabel('Total score')
```

```
plt.legend(loc='upper center', bbox_to_anchor=(0.5, -0.35), ncol=3,
 ↪  fontsize=11)
plt.xticks(rotation=45)
plt.show()
```

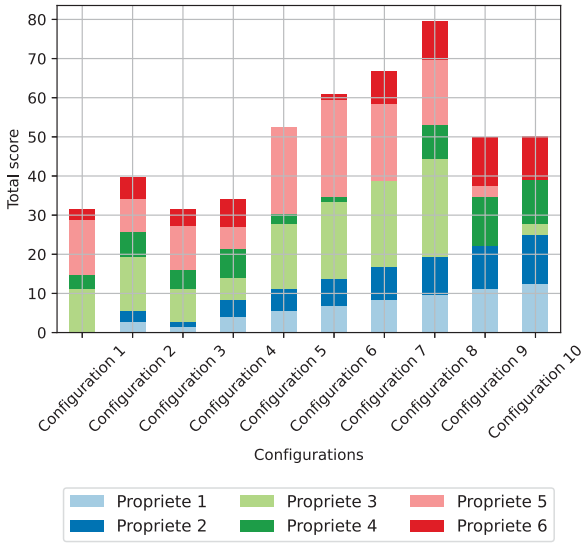

Figure-A III-1 Exemple de graphique en bar empilée pour choisir la meilleure combinaison parmi de nombreux critères. Ici le meilleur choix est la configuration n°7

ANNEXE IV

FABRICATION DE DIRIGEABLE PYRAMIDAL EN MYLAR ET CONCEPTION DE GONDOLES ULTRALÉGÈRES

En partenariat avec une équipe de McGill (Aerospace Mechatronics Lab - AML), un dirigeable pyramidal a été créé. L'objectif de ce petit aérostat d'intérieur (< 1 m^3) était de gagner en expérience de création d'enveloppe à partir de M-PET (Metalized Polyethylene) ou plus communément appelé mylar et explorer la fabrication de formes polyédriques avec ce cas le plus simple de la pyramide. Le mylar a de bonnes propriétés de perméabilité à l'hélium et est extrêmement léger (environ 30 g/m^2) par rapport aux enveloppes en polyuréthane déjà utilisées au lab INIT Robots (environ 70 g/m^2). Deux techniques d'assemblage ont été testées : le soudage thermique et le collage. Les meilleures performances de perméabilité ont été obtenues avec la *Helmer Rubber Cement*, une colle élastique. En dessous, une gondole développé par AML a permis de faire plusieurs vols d'essais et d'améliorer des choix de positionnement des actuateurs.

Plusieurs conclusions ont été retirées des vols lors de la résidence de juillet (dirigeable pyramidal, gondole v1, Figure IV-1) puis de fin août 2022 (dirigeable en « coussin », gondole v2) :

- privilégier l'assemblage des panneaux sur des surfaces planes ;
- les couvertures de survie ont des faiblesses importantes en raison des pliages qui fendillent la fine feuille d'aluminium garante de l'essentiel de l'étanchéité à l'hélium ;
- l'exosquelette en tiges de fibre de carbone doit être placé à l'extérieur. À l'intérieur, il ne peut pas correctement maintenir la forme du ballon, surtout dans les parties supérieures où l'hélium a tendance à gonfler fortement l'enveloppe ;
- une attention toute particulière doit être accordée à la liaison entre la gondole et le reste du ballon afin de correctement transmettre les efforts de la propulsion ;
- le vol en mode « manuel » exploite mal le moteur de contrôle du lacet

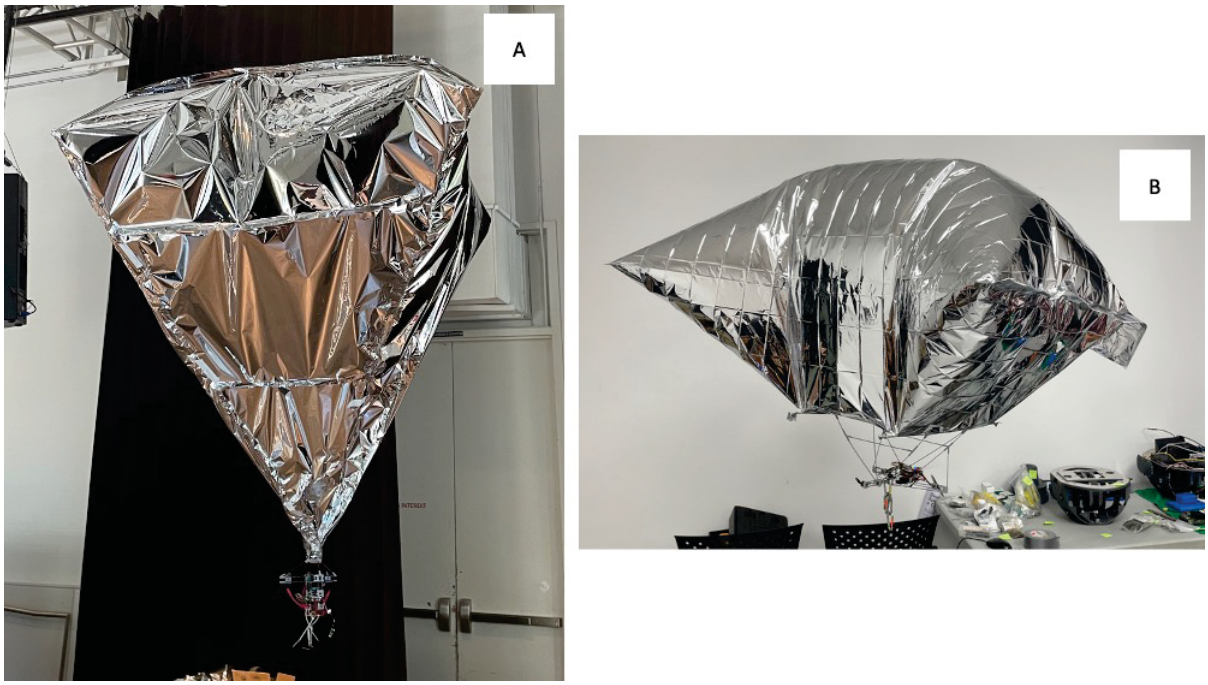

Figure-A IV-1 Dirigeable de démonstration pyramidal -A- (juillet 2022) et en « coussin » -B- (août 2022)

Il est cependant important de mentionner que ce projet n'aborde pas la mécatronique ou le contrôle du drone. Ces aspects sont couverts par AML et déterminés par les travaux existants.

Les techniques de fabrication additive ont été exploitées pour proposer une conception allégée d'une gondole de dirigeable fondée sur une plateforme "Crazyflie" [1]. La précédente conception « classique » a été améliorée avec les outils de *Generative Design* afin de proposer une architecture tout aussi légère mais qui augmente l'envergure. Cela permet d'avoir un meilleur contrôle du lacet (Figure IV-2). La nouvelle gondole est en nylon PA12 (5 grammes), imprimé sur une machine SLS EOS P110 Formiga.

[1] https ://www.bitcraze.io/products/old-products/crazyflie-2-0/

Figure-A IV-2 Ancienne (haut) et nouvelle (bas) gondole pour petit dirigeable d'intérieur. L'envergure est multipliée par trois à masse égale

ANNEXE V

PROTOCOLE DE FABRICATION DES MICRO-TREILLIS EN RÉSINE PHOTOSENSIBLE DU CHAPITRE 5

1. Avant-propos

Cette annexe récapitule le protocole de fabrication donné aux étudiants ayant participé à la fabrication des 144 échantillons de la campagne d'expérience.

2. Consignes générales

- Lien avec tous les fichiers nécessaires : https://git.initrobots.ca/lcatar/micro-lattices-patches-manufacturing
- Les fichiers ont déjà été tranchés (dossier 1-Chitubox). J'ai néanmoins ajouté les fichiers .STL au besoin ainsi que le profil de matériaux pour la machine.
- Ne pas manipuler les micro-treillis, en particulier la famille 50. Manipuler uniquement la base des échantillons.

3. Instructions pour l'impression

1. Sécher le lit d'impression.
2. Enlever le réservoir de résine.
3. Visser le lit sur l'axe z.
4. Dévisser les deux vis de la rotule.
5. Glisser une feuille de papier sur l'écran LCD.
6. Abaisser le lit (tool $\rightarrow$ manual $\rightarrow$ home) et centrer manuellement le lit parallèle aux axes x et y.
7. Une fois le lit en bas, serrer les 2 vis de la rotule.
8. Relever le lit de 50 mm.
9. Enlever la feuille de papier et remettre le réservoir de résine en serrant les 2 vis du réservoir.
10. Abaisser de nouveau le lit en faisant « home » pour chasser les bulles d'air.

11. Recharger en résine si nécessaire.
12. Sélectionner le fichier sur la clé USB (”pattern_material”) puis lancer l’impression.

4. Fin d’impression

1. Préparer une zone avec du papier absorbant pour poser le lit.
2. Préparer le bac plastique d’alcool IPA.
3. Mettre en place le bac en inox d’IPA dans la station Prusa.
4. Sortir les paniers de la Prusa et de la station à ultrasons.
5. Dévisser le lit de l’axe z.
6. Orienter le lit à 45° puis 90° au-dessus du réservoir pendant quelques secondes pour évacuer le maximum de résine.
7. Plonger le lit dans le bac plastique d’IPA (sans que les treillis touchent le fond) pour faciliter le décollement des patchs.
8. Poser le lit sur le papier absorbant.
9. Découper délicatement à la pince les supports (Diamant et Gyroïde).
10. Utiliser la spatule pour décoller les patchs. La spatule doit rester parallèle au lit. Ne pas faire levier au risque d’abimer les micro-treillis.
11. Préparer les patchs pour le nettoyage dans les paniers.
12. Mettre 3 patchs dans le panier ultrasons et trois patchs dans le panier de la Prusa.
13. Lancer le premier cycle de nettoyage : 3 minutes pour les 2.
14. À la fin du cycle, enlever les deux paniers, sécher 5 minutes les échantillons dans le déshydrateur électrique (45°C).
15. Inverser les machines pour le 2ème cycle de nettoyage de 3 minutes.
16. Séchage de 10 minutes dans le déshydrateur.
17. Nettoyage du lit à l’IPA dans le bac plastique puis essuyer consciencieusement au papier absorbant. Il ne faut surtout pas de restes d’IPA dans la MSLA.
18. Enlever le bac d’IPA en inox de la station Prusa.
19. Installer les échantillons dans le rack de durcissement. Vérifier que les échantillons sont complètement secs avant de les installer.

20. Remplir le bécher d'eau puis immerger le rack dans le bécher.
21. 30 minutes (soft) ou 5 minutes (rigide) de durcissement en plaçant le bécher au centre de la station.
22. Séchage de 10 minutes dans le déshydrateur.
23. Stocker les échantillons dans la boite transparente avec les spacers de protection.
24. Cocher la fabrication dans le Google Sheet : Lien du tableau de suivi de la fabrication.

5. Maintenances

5.1 Changements de résine

1. Vider la résine dans la bouteille correspondante (sauf si problème d'impression auparavant, il ne faut pas remettre dans la bouteille des particules solidifiées, la résine doit alors être filtrée).
2. Plonger le réservoir dans un bac d'eau savonneuse. Frotter. Attention de ne pas rayer ou forcer sur le film FEP transparent. Ne pas utiliser d'IPA avec le FEP au risque de l'opacifier.
3. Essuyer avec le papier absorbant (soin aux angles intérieurs du bac).
4. Remettre le réservoir et le remplir lors du prochain cycle d'impression.

5.2 Échec d'impression

1. Si la pièce s'est décrochée pendant l'impression et qu'elle est restée collée au fond du réservoir, procéder au vidage du réservoir en filtrant la résine.
2. Avec la spatule en plastique, décoller la résine durcie.
3. Suivre la même procédure qu'un changement de résine.
4. Privilégier un autre job et faire attention à l'étape de montage du lit, cause la plus récurrente d'échec.

6. Paramètres d'impression

	Build (Rigide)	Tenacious (Souple)
Temps d'exposition (s)	2.5	3.5
Distance de levage (mm)	7	10
Vitesse de levage	60	40
Temps d'exposition base (s)	35	42
Vitesse de retrait (mm/min)	200	200

7. Paramètres de nettoyage et durcissement

	Build (Rigide)	Tenacious (Souple)
Nettoyage à l'IPA (min)	2 fois 3 minutes	2 fois 3 minutes
Exposition aux UV (min)	5	30
Durcissement dans l'eau	non	oui

8. Propriétés mécaniques des résines

	Build (Rigide)	Tenacious (Souple)
Résistance à la traction	50 MPa	30 MPa
Module d'Young	1050 MPa	800 MPa
Élongation à la rupture	8%	70 %
Dureté	D 85	D 65

ANNEXE VI

PROTOCOLE D'INITIALISATION ET D'UTILISATION DU BANC D'ESSAI D'IMPACT LIBÉRÉ

1. Procédure d'utilisation du banc

1.1 Configuration de Testlab pour la 1ère fois

- Sur le chariot SCADAS, allumer le système d'acquisition puis la station
- Sur le Bureau, ouvrir LMS Test.Lab 16A
- Signature/Signature acquisition
- New project
- Aller à "Channel Setup"
- cocher les pistes qui nous intéressent et les remplir ainsi :

Description	Physical Channel	Current Channel used	InputMode	Measured Quantity	Actual sensitivity
Load 1	Input 1	Input 1	ICP	Force	2248 mV/kN
Load 2	Input 2	Input 2	ICP	Force	2248 mV/kN
Load 3	Input 3	Input 4	ICP	Force	2248 mV/kN
Acceleromètre	Input 4	Input 5	ICP	Acceleration	100 mV/g
Potentiomètre	Input 5	Input 6	Voltage DC	Displacement	208 mV/mm
Trigger	Input 6	Input 7	Voltage DC	Voltage	1000 mV/V

Tableau-A VI-1 Configuration des pistes

L'alimentation du potentiomètre est du 5.2 V (5200 mV) pour 25 mm de course maximale.

- Aller à "Tracking setup"
- "Duration" pour Time fixé à 30 secondes

1.2 Avant les essais

- allumer le laptop ubuntu
- ouvrir le terminal puis lancer

```
sudo su
```

- redéfinir la latence du port UART :

```
echo 1 > /sys/bus/usb-serial/devices/ttyUSB0/latency_timer
```

- fermer en lançant `exit`
- `cd impactbench`
- brancher chariot mobile SCADAS
- connecter le port ethernet, connecter le cable SCADAS à l'adaptateur
- allumer SCADAS
- allumer station SCADAS
- Testlab 16.A, ouvrir le fichier `impactbench.lms`
- brancher alimentation du banc d'impact
- brancher le boîtier de commande
- test des commutateurs bistables
- allumer caméra haute vitesse
- allumer panneaux LED et le générateur LED

1.3 Pendant les essais

- Arm SCADAS
- Play : 30s d'enregistrement
- Record sur la caméra haute vitesse : 11s d'enregistrement
- `run_auto`, inscrire le numéro de test : 5s d'enregistrement du Leddar
- switch boîtier de commande du moteur
- impact
- mettre en sécurité le moteur
- désarmer le solénoïde

1.4 Sauvegarder les données

- Aller à la section "Navigator"
- + Section 1
- n° du run
- Throughput
- Select all points
- clique droit -> export to -> .txt
- nommer selon la convention `PCB_motif_compacité_matériau.txt`

2. Mesure de vitesse - capteur LeddarOne

Leddar SDK

```
sudo apt install -y cmake libusb-1.0-0-dev
git clone https://github.com/leddartech/LeddarSDK.git
cd LeddarSDK/src
mkdir release
cd release
cmake ..
make
cd ../LeddarPy
python3 setup.py install --user
```

Pour augmenter le datarate : https://github.com/leddartech/LeddarSDK/issues/20

3. Mesure de déplacement — capteur potentiométrique

Installer Phidget :

```
curl -fsSL https://www.phidgets.com/downloads/setup_linux | sudo -E bash -
```

```
sudo apt-get install -y libphidget22
pip3 install Phidget22
sudo cp 99-libphidget22.rules /etc/udev/rules.d/
```

BIBLIOGRAPHIE

52900, I. (2015). ISO/ASTM 52900.

Abrate, S., Epasto, G., Kara, E., Crupi, V., Guglielmino, E. & Aykul, H. (2018). Computed tomography analysis of impact response of lightweight sandwich panels with micro lattice core. *Proceedings of the Institution of Mechanical Engineers, Part C : Journal of Mechanical Engineering Science*, 232(8), 1348–1362. doi : 10.1177/0954406218766383. Publisher : IMECHE.

Abueidda, D. W., Elhebeary, M., Shiang, C.-S. A., Pang, S., Abu Al-Rub, R. K. & Jasiuk, I. M. (2019). Mechanical properties of 3D printed polymeric Gyroid cellular structures : Experimental and finite element study. *Materials & Design*, 165, 107597. doi : 10.1016/j.matdes.2019.107597.

Adeel, S., Suvarna, S. & Pant, R. (2017). Design and Development of an easily Deployable indoor Finless airship.

Adrien, B. (2024). Elios 3 - Digitizing the inaccessible. Repéré à https://www.flyability.com/elios-3.

Alderson, A. & Alderson, K. L. (2007). Auxetic materials. *Proceedings of the Institution of Mechanical Engineers, Part G : Journal of Aerospace Engineering*, 221(4), 565–575. doi : 10.1243/09544100JAERO185. Publisher : IMECHE.

AlMahri, S., Santiago, R., Lee, D.-W., Ramos, H., Alabdouli, H., Alteneiji, M., Guan, Z., Cantwell, W. & Alves, M. (2021). Evaluation of the dynamic response of triply periodic minimal surfaces subjected to high strain-rate compression. *Additive Manufacturing*, 46, 102220. doi : 10.1016/j.addma.2021.102220.

Alsalla, H., Hao, L. & Smith, C. (2016). Fracture toughness and tensile strength of 316L stainless steel cellular lattice structures manufactured using the selective laser melting technique. *Materials Science and Engineering : A*, 669, 1–6. doi : 10.1016/j.msea.2016.05.075.

Anil, L. S., Kshirsagar, A. & Pant, R. S. (2016). Design and Fabrication of a Portable Semi-Rigid Airship. *The Institution of Engineers (India)*, 45.

Ashby, M. (2006). The properties of foams and lattices. *Philosophical Transactions of the Royal Society A : Mathematical, Physical and Engineering Sciences*, 364(1838), 15–30. doi : 10.1098/rsta.2005.1678. Publisher : Royal Society.

Ashby, M. F. (2005). Cellular Solids – Scaling of Properties. Repéré à https://onlinelibrary.wiley.com/doi/10.1002/3527606696.ch1a. ISBN : 9783527606696.

Aurenhammer, F. (1991). Voronoi diagrams—a survey of a fundamental geometric data structure. *ACM Computing Surveys*, 23(3), 345–405. doi : 10.1145/116873.116880.

Ayachit, U. (2015). *The paraview guide : a parallel visualization application*. Kitware, Inc.

Balaji, R., Talasila, E. R., Oblisamy, L., Ajith, V. S. & Basithrahman, A. (2022). Design and Structural Analysis of Nano-satellite. *Recent Advances in Manufacturing, Automation, Design and Energy Technologies*, (Lecture Notes in Mechanical Engineering), 515–521. doi : 10.1007/978-981-16-4222-7_58.

Banerjee, H., Li, T. K., Ponraj, G., Kirthika, S. K., Lim, C. M. & Ren, H. (2020). Origami-Layer-Jamming Deployable Surgical Retractor With Variable Stiffness and Tactile Sensing. *Journal of Mechanisms and Robotics*, 12(031010). doi : 10.1115/1.4045424.

Barrowman, J. (1967). *The Practical Calculation of the Aerodynamic Characteristics of Slender Finned Vehicles*.

Beaman, J. J., Bourell, D. L., Seepersad, C. C. & Kovar, D. (2020). Additive Manufacturing Review : Early Past to Current Practice. *Journal of Manufacturing Science and Engineering*, 142(110812). doi : 10.1115/1.4048193.

Bhovad, P. & Li, S. (2018, November). Using Multi-Stable Origami Mechanism for Peristaltic Gait Generation : A Case Study. doi : 10.1115/DETC2018-85932.

Bhovad, P., Kaufmann, J. & Li, S. (2019). Peristaltic locomotion without digital controllers : Exploiting multi-stability in origami to coordinate robotic motion. *Extreme Mechanics Letters*, 32, 100552. doi : 10.1016/j.eml.2019.100552.

Bhushan, B. & Caspers, M. (2017). An overview of additive manufacturing (3D printing) for microfabrication. *Microsystem Technologies*, 23(4), 1117–1124. doi : 10.1007/s00542-017-3342-8.

Biju, M. & Pant, R. S. (2017). Design and Development of an Indoor Autonomous Airship. Dans *23rd AIAA Lighter-Than-Air Systems Technology Conference*. American Institute of Aeronautics and Astronautics. doi : 10.2514/6.2017-3996.

Bikas, H., Lianos, A. K. & Stavropoulos, P. (2019). A design framework for additive manufacturing. *The International Journal of Advanced Manufacturing Technology*, 103(9), 3769–3783. doi : 10.1007/s00170-019-03627-z.

Blazy, J.-S. (2003). *Comportement mécanique des mousses d'aluminium : caractérisations expérimentales sous sollicitations complexes et simulations numériques dans le cadre de l'élasto-plasticité compressible*. (Thèse de doctorat).

Bobbert, F. S. L., Janbaz, S., van Manen, T., Li, Y. & Zadpoor, A. A. (2020). Russian doll deployable meta-implants : Fusion of kirigami, origami, and multi-stability. *Materials & Design*, 191, 108624. doi : 10.1016/j.matdes.2020.108624.

Bogue, R. (2019). Disaster relief, and search and rescue robots : the way forward. *Industrial Robot : the international journal of robotics research and application*, 46(2), 181–187. doi : 10.1108/IR-11-2018-0227. Publisher : Emerald Publishing Limited.

Boniotti, L., Beretta, S., Foletti, S. & Patriarca, L. (2017). Strain concentrations in BCC micro lattices obtained by AM. *Procedia Structural Integrity*, 7, 166–173. doi : 10.1016/j.prostr.2017.11.074.

Boniotti, L., Foletti, S., Beretta, S. & Patriarca, L. (2019). Analysis of strain and stress concentrations in micro-lattice structures manufactured by SLM. *Rapid Prototyping Journal*, 26(2), 370–380. doi : 10.1108/RPJ-10-2018-0270. Publisher : Emerald Publishing Limited.

Bourell, D., Kruth, J. P., Leu, M., Levy, G., Rosen, D., Beese, A. M. & Clare, A. (2017). Materials for additive manufacturing. *CIRP Annals*, 66(2), 659–681. doi : 10.1016/j.cirp.2017.05.009.

Briod, A., Kornatowski, P., Zufferey, J.-C. & Floreano, D. (2014). A Collision-resilient Flying Robot. *Journal of Field Robotics*, 31(4), 496–509. doi : 10.1002/rob.21495. _eprint : https ://onlinelibrary.wiley.com/doi/pdf/10.1002/rob.21495.

Bruschi, G., Tsang, K., Nishioka, T. & Wang, R. (2003). *DRAG COEFFICIENT OF A CYLINDER*.

Brèches, P.-Y. (2015). *Dynamics Modeling and State Feedback Control of a Lighter-than-air Cubic Blimp*. (Thèse de doctorat, Université de McGill).

Calladine, C. (1978). Buckminster Fuller's "Tensegrity" structures and Clerk Maxwell's rules for the construction of stiff frames. *International Journal of Solids and Structures*, 14(2), 161–172. doi : 10.1016/0020-7683(78)90052-5.

Callens, S. & Zadpoor, A. (2017). From flat sheets to curved geometries : Origami and kirigami approaches. *Materials Today*. doi : 10.1016/j.mattod.2017.10.004.

Cao, S., Qiu, Y., Wei, X.-F. & Zhang, H.-H. (2015). Experimental and theoretical investigation on ultra-thin powder layering in three dimensional printing (3DP) by a novel double-smoothing mechanism. *Journal of Materials Processing Technology*, 220, 231–242. doi : 10.1016/j.jmatprotec.2015.01.016.

Carneiro, V. H., Rawson, S. D., Puga, H. & Withers, P. J. (2021). Macro-, meso- and microstructural characterization of metallic lattice structures manufactured by additive manufacturing assisted investment casting. *Scientific Reports*, 11(1), 4974. doi : 10.1038/s41598-021-84524-y. Bandiera_abtest : a Cc_license_type : cc_by Cg_type : Nature Research Journals Number : 1 Primary_atype : Research Publisher : Nature Publishing Group Subject_term : Engineering ;Materials science ;Mechanical engineering Subject_term_id : engineering ;materials-science ;mechanical-engineering.

Catar, L., Tabiai, I. & St-Onge, D. (2022, November). Additive Manufacturing Strategy for Ultra-Lightweight High Value-Added Components. doi : 10.1115/DETC2022-88458.

Catar, L., Tabiai, I. & St-Onge, D. (2024a). Polymer Micro-Lattice buffer structure Free Impact absorption. arXiv. arXiv :2408.02909 [cond-mat, physics :physics], doi : 10.48550/arXiv.2408.02909.

Catar, L., Tabiai, I. & St-Onge, D. (2024b). Tensile Tests of Different Families of Ultra-Lightweight Photosensitive Polymer Micro-Lattices.

Ceruti, A. & Marzocca, P. (2014). Conceptual Approach to Unconventional Airship Design and Synthesis. *Journal of Aerospace Engineering*, 27(6), 04014035. doi : 10.1061/(ASCE)AS.1943-5525.0000344. Publisher : American Society of Civil Engineers.

Chen, T., Bilal, O. R., Lang, R., Daraio, C. & Shea, K. (2019). Autonomous Deployment of a Solar Panel Using Elastic Origami and Distributed Shape-Memory-Polymer Actuators. *Physical Review Applied*, 11(6), 064069. doi : 10.1103/PhysRevApplied.11.064069. Publisher : American Physical Society.

Chillara, V. S. C. & Dapino, M. J. (2019). Review of Morphing Laminated Composites. *Applied Mechanics Reviews*, 72(010801). doi : 10.1115/1.4044269.

Cho, S., Mishra, V., Tao, Q., Vamell, P., King-Smith, M., Muni, A., Smallwood, W. & Zhang, F. (2017, August). Autopilot design for A class of miniature autonomous blimps. *2017 IEEE Conference on Control Technology and Applications (CCTA)*, pp. 841–846. doi : 10.1109/CCTA.2017.8062564.

Chu, W.-S., Kim, M.-S., Jang, K.-H., Song, J.-H., Rodrigue, H., Chun, D.-M., Cho, Y. T., Ko, S. H., Cho, K.-J., Cha, S. W., Min, S., Jeong, S. H., Jeong, H., Lee, C.-M., Chu, C. N. & Ahn, S.-H. (2016). From design for manufacturing (DFM) to manufacturing for design (MFD) via hybrid manufacturing and smart factory : A review and perspective of paradigm shift. *International Journal of Precision Engineering and Manufacturing-Green Technology*, 3(2), 209–222. doi : 10.1007/s40684-016-0028-0.

Cingesar, I. K., Marković, M.-P. & Vrsaljko, D. (2022). Effect of post-processing conditions on polyacrylate materials used in stereolithography. *Additive Manufacturing*, 55, 102813. doi : 10.1016/j.addma.2022.102813.

Clough, E. C., Plaisted, T. A., Eckel, Z. C., Cante, K., Hundley, J. M. & Schaedler, T. A. (2019). Elastomeric Microlattice Impact Attenuators. *Matter*, 1(6), 1519–1531. doi : 10.1016/j.matt.2019.10.004.

Cloutier, J.-S. & Ménard, C. (2017). D'immenses galeries souterraines découvertes dans une caverne sous les pieds des Montréalais. Publisher : Radio-Canada.ca, Repéré à https://ici.radio-canada.ca/nouvelle/1070663/galeries-souterraines-decouvertes-caverne-saint-leonard-montreal-speleologues.

Coulter, F. B., Coulter, B. S., Marks, J. R. & Ianakiev, A. (2018a). Production Techniques for 3D Printed Inflatable Elastomer Structures : Part I—Fabricating Air-Permeable Forms and Coating with Inflatable Silicone Membranes via Spray Deposition. *3D Printing and Additive Manufacturing*, 5(1), 5–16. doi : 10.1089/3dp.2017.0068. Publisher : Mary Ann Liebert, Inc., publishers.

Coulter, F. B., Coulter, B. S., Papastavrou, E. & Ianakiev, A. (2018b). Production Techniques for 3D Printed Inflatable Elastomer Structures : Part II—Four-Axis Direct Ink Writing on Irregular Double-Curved and Inflatable Surfaces. *3D Printing and Additive Manufacturing*, 5(1), 17–28. doi : 10.1089/3dp.2017.0069. Publisher : Mary Ann Liebert, Inc., publishers.

Cozmei, M., Hasseler, T., Kinyon, E., Wallace, R., Deleo, A. A. & Salviato, M. (2020). Aerogami : Composite origami structures as active aerodynamic Ccontrol. *Composites Part B : Engineering*, 184, 107719. doi : 10.1016/j.compositesb.2019.107719.

Cross, N. (2011). *Design Thinking : Understanding How Designers Think and Work*. Berg.

Cui, X., Zhao, L., Wang, Z., Zhao, H. & Fang, D. (2012). Dynamic response of metallic lattice sandwich structures to impulsive loading. *International Journal of Impact Engineering*, 43, 1–5. doi : 10.1016/j.ijimpeng.2011.11.004.

Da, D. & Qian, X. (2020). Fracture resistance design through biomimicry and topology optimization. *Extreme Mechanics Letters*, 40, 100890. doi : 10.1016/j.eml.2020.100890.

da S. Vieira, J., Lopes, F. P. D., de Moraes, Y. M., Monteiro, S. N., M. Margem, F., Margem, J. I. & Souza, D. (2018). Comparative Mechanical Analysis of Epoxy Composite Reinforced with Malva/Jute Hybrid Fabric by Izod and Charpy Impact Test. *Characterization of Minerals, Metals, and Materials 2018*, pp. 177–183. doi : 10.1007/978-3-319-72484-3_19.

Das, S., Chakraborty, S., Rai, N., Dhar, A., Sadhu, A., Gautam, B., Verma, P., Singh, A., Sherpa, C. & Chakraborty, M. (2019, March). Eastern Himalayan Glaciar Hazard Analysis Using UAV-A Brief Approach. *2019 URSI Asia-Pacific Radio Science Conference (AP-RASC)*, pp. 1–4. doi : 10.23919/URSIAP-RASC.2019.8738483.

Davis, R. & John, P. (2018). *Application of Taguchi-Based Design of Experiments for Industrial Chemical Processes*. IntechOpen. doi : 10.5772/intechopen.69501.

de Sousa, R. A., Gonçalves, D., Coelho, R. & Teixeira-Dias, F. (2012). Assessing the effectiveness of a natural cellular material used as safety padding material in motorcycle helmets. *SIMULATION*, 88(5), 580–591. doi : 10.1177/0037549711414735. Publisher : SAGE Publications Ltd STM.

Deshpande, V. S., Ashby, M. F. & Fleck, N. A. (2001a). Foam topology : bending versus stretching dominated architectures. *Acta Materialia*, 49(6), 1035–1040. doi : 10.1016/S1359-6454(00)00379-7.

Deshpande, V. S., Fleck, N. A. & Ashby, M. F. (2001b). Effective properties of the octet-truss lattice material. *Journal of the Mechanics and Physics of Solids*, 49(8), 1747–1769. doi : 10.1016/S0022-5096(01)00010-2.

Després, N., Cyr, E., Setoodeh, P. & Moham-madi, M. (2020). Deep Learning and Design for Additive Manufacturing : A Framework for Microlattice Architecture. *JOM*, 72(6), 2408–2418. doi : 10.1007/s11837-020-04131-6.

Dharmalingam, L. K., Aute, V. & Ling, J. (2022). Review of Triply Periodic Minimal Surface (TPMS) based Heat Exchanger Designs.

Dizon, J. R. C., Gache, C. C. L., Cascolan, H. M. S., Cancino, L. T. & Advincula, R. C. (2021). Post-Processing of 3D-Printed Polymers. *Technologies*, 9(3), 61. doi : 10.3390/technologies9030061. Number : 3 Publisher : Multidisciplinary Digital Publishing Institute.

Dmitriev, A. & Mitroshkina, T. (2019). Improving the Efficiency of Aviation Products Design Based on International Standards and Robust Approaches. *IOP Conference Series : Materials Science and Engineering*, 476(1), 012009. doi : 10.1088/1757-899X/476/1/012009. Publisher : IOP Publishing.

Dong, G., Tang, Y. & Zhao, Y. F. (2017). A Survey of Modeling of Lattice Structures Fabricated by Additive Manufacturing. *Journal of Mechanical Design*, 139(100906). doi : 10.1115/1.4037305.

Doyoyo, M. & Hu, J. W. (2006). Multi-axial failure of metallic strut-lattice materials composed of short and slender struts. *International Journal of Solids and Structures*, 43(20), 6115–6139. doi : 10.1016/j.ijsolstr.2005.12.001.

Drücker, S., Inman, S. & Fiedler, B. (2018). Simulation and optimization of the load introduction geometry of additively manufactured lattice structure specimens. *ECCM 2018 - 18th European Conference on Composite Materials*. Accepted : 2020-01-28T12 :08 :18Z ISBN : 9781510896932.

du Plessis, A., Yadroitsava, I., Yadroitsev, I., le Roux, S. & Blaine, D. (2018). Numerical comparison of lattice unit cell designs for medical implants by additive manufacturing. *Virtual and Physical Prototyping*, 13(4), 266–281. doi : 10.1080/17452759.2018.1491713. Publisher : Taylor & Francis _eprint : https ://doi.org/10.1080/17452759.2018.1491713.

Duffner, J., Liu, M., Mandy, C., Panish, R. & Landis, G. (2007, September). Conceptual Design of an Airship Mission to Titan. *AIAA SPACE 2007 Conference & Exposition*. doi : 10.2514/6.2007-6265.

Durão, L. F. C. S., Barkoczy, R., Zancul, E., Lee Ho, L. & Bonnard, R. (2019). Optimizing additive manufacturing parameters for the fused deposition modeling technology using a design of experiments. *Progress in Additive Manufacturing*, 4(3), 291–313. doi : 10.1007/s40964-019-00075-9.

Echeta, I., Dutton, B., Leach, R. K. & Piano, S. (2021). Finite element modelling of defects in additively manufactured strut-based lattice structures. *Additive Manufacturing*, 47, 102301. doi : 10.1016/j.addma.2021.102301.

Edge, H., Collins, J., Brown, A., Coatney, M., Roget, B., Slegers, N. & Johnson, A. (2010). *Lighter-Than-Air and Pressurized Structures Technology for Unmanned Aerial Vehicles (UAVs) :*. Fort Belvoir, VA. Repéré le 2022-08-11 à http://www.dtic.mil/docs/citations/ADA513823.

Evans, A. G., Hutchinson, J. W., Fleck, N. A., Ashby, M. F. & Wadley, H. N. G. (2001). The topological design of multifunctional cellular metals. *Progress in Materials Science*, 46(3), 309–327. doi : 10.1016/S0079-6425(00)00016-5.

Evans, A. G., He, M. Y., Deshpande, V. S., Hutchinson, J. W., Jacobsen, A. J. & Carter, W. B. (2010). Concepts for enhanced energy absorption using hollow micro-lattices. *International Journal of Impact Engineering*, 37(9), 947–959. doi : 10.1016/j.ijimpeng.2010.03.007.

Evans, A. G., Hutchinson, J. W. & Ashby, M. F. (1998). Multifunctionality of cellular metal systems. *Progress in Materials Science*, 43(3), 171–221. doi : 10.1016/s0079-6425(98)00004-8. MAG ID : 2121323562.

F2792-12a, A. I. (2012). *Standard terminology for additive manufacturing technologies*.

Falanga, D., Kleber, K., Mintchev, S., Floreano, D. & Scaramuzza, D. (2019). The Foldable Drone : A Morphing Quadrotor That Can Squeeze and Fly. *IEEE Robotics and Automation Letters*, 4(2), 209–216. doi : 10.1109/LRA.2018.2885575.

Faludi, J., Bayley, C., Bhogal, S. & Iribarne, M. (2015). Comparing environmental impacts of additive manufacturing vs traditional machining via life-cycle assessment. *Rapid Prototyping Journal*, 21(1), 14–33. doi : 10.1108/RPJ-07-2013-0067. Publisher : Emerald Group Publishing Limited.

Feng, G.-z., Wang, J., Li, X.-y., Xiao, L.-j. & Song, W.-d. (2022). Mechanical behavior of Ti–6Al–4V lattice-walled tubes under uniaxial compression. *Defence Technology*, 18(7), 1124–1138. doi : 10.1016/j.dt.2021.05.012.

Fina, F., Goyanes, A., Madla, C. M., Awad, A., Trenfield, S. J., Kuek, J. M., Patel, P., Gaisford, S. & Basit, A. W. (2018). 3D printing of drug-loaded gyroid lattices using selective laser sintering. *International Journal of Pharmaceutics*, 547(1), 44–52. doi : 10.1016/j.ijpharm.2018.05.044.

Forget, D. & Faure, L. (2019). La caverne de Saint-Léonard présente-t-elle un danger ? Publisher : Radio-Canada.ca, Repéré à https://ici.radio-canada.ca/nouvelle/1148535/montreal-grotte-galerie-securite-geologie-calcaire-maison.

Fossati, M. (2022). Origami engineering : evaluation of patterns for deployable space structures. Accepted : 2023-03-08T13 :59 :05Z.

Garcia-Colomo, A., Wood, D., Martina, F. & Williams, S. W. (2020). A comparison framework to support the selection of the best additive manufacturing process for specific aerospace applications. *International Journal of Rapid Manufacturing*, 9(2-3), 194–211. doi : 10.1504/IJRAPIDM.2020.107736. Publisher : Inderscience Publishers.

Garcia-Taormina, A. R., Alwen, A., Schwaiger, R. & Hodge, A. M. (2021). A review of coated nano- and micro-lattice materials. *Journal of Materials Research*, 36(18), 3607–3627. doi : 10.1557/s43578-021-00178-6.

Gawale, A. C., Raina, A. A., Pant, R. S. & Jahagirdar, Y. P. (2008). DESIGN, FABRICATION AND OPERATION OF REMOTELY CONTROLLED AIRSHIPS IN INDIA. 12.

Gibson, I., Rosen, D., Stucker, B. & Khorasani, M. (2021). Design for Additive Manufacturing. Dans Gibson, I., Rosen, D., Stucker, B. & Khorasani, M. (Éds.), *Additive Manufacturing Technologies* (pp. 555–607). Cham : Springer International Publishing. doi : 10.1007/978-3-030-56127-7_19.

Gibson, L. J. & Ashby, M. F. (1997). *Cellular Solids : Structure and Properties*. Cambridge University Press.

Gorjup, G. & Liarokapis, M. (2020). A Low-Cost, Open-Source, Robotic Airship for Education and Research. *IEEE Access*, 8, 70713–70721. doi : 10.1109/ACCESS.2020.2986772.

Gu, D. D., Meiners, W., Wissenbach, K. & Poprawe, R. (2012). Laser additive manufacturing of metallic components : materials, processes and mechanisms. *International Materials Reviews*, 57(3), 133–164. doi : 10.1179/1743280411Y.0000000014.

Guerra Silva, R., Torres, M. J., Zahr Viñuela, J. & Zamora, A. G. (2021). Manufacturing and Characterization of 3D Miniature Polymer Lattice Structures Using Fused Filament Fabrication. *Polymers*, 13(4), 635. doi : 10.3390/polym13040635. Number : 4 Publisher : Multidisciplinary Digital Publishing Institute.

Guillon, D. (2008). *Étude des mécanismes d'absorption d'énergie lors de l'écrasement progressif de structures composites à base de fibre de carbone*. (PhD Thesis).

Gümrük, R. & Mines, R. (2013). Compressive behaviour of stainless steel micro-lattice structures. *International Journal of Mechanical Sciences*, 68(68), 125–139. doi : 10.1016/j.ijmecsci.2013.01.006. MAG ID : 2075516086.

Gümrük, R., Mines, R. A. W. & Karadeniz, S. (2013). Static mechanical behaviours of stainless steel micro-lattice structures under different loading conditions. *Materials Science and Engineering : A*, 586, 392–406. doi : 10.1016/j.msea.2013.07.070.

Hart, S. G. (2006). Nasa-Task Load Index (NASA-TLX) ; 20 Years Later. *Proceedings of the Human Factors and Ergonomics Society Annual Meeting*, 50(9), 904–908. doi : 10.1177/154193120605000909. Publisher : SAGE Publications Inc.

Hart, S. G. & Staveland, L. E. (1988). Development of NASA-TLX (Task Load Index) : Results of Empirical and Theoretical Research. Dans *Advances in Psychology* (vol. 52, pp. 139–183). Elsevier. doi : 10.1016/S0166-4115(08)62386-9.

Hassan, I. M., Enab, T. A., Fouda, N. & Eldesouky, I. (2023). Design, fabrication, and evaluation of functionally graded triply periodic minimal surface structures fabricated by 3D printing. *Journal of the Brazilian Society of Mechanical Sciences and Engineering*, 45(1), 66. doi : 10.1007/s40430-022-03972-3.

Hassanalian, M. & Abdelkefi, A. (2017). Classifications, applications, and design challenges of drones : A review. *Progress in Aerospace Sciences*, 91, 99–131. doi : 10.1016/j.paerosci.2017.04.003.

Hecks, K. (1972). Pressure airships : a review. *The Aeronautical Journal*, 76(743), 647–656. doi : 10.1017/S0001924000044225.

Huang, Y.-W., Lu, C.-L., Chen, K.-L., Ser, P.-S., Huang, J.-T., Shen, Y.-C., Chen, P.-W., Chang, P.-K., Lee, S.-C. & Wang, H.-C. (2019). Duckiefloat : a Collision-Tolerant Resource-Constrained Blimp for Long-Term Autonomy in Subterranean Environments. arXiv. arXiv :1910.14275 [cs], doi : 10.48550/arXiv.1910.14275.

Hudson, N., Talbot, F., Cox, M., Williams, J., Hines, T., Pitt, A., Wood, B., Frousheger, D., Lo Surdo, K., Molnar, T., Steindl, R., Wildie, M., Sa, I., Kottege, N., Stepanas, K., Hernandez, E., Catt, G., Docherty, W., Tidd, B., Tam, B., Murrell, S., Bessell, M., Hanson, L., Tychsen-Smith, L., Suzuki, H., Overs, L., Kendoul, F., Wagner, G., Palmer, D., Milani, P., O'Brien, M., Jiang, S., Chen, S. & Arkin, R. (2022). Heterogeneous Ground and Air Platforms, Homogeneous Sensing : Team CSIRO Data61's Approach to the DARPA Subterranean Challenge. *Field Robotics*, 2(1), 595–636. doi : 10.55417/fr.2022021.

Hwang, H.-Y. (2021). Effects of perforated crease line design on mechanical behaviors of origami structures. *International Journal of Solids and Structures*, 230-231, 111158. doi : 10.1016/j.ijsolstr.2021.111158.

Intrigila, C., Nodargi, N. A. & Bisegna, P. (2022). The compressive response of additively-manufactured hollow truss lattices : an experimental investigation. *The International Journal of Advanced Manufacturing Technology*. doi : 10.1007/s00170-022-08716-0.

Ismail, M. F., Sultan, M. T. H., Hamdan, A., Shah, A. U. M. & Jawaid, M. (2019). Low velocity impact behaviour and post-impact characteristics of kenaf/glass hybrid composites with various weight ratios. *Journal of Materials Research and Technology*, 8(3), 2662–2673. doi : 10.1016/j.jmrt.2019.04.005.

Jeong, H. S., Lyu, S.-K. & Park, S. H. (2021). Effective strut-based design approach of multi-shaped lattices using equivalent material properties. *Journal of Mechanical Science and Technology*, 35(4), 1609–1622. doi : 10.1007/s12206-021-0324-7.

Joshi, R., Raina, A. & Pant, R. (2009). Conceptual Design of an Airship Using Knowledge-Based Engineering. Dans *18th AIAA Lighter-Than-Air Systems Technology Conference*. American Institute of Aeronautics and Astronautics. doi : 10.2514/6.2009-2861.

Kantor, G., Wettergreen, D., Ostrowski, J. P. & Singh, S. (2001, October). Collection of environmental data from an airship platform. *Sensor Fusion and Decentralized Control in Robotic Systems IV*, 4571, 76–83. doi : 10.1117/12.444171.

Kim, S.-H., Lee, H. R., Yu, S. J., Han, M.-E., Lee, D. Y., Kim, S. Y., Ahn, H.-J., Han, M.-J., Lee, T.-I., Kim, T.-S., Kwon, S. K., Im, S. G. & Hwang, N. S. (2015). Hydrogel-laden paper scaffold system for origami-based tissue engineering. *Proceedings of the National Academy of Sciences*, 112(50), 15426–15431. doi : 10.1073/pnas.1504745112. Publisher : Proceedings of the National Academy of Sciences.

Kim, S.-J., Lee, D.-Y., Jung, G.-P. & Cho, K.-J. (2018). An origami-inspired, self-locking robotic arm that can be folded flat. *Science Robotics*, 3(16), eaar2915. doi : 10.1126/scirobotics.aar2915.

Kisgergely, B. (2020). Minimum wall thickness for 3D printing. Repéré à https://formlabs.com/blog/minimum-wall-thickness-3d-printing/.

Klocke, F., Arntz, K., Teli, M., Winands, K., Wegener, M. & Oliari, S. (2017). State-of-the-art Laser Additive Manufacturing for Hot-work Tool Steels. *Procedia CIRP*, 63, 58–63. doi : 10.1016/j.procir.2017.03.073.

Konstantinov, L. (2003). The basics of Theory of Gas and Heat Airships. 21.

Korotkin, A. I. (2009). *Added Masses of Ship Structures*. Dordrecht : Springer Netherlands. doi : 10.1007/978-1-4020-9432-3.

Kresling, B. (2008). Natural twist buckling in shells : from the hawkmoth&#39 ;s bellows to the deployable Kresling-pattern and cylindrical Miura-ori. *IASS-IACM 2008 Spanning Nano to Mega*.

Kresling, B. (2020). The Fifth Fold : Complex Symmetries in Kresling-origami Patterns. *Symmetry : Culture and Science*, 31, 403–416. doi : 10.26830/symmetry_2020_4_403.

Krátký, V., Petráček, P., Báča, T. & Saska, M. (2021). An autonomous unmanned aerial vehicle system for fast exploration of large complex indoor environments. *Journal of Field Robotics*, 38(8), 1036–1058. doi : 10.1002/rob.22021. _eprint : https ://onlinelibrary.wiley.com/doi/pdf/10.1002/rob.22021.

Kuribayashi, K., Tsuchiya, K., You, Z., Tomus, D., Umemoto, M., Ito, T. & Sasaki, M. (2006). Self-deployable origami stent grafts as a biomedical application of Ni-rich TiNi shape memory alloy foil. *Materials Science and Engineering A : Structural Materials : Properties, Microstructure and Processing*, 419(1-2), 131–137. Repéré à https://research.monash.edu/en/publications/self-deployable-origami-stent-grafts-as-a-biomedical-application-. Publisher : Elsevier.

Larsson, M. (2018). Standardization and Modularization. Dans *Circular Business Models : Developing a Sustainable Future* (pp. 151–162). Cham : Springer International Publishing. doi : 10.1007/978-3-319-71791-3_11.

Laverne, F., Segonds, F. & Dubois, P. (2016). Fabrication additive - Principes généraux. *Conception et Production*. doi : 10.51257/a-v2-bm7017.

Le Mestre, R., Doaré, O. & Schotté, J. (2019, May). Modélisation des effets des fluides externes et internes sur le comportement dynamique des dirigeables déformables. *CSMA 2019*. Repéré à https://hal.archives-ouvertes.fr/hal-02196594.

Lee, D.-Y., Kim, J.-K., Sohn, C.-Y., Heo, J.-M. & Cho, K.-J. (2021). High–load capacity origami transformable wheel. *Science Robotics*, 6(53), eabe0201. doi : 10.1126/scirobotics.abe0201.

Li, M., Zhou, Z., Hao, B., Yu, C., Chen, Y. & Ma, J. (2023). Design and deformation analysis of an inflatable metallic cylinder based on the Kresling origami pattern. *Thin-Walled Structures*, 188, 110859. doi : 10.1016/j.tws.2023.110859.

Li, Y. & Nahon, M. (2007). Modeling and Simulation of Airship Dynamics. *Journal of Guidance Control Dynamics*, 30, 1691–1700. doi : 10.2514/1.29061.

Li, Y., Nahon, M. & Sharf, I. (2011). Airship dynamics modeling : A literature review. *Progress in Aerospace Sciences*, 47(3), 217–239. doi : 10.1016/j.paerosci.2010.10.001.

Liao, L. & Pasternak, I. (2009). A review of airship structural research and development. *Progress in Aerospace Sciences*, 45(4), 83–96. doi : 10.1016/j.paerosci.2009.03.001.

Ligon, S. C., Liska, R., Stampfl, J., Gurr, M. & Mülhaupt, R. (2017). Polymers for 3D Printing and Customized Additive Manufacturing. *Chemical Reviews*, 117(15), 10212–10290. doi : 10.1021/acs.chemrev.7b00074. Publisher : American Chemical Society.

Liu, G., Zhang, X., Chen, X., He, Y., Cheng, L., Huo, M., Yin, J., Hao, F., Chen, S., Wang, P., Yi, S., Wan, L., Mao, Z., Chen, Z., Wang, X., Cao, Z. & Lu, J. (2021). Additive manufacturing of structural materials. *Materials Science and Engineering : R : Reports*, 145, 100596. doi : 10.1016/j.mser.2020.100596.

Lu, C.-L., Huang, J.-T., Huang, C.-I., Liu, Z.-Y., Hsu, C.-C., Huang, Y.-Y., Huang, S.-C., Chang, P.-K., Ewe, Z. L., Huang, P.-J., Li, P.-L., Wang, B.-H., Yim, L.-S., Huang, S.-W., Bai, M. & Wang, H.-C. (2022). A Heterogeneous Unmanned Ground Vehicle and Blimp Robot Team for Search and Rescue using Data-driven Autonomy and Communication-aware Navigation. *Field Robotics*, 2(1), 557–594. doi : 10.55417/fr.2022020.

Lynch, J. & Raney, J. (2020). Volumetric Origami-based Deployable Modular Space Structures with Tailorable Stiffness. Dans *AIAA Scitech 2020 Forum*. American Institute of Aeronautics and Astronautics. doi : 10.2514/6.2020-0110.

Maconachie, T., Leary, M., Lozanovski, B., Zhang, X., Qian, M., Faruque, O. & Brandt, M. (2019). SLM lattice structures : Properties, performance, applications and challenges. *Materials & Design*, 183, 108137. doi : 10.1016/j.matdes.2019.108137.

Marin, E., Boschetto, F., Zanocco, M., Doan, H. N., Sunthar, T. P. M., Kinashi, K., Iba, D., Zhu, W. & Pezzotti, G. (2021). UV-curing and thermal ageing of methacrylated stereo-lithographic resin. *Polymer Degradation and Stability*, 185, 109503. doi : 10.1016/j.polymdegradstab.2021.109503.

Maskery, I., Sturm, L., Aremu, A. O., Panesar, A., Williams, C. B., Tuck, C. J., Wildman, R. D., Ashcroft, I. A. & Hague, R. J. M. (2018). Insights into the mechanical properties of several triply periodic minimal surface lattice structures made by polymer additive manufacturing. *Polymer*, 152, 62–71. doi : 10.1016/j.polymer.2017.11.049.

Maxwell, J. C. (1864). On the calculation of the equilibrium and stiffness of frames. *The London, Edinburgh, and Dublin Philosophical Magazine and Journal of Science*. doi : 10.1080/14786446408643668. Publisher : Taylor & Francis Group.

McCormick, N. & Lord, J. (2010). Digital Image Correlation. *Materials Today*, 13(12), 52–54. doi : 10.1016/S1369-7021(10)70235-2.

Meddahi, Y. (2015). *Modélisation, Estimation et Commande d'un Ballon Dirigeable Autonome*. (Thesis, University of sciences and technology on Oran). Repéré à Accepted : 2015-02-24T10 :01 :38Z.

Medellin-Castillo, H. I. & Pedraza Torres, J. E. (2010, July). Rapid Prototyping and Manufacturing : A Review of Current Technologies. pp. 609–621. doi : 10.1115/IMECE2009-11750.

Medellin-Castillo, H. I. & Zaragoza-Siqueiros, J. (2019). Design and Manufacturing Strategies for Fused Deposition Modelling in Additive Manufacturing : A Review. *Chinese Journal of Mechanical Engineering*, 32(1), 53. doi : 10.1186/s10033-019-0368-0.

Meloni, M., Cai, J., Zhang, Q., Sang-Hoon Lee, D., Li, M., Ma, R., Parashkevov, T. E. & Feng, J. (2021). Engineering Origami : A Comprehensive Review of Recent Applications, Design Methods, and Tools. *Advanced Science*, 8(13), 2000636. doi : 10.1002/advs.202000636. _eprint : https ://onlinelibrary.wiley.com/doi/pdf/10.1002/advs.202000636.

Menard, K. P. & Menard, N. (2020). *Dynamic Mechanical Analysis* (éd. 3). Boca Raton : CRC Press. doi : 10.1201/9780429190308.

Mieszala, M., Hasegawa, M., Guillonneau, G., Bauer, J., Raghavan, R., Frantz, C., Kraft, O., Mischler, S., Michler, J. & Philippe, L. (2017). Micromechanics of Amorphous Metal/Polymer Hybrid Structures with 3D Cellular Architectures : Size Effects, Buckling Behavior, and Energy Absorption Capability. *Small*, 13(8), 1602514. doi : 10.1002/smll.201602514. _eprint : https ://onlinelibrary.wiley.com/doi/pdf/10.1002/smll.201602514.

Mines, R. A. W., Tsopanos, S., Shen, Y., Hasan, R. & McKown, S. T. (2013). Drop weight impact behaviour of sandwich panels with metallic micro lattice cores. *International Journal of Impact Engineering*, 60, 120–132. doi : 10.1016/j.ijimpeng.2013.04.007.

Mir, M., Ali, M. N., Sami, J. & Ansari, U. (2014). Review of Mechanics and Applications of Auxetic Structures. *Advances in Materials Science and Engineering*, 2014, e753496. doi : 10.1155/2014/753496. Publisher : Hindawi.

Mistri, S. R. & Pant, R. S. (2017). Design and Fabrication of a Quick Dismantlable Remotely Controlled Semirigid Finless Airship. *Innovative Design and Development Practices in Aerospace and Automotive Engineering*, (Lecture Notes in Mechanical Engineering), 103–116. doi : 10.1007/978-981-10-1771-1_16.

Moosburger-Will, J., Greisel, M., Sause, M., Horny, R. & Horn, S. (2014). *Physical properties of partially cross-linked RTM6 epoxy resin*.

Moradi, M., Hasani, A., Pourmand, Z. & Lawrence, J. (2021). Direct laser metal deposition additive manufacturing of Inconel 718 superalloy : Statistical modelling and optimization by design of experiments. *Optics & Laser Technology*, 144, 107380. doi : 10.1016/j.optlastec.2021.107380.

Márquez, H. (2003). *Nonlinear Control Systems : Analysis and Design*. Hoboken, NJ.

Nayfeh, A. H. & Hefzy, M. S. (1978). Continuum modeling of three-dimensional truss-like space structures. *AIAA Journal*, 16(8), 779–787. doi : 10.2514/3.7581. Publisher : American Institute of Aeronautics and Astronautics _eprint : https ://doi.org/10.2514/3.7581.

Nayyeri, P., Zareinia, K. & Bougherara, H. (2022). Planar and nonplanar slicing algorithms for fused deposition modeling technology : a critical review. *The International Journal of Advanced Manufacturing Technology*, 119(5), 2785–2810. doi : 10.1007/s00170-021-08347-x.

Nazir, A., Abate, K. M., Kumar, A. & Jeng, J.-Y. (2019). A state-of-the-art review on types, design, optimization, and additive manufacturing of cellular structures. *The International Journal of Advanced Manufacturing Technology*, 104(9), 3489–3510. doi : 10.1007/s00170-019-04085-3. MAG ID : 2956815218.

Newman, J. N. (2018). *Marine Hydrodynamics*. The MIT Press. Repéré à https://library.oapen.org/handle/20.500.12657/26039.

Nitta, Y., Inai, S., Matsumura, K., Ishida, M., Onai, T. & Nishitani, A. (2017). The Visual Inspection Methodology for Ceiling Utilizing the Blimp. *Procedia Engineering*, 188, 256–262. doi : 10.1016/j.proeng.2017.04.482.

Novelino, L. S., Ze, Q., Wu, S., Paulino, G. H. & Zhao, R. (2020). Untethered control of functional origami microrobots with distributed actuation. *Proceedings of the National Academy of Sciences*, 117(39), 24096–24101. doi : 10.1073/pnas.2013292117.

Nowak, A. (2015). Application of Voronoi diagrams in contemporary architecture and town planning. *Challenges of Modern Technology*, Vol. 6(no. 2). Repéré à http://yadda.icm.edu.pl/baztech/element/bwmeta1.element.baztech-5259df1a-e1f7-442f-a68c-10c0c2b35c96.

Onal, C. D., Wood, R. J. & Rus, D. (2013). An Origami-Inspired Approach to Worm Robots. *IEEE/ASME Transactions on Mechatronics*, 18(2), 430–438. doi : 10.1109/TMECH.2012.2210239. Conference Name : IEEE/ASME Transactions on Mechatronics.

O'Neil, J., Salviato, M. & Yang, J. (2023). Energy absorption behavior of filament wound CFRP origami tubes pre-folded in Kresling pattern. *Composite Structures*, 304, 116376. doi : 10.1016/j.compstruct.2022.116376.

Pagano, A., Yan, T., Chien, B., Wissa, A. & Tawfick, S. (2017). A crawling robot driven by multi-stable origami. *Smart Materials and Structures*, 26(9), 094007. doi : 10.1088/1361-665X/aa721e.

Palossi, D., Gomez, A., Draskovic, S., Keller, K., Benini, L. & Thiele, L. (2017, May). Self-Sustainability in Nano Unmanned Aerial Vehicles : A Blimp Case Study. pp. 79–88. doi : 10.1145/3075564.3075580.

Park, C.-Y., Lee, Y.-A., Jang, J. & Han, M.-W. (2023). Origami and Kirigami Structure for Impact Energy Absorption : Its Application to Drone Guards. *Sensors*, 23(4), 2150. doi : 10.3390/s23042150. Number : 4 Publisher : Multidisciplinary Digital Publishing Institute.

Park, S.-i. & Rosen, D. W. (2016). Quantifying effects of material extrusion additive manufacturing process on mechanical properties of lattice structures using as-fabricated voxel modeling. *Additive Manufacturing*, 12, 265–273. doi : 10.1016/j.addma.2016.05.006.

Patpatiya, P., Chaudhary, K., Shastri, A. & Sharma, S. (2022). A review on polyjet 3D printing of polymers and multi-material structures. *Proceedings of the Institution of Mechanical Engineers, Part C : Journal of Mechanical Engineering Science*, 236(14), 7899–7926. doi : 10.1177/09544062221079506. Publisher : IMECHE.

Patterson, A. E., Pereira, T. R., Allison, J. T. & Messimer, S. L. (2021). IZOD impact properties of full-density fused deposition modeling polymer materials with respect to raster angle and print orientation. *Proceedings of the Institution of Mechanical Engineers, Part C : Journal of Mechanical Engineering Science*, 235(10), 1891–1908. doi : 10.1177/0954406219840385. Publisher : IMECHE.

Pham, D. T. (1977). *Quelques rappels sur la notion de masse ajoutée en mécanique des fluides*.

Pierre-Etienne, C. (2018). Une caverne exceptionnelle | UQAM. Section : Recherche, Repéré à https://actualites.uqam.ca/2018/une-caverne-exceptionnelle-saint-leonard/.

Poli, C. (2001). *Design for Manufacturing : A Structured Approach*. Butterworth-Heinemann.

Preez, V., Futerman, R. & Barnes, V. (2014). *Understanding group work in Higher Education : Establishing a culture of deliberation amongst design students.*

Ram, C. V. & Pant, R. S. (2010). Multidisciplinary Shape Optimization of Aerostat Envelopes. *Journal of Aircraft*, 47(3), 1073–1076. doi : 10.2514/1.46744.

Ramakrishna, S., Hamada, H., Maekawa, Z. & Sato, H. (1995). Energy Absorption Behavior of Carbon-Fiber-Reinforced Thermoplastic Composite Tubes. *Journal of Thermoplastic Composite Materials*, 8(3), 323–344. doi : 10.1177/089270579500800307. Publisher : SAGE Publications Ltd STM.

Rashed, M. G., Ashraf, M., Mines, R. A. W. & Hazell, P. J. (2016). Metallic microlattice materials : A current state of the art on manufacturing, mechanical properties and applications. *Materials & Design*, 95, 518–533. doi : 10.1016/j.matdes.2016.01.146.

Rathbun, H., Radford, D., Xue, Z., He, M., Yang, J., Deshpande, V., Fleck, N. A., Hutchinson, J. W., Zok, F. W. & Evans, A. G. (2006). Performance of metallic honeycomb-core sandwich beams under shock loading. *International Journal of Solids and Structures*, 43(6), 1746–1763. doi : 10.1016/j.ijsolstr.2005.06.079. MAG ID : 2107419865.

Rowe, P. G. (1986). *Design Thinking*. Cambridge, MA, USA : MIT Press.

Rumayshah, K. K., Prayoga, A. & Moelyadi, M. A. (2018). Design of High Altitude Long Endurance UAV : Structural Analysis of Composite Wing using Finite Element Method. *Journal of Physics : Conference Series*, 1005(1), 012025. doi : 10.1088/1742-6596/1005/1/012025. Publisher : IOP Publishing.

SakshiKokil-Shah, Sur, A., Darvekar, S. & Shah, M. (2021). Recent Advancements of Micro-Lattice Structures : Application, Manufacturing Methods, Mechanical Properties, Topologies and Challenges. *Arabian Journal for Science and Engineering*, 46(12), 11587–11600. doi : 10.1007/s13369-021-05992-y.

Salas Gordoniz, J. E., Reeves, N. & St-Onge, D. (2021, November). Modular Foldable Airship Concept for Subterranean Exploration. doi : 10.1115/DETC2021-69954.

Salas Gordoniz, J. E., Reeves, N. & St-Onge, D. (2022). Scutigera : Design, Modeling, and Experiments for an Artistic Multibody Airship Concept. *Journal of Mechanisms and Robotics*, 14(4). doi : 10.1115/1.4053926. Publisher : American Society of Mechanical Engineers Digital Collection.

Salas Gordoniz, J. E., Saad, M. & St-Onge, D. (2024). Intuitive physics-driven approach : Design and calibration of a flight controller for indoor blimps. Repéré à https://espace2.etsmtl.ca/id/eprint/28775/.

Sangwin, C. (2024). On Heron's Formula for the Area of a Plane Triangle. *The College Mathematics Journal*, 0(0), 1–10. doi : 10.1080/07468342.2024.2318191. Publisher : Taylor & Francis _eprint : https ://doi.org/10.1080/07468342.2024.2318191.

Santos, A., González Lema, C., Miño Puga, M., Párraga, C. & Calderon, F. (2017, January). Design Thinking as a methodology for solving problems : contributions from academia to society. doi : 10.18687/LACCEI2017.1.1.256.

Saremian, R., Badrossamay, M., Foroozmehr, E., Kadkhodaei, M. & Forooghi, F. (2021). Experimental and numerical investigation on lattice structures fabricated by selective laser melting process under quasi-static and dynamic loadings. *The International Journal of Advanced Manufacturing Technology*, 112(9), 2815–2836. doi : 10.1007/s00170-020-06112-0.

Sauro, J. (2014). Assessing the Validity of Your Research – MeasuringU. Repéré à https://measuringu.com/validity-research/.

Schaedler, T. A. & Carter, W. B. (2016). Architected Cellular Materials. *Annual Review of Materials Research*, 46(Volume 46, 2016), 187–210. doi : 10.1146/annurev-matsci-070115-031624. Publisher : Annual Reviews.

Schaedler, T. A., Ro, C. J., Sorensen, A. E., Eckel, Z., Yang, S. S., Carter, W. B. & Jacobsen, A. J. (2014). Designing Metallic Microlattices for Energy Absorber Applications. *Advanced Engineering Materials*, 16(3), 276–283. doi : 10.1002/adem.201300206. _eprint : https ://onlinelibrary.wiley.com/doi/pdf/10.1002/adem.201300206.

Schneider, J. & Kumar, S. (2023). Comparative performance evaluation of microarchitected lattices processed via SLS, MJ, and DLP 3D printing methods : Experimental investigation and modelling. *Journal of Materials Research and Technology*, 26, 7182–7198. doi : 10.1016/j.jmrt.2023.09.061.

Segonds, F. (2019). Créativité et fabrication additive - Infographie. *Fabrication additive – Impression 3D*. doi : 10.51257/a-v1-ibm7017.

Shahrubudin, N., Lee, T. C. & Ramlan, R. (2019). An Overview on 3D Printing Technology : Technological, Materials, and Applications. *Procedia Manufacturing*, 35, 1286–1296. doi : 10.1016/j.promfg.2019.06.089.

Sharf, I., Laumonier, B., Persson, M. & Robert, J. (2008, May). Control of a fully-actuated airship for satellite emulation. *2008 IEEE International Conference on Robotics and Automation*, pp. 2218–2219. doi : 10.1109/ROBOT.2008.4543542.

Sharf, I., Persson, S., St-Onge, D. & Reeves, N. (2013). *Development of Aerobots for Satellite Emulation, Architecture and Art*. doi : 10.1007/978-3-319-00065-7_13.

Slotine, J.-J. E. & Li, W. (1991). *Applied nonlinear control*. Englewood Cliffs, N.J : Prentice Hall.

Smith, M., Guan, Z. & Cantwell, W. J. (2013). Finite element modelling of the compressive response of lattice structures manufactured using the selective laser melting technique. *International Journal of Mechanical Sciences*, 67, 28–41. doi : 10.1016/j.ijmecsci.2012.12.004. MAG ID : 2016460082.

St-Onge, D. (2011). *MODÉLISATION ET COMMANDE D'UN ROBOT VOLANT ROBUSTE*. (Thèse de doctorat, Université Laval).

St-Onge, D., Reeves, N. & Gosselin, C. (2011, June). [VOILES | SAILS] : A modular architecture for a fast parallel development in an international multidisciplinary project. *2011 15th International Conference on Advanced Robotics (ICAR)*, pp. 482–488. doi : 10.1109/ICAR.2011.6088614.

Steenhuis, H.-J. & Pretorius, L. (2016). Consumer additive manufacturing or 3D printing adoption : an exploratory study. *Journal of Manufacturing Technology Management*, 27(7), 990–1012. doi : 10.1108/JMTM-01-2016-0002. Publisher : Emerald Group Publishing Limited.

Stockbridge, C., Ceruti, A. & Marzocca, P. (2012). Airship Research and Development in the Areas of Design, Structures, Dynamics and Energy Systems. *International Journal of Aeronautical and Space Sciences*, 13, 170–187. doi : 10.5139/IJASS.2012.13.2.170.

Suvarna, S., Joshi, A., Dubey, A. & Pant, R. (2019). *Design and Fabrication of a High Endurance, Cost-Effective, Auto-Stabilised Airship*.

Suzuki, H. & Wood, R. J. (2020). Origami-inspired miniature manipulator for teleoperated microsurgery. *Nature Machine Intelligence*, 2(8), 437–446. doi : 10.1038/s42256-020-0203-4. Publisher : Nature Publishing Group.

Syam, W. P., Jianwei, W., Zhao, B., Maskery, I., Elmadih, W. & Leach, R. (2018). Design and analysis of strut-based lattice structures for vibration isolation. *Precision Engineering*, 52, 494–506. doi : 10.1016/j.precisioneng.2017.09.010.

Tabiai, I., Delorme, R., Therriault, D. & Levesque, M. (2018). In-situ Full Field Measurements During Inter-Facial Debonding in Single Fiber Composite Under Transverse Load. *Experimental Mechanics*, 58(9), 1451–1467. doi : 10.1007/s11340-018-0429-9.

Tang, Y. & Zhao, Y. F. (2016). A survey of the design methods for additive manufacturing to improve functional performance. *Rapid Prototyping Journal*, 22(3), 569–590. doi : 10.1108/RPJ-01-2015-0011. Publisher : Emerald Group Publishing Limited.

Tao, Q. (2020). *Design and Control of an Indoor Miniature Autonomous Blimp*. (Thèse de doctorat, Georgia Tech). Repéré à Publisher : Georgia Institute of Technology.

Thomas, M., Davoine, C. & Drawin, S. (2019). Fabrication additive en aéronautique et en spatial. *Travail des matériaux - Assemblage*. doi : 10.51257/a-v1-bm7940.

Thompson, M. K., Moroni, G., Vaneker, T., Fadel, G., Campbell, R. I., Gibson, I., Bernard, A., Schulz, J., Graf, P., Ahuja, B. & Martina, F. (2016). Design for Additive Manufacturing : Trends, opportunities, considerations, and constraints. *CIRP Annals*, 65(2), 737–760. doi : 10.1016/j.cirp.2016.05.004.

Thor I., F. (1994). *Guidance and control of Ocean Vehicles* (éd. John Wilez & Sons). Norway.

Titenkov, S. V. & Zhuravlev, V. Y. (2018). PROSPECTS FOR THE DEVELOPMENT OF THE SYSTEM OF BENDING PIPELINES OF 3D CONFIGURATION IN PRODUCTION. *Siberian Aerospace Journal*, 19(4), 703–715. doi : 10.31772/2587-6066-2018-19-4-703-715. Number : 4.

Tonelli, D., Pietroni, N., Puppo, E., Froli, M., Cignoni, P., Amendola, G. & Scopigno, R. (2016). Stability of Statics Aware Voronoi Grid-Shells. *Engineering Structures*, 116, 70–82. doi : 10.1016/j.engstruct.2016.02.049.

Tripathi, K., Kukreja, K. & Gupta, N. (2022). Fabrication of Isogrids by Conventional and Unconventional Techniques : A Comparative Review Study. *Recent Advances in Industrial Production*, pp. 429–436. doi : 10.1007/978-981-16-5281-3_41.

Turner, D., Crozier, P. & Reu, P. (2015). *Digital Image Correlation Engine* (Rapport n°DICE ; 003748MLTPL00).

Ushijima, K., Cantwell, W., Mines, R., Tsopanos, S. & Smith, M. (2011). An investigation into the compressive properties of stainless steel micro-lattice structures. *Journal of Sandwich Structures & Materials*, 13(3), 303–329. doi : 10.1177/1099636210380997. Publisher : SAGE Publications.

Vanderesse, N., Richter, A., Nuno, N. & Bocher, P. (2018). Measurement of deformation heterogeneities in additive manufactured lattice materials by Digital Image Correlation : Strain maps analysis and reliability assessment. *Journal of the Mechanical Behavior of Biomedical Materials*, 86, 397–408. doi : 10.1016/j.jmbbm.2018.07.010.

Vaughn, D. G., Canning, J. M. & Hutchinson, J. W. (2005). Coupled Plastic Wave Propagation and Column Buckling. *Journal of Applied Mechanics*, 72(1), 139–146. doi : 10.1115/1.1825437.

Vilardell, A. M., Takezawa, A., du Plessis, A., Takata, N., Krakhmalev, P., Kobashi, M., Yadroitsava, I. & Yadroitsev, I. (2019). Topology optimization and characterization of Ti6Al4V ELI cellular lattice structures by laser powder bed fusion for biomedical applications. *Materials Science and Engineering : A*, 766, 138330. doi : 10.1016/j.msea.2019.138330.

von Braun, C. F. (1975). Airships in the future. Approaching the unknowns. *Futures*, 7(6), 475–484. doi : 10.1016/0016-3287(75)90004-X.

W, M. B. (2017). Aerodynamics, aeronautics, and flight mechanics. Repéré à http://archives.umc.edu.dz/handle/123456789/123142. Accepted : 2017-01-04T09 :50 :38Z ISBN : 9780471575061 Publisher : John Wiley.

Wakil, S. D. E. (2019). *Processes and Design for Manufacturing, Third Edition*. CRC Press.

Wang, H.-C. (2022). A Heterogeneous Unmanned Ground Vehicle and Blimp Robot Team for Search and Rescue using Data-driven Autonomy and Communication-aware Navigation. *Field Robotics*, 38.

Wu, Y., Fang, J., Wu, C., Li, C., Sun, G. & Li, Q. (2023). Additively manufactured materials and structures : A state-of-the-art review on their mechanical characteristics and energy absorption. *International Journal of Mechanical Sciences*, 246, 108102. doi : 10.1016/j.ijmecsci.2023.108102.

Xiao, L. & Song, W. (2018). Additively-manufactured functionally graded Ti-6Al-4V lattice structures with high strength under static and dynamic loading : Experiments. *International Journal of Impact Engineering*, 111, 255–272. doi : 10.1016/j.ijimpeng.2017.09.018. MAG ID : 2763006544.

Xiao, L., Song, W. & Xu, X. (2020a). Experimental study on the collapse behavior of graded Ti-6Al-4V micro-lattice structures printed by selective laser melting under high speed impact. *Thin-Walled Structures*, 155, 106970. doi : 10.1016/j.tws.2020.106970.

Xiao, L., Xu, X., Song, W. & Hu, M. (2020b). A Multi-Cell Hybrid Approach to Elevate the Energy Absorption of Micro-Lattice Materials. *Materials*, 13(18), 4083. doi : 10.3390/ma13184083. Number : 18 Publisher : Multidisciplinary Digital Publishing Institute.

Xiao, R., Li, X., Jia, H., Surjadi, J. U., Li, J., Lin, W., Gao, L., Chirarattananon, P. & Lu, Y. (2021). 3D printing of dual phase-strengthened microlattices for lightweight micro aerial vehicles. *Materials & Design*, 206, 109767. doi : 10.1016/j.matdes.2021.109767.

Xiong, J., Mines, R., Ghosh, R., Vaziri, A., Ma, L., Ohrndorf, A., Christ, H.-J. & Wu, L. (2015). Advanced Micro-Lattice Materials. *Advanced Engineering Materials*, 17(9), 1253–1264. doi : 10.1002/adem.201400471. _eprint : https ://onlinelibrary.wiley.com/doi/pdf/10.1002/adem.201400471.

Yan, C., Hao, L., Hussein, A. & Young, P. (2015). Ti–6Al–4V triply periodic minimal surface structures for bone implants fabricated via selective laser melting. *Journal of the Mechanical Behavior of Biomedical Materials*, 51, 61–73. doi : 10.1016/j.jmbbm.2015.06.024.

Yang, C.-M., Ju-Ying, H., Yuan-Li, W. & Yu-Hsuan, L. (2019). Analysis of Mercedes-Benz Concept Car Using Biomimicry Design Spiral and Template Analysis-An Exploratory Study. 49–56.

Yang, M., Defillion, J., Scarpa, F. & Schenk, M. (2023). Volume Optimisation of Multi-stable Origami Bellows for Deployable Space Habitats. *Acta Mechanica Solida Sinica*, 36(4), 514–530. doi : 10.1007/s10338-023-00401-3.

Yasuuda, H., Gopalarethinam, B., Kunimine, T., Tachi, T. & Yang, J. (2019). Origami-Based Cellular Structures with In Situ Transition between Collapsible and Load-Bearing Configurations. *Advanced Engineering Materials*, 21(12), 1900562. doi : 10.1002/adem.201900562. _eprint : https ://onlinelibrary.wiley.com/doi/pdf/10.1002/adem.201900562.

Yeo, S. J., Oh, M. J. & Yoo, P. J. (2019). Structurally Controlled Cellular Architectures for High-Performance Ultra-Lightweight Materials. *Advanced Materials*, 31(34), 1803670. doi : 10.1002/adma.201803670. _eprint : https ://onlinelibrary.wiley.com/doi/pdf/10.1002/adma.201803670.

Yoder, M., Thompson, L. & Summers, J. (2019). Size effects in lattice-structured cellular materials : edge softening effects. *Journal of Materials Science*, 54. doi : 10.1007/s10853-018-3103-9.

Zhang, H., Zhou, H., Zhou, Z., Huizhong, Z., Zhang Xiaoyu, Zhang, X., Yang, J., Lei Hongshuai, Lei, H. & Han, F. (2021a). Energy absorption diagram characteristic of metallic self-supporting 3D lattices fabricated by additive manufacturing and design method of energy absorption structure. *International Journal of Solids and Structures*, 111082. doi : 10.1016/j.ijsolstr.2021.111082. MAG ID : 3160303303.

Zhang, J., Li, T., Wang, C. & Yan, X. (2021b). Aerodynamic Drag Characteristics of Miura-Ori Composite Structure. *Journal of Aerospace Engineering*, 34(4), 06021004. doi : 10.1061/(ASCE)AS.1943-5525.0001273.

Zhang, J. & Yanagimoto, J. (2021). Topology optimization of microlattice dome with enhanced stiffness and energy absorption for additive manufacturing. *Composite Structures*, 255, 112889. doi : 10.1016/j.compstruct.2020.112889.

Zhang, R., Hao, G., Zhang, K. & Li, Z. (2023). Unmanned aerial vehicle navigation in underground structure inspection : A review. *Geological Journal*, 58(6), 2454–2472. doi : 10.1002/gj.4763. _eprint : https ://onlinelibrary.wiley.com/doi/pdf/10.1002/gj.4763.

Zhang, Z., Chen, G., Wu, H., Kong, L. & Wang, H. (2020). A Pneumatic/Cable-driven Hybrid Linear Actuator with Combined Structure of Origami Chambers and Deployable Mechanism. *IEEE Robotics and Automation Letters*, 1–1. doi : 10.1109/LRA.2020.2976324.

Zhang, Z., Fan, W., Chen, G., Luo, J., Lu, Q. & Wang, H. (2021c, April). A 3D Printable Origami Vacuum Pneumatic Artificial Muscle with Fast and Powerful Motion. *2021 IEEE 4th International Conference on Soft Robotics (RoboSoft)*, pp. 551–554. doi : 10.1109/RoboSoft51838.2021.9479194.

Zheng, X., Lee, H., Weisgraber, T. H., Shusteff, M., DeOtte, J., Duoss, E. B., Kuntz, J. D., Biener, M. M., Ge, Q., Jackson, J. A., Kucheyev, S. O., Fang, N. X. & Spadaccini, C. M. (2014). Ultralight, ultrastiff mechanical metamaterials. *Science*, 344(6190), 1373–1377. doi : 10.1126/science.1252291. Publisher : American Association for the Advancement of Science Section : Report.

Zheng, Z., Li, J., Agrawal, P., Lei, Z., John-Sabu, A. & Mehta, A. (2021). User Based Design and Evaluation Pipeline for Indoor Airships. arXiv. arXiv :2110.09748 [cs, eess], Repéré à http://arxiv.org/abs/2110.09748.

Zirbel, S. A., Trease, B. P., Thomson, M. W., Lang, R. J., Magleby, S. P. & Howell, L. H. (2015, May). HanaFlex : a large solar array for space applications. *Micro- and Nanotechnology Sensors, Systems, and Applications VII*, 9467, 179–187. doi : 10.1117/12.2177730.